Cape Peninsula
University of Technology

DEVELOPMENT OF MICRO-NUCLEAR GENERATORS FOR AUTONOMOUS SYSTEMS

by

OLUKAYODE LAWRENCE AYODELE

Thesis submitted in fulfilment of the requirements for the degree

Doctor of Engineering: Mechanical Engineering

in the Faculty of Engineering and the Built Environment

at the Cape Peninsula University of Technology

Supervisor: Prof MTE Kahn

Bellville: August 2022

DECLARATION

I, Olukayode Lawrence Ayodele, declare that the contents of this dissertation/thesis represent my own unaided work, and that the thesis has not previously been submitted for academic examination towards any qualification. Furthermore, it represents my own opinions and not necessarily those of the Cape Peninsula University of Technology.

22 August 2022

Signed **Date**

ABSTRACT

As concerns over clean power generation grow, it is a relief that a considerable quantity of underutilized waste heat could be used to provide clean power for hundreds of years. The increased interest in space research, satellite operations, structural health monitoring, and terrestrial monitoring in hostile and inaccessible zones places a high demand for energy sources for autonomous systems. In the same vein, there is also a growing interest in reliable and low-cost power sources for utility applications.

Conventional electrochemical batteries that could be used for utility-scale energy storage are plagued by low energy storage density, short life, disposal of unwanted batteries, and related undesired maintenance requirements of recharging or replacement, which endangers the environment. Wind, fuel cell, and solar energy sources being exploited to mitigate the adverse effect of environmental threats posed by batteries and fossil fuels are costly to acquire and maintain.

The availability of energy sources derived from waste heat from radioactive decay for domestic appliances and industrial equipment will also help alleviate the effects of climate change, which continues to threaten the environment due to fossil fuel energy-based sources that emit harmful carbon monoxide into the atmosphere. A combination of energy from waste heat, harvested via thermoelectricity and existing battery technology to produce a hybrid energy source will guarantee secured energy for a long period.

Based on the Seebeck effect, thermoelectric energy generation may considerably contribute to sustainable energy development and meet the growing demand for power in utility applications.

Mathematical modeling of the energy from waste heat, existing battery technologies, and a hybrid energy source are considered, and their performances are established using the MATLAB/Simulink environment. Results confirmed the comparative advantage of hybrid energy source over and above the respective electrochemical batteries and waste heat energy source in terms of effectiveness and performance efficiency.

Since batteries are required to operate in a constantly changing environment, the effects of temperatures on batteries were investigated. The results show that the performances of batteries decrease with a decrease in ambient temperature and that the higher the maximum operating capacity, the higher the internal temperature of the battery.

ACKNOWLEDGEMENTS

My profound gratitude goes to the Almighty God, who has made this thesis possible despite all the challenges encountered.

My deepest gratitude also goes to my supervisor, Prof MTE Khan, for his unflinching support, guidance, patience, and encouragement throughout the very long journey.

I would like to express my profound appreciation to the members of my family and friends for their invaluable support at critical periods.

Special gratitude goes to Dr Senthil Krishnamurthy for his support and helpful critiques that assisted greatly in the completion of this research.

The guidance and support provided by Prof Oluwaseun Oyekola are also much appreciated.

Finally, I would also like to profusely thank all my colleagues at the Cape Peninsula University of Technology for their support.

DEDICATION

This thesis is dedicated to my loved ones, and in particular, my mother, Mrs Bolawe Esther Ayodele, whose dedicated effort provided me with a sound foundational educational platform.

TABLE OF CONTENTS

LIST OF FIGURES

LIST OF TABLES

GLOSSARYS

A : Frequency factor
A_S : Area of the battery
AMTEC : Alkali metal thermo electric converter
C_P : Heat capacity
CBCF : Carbon-bonded carbon fiber
D : Duty cycle
DC : Direct current
eV : Electron volt
E : Activation energy
E_o : Fully charged battery voltage
EOC : End of charge
FWPF : Fine weave pierced fabric
GIS : Graphite impact shell
h : heat transfer coefficient
H : Hydrogen
H^+ : Hydrogen ion
i : Current
i* : Filtered current
J : Moment of inertia
K : Polarization coefficient/Polarization resistance
K_e : motor constant
K_i : Integral gain
K_p : Proportional gain
K_t : armature constant
keV : Kilo electron volt
Li-ion : lithium ion
m : mass
MEMS : Micro electrical mechanical systems
MER : Mars exploratory rovers
MMRTG : Multi-mission radioisotope thermoelectric generator
MOSFET : Metal–oxide–semiconductor field-effect transistor
MSL : Mars science laboratory
mV : milli volt
NASA : National aeronautics and space administration
NiCd : Nickel Cadmium
NiMH : Nickel Metal Hybride

O : Oxygen

O^- : Oxygen ion

OCV : Open circuit voltage

PbO_2 : Lead oxide

PF : Power factor

PI : Proportional integral

Q : Battery charge

Q_{gen} : Quantity of heat generated

R : Internal resistance

R_{th} : Convection thermal resistance

RIT : Rochester Institute of Technology

RPS : Radioisotope power systems

RTG : Radioisotope thermoelectric generators

RTE : Radioisotope thermoelectric energy

SoC : State of charge

t : Time

t_c : Thermal time constant

T : Average absolute temperature

T_a : Ambient temperature

T_C : Cold side temperature

T_{ref} : Nominal ambient temperature

T_{surf} : Surface temperature

TEG : Thermoelectric Generator

TEM : Thermoelectric module

T_H : Hot side temperature

T_{load} : Motor load

T_m : Motor torque

TPV : Thermophotovoltaic

U_o : Open circuit voltage

U_t : Terminal voltage

V_b : Battery voltage

V_e : Electromotive force

W : Power

Z : Figure of merit

ZT : Dimensionless figure of merit

^oC : Degrees in Celsius

μW : Micro-watts

ω_m : Motor speed

ω_{ref} : Reference speed

α : Seebeck coefficient

σ : Electrical conductivity

λ : Thermal conductivity

$\frac{E}{T}$: Voltage temperature coefficient

$\frac{\Delta Q}{\Delta T}$: Maximum capacity temperature coefficient

α : Arrhenius rate constant for polarization resistance

β : Arrhenius rate constant for internal resistance

CHAPTER ONE

GENERAL INTRODUCTION

1.1 Introduction

Throughout history, the earth and its environment have been the provider of good things such as fertile land, air, water, and energy sources. Technological advancement has been important in allowing us to use energy more effectively to get what we want. The dependence of human beings on energy is associated with human survival as energy has been central to human existence and development. Access to energy is crucial for technological advancement and economic growth. The ever-increasing world population growth and the continued significant depletion of natural energy sources bring about the rising environmental and economic costs to generate electrical energy that meet the world energy requirement.

In order to ensure the sustainability of non-endangered earth for future generations, solutions must be found to the current energy crisis and the inherent drawbacks associated with the reliance on energy from fossil fuels. The growing concern over the continued usage of fossil fuels for electrical energy generation and hence the need to considerably reduce dependence on this energy source has compelled a pragmatic move towards developing cleaner, safer, and more renewable energy systems. Solar, wind, and other non-renewable energy sources are increasingly being explored as technological advancement increases their efficiencies and allows for practical applications. Human and industrial activities release a vast amount of waste heat to the environment. The exploitation of this waste heat to generate electrical energy will go a long way to solve the current world energy shortage crisis and mitigate the environmental challenges associated with fossil fuels when used to generate electrical energy.

1.2 Research problem

The existing electrochemical batteries used for micro-scale devices in autonomous systems applications, including sensors for toxic gas and sensors in remote, inaccessible locations for environmental monitoring or hermetic environments such as extreme heat, cold, or corrosive conditions are afflicted by low energy density, short life, undesired maintenance requirements of recharging or replacement. Thus, it is timely to explore alternative energy storage options to hinder the drawbacks of electrochemical batteries. Several alternative energy storage options can be considered. The problem in this research is to investigate a hybrid battery comprising electrochemical and nuclear batteries to enhance the efficiency, reliability and lifespan of the energy storage device.

1.3 Background to the research problem

Over the past 20 years, breakthroughs in manufacturing techniques have led to the development of a variety of devices at the micro-scale level ranging from mili to nanometers. However, it has proven difficult to achieve similar progress in developing micro-scale power units that could power such miniature devices (Guo et al., 2008). The traditional electrochemical batteries still being utilized in several micro-scale and nano-scale devices lead to bulky systems and frequent recharging or replacement of batteries in addition to low energy density and limited life span (Duggirala et al., 2004). Harnessing radiation energy from the spontaneous decay of radioisotopes to generate electrical energy for macro-scale devices has been under development since the 1950s. Still, the exploration of radioactive micropower generation has not been extensively investigated.

1.4 Objective of the research

This study aims to model and simulate a hybrid energy storage system combining electrochemical and nuclear batteries. The modeling and simulation are carried out using Matlab/Simulink environment. The specific objectives of the study include:

- Developing the Simulink models of electrochemical batteries including NiCd, NiMH, Lead-Acid and Li-ion batteries.
- Developing the Simulink model of nuclear battery
- Developing the Simulink of the integrated energy storage combining electrochemical and nuclear batteries, and auxiliary components
- Assessing the effect of temperature on the hybrid battery system

1.5 Scope and limitation of the research

Owing to the concerns of environmental hazards associated with radiation emission, this research is constrained as follows:

- Plutonium-238, a radioisotope that is largely used for biological purposes, will be used as the heat source
- Nuclear reactor energy generation will not be investigated
- Radioisotope energy source will be solely based on the static conversion of heat energy into electrical energy, i.e., dynamic energy conversion system will not be investigated
- Rechargeable electrochemical batteries are considered

1.6 Significance of the research

Realizing miniaturized power units with a long lifetime for applications in harsh and unreachable environments where the replacement of electrochemical batteries would be costly or nearly impossible is a significant necessity for the success of systems operating in such environments. To lessen the existing environmental impact of global warming, energy-scavenging methods of capturing ambient energy such as wind and solar are being used. In addition to their inherent disadvantages, the availability of these methods for scavenging energy at the micro level presents a significant problem.

Innovative methods for micro-scale energy conversion into useful forms can considerably enhance the growth of sustainable energy sources and satisfy the increasing demand for electricity in small-scale applications. Compact power units with a high power density and a long lifetime are necessary to operate a micro-system where the power supply does not take up most of the volume. Due to their low energy density and negative environmental effects on the disposal of used batteries, traditional electrochemical batteries fall short of these standards (Chou et al., 2011).

The underlined merit of this research is that it will provide an alternative source of energy that has the potential to replace fossil fuel energy-based sources that threaten the atmosphere due to their emissions of undesirable carbon monoxide. It will also provide an alternative to electrochemical batteries, fuel cells, solar, and wind energy sources that have their inherent limitations. Electrical energy derivable from radioisotopes has an energy density that can be about a hundred times higher than electrochemical batteries and ten times higher than hydrogen-based fuel cell fuels. Micro-nuclear generators, based on spontaneous decay of readily available radioisotopes, will produce a completely ‘green’ energy that is reliable and cheaper to operate and maintain. The possibility of having the radioisotope-based power source on a micro-scale will be a considerable breakthrough for autonomous systems that can function over a considerable life span.

1.7 Brief overview of the chapters

Chapter one covers the introduction to this dissertation wherein the following were highlighted: the research problem, background to the research problem, objective of the research, scope, and limitation of the research, and the significance of the research. Chapter two presents a literature review with a focus on waste heat exploitation technologies. Chapter three presents theories on nuclear and electrochemical batteries. Modelling and simulation of electrochemical and nuclear batteries for utility applications are presented in chapter four. Chapter five was dedicated to the modeling and simulation of the hybrid battery system. Conclusion and recommendations are presented in chapter six.

1.8 Publications

1.8.1 Journal articles

Ayodele, O.L., Oladele, K.O. and Kahn, M.T.E. 2016. Maximizing the potential of waste for generation of environmentally friendly energy. *Transylvanian review* vol. XX1V, no 10: 1996-2005.

Ayodele, O.L. and Kahn, M.T.E. 2016. Exploiting underutilized waste heat to generate environmentally friendly energy. *International Academy of Science*, *Engineering and Technology,* 2016, vol. 5, issue 2: 1-10

Ayodele, O.L., Oladele, K.O. and Kahn, M.T. 2019. Nuclear battery: a source of environmentally friendly energy. *Journal* of *Engineering, Design and Technology,* 2019, vol. 17, issue 1: 172 – 182

1.8.2 Conference

Ayodele O.L. and Kahn, M.T.E. 2014. Underutilise waste heat as potential to generate environmentally friendly energy. *Proceedings of the 11th conference on the industrial and commercial use of energy*, 2014, pp. 367-372

CHAPTER TWO
LITERATURE REVIEW

2.1 Introduction

The growing interest in earth monitoring, satellite activity, space exploration, and structural health monitoring in extreme and inaccessible environments has increased the demand for power sources for autonomous systems. Autonomous systems are designed to operate in known or unfamiliar environments for as long as possible for processing, providing, and storing data without being connected to an electrical grid. The system may operate for long periods in an external natural or industrial environment without human intervention. Autonomous systems, including actuators, environmental intelligence devices, and wireless sensor networks, can operate within a range of less than a few cubic centimeters and with less than a few hundred microwatts (μW) of power (CATRENE, 2009).

Energy is provided through electrochemical batteries, solar panels, fuel cells, and radioisotope generators for large-scale autonomous operations. Each of these energy sources has unique advantages and disadvantages. Current solar panels, in particular, can produce considerable power. However, solar panels have some disadvantages that come with them, some of which are: that they must be pointed at the sun, so they are ineffective whenever planetary systems or other objects obstruct the sun. Other disadvantages involve: they are comparatively costly to build, massive and fragile structures susceptible to damage from environmental factors, such as solar flares and meteorites or even mechanical issues. The amount of sunlight diminishes with the square of the distance between the sun and the satellite. Hence, the farther the satellite is from the sun, the less energy the solar panel produces. The sun's rays are 25 times more intense at the surface of the earth than on Jupiter (Weiling & Shantung, 2004). Low power generation for indoor applications is challenging due to solar cells' reliance on daylight solar lighting.

Fuel cells are characterized by a longer life than electrochemical batteries and are refueled, so they do not need to be recharged. In theory, fuel cells generate electric power as long as they are supplied with fuel. They are highly efficient, easy to build, emit nearly zero emissions, and operate quietly as they have no moving parts (Larminie & Dicks, 2003). They also operate at very high temperatures (400 -1000 ^{0}F), and managing the waste heat is frequently a major issue to deal with (Coutts, 1997). Currently, fuel cells serve as power sources on space shuttles and are very effective for other near-Earth missions. However, despite their benefits, they are relatively costly due to the high fuel cost associated with long flights.

Electrochemical batteries are robust, efficient, frequently used, and have a clear technological foundation. However, these batteries have the drawback of having a short lifetime, and rechargeable batteries used in remote locations require recharging from other power sources like photovoltaic panels (Rayment & Sherwin, 2003). Besides the aforementioned inadequacies, size is also a drawback. In some applications, an electrochemical battery adds approximately 40% to the size of a small device which it is required to be powered, hence a bulky system. Electrochemical batteries are also plagued with a tendency to degrade under harsh environmental conditions (Manasse et al., 1976). Batteries include chemicals damaging to the environment. These chemicals include cadmium, lead, lithium, mercury, sulfuric acid, zinc, and lithium. As a result, batteries exhibit toxicity that can harm both humans and the environment. This makes disposing of used and unneeded batteries a challenge (Riffat & Ma, 2003).

The exploitation of energy sources in the form of waste heat would help reduce the adverse effect of environmentally threatening global warming from fossil fuel-based energy systems, which endanger the ecosystem by releasing carbon monoxide into the atmosphere. Due to its relative advantages over other energy generation methods, thermoelectric energy generation, which is based on the Seebeck effect (Carmo et al., 2011), can substantially contribute to sustainable energy systems advancement and meet the increasing demand for "green" and flexible power in small scale applications.

Thermoelectric generator, which provides an alternative power source, possesses the following advantages: absence of toxic residuals, compact, extremely reliable, simple, independent of position (i.e., not affected by gravity), scalable, runs silently, and practically maintenance-free. Waste energy sources include but are not limited to power plants, factories, motor vehicles, human bodies, computers, and radioactivity (Tie & Tan, 2013). Despite the aforementioned merits, a thermoelectric generator exhibits a relatively low efficiency which is typically less than 10% (Sethumadhavan & Burger, 2006). Low efficiency is not a significant downside for low power generation but is a disadvantage for large power generation. This drawback has limited the application of thermoelectric generators to specialized military, medical, and aerospace missions, including radioisotope power for deep space probes and remote power such as oil pipelines and sea buoys, whereby safety and reliability are more important than cost. Since the sources of heat for a thermoelectric generator is almost free, as in the case of waste heat, where the comparatively low efficiency of the thermoelectric generation is not an overriding consideration, the running cost of a thermoelectric generator compensates for the relatively high construction cost (Rowe, 1999).

2.2 Waste heat exploitation technologies

2.2.1 Thermoelectric generators

The Seebeck effect, which is a phenomenon in which a temperature gradient generates an electrical voltage, is used by Thermoelectric Generators (TEGs), solid-state devices, to transform thermal energy from a temperature gradient directly into electricity (Carmo et al., 2011). TEG components do not need operating fluids or moving parts. Due to these characteristics, TEG is incredibly adaptable for standalone nodes in wireless sensor networks with harvesting capabilities. TEGs are dependable energy technologies that do not vibrate or make noise because they do not have mechanical moving parts. Compared to other useful energy sources, they are comparatively small in size and light in weight (Riffat & Ma, 2003). TEGs are small, extremely reliable, quiet, and eco-friendly. TEGs have a broad range of applications in both small and large-scale devices because of the characteristics above and the fairly low operating and maintenance expenses.

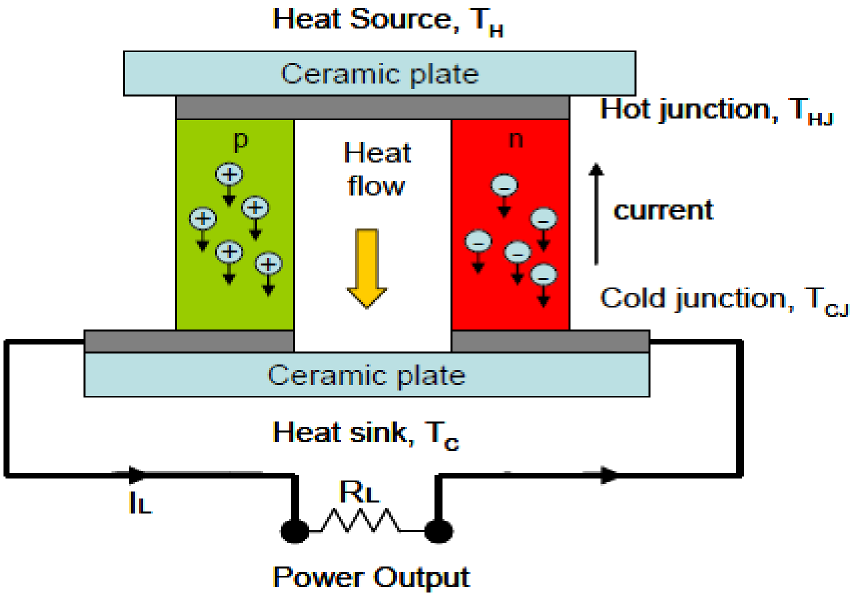

Figure 2. 1: Schematic diagram showing the basic concept of a simple thermoelectric power generator operating on the Seebeck effect (Ismail & Ahmed, 2009)

Figure 2.1 depicts the schematic of a straightforward thermoelectric generator that uses the Seebeck effect. The Seebeck voltage is a type of electrical voltage produced by the movement of heat and charge carriers. Due to the temperature difference between the heat source and the heat sink, a resistive load placed across the output terminals of thermoelectric materials (n-type and p-type semiconductors) will generate electricity. The electrons in the n-type semiconductor (negative charge carriers) absorb the thermoelectric couple's heat source and transfer it to the heat sink. In contrast, the holes in the p-type semiconductor (positive charge carriers) absorb the thermoelectric couple's heat source. Section 2.5 describes a thermoelectric module made up of mixtures of n-type and p-type semiconductors.

2.2.2 Performance characteristics of thermoelectric generators

The performance of a power source is vital and one of the performance measures of a TEG's efficiency. The TEG efficiency can be described in terms of its operating temperature and the "goodness factor," also referred to as a thermoelectric figure-of-merit Z. The goodness factor is given as follows (Ismail & Ahmed, 2009):

$$Z = \frac{\alpha^2 \sigma}{\lambda} \tag{2.1}$$

where α, σ and λ represent the Seebeck coefficient, the electrical conductivity, and the thermal conductivity, respectively. For a given temperature difference, the Seebeck coefficient, which determines the output voltage, is given by:

$$\alpha = \frac{dV}{dT} \tag{2.2}$$

The Seebeck coefficient of metals is generally in the range of 0 to 50 $\mu\mathrm{mK}^1$, while the Seebeck coefficient of semiconductors could reach over 350 $\mu\mathrm{mK}^1$ (Qiu & Hayden, 2008)

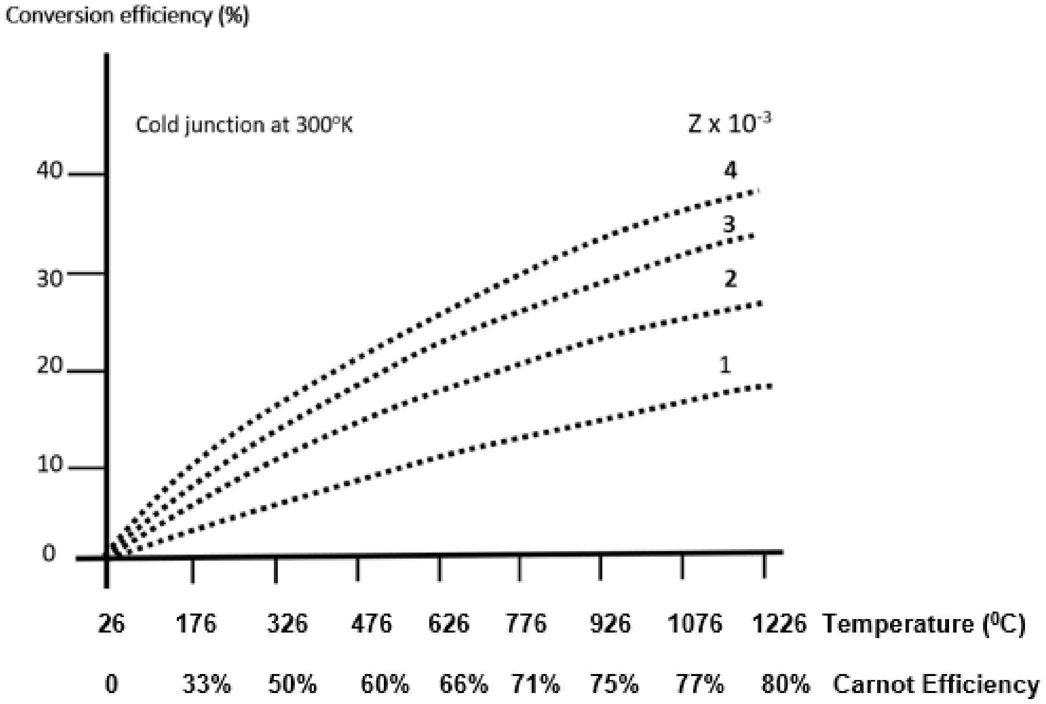

Figure 2. 2: Efficiency expressed in terms of temperature and figure-of-merit (Rowe, 2006)

Figure 2.2 illustrates the relationship between the operating temperature difference and the conversion efficiency for a variety of values of the material’s figure-of-merit (Rowe, 2006). A temperature rise corresponds to an increase in conversion efficiency. Additionally, a rise in the figure of merit results in a matching rise in conversion efficiency.

The figure-of-merit is frequently stated in its non – dimensional form through the multiplication of Z and T, and expressed as follows:

$$ZT = \frac{\alpha^2 \sigma T}{\lambda} \tag{2.3}$$

Where T is the thermoelectric module average absolute temperature of the cold and hot junctions, i.e.

$$T = \frac{T_H + T_L}{2} \tag{2.4}$$

The performance variable without dimensions ZT plays a crucial role in Seebeck-based sensing systems, such as infrared heat detectors (Carmo et al., 2011).

The electrical power factor (PF), an additional performance component for a TEG, is described as the electric power per unit area through which the heat flows per unit temperature gradient between the hot and cold junctions, and it is given as:

$$PF = \alpha^2 \sigma \tag{2.5}$$

Equation 2.5, a relative simplicity over Equation 2.1, is a commonly used figure-of-merit because it relates just the electrical properties $(\alpha \; and \; \sigma)$ while ignoring the thermal conductivity (λ), which is the most difficult property to measure out of the three properties $(\alpha, \sigma \; and \; \lambda)$ of the thermoelectric materials.

The efficiency of a TEG is measured as the ratio of energy provided to the load through the cold junction to the heat energy received at the hot junction (Rowe, 2006). Most commercially available TEGs produce power in the microwatt to multi-kilowatt range (Rowe, 1999). Due to the presently offered thermoelectric materials' fairly low dimensionless ZT, TEGs often display low efficiency (Ismail & Ahmed, 2009). As a result, it might be stated as follows (Ismail & Ahmed, 2009):

$$\eta = \frac{\dot{Q}_H - \dot{Q}_L}{\dot{Q}_H} = \frac{\dot{W}_e}{\dot{Q}_H} \tag{2.6}$$

Where η is the efficiency, $\dot{Q}_H$ is the heat transfer rate from the high-temperature heat source kept at a hot junction temperature T_H, $\dot{Q}_L$ is the heat rejection rate at a low temperature to the heat sink kept at a cold junction temperature T_L, $\dot{W}_e$ is the electric power output.

2.2.3 Thermoelectric materials

One of the significant factors influencing the performance of TEGs is the choice of thermoelectric materials. Going by Equation 2.5, a good thermoelectric material must have a significant Seebeck coefficient (to enhance the generation of large voltages and minimize electrical resistivity), which is found in low carrier concentration semiconductors or insulators, and a large electrical conductivity (to minimize electrical resistance), which is found in high carrier concentration metals. The thermoelectric power factor (PF) maximizes somewhere between metals and semiconductors, as shown in Figure 2.3 (Snyder & Ursell, 2003). Good thermoelectric material also needs low thermal conductivity to maintain a large temperature gradient across the thermocouples. Thermal conductivity in such materials comes from two sources of heat transport: phonons and electrons (or holes).

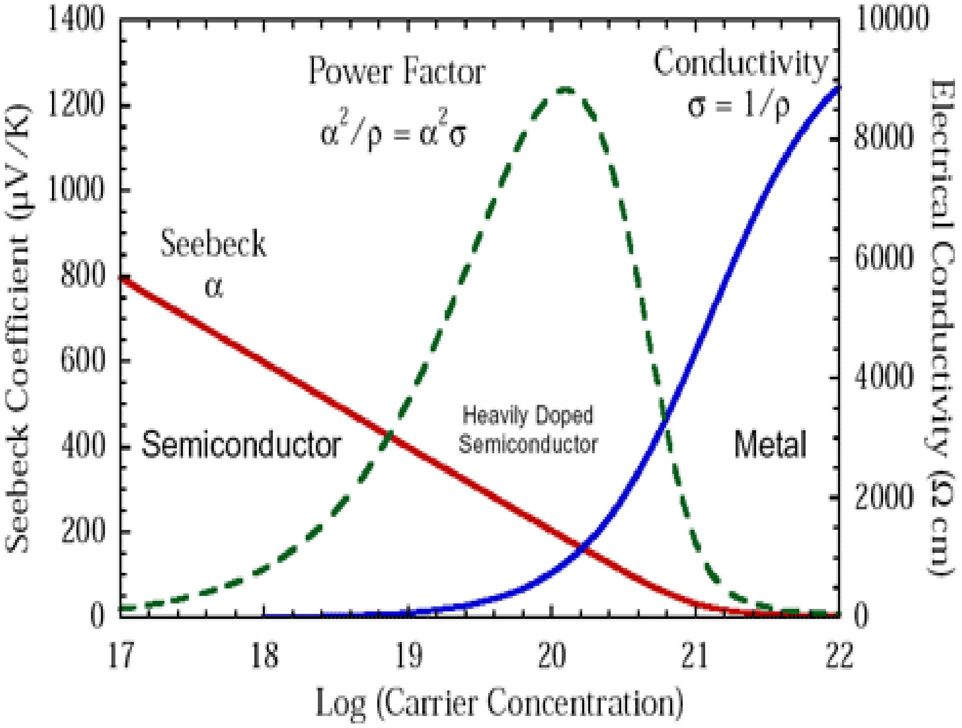

Figure 2. 3: Variation of Seebeck coefficient and electrical conductivity of metal and semiconductor (Snyder & Ursell, 2003)

Of the many materials known to date, relatively few have been identified as suitable thermoelectric materials. Early works on TEGs mostly utilized metal-based thermoelectric materials that yield very small figure-of-merit values because metals do not possess the ideal thermoelectric properties since they are associated with high electrical and thermal conductivity (Snyder & Ursell, 2003). However, several semiconductor materials are being developed with the advancement in technology. Semiconductor materials are good conductors of electricity, poor conductors of heat, and exhibit large values of the Seebeck coefficient (Bass, 1999). These semiconductors are heavily doped to create an excess of electrons (n-type) and heavily doped to create excess holes or deficiency of electrons (p-type). The electrons and holes function as both charge carriers and energy carriers. The dimensionless figure-of-merit ZT of some selected materials for n-type and p-type thermoelectric materials are shown in Figure 2.4 and Figure 2.5, respectively (Snyder & Toberer, 2008)

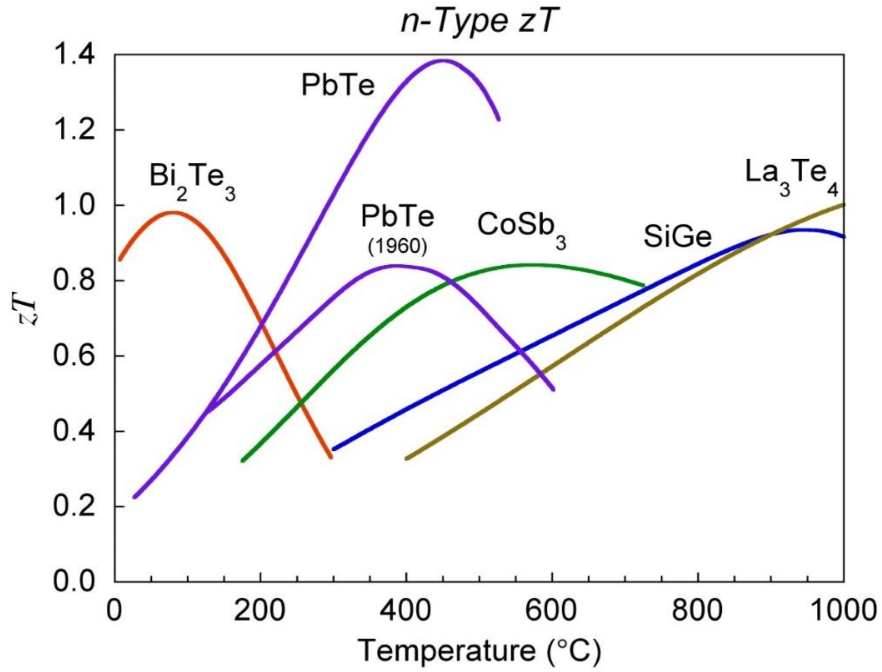

Figure 2. 4: Dimensionless figure-of-merit for n-type thermoelectric materials (Snyder & Toberer, 2008)

As current flows from one semiconductor leg to the other when an n-type or p-type semiconductor develops a negative charge on the cold side and a positive charge there, respectively. A combination of multiple p-n legs connected in series will be needed to produce higher electrical voltage because a single p-n leg of a semiconductor used in a thermoelectric device can only produce a few millivolts.

Currently, silicon germanium (SiGe), tellurides of antimony, germanium, and silver (TAGS), lead telluride (PbTe), lead-tin telluride (PbSnTe), and bismuth telluride (BiTe) are the most commonly used thermocouples. However, many more materials have been used in the past, and some are still being researched in the pursuit of the ideal thermocouple with higher efficiency, lower mass, and more stable performance over an extended period (Lange & Carroll, 2008).

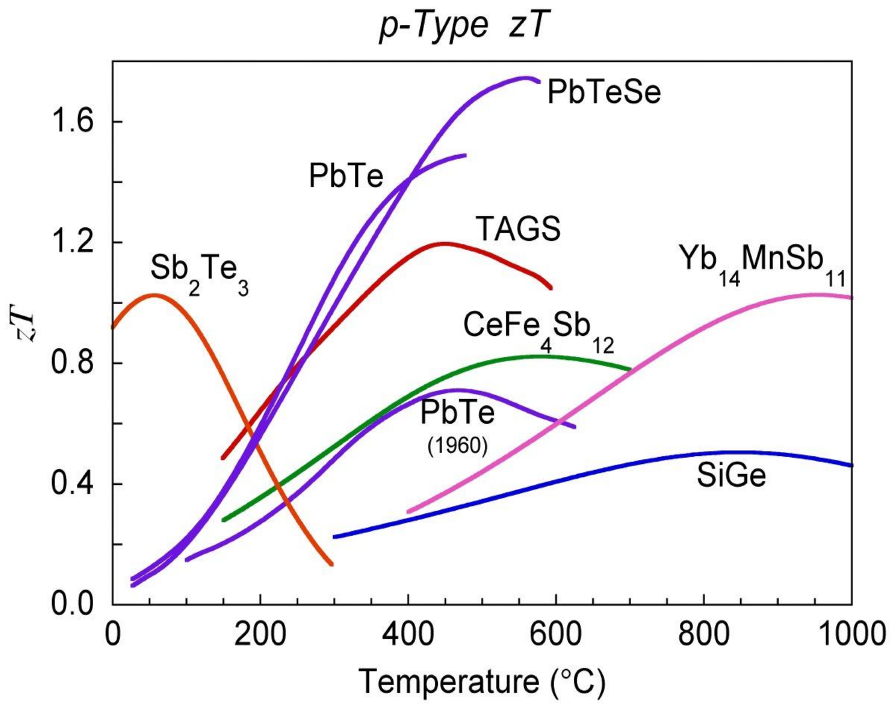

Figure 2. 5: Dimensionless figure-of-merit for p-type thermoelectric materials (Snyder & Toberer, 2008)

As stated in Equation 2.1, the figure-of-merit Z, which influences the efficiency of a TEG, is given by $Z = \frac{\alpha^2\sigma}{\lambda}$. This means that effective thermoelectric materials should have a high Seebeck coefficient, a low thermal conductivity λ, to maintain the temperature difference between the hot and the cold side, and a high electrical conductivity σ to allow the conduction of electricity (Shakouri, 2011).

Thermoelectric materials can be categorized into two types: established materials and new materials (Rowe, 2006). The established materials can be classified into three groups depending on the temperature range of operation. Thermoelectric materials made from alloys of bismuth (Bi) in combinations with antinomy (An), tellurium (Te), or selenium (Se) are suitable for low temperatures of about 450 ^{O}K, and alloys of lead (Pb) for intermediate temperatures in the range up to 850 ^{O}K while for high temperatures of up to 1300^{O}K, alloys of silicon germanium (SiGe) are suitable thermoelectric materials. Although the above-mentioned materials remain the cornerstone for thermoelectric generation, significant advances have been made in synthesizing new materials and fabricating material structures with improved thermoelectric performance.

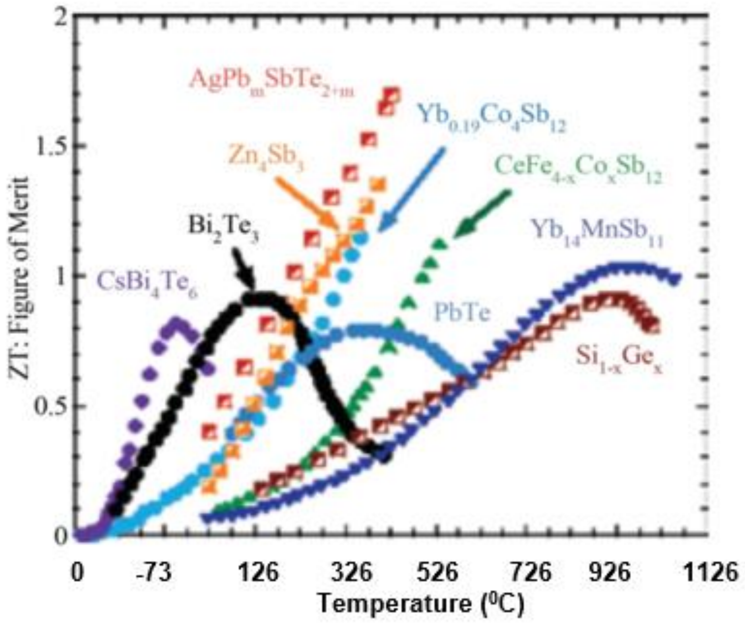

Figure 2. 6: Figure-of-merit of a number (ZT) as a function of temperature for several high-efficiency bulk temperature materials (Tritt & Subramanian, 2006).

Among the commercially available thermoelectric materials, Bi2Te3 (bismuth telluride alloys), due to the exhibition of relatively high figure-of-merit $ZT \approx 1$ (Hochbaum et al., 2008), are mostly used for thermoelectric devices operating at temperature $T \approx 300^0 K$. Efforts have focused primarily on improving the material's figure of merit, and hence the conversion efficiency, by reducing the lattice thermal conductivity (Rowe, 2006). Thermoelectric materials with improved figure-of-merit have been developed, as shown in Figure 2.6 (Tritt & Subramanian, 2006).

2.2.4 Thermoelectric module

The thermopile is a TEG's main component (Rowe, 1994). As depicted in Figure 2.7, a thermopile, also termed a thermoelectric module, is a structure made of several thermocouples (combinations of n-type and p-type thermoelectric materials), which are positioned between hot and cold plates and coupled electrically and thermally in series (Strasser et al., 2004). Section 2.2 discussed a thermoelectric module's single couple (Figure 2.1). The importance of the thermocouple configuration in series and parallel is to increase reliability by reducing the impact of a single open circuit or short circuit failure on total power (Schmidt et al., 2011).

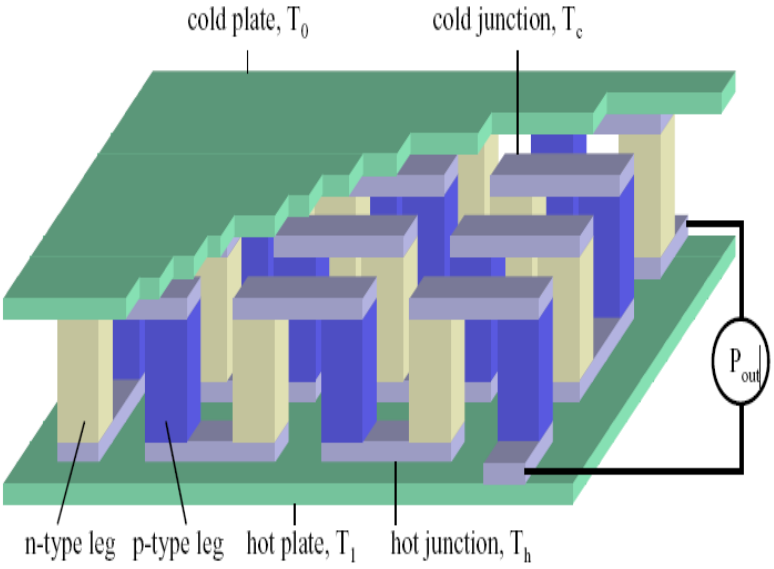

Figure 2. 7: Thermoelectric module (Strasser et al., 2004)

The electrical arrangement of the thermocouples in series also increases output voltage since the voltage induced over each thermocouple is very small. Specifically, connecting k amount of thermocouples in series scales up the open circuit voltage by a factor k. Conventional thermoelectric modules consist of a minimum of 3 thermocouples, rising to 127 thermocouples for larger devices (Riffat & Ma, 2003).

The cold and hot plates are made of ceramic plates (substrates), providing mechanical integrity and electrical insulation for the n-type and p-type thermoelectric materials. However, there are very few thermoelectric modules without ceramic plates, which could eliminate the thermal resistance associated with ceramic plates, but then the mechanical integrity is compromised due to fragility. Ceramic plates are commonly made from alumia. Still, when large lateral heat transfer is required, materials such as berylia and aluminium nitride are desired due to their relatively higher thermal conductivity. Copper-based highly conducting metal strips are used to establish the junctions joining the thermoelectric components between the hot and cold plates.

2.2.5 Application of thermoelectric generators

Thermoelectric generators have found applications from small devices such as wristwatches and cellphones to large devices such as missions in space and heating of buildings in remote villages. In an attempt to develop and market the heat-powered wristwatch SEIKO THERMIC in 1998, the Japanese company Seiko Instruments Inc. took advantage of the temperature gradient (1–3^{o}C) between body and ambient temperatures (Kishi et al., 1999). A micro-thermoelectric gadget made of bismuth telluride components was used in the watch. The user's arm acts as the hot end, transferring heat to the watch's back lid, while the wristwatch case, which effectively conducts heat from the back lid, acts as the cold end. The Seiko watch typically generates 0.1% efficiency and 300 mV of open-circuit voltage from a 1.5 K temperature gradient (Snyder, 2008).

Several top automakers, including Volkswagen, Volvo, Ford, and BMW, have used waste heat from exhausts to enhance the fuel economy of their vehicles. The systems they use, called TEG waste-to-heat recovery systems, have a potential power output of about 1 kW. (Snyder, 2008). Taguchi invented an exhaust gas-based thermoelectric power generator for the automobile (Shameer & Christopher, 2013). Waste heat from exhaust gases was converted directly into electrical power. Yu & Chau (2010) reported that a TEG with a figure-of-merit of 1.25 and conversion efficiency of about 10% could be utilized to harness 35 – 40% of the energy from the automobile exhaust manifold to enhance fuel efficiency by up to 16% while the average thermal gradient is approximately 250 ^{o}C (Yu & Chau, 2009). Hsu et al. (2011) reported that a TEG which converts heat from the exhaust pipe of an automobile at a temperature of 30^{o}C produced total output power of 12.41 W (Hsu et al., 2011).

Experimental research has been done on the use of waste heat from firewood home stoves to create power (Rinalde et al., 2010). For the purpose of electrifying rural dwellings, TEGs that non-technical users could operate were created. The prototype's simplicity confirms the feasibility of local development of this technology. The developed TEG is a potential source of environmentally friendly energy generation because it operates on leftover heat that would have otherwise been lost and might be used in rural areas. The developed TEG is a desirable solution for low-income rural dwellings because to the simplicity of its design and cheap operating costs. In order to produce 100 W of electrical power for household use, heat energy from the stovetop surface at temperatures between 100 and 300^{o}C was also used (Nuwayhid et al., 2003).

A thermoelectric self-powered heating system for residential use was designed, demonstrating thermoelectric generation's excellent applicability to heaters (Qiu & Hayden, 2008). The output power of the developed TEG was approximately 550W. TEG utilizes heat from gas burners. The temperature gradient between the cold junction (room environment) and the hot junction (heat from the burner) was around 535°C. It was revealed that the power output increases as the temperature gradient increases. The household heating system achieved self-powering because the TEG output was sufficient to run the entire electrical appliances. Batteries can be charged with excess power, which can also be utilized to power additional electrical loads. It was argued that the generation of electricity is essentially 100% efficient because, in this case, for a thermoelectric self-powered heating system, the dissipated heat is recovered for subsequent conversion. Efficiency, however, is not always the most important criterion when choosing a technology. As a result, thermoelectric self-powered heating systems might be viable from an economic standpoint and lower carbon dioxide emissions.

Over the past 30 years, TEG has continuously powered aerospace missions in space zones where the utilization of photovoltaic power is not logistically practicable. When radioactive materials spontaneously decay into nonradioactive ones, heat is produced. This heat can be used by radioisotope thermoelectric generators (RTGs) to produce hundreds of watts of electrical power through either a static or dynamic energy conversion mechanism employing the Seebeck effect (NASA, 2006). The military (Chou et al., 2011), gas and heat sensors (Ghamaty et al., 2003), remote telephony, navigation, and instrument protection are some fields where TEGs have found their use (Gulian et al., 2000).

2.3 Overview of radioactive wastes

The release of massive energy and radioactive materials occurs as a result of two fundamental nuclear processes, namely the fission of nuclei like ^{235}U and ^{239}Pu, and the fusion of atoms such as hydrogen. In the nuclear industry, as in many other industrial plants, waste materials that are unneeded and unwanted are produced; these residues are potentially dangerous.

International Atomic Energy Agency (IAEA), defines radioactive waste as "Any item that contains or is polluted by radionuclides at concentrations or radioactivity levels greater than the exempted quantities determined by the relevant authorities, and for which no use is anticipated" (IAEA, 2009). Although national legislation typically decides this point, it should be acknowledged that one person's waste may be another person's resource in some cases, including radioactive waste.

2.3.1 Classification of radioactive waste

Due to the radiation it emits, radioactive waste needs to be handled and managed properly to protect workers, the general public, and the environment. However, not every radioactive waste created carries the same level of risk.

It is simpler to decide how to manage the wastes produced and to find appropriate disposal choices when radioactive wastes are classified. Comparisons are challenging since waste classification definitions differ from nation to nation. The IAEA established a waste management database (IAEA, 2009) that aims to harmonize waste declarations to get around this (Table 2.1).

Table 2. 1: Waste classes defined by the IAEA (De Sanctis et al., 2016).

Waste class	**Characteristics**	**Disposal options**
Exempt Waste (EW)	Activity levels at or below clearance levels	No radiological restrictions normal landfill
Short-lived (L/ILW-SL)	Restricted long-lived radionuclide concentrations	Near-surface or geological repository
Long-lived (L/ILW-LL)	Long-lived radionuclide concentrations exceed limitations for short-lived wastes	Geological disposal facility
High-level waste (HLW)	Thermal power greater than about 2 kW/m^3 and long-lived radionuclide concentrations exceeding limitations for short-lived wastes	Geological disposal facility

In addition to the types of waste mentioned above, it is important to mention another category of waste that are more difficult to regulate because they result from non-nuclear industrial activities that involve the handling of raw materials like rocks, soils, and minerals that contain naturally occurring radioactive materials (NORM) Sometimes industrial activities can concentrate these materials, enhancing their inherent radioactivity. This might lead to (Ojovan & Lee, 2014):

- exposure risk to radiation for both workers and the general population.
- unacceptable environmental radioactive pollution
- the necessity of adhering to legal criteria for waste disposal.

The regulation of these materials varies from nation to nation, and it has only lately been recognized that some form of control is necessary to maintain the proper level of environmental protection. Despite this, these waste categories are not currently managed in a way that is compatible with wastes generated by the nuclear sector that have a similar amount of radioactivity.

2.3.2 Origin of radioactive waste

Before treatment, radioactive wastes resemble other industrial pollutants in appearance. Nuclear reactor waste normally consists of items like machinery, tools, pipes, sludge, water purification resins, protective clothes, etc., just as in other sectors. The presence of radioactivity in one way or another in these materials is the only distinction. The creation of radioactive waste, however, is not restricted to the nuclear power industry; it also happens in all industries that use radioisotopes or handle or create NORM. Furthermore, waste from military applications is a topic that is frequently avoided due to political sensitivities. Lots many other businesses produce radioactive waste as a byproduct of their operations, as do other research endeavours.

Nuclear power currently provides around 20% of the electricity needed worldwide in 32 nations (437 reactors, 389.5 GW(e) at the end of 2021) (Gospodarczyk, 2022). The nuclear fuel cycle provides the most comprehensive picture of the radioactive wastes that the civilian nuclear industry generates from a variety of sources (Figure 2.8). This cycle outlines each stage from uranium mining through reactor operation and either recycling (referred to as the "closed cycle" in the nuclear industry) or direct disposal of spent fuel (once-through cycle).

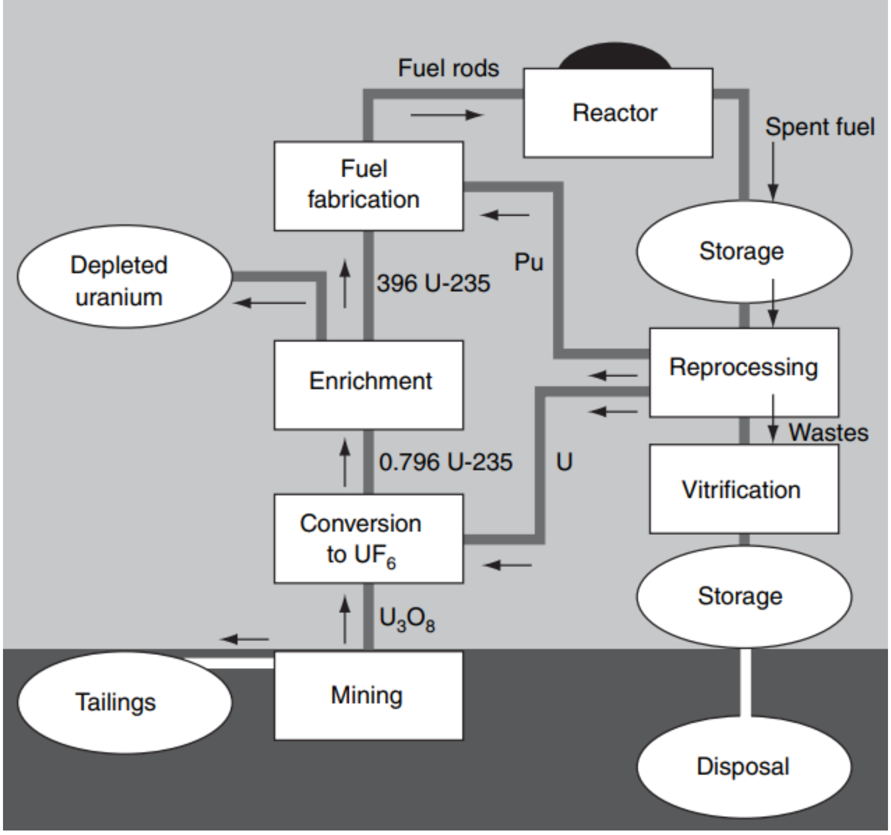

Figure 2. 8: Nuclear fuel cycle (McGinnes, 2007)

The waste produced from the commercial processes applied in each part of this cycle includes mining waste, fuel production waste, reactor operation waste, spent fuel reprocessing waste, decommissioning of reactor waste, research, industry and medicine wastes, and military waste

2.3.2.1 Mining

The majority of mining waste is made up of "tailings," or, the waste products left over after the uranium ore has been processed to create "yellow cake," or uranium oxide, U_3O_8, through milling and acid leaching. It takes between 45,000 and 50,000 tonnes of uranium ore (100%) to generate 200 tonnes (0.4%) of yellow cake, which is enough fuel to power a typical big light water reactor for a year (with an electricity output of 1 GW(e)) (Alexander & McKinley, 2006). There are then between 43,000 and 48,000 tonnes (99.6%) of tailings that need additional management. When open-cast mining is finished, the tailings are typically returned to the pit where the uranium ore was first removed, and the location is then renovated for future use (Alexander & McKinley, 2006). The storage facilities used to manage the tailings during mining operations are typically converted into a long-term stable structure, and the site is then restored for future usage in mines where replacing the tailings is typically not economically possible.

2.3.2.2 Production of fuel

Conversion, enrichment, and fuel fabrication are the three processes involved in the manufacturing of fuel from yellow cake. For the enrichment process (centrifugation or diffusion), where the U-235 content of the gaseous UF_6 is increased from naturally occurring levels of 0.7 wt% to levels of between 2 and 4.95 wt%, the U_3O_8 powder is converted to UF_6, which is a gas at temperatures above $56^{O}C$ (McGinnes, 2007). Finally, the enriched UF_6 is transformed into a UO_2 powder for compression and sintering into fuel pellets that are subsequently made into fuel assemblies.

Small amounts of uranium-containing liquid and solid waste are produced by these activities, and these wastes are packaged for storage and disposal. L/ILW-LL is the standard classification for these wastes (McGinnes, 2007). Most of the depleted uranium produced by enrichment processes is recovered. In the nuclear fuel cycle, a part can then be recycled by mixing it with used plutonium or using it to dilute highly enriched uranium from decommissioned nuclear bombs to create fuel for nuclear reactors. Due to its high density, depleted uranium in its metallic state is utilized by the military, in addition to the nuclear fuel cycle, as armor or ammunition casings.

2.3.2.3 Operation of a reactor

200-350 m^3 of L/ILW and 25 tonnes of spent fuel will be produced annually, assuming that a typical large light water reactor has a capacity of 1 GW(e) (Alexander & McKinley, 2006). This translates to a disposal volume of approximately 75 m^3 after encapsulation, if the spent fuel is disposed of directly. If the spent fuel is reprocessed, this results in around 3 m^3 of vitrified waste (HLW), which when placed in a disposal canister, has a disposal volume of about 30 m^3. Low- and intermediate-level waste is typically generated during routine reactor operations, such as cleaning the fuel storage ponds and reactor coolant systems or decontaminating equipment. Other wastes are made up of different kinds of radioactive metal parts or filters that were used in or close to the reactor.(Alexander & McKinley, 2006)

2.3.2.4 Reprocessing

A spent fuel assembly primarily consists of numerous long rods that are held together by grids, relatively large metallic end and bottom components, and spent fuel pellets. Reprocessing is intended to remove the uranium (95%) and plutonium (1%), which are both present in spent fuel pellets, from the fissionable and transuranic elements (4%). Reprocessing would yield 1 tonne of fission products and transuranic, 23.75 tonnes of uranium, and 0.25 tonnes of plutonium for the 25 tonnes of fuel spent fuel.(McGinnes, 2007)

The reprocessing procedure consists of breaking up the fuel rods into tiny pieces and dissolving the fuel pellets in concentrated nitric acid. Following that, uranium and plutonium are extracted from the liquid containing spent fission products and transuranic. Then, the uranium and plutonium are separated, cleaned, and reused. The high-level waste liquid is dried using a calcination process to generate a solid, which is then combined with borosilicate glass and vitrified. The liquid contains fission products as well as actinide (both transuranic and residual uranium and plutonium) isotopes. The finished glass is then cast into storage containers made of stainless steel. It is envisaged for each of these containers to be placed separately in a large metal container for geological disposal. After the spent fuel is dissolved, the residual structural components of the fuel, as well as significantly polluted items (such as pumps, clothing, etc.) and process remnants (effluent treatment), are classified as L/ILW-LL. Other wastes are prepared and disposed of as L/ILW-SL, such as items that are lightly polluted (McGinnes, 2007).

2.3.2.5 Decommissioning of reactors

Buildings at nuclear reactors are often decontaminated and removed after shutdown. The first stage consists of removing all the spent fuel, which accounts for 99 % of the radioactivity, from the site (Alexander & McKinley, 2006). This then enables the plant to change its license status from operating to decommissioning. The majority of radioactive waste produced during decommissioning operations is classified as L/ILW-SL and comes from contaminated or activated components. Some of the reactor core components may be categorized as L/ILW-LL depending on national legislation and initial impurity levels (particularly uranium and thorium). A significant portion of the waste produced during the decommissioning of nuclear sites comes from the demolition of support structures, such as office buildings, which are not exposed to radiation or radioactive materials. These plants can be shut down using traditional methods, and the garbage that results can either be recycled or dumped at a traditional landfill. The predicted amount of decommissioning waste from a modern light water reactor is 10 tonnes per MW(e) of installed capacity or roughly 10,000 tonnes in the case of a 1 GW(e) reactor (Alexander & McKinley, 2006).

2.3.2.6 Research, industry, and medicine

2.3.2.6.1 Research

Universities and other research institutions employ both open and closed sources, which need to be managed and disposed of properly. Most sources have a low activity level and/or a brief half-life. However, there are certain outliers, such as massive but short-lived Carbon monoxide-60 sources used in radiation research and high-level long-lived sources like Radium-226 and Americium-241 utilized in biological and/or agricultural research (McGinnes, 2007). Research reactors generate operational, decommissioning, and spent fuel wastes on a lesser scale than a commercial nuclear power station.

The generation of particle accelerators has beam currents that are now high enough to result in the production of a significant amount of neutrons (leakage of the proton beam results not only in a cascade of nuclides from spallation reactions but also produces secondary neutrons), activating a significant portion of the materials used in their construction. This is due to the continued development of particle accelerators. The amount of decommissioning waste and its activities are anticipated to be in the same order of magnitude as for a 1 GW(e) nuclear power plant that has worked for more than 40 years after one of the particle accelerators has functioned for 40 years (McGinnes, 2007).

2.3.2.6.2 Industry

Industries employ radioactive materials for a variety of purposes. These sources are handled as radioactive waste when they no longer release enough penetrating radiation to be useful. Industrial sources are typically short-lived, and any waste they produce can be disposed of in facilities that are close to the surface. However, if enough sources are disposed of collectively, such as when thousands of Am-241 smoke detector sources are compressed into steel tubes, this might be categorized as L/ILW-LL. Various industrial processes require processing raw materials including rocks, soils, and minerals that contain NORM. The principal industries that produce these wastes are (Alexander & McKinley, 2006):

- Oil and gas exploration and production - minerals, including a variety of radionuclides, but particularly Radium-226, are left behind in evaporation lagoons or dumps below offshore oil rigs or deposited as scale in pipes and oil field equipment. It's interesting to note that the primary source of radioactive leaks into northern European waters is the oil and gas industry.
- Uranium, thorium, and other radionuclides are all found in coal. When coal is burned to create fly ash, the radionuclides within are concentrated more than they were in the original coal.
- Increased amounts of naturally occurring uranium, thorium, and potassium radionuclides result from the processing of phosphate-containing rock to make phosphate fertilizers.
- Treatment of water: Some waters, particularly mineral waters, have trace amounts of uranium and thorium. As a result of the purification procedures used to clean the water before consumption, such as filter sludges, ion-exchange resins, granulated activated carbon, etc., these radionuclides become concentrated.
- Uranium and thorium series radionuclides may be present in higher concentrations in metal smelting slags, particularly from the tin smelting process.

2.3.2.6.3 Medicine

Nuclear medicine uses two different types of radionuclides, namely, open sources and sealed sources. Open sources present low activity and comprise radioactively labeled chemical compounds used for imaging of internal organs, studying bodily functions and localised irradiation of cancer cells, whereas sealed sources, have high activity and are utilized for the irradiation of tumours.

L/ILW-SL is mostly produced when radioisotopes (open sources) are used in medicine for diagnosis and treatment. This debris often consists of paper, rags, tools, clothing, and filters that have been contaminated with trace levels of radiation, most of it transient. Before being dumped in regular landfills, the majority of these wastes are stored to decompose for months to years at a time. Radioactive waste in this case refers to sealed sources that have deteriorated to the point that they no longer release enough penetrating radiation to be used in therapy. While sources containing considerable amounts of Radium-226 are regarded as L/ILW-LL because they need to be stored and disposed of geologically, sources like Carbon monoxide-60 are treated as L/ILW-SL (Alexander & McKinley, 2006).

2.3.2.7 Military wastes

Military wastes result from manufacturing nuclear weapons, depleted uranium weapons and armor, as well as less-sophisticated products like thorium mantles used in gas lights (the military have a tendency to stockpile, which leads to an accumulation of materials that cannot be disposed of in the same manner as household refuse). Military wastes are identical to those produced by the nuclear fuel cycle in terms of their physical characteristics since uranium must be mined to create feedstock for uranium-235 enrichment or to fuel reactors that produce spent fuel from which plutonium can be extracted through reprocessing to manifacture nuclear weapons (McGinnes, 2007). Reactor operational and decommissioning wastes as well as wastes from reprocessing that are generally of sorts that are comparable to those generated in the civilian program result from this. The spectrum of radioactivity linked to these wastes is varied. The operational wastes from the handling of plutonium, for instance, include the same types of protective clothing used in the civilian program for the manufacture of MOX, such as rubber gloves, overalls, overshoes, glove boxes, etc.(McGinnes, 2007). The difference is that the associated radioactivity is made up of a different spectrum of plutonium isotopes in the case of military applications, and of course, the volumes of these types of wastes are significantly higher in the case of military applications.

2.3.3 Concern about radioactive sources

The potential hazard index, which is defined in terms of nuclide availability, activity, maximum allowable intake yearly, and half-life, is used to quantify the radiotoxicity of a certain radionuclide. This depends on several variables, including the radionuclide's physical half-life, biological half-life, the sensitivity of the organ or tissue where it is likely to concentrate, and the ionizing power of the radiation it emits, which is dependent on the energy of the radiation it emits. These factors lead one to the conclusion that radioactive nuclides of elements including ^{137}Cs, ^{90}Sr, and ^{131}I are the most dangerous to human life (IAEA, 2006). On the other hand, some long-lived nuclides like ^{239}Pu, ^{241}Am, and ^{237}Np represent a long-term threat to the next generations.

Although natural disasters should be dreaded just as much as man-made ones, the atomic bomb's legacy has left the public with a particular impression of the risks associated with the use and misuse of nuclear facilities, activities, and wastes. Due to its heat and radiation output, high-level radioactive waste is the most hazardous and might remain dangerous for tens of thousands to millions of years. Environmental effects of gradients in temperature, chemical composition, and radioactivity can last up to 500 000 years (IAEA, 2006).

2.3.4 Determining the amount of radioactive waste

Radioactive waste levels are expressed in terms of volume (in cubic meters) or tonnage. Another approach is to estimate the radioactivity in bequerels of such waste (Bq) (IAEA, 2008). Because one needs to know the volume or weight of the trash handled for disposal purposes as well as the radioactivity contained therein, both measures are helpful. The sea is a reservoir for thousands of EBq of radioactivity, and nuclear waste from natural sources, such as mining and related operations, could have produced this waste. In contrast, it is estimated that during the Cold War, military nuclear operations released more than 1000 EBq of nuclear debris into the atmosphere (IAEA, 2008). About 1000 EBq of residual waste was produced during the production of weapon-grade material, and a smaller amount of waste may have been produced after mishaps involving nuclear submarines and satellites powered by nuclear energy.

According to estimations, the amount of nuclear waste generated under the civilian regime over the past 50 years as a result of nuclear power production worldwide is on the order of 1000 EBq and is increasing at a rate of about 100 EBq per year (IAEA, 2008). A big nuclear power station with a 1000 MW electricity-generating capacity typically generates 460 tonnes of low-level radioactive waste, 310 tonnes of intermediate-level radioactive waste, and 27 tonnes of high-level radioactive waste (Rao, 2001).

2.3.5 Disposal of radioactive waste

There is universal agreement among all nations that use nuclear energy to varying degrees that disposal is the only conclusive safe solution (endpoint) for the long-term management of nuclear waste. As defined by references, disposal is the placing of waste in a suitable facility without the goal of retrieving it. Another definition of disposal is the almost total removal of harmful substances from all biological cycles (biosphere).

While the idea of dumping nuclear waste into subduction zones or outer space currently seems impractical, the idea of dumping it into stable geological formations is thoroughly thought out. Therefore, all efforts are focused on organizing the disposal so that, even in the very distant (remote) future, the likelihood of any radioactive interaction with the biosphere is almost nonexistent or, if remotely conceivable, is minimalized to a low degree. Usually, solid trash that has been placed in appropriate receptacles is subject to disposal. Additionally, the waste may first be immobilized in a durable waste form, which is typically the case. To reduce any risk of radionuclide movement within the biosphere, this permits safe handling, storage, and disposal and is a component of a multi-barrier approach, which can also include the designed disposal configuration and geological environment. The choice of a disposal method is influenced by a variety of factors, including technical ones like waste characteristics and inventories, administrative ones like the country's radioactive waste management policy and overall waste management strategy, legal and regulatory requirements at the national level, political decisions and social acceptance, and natural ones like the country's climatic conditions, site characteristics, and the availability of suitable host media (Ojovan & Steinmetz, 2022).

2.3.5.1 Goals of Disposition

The goal of the disposal facilities is to prevent or minimize interactions between the waste and the environment and, most crucially, between the waste form and the natural waters. There are numerous ways to achieve this, including by making the right choices regarding (Ojovan & Steinmetz, 2022):

a) the site (such as using an arid region or unsaturated, mountainous site, etc.);
b) the depth at which the installation will take place (near-surface, above/below grade, intermediate depth, deep geological);
c) the use of water-resistant caps (runoff drainage layer, clay barrier);

d) long-lasting containment (borehole disposal), etc.

The protection from unintentional human entry is another major concern, as is the extent to which institutional controls, engineered barriers, and depth of disposal may be used to prevent or reduce this exposure scenario.

The following three basic principles are frequently applied in a graded manner when decisions on disposal technology selection are made (Ojovan & Steinmetz, 2022):

I. The simplest disposal method that is consistent with waste dangers and for which safety and environmental protection can be shown is used to the disposing of nuclear waste.
II. The most dangerous wastes are disposed of utilizing higher engineering standards to provide increased containment and/or at the greatest depths available to increase isolation from the surface environment.
III. When there are already disposal facilities in place, using them before building new ones is taken into consideration.

2.3.6 Conversion of radiation from radioactive sources into energy

Ions, such as fission products and alpha particles, as well as beta particles, gamma rays, X-rays, and neutrons are all examples of ionizing radiation. There is a distinctive range for each kind of ionizing radiation source. Alpha particles and other swift heavy ions, such as fission fragments, deposit their energy within a material over a few micrometers. Over a millimeter-sized area, electrons disperse their energy.

In the end, ionizing radiation interacts with matter to produce heat and ionization. Ion pairs created in the material are typically used by direct energy conversion devices to generate current. The energy from the ions will likewise end up as heat if no mechanism uses the ionization. About 40–50% of the energy of contact between ionizing radiation and matter typically goes into ionization, and the remaining energy is immediately transformed into heat (Prelas et al., 2014). The highest theoretical efficiency for the formation of ion pairs will be restricted to between 40 and 50% if the mechanism of energy transduction does not make use of the heat generated by the radiation interactions (Prelas et al., 2014). The greatest theoretical efficiency of each conversion mechanism will also be constrained by system-specific process inefficiencies.

The ionization created when solids, liquids, and gases are exposed to ionizing radiation has a range of end-uses, as shown in Figure 2.9.

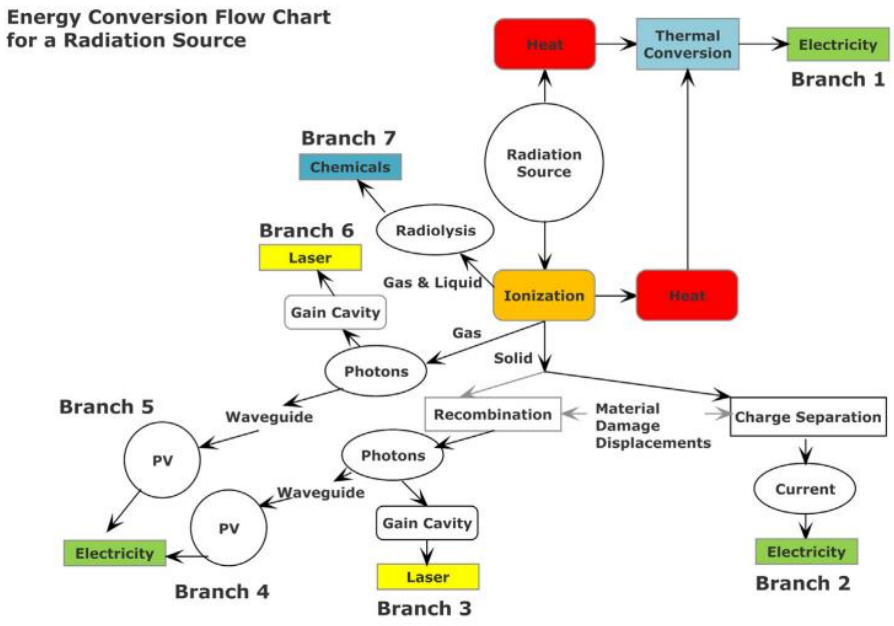

Figure 2. 9: Energy conversion flow chart from a radiation source (Prelas et al., 2014)

The radiation source, represented as a circle, interacts with the material and splits into the creation of heat and ion pairs. With various transducers, the ions can be exploited to create a wide range of beneficial byproducts, like electricity, laser light, or chemicals. In Branch 1, the heat generated by the recombining ions is added to the heat created by the initial contacts of the radiation source and the substance. Then, a secondary system is powered by this heat to create electricity. The RTG (Schmidt et al., 2011), thermionic energy conversion, thermophotovoltaic (Nelson, 2003), and the Alkali Metal Thermal to Electric Converter (AMTEC) are examples of heat-based nuclear battery technologies that fit within Branch 1. Additionally, it is utilized in commercial nuclear power plants' steam cycle. Branch 2 is typical of alphavoltaics, betavoltaics, reciprocating cantilevers, etc. Branch 2 exclusively uses the energy from the ion pairs. Branch 3 drives a solid-state nuclear-pumped laser exclusively using the energy from the ion pairs. Branch 4 uses a solid-state Photon Intermediate Direct Energy Conversion (PIDEC) device to make use of the energy from ion pairs (Prelas et al., 2014). Branch 6 uses the ion pair energy to power a gaseous nuclear-pumped laser. Branch 7 uses radiolysis to produce chemicals using the energy from the ion pairs. Since the heat generated during the interaction of radiation with matter is lost, branches that only use the energy from ion pair formation are naturally constrained to a maximum theoretical efficiency of 40 to 50% (Prelas et al., 2014).

CHAPTER THREE
THEORY ON NUCLEAR AND ELECTROCHEMICAL BATTERIES

3.1 Nuclear batteries

The pragmatic shift towards the realization of cleaner, safer, and renewable energy sources has been made necessary by the rising concerns over the ongoing use of fossil fuels for electrical energy generation and the need to substantially reduce dependence on this non-renewable energy source as well as the necessity for long-lasting power supplies. This function can only be fulfilled by a nuclear battery, which is an apparatus that transforms radiation energy released by radioactive isotopes during their natural decay into electricity. Energy particles from natural radioactivity can be used to create power. Radiation energy has long been transformed into electrical energy. When English physicist Henry Moseley first exhibited the beta cell in 1913, utilizing radium as a radioactive source, nuclear battery technology was born (Moseley & A, 1913). Since then, extensive research on nuclear battery technology has been conducted for applications that require long-lasting power sources. More recently, with the development of silicon technology, research on nuclear batteries has increased.

The atomic energy released by the radioisotope, just like in a nuclear reactor, is essentially what powers a nuclear battery. However, a nuclear battery focuses on the spontaneous disintegration of the atomic nucleus of the radioactive isotopes to produce electricity. In contrast, a nuclear power plant depends on artificially initiated nuclear fission or fission in a nuclear reactor. An electron can traverse the semiconductor's energy band-gap by absorbing enough of the energetic particles generated during radioactive decay. A nuclear battery's essential components are a radioisotope heat source, sometimes referred to as fuel, and a device that transforms the radiation energy from spontaneous radioactive decay into electrical power. These two components are analogous to fossil fuels and combustion engines.

One advantage of nuclear batteries is their high energy density, which can be up to ten times more than that of hydrogen fuel cells and 1,000 times greater than that of electrochemical batteries. Furthermore, nuclear batteries can be used in isolated and harsh areas and have an unusually long life (depending on the radioactive material used), cheap maintenance and operational costs. The energy conversion processes used in nuclear batteries can work in challenging conditions. Nuclear batteries have another benefit in that the radioisotope burns at the same rate as its half-life. In other words, if the radioisotope powering a nuclear battery has a half-life of 80 years, it will still be able to generate half of its initial starting power after 80 years. Nuclear batteries can be used in various ways due to these characteristics.

Despite the advantages of nuclear batteries, they are expensive, have poor conversion efficiency, and face widespread criticism because of the danger that radioactive isotope leakage brings to the ecosystem. Nuclear batteries are still cost-competitive today, nevertheless, because of the inexpensive radioactive isotopes readily available on the market and the expanding low-power electronics sector.

3.1.1 Radioisotopes for nuclear batteries

The acceptability and use of nuclear batteries depend on the choice of adequate radioisotope materials. These radioisotope materials are generally referred to as fuels. A radioisotope for a nuclear battery must be chosen after considering several parameters. These include the nuclear battery's scale lengths, half-life, radiation decay energy, production technique, low radiation emissions, and capability of producing various radiation types using radiated energy. For the radioisotope to affordably fulfil the mission's needs, it must be produced in sufficient quantities and on schedule. It must be able to be made and utilized safely in all typical and accident-prone settings (Lange & Carroll, 2008).

The radioisotope heat source's half-life, which must outlast the nuclear battery's operating life, determines how long a nuclear battery can last. The amount of time it takes for an original isotope to split in half is known as its half-life. The radiation time scale varies depending on the isotope, as indicated in Table 3.1. One aspect that affects the radioisotope's power density is the radiation's energy of decay. Given that affordability is a key component in nuclear battery design, the isotope's production process is equally crucial. While some radioisotopes are byproducts of nuclear processes, others are produced naturally as part of the decay chain (i.e. fission or fusion). In contrast, others can be deliberately engineered by irradiating target materials in a nuclear reactor or a massive accelerator plant (Lange & Carroll, 2008).

All around the planet, radioisotopes that occur naturally are widely dispersed. However, there are problems with extraction and a lack of supply. By-products of nuclear reactions are inexpensive because they can be made from spent nuclear fuel, while intentionally created isotopes that need irradiation or accelerators are often more costly. The potential for the radioisotope to produce other types of radiation is also crucial, especially if the radiation is gamma, as the need for extra shielding will increase the cost and weight of the apparatus, negating its benefit of portability. Only a few radioisotopes can be used because they have the necessary half-lives, radiation levels, power densities, cost and schedule, and availability. The list of commonly utilized radioisotopes is provided in Table 3.1 below.

Table 3. 1: Comparative analysis of radioactive components for RTGs

Radioisotope	Half-life	Radiation Type
Plutonium-238 (^{238}Pu)	87.74 annum	Mainly Alpha (α)
Srontium-90 (^{90}Sr)	28.6 annum	Mainly Beta (β)
Polonium-210 (^{210}Po)	138 days	Mainly Alpha (α)
Americium-241 (^{241}Am)	432 annum	Alpha(α), Beta(β)
Cerium-144 (^{144}Ce)	290 days	Beta (β), Gamma (γ)
Curium-242 (^{242}Cm)	162 days	Mainly Alpha (α)
Curium-244 (^{244}Cm)	18.1 annum	Mainly Alpha (α)

3.1.2 Nuclear batteries classification

The method utilized to transform the heat produced by radiation into electricity is typically used to classify nuclear batteries. Since efficiency affects price, availability, size, and mass, it is a crucial factor to consider when choosing a power conversion system. Nuclear batteries can be divided into two categories: thermal conversion batteries and non-thermal conversion batteries. The temperature difference between the radioisotope and the components of the energy conversion mechanism determines how well thermal conversion batteries work. While prominent non-thermal conversion processes include alphavoltaic, betavoltaic, direct charge, and optoelectric, substantial thermal conversion mechanisms include alkali metal thermoelectric converter (AMTEC), piezoelectric, thermoelectricity, thermionic, thermophotovoltaic, and Stirling generator. In Figure 3.1, the classification of nuclear batteries is schematically depicted.

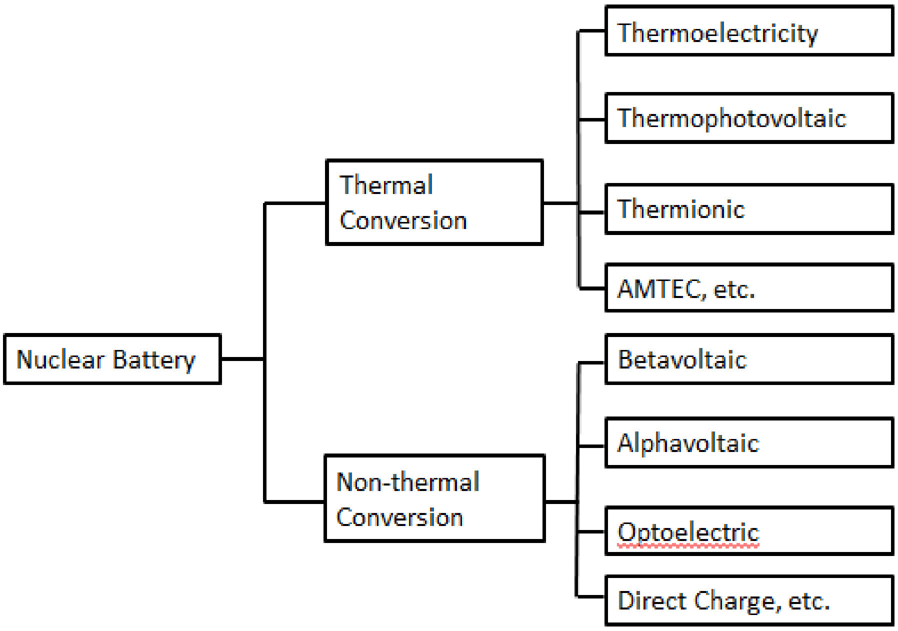

Figure 3. 1: Classification of nuclear batteries

The non-thermal conversion nuclear battery, in contrast to the thermal conversion-based nuclear battery, is dependent on the heat temperature produced by the radioactive isotope rather than the temperature difference. It is challenging to shrink thermal devices, like RTGs, to the micro-scale because, as size is reduced, the surface-to-volume ratio rises, raising relative heat losses and lowering device efficiency. As a result, non-thermal nuclear batteries have frequently been the micro-battery design's focus.

Non-thermal conversion nuclear batteries can be divided into direct conversion, indirect conversion, and direct charge degradation based on how the radiation heat is used to generate power. Since there is no need for an intermediate component, the direct conversion mechanism is also known as a one-phase conversion mechanism. The alphavoltaic, betavoltaic, and reciprocating cantilever converters are prominent non-thermal converters. Photon intermediate direct energy conversion is a unique non-thermal thermal converter that produces electricity by interacting with the heat from heat decay (PIDEC). The following chapter goes into great detail on PIDEC technology.

3.1.3 Radioisotope thermoelectric generator

In situations where photovoltaic panels are impractical, radioisotope generators, referred to as Radioisotope Power Systems (RPS), are typically the most favorable power sources. These RPS are used for unmanned and poorly maintained facilities where batteries and fuel cells are unable to provide power economically for long durations (Sanchez-Torres, 2011). Nuclear generators based on radioisotopes are dependable and have a long lifetime, but they are somewhat costly and face strong popular opposition because of environmental concerns (Lange & Carroll, 2008). A radioisotope-based nuclear generator makes use of the heat created when radioactive materials spontaneously decay into nonradioactive ones. Radioisotope generators are distinct from nuclear reactor power generators, which are dependent on controlled nuclear fission or fusion of radioactive materials due to the natural decay of the radioactive materials. The Seebeck effect, which is the conversion of the temperature gradient caused by the heat decay to electricity, is the basis of the Radioisotope Thermoelectric Generator (RTG). In chapter two, there was a lot of discussion on thermoelectricity.

Any RTG's two main parts are a heat source and an energy conversion system, just like conventional nuclear batteries (Lange & Carroll, 2008). Through the use of a static or dynamic energy conversion device, the heat produced by the spontaneous decay of radioactive materials can be turned into electricity. The dynamic energy conversion systems employ rotating and reciprocating engines and working fluids to convert heat into mechanical energy, which is then converted into usable electric power. In contrast to its dynamic counterpart, the static energy conversion system has no moving parts and, as a result, has a relative price advantage over the dynamic conversion system in terms of maintenance and operational expenses. The static conversion system has the benefit over its dynamic equivalent of being smaller and lighter.

RTGs are incredibly reliable during operational lives of several decades, small in design, robust, and radiation resistant. They are also simple to adapt to a wide range of applications and don't emit noise, vibration, or torque while operating. As soon as the heat source is attached, they can start producing electrical power (direct current and voltage) without needing any start-up components. The power output may be easily controlled during the design phase by keeping a matching resistive load on the thermocouples.

Researchers K.C. Jordan and J.H. Birden developed the first RTG, which produced 1.8 mWe of electrical power, in 1954 while they were employed at the Mound Laboratory of the US Atomic Energy Commission (AEC) (Bennett, 2008). Since then, RTGs have improved and/or made it possible for difficult space missions. RTGs offer remarkable performance reliability, but their potential is constrained by the poor conversion efficiency of thermoelectric materials. According to O'Brien et al., system efficiencies typically range from 4 to 6%. Additionally, radioactive material leaking will harm the ecosystem. Figure 3.2 depicts an RTG module.

RTGs have indeed been satisfactorily used in satellites and space missions (on a macro scale), but their use at the micro size has not yet been fully realized. The use of RTGs in National Aeronautics and Space Administration (NASA) missions is described in (Schmidt et al., 2011). RTGs have been used by the previous USSR for their space missions, albeit this is not well documented. RTGs are a reliable technology of sustainable energy. The requirement for portable power applications for autonomous operation, which calls for longer-lasting, small, lightweight, and high energy density power sources, will be satisfied by the effective development of micro-RTGs.

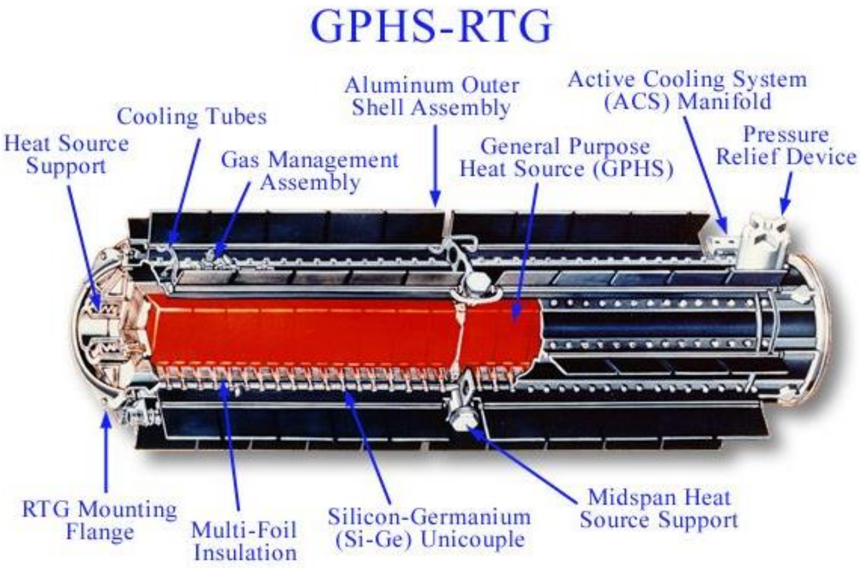

Figure 3. 2: Radioisotope thermoelectric generator module (El-Genk et al., 2003)

Figure 3.3 depicts an RTG's fundamental features. Three fundamental components make up a standard RTG: a radioisotope heat source that generates thermal power, a converter (thermocouples) that converts some of the thermal power into electricity, and a radiator that rejects the majority of the thermal power that is still unconverted to space (Cataldo & Bennett, 2016). The thermocouples' outer ends are attached to a heat sink, and their inner ends are inserted into the container's walls together with the radioactive material.

The creation and use of RTGs must be done safely as radioactive decay produces harmful undesired radiation. In order to maintain the fuel contained and avoid human ingestion or inhalation, fuel encapsulation is a key component of the design of RTGs. The General Purpose Heat Source is made up of radioisotope fuel and other components that ensure its safe handling (GPHS).

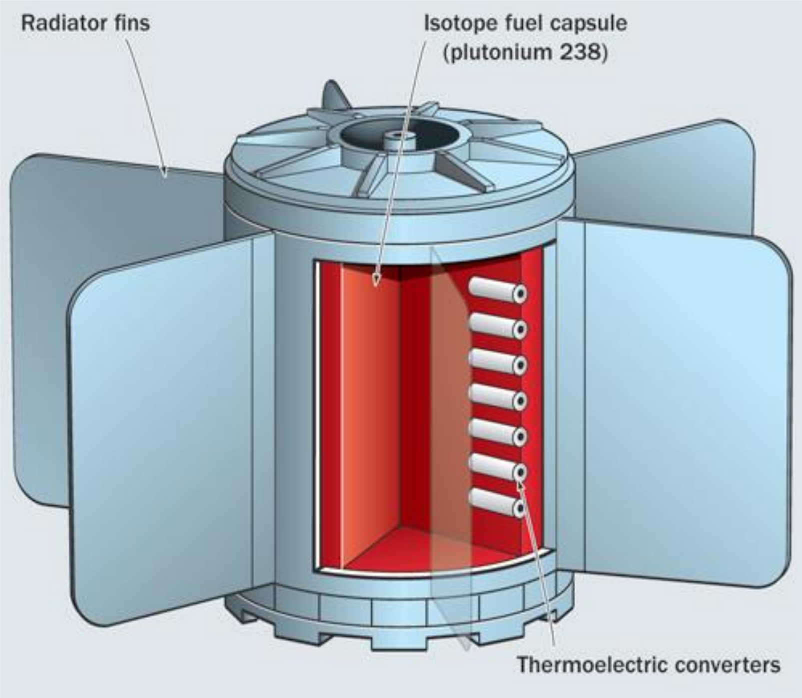

Figure 3. 3: Cutaway view of a radioisotope thermoelectric generator (Cataldo & Bennett, 2016)

The five primary components of the GPHS module assembly are shown in Figure 3.4 and are carbon-bonded carbon fiber (CBCF) insulation, the fuel, fuel cladding, graphite impact shell (GIS), and fine weave perforated fabric (FWPF) aeroshell. In high-operating temperature and simulated accident scenarios, the fuel-clad iridium alloy gives oxidation resistance and chemical compatibility with the fuel and graphite (of the GIS). The fuel cladding's damage is kept to a minimum by the GIS, the fuel cladding's peak temperature is kept to a minimum by the CBCF during unintentional reentry, and the temperature is kept high enough to guarantee the fuel cladding's ductility during the subsequently postulated impact. The aeroshell was made to incorporate the GIS under a variety of reentry conditions and to add extra protection against impacts on hard surfaces at terminal velocity. Additionally, the aeroshell shields the fuel-clad from hypothetical explosion overpressures and fragment hits and can offer safety in the case of a propellant fire.

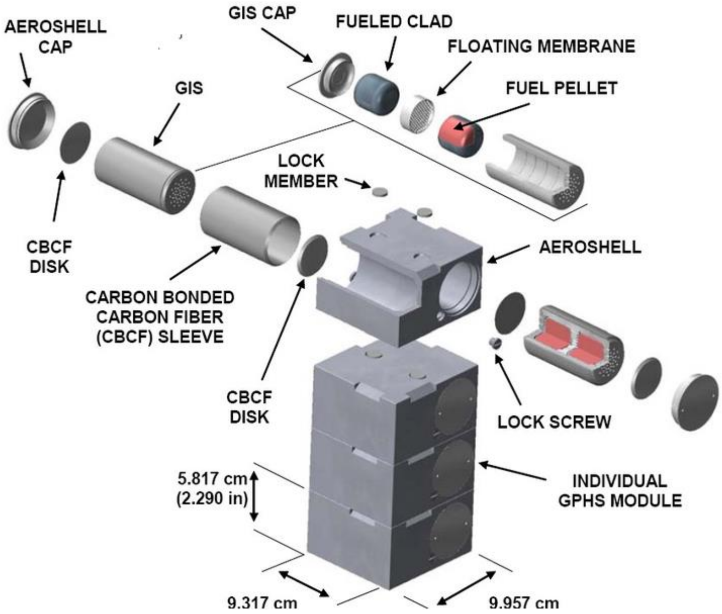

Figure 3. 4: GPHS (General Purpose Heat Source) module assembly (Schmidt et al., 2011)

The Seebeck effect is used by RTG, which serves as the foundation for the micro-nuclear generator, to transform heat produced by the radioactive elements' spontaneous disintegration into electricity (Jiang, 2013). The following equation describes how an open circuit output voltage, V_G is produced when a temperature differential exists between two thermal surfaces (hot and cold junctions of two dissimilar materials that may be metals or semiconductors):

$$V_G = N\alpha\Delta T \tag{3.1}$$

Where, N, α, and ΔT represent the number of thermocouples, the TEG materials Seebeck, and the temperature difference applied, respectively.

3.1.3.1 Radioisotope thermoelectric generators for space missions

Since about the 1960s, the United States of America (U.S.) has consistently used RTGs to supply electricity for its aerospace missions (Bennett & Skrabek, 1996). Appendix 1 provides a chronological summary of some NASA missions that have made use of RTGs (Schmidt et al., 2011). The former U.S.S.R. has employed RTGs for her space missions, despite this fact not being well reported.

3.1.4 Thermophotovoltaic nuclear battery

In the thermophotovoltaic (TPV) power generation process, radiated heat is directly transformed into electricity using photons produced by the thermal emitter. A TPV device will, in theory, obtain energy from any emitter with a temperature that is higher than that of the TPV device, even though its temperature ranges from 900 ^{o}C to roughly 1300 ^{o}C (Shakouri, 2011). According to reports, a TPV has an efficiency of around 20% (Shakouri, 2011).

3.1.4.1 Components of thermophotovoltaic nuclear battery

Typically, a heat emitter and a photovoltaic cell make up a basic TPV device (Figure 3.5). A filter and a reflector are included in a fundamental TPV, nevertheless, to maximize efficiency and reduce the loss of radiant heat that isn't transformed. In order to reflect non-ideal wavelengths back to the emitter, filters are necessary; nevertheless, in actual use, imperfect filters are frequently encountered. In order to maximize the effectiveness of a TPV, a reflector should be put behind the converter and anywhere else in the system where photons might not be efficiently directed to the collector. The photons that are reflected are sent back to the emitter where they might be reabsorbed to produce heat and more photons. In order to convert the reflected photons, they can also be sent back to the photovoltaic cell. In an idealized TPV system, all photons are converted into electricity by using photon recycling and selective emission.

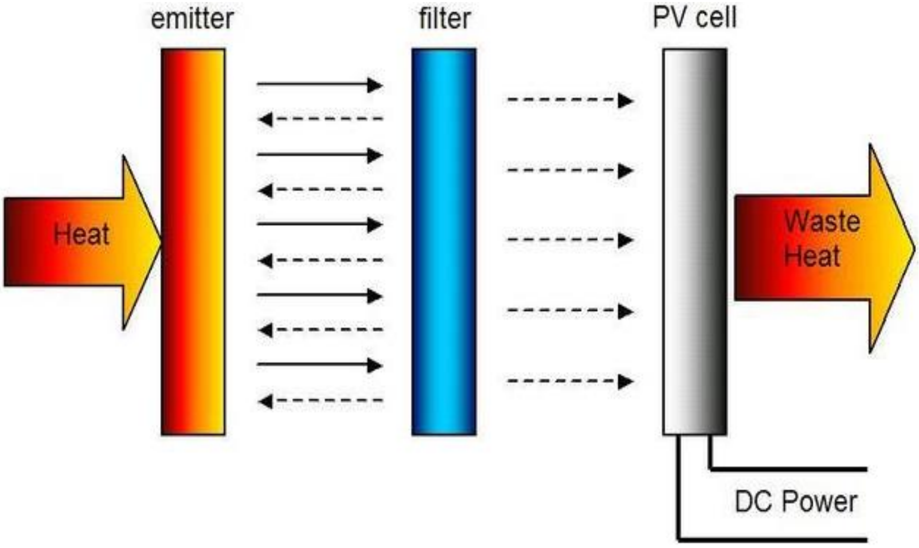

Figure 3. 5: Schematic representation of thermophotovoltaic energy conversion

Efficiency, temperature resistance, and price are the three main criteria to be taken into account when choosing an emitter for TPV. Since efficiency rises with temperature, the capacity of the emitter to operate at high temperatures is the most important component of the three. The most popular emitter is silicon carbide, which is incredibly affordable to produce, thermally stable up to about 1700 ^{o}C, and a suitable option for industrial applications (Bitnar, 2003). The most often utilized selective emitters for TPVs are tungsten and rare-earth oxides (such ytterbium oxide and erbium oxide). In the visible and near-IR range, tungsten has a greater emissivity of 0.45 to 0.47 and a lower emissivity of 0.1 to 0.2 in the IR range. The near-IR area of rare-earth oxides emits narrow band wavelengths, enabling the emission spectra to be tailored to better match the absorption properties.

Due to its commercial availability, extremely low price, scalability, and ease of manufacturing, silicon is the most widely used material for solar cells. However, its relatively wide bandgap of 1.1 eV restricts its application to lower operating temperatures. Photovoltaic cells can also be made from germanium, gallium antimonide, and indium alloys such as indium gallium arsenide (InGaAsSb), indium gallium arsenide (InGaAs), and indium phosphide arsenide antimonide (InPAsSb) (Bitnar, 2003).

3.1.4.2 Applications of thermophotovoltaic nuclear battery

Similar to other nuclear batteries, TPVs are completely silent, have no moving components, and cost very little to operate and maintain. Because of these features, TPVs are appropriate for portable and remote electricity-generating applications. TPVs have been shown to be helpful in both commercial and military applications. The necessity for portable power units for soldiers has arisen as a result of the increased use of electronics in combat. Typical diesel generators are too heavy for personal use on the battlefield. Electrochemical batteries are also impractical for use in battle due to their bulk and necessity for recharging. Scalability enables TPVs to be smaller and lighter to be used for tactical warfare applications in addition to the specific features of TPVs. For the army, JX Crystals developed a TPV-based battery charger device that could operate at 1250 ^{o}C and 230 W of power (Guazzoni & Mathews, 2004).

In many homes located in remote regions, especially in developing countries where power line extensions can be extremely expensive and impractical, TPVs provide a continuous power supply to homes that are not connected to the power grid. TPVs cogenerate heat and power in such homes in cold seasons (Wilt et al., 2007). Due to the merit of silent operation, TPVs are being proposed for use in recreational vehicles where noisy conventional generators are not allowed (Coutts, 1997).

It is noteworthy mentioning that TPVs, like other nuclear batteries, have drawbacks despite their merits. Unconverted thermal emission is a major source of inefficiency. Consequently, in the design of a TPV, it is usually desired to match the optical properties of thermal emission (wavelength, polarization, direction) with the emitters.

3.1.5 Betavoltaic nuclear battery

Although the betavoltaic cell has been in development for more than 60 years, research and development have been hampered by its limited low power applications, quick semiconductor deterioration, lack of available, and expensive radioactive elements.

Paul Rappaport reported the first betavoltaic device in 1954; it produced 0.8 microwatts with an efficiency of 0.2% and deteriorated quickly as a result of radiation damage (Rappaport, 1954). Ever since, a number of other researchers have continued research into betavoltaics. Still, the most extensive effort to create a workable betavoltaic power source was made by the DWDL (Donald W. Douglas Laboratories) Labs team from 1968 to 1974 (Olsen, 1974).

The development of betavoltaic nuclear batteries, like other radioisotope-powered batteries, was motivated by the requirement for long-lasting, dependable, high-energy density, low operating and maintenance costs power sources to function small electrical equipment in challenging and inhospitable contexts. Electricity is produced using betavoltaic batteries using energy from a radioactive source that emits beta particles (electrons).

In applications where electrochemical battery use is impractical due to size or inaccessible zones where battery replacement is not practicable, the betavoltaic battery offers an alternative to electrochemical batteries. In low-power electrical applications with a long energy source lifespan, such as implantable medical devices or military and space applications, betavoltaics are especially well-suited.

3.1.5.1 Principle of operation

Similar to a photovoltaic cell, a betavoltaic cell produces electricity. However, as the name suggests, a betavoltaic battery works on the basis of the betavoltaic effect, which produces extra electron-hole pairs by impinging high-energy beta particles from radioisotope decay onto p-n semiconductors in order to produce current. From Figure

3.6, the basic workings of a simple betavoltaic unit consist of a layer of beta-emitting radioisotope put next to a semiconductor p-n junction. Tritium (H3), an isotope of hydrogen, and nickel (Ni63), an isotope of nickel, are both frequently used radioactive sources because their energy spectra are suited for absorption in the p-n semiconductor. SiC and GaN, on the other hand, are frequently utilized for p-n semiconductors due to their comparative superior radiation resistance.

Since the average kinetic energy of typical beta particles employed in betavoltaic technologies is in the range of keV, a single beta particle can produce several electron-hole pairs (Olsen, 1973). As the beta particle slows down, it penetrates the p-n junction, hits atoms, and produces electron-hole pairs. The electrons and holes are propelled to the n- and p-sides of the semiconductor, respectively. When a load is attached, the electrons move from the n-side through the beta decay, which doesn't happen at certain discrete energies but rather from a continuous energy spectrum that varies for each isotope. Electron-hole pairs are swiftly recombined outside the depletion layer, producing a zero net current. A portion of the kinetic energy will result in the generation of electron-hole pairs as some of it is lost to the lattice and some are lost via the emission of acoustic and optical phonons, respectively (Olsen et al., 2012).

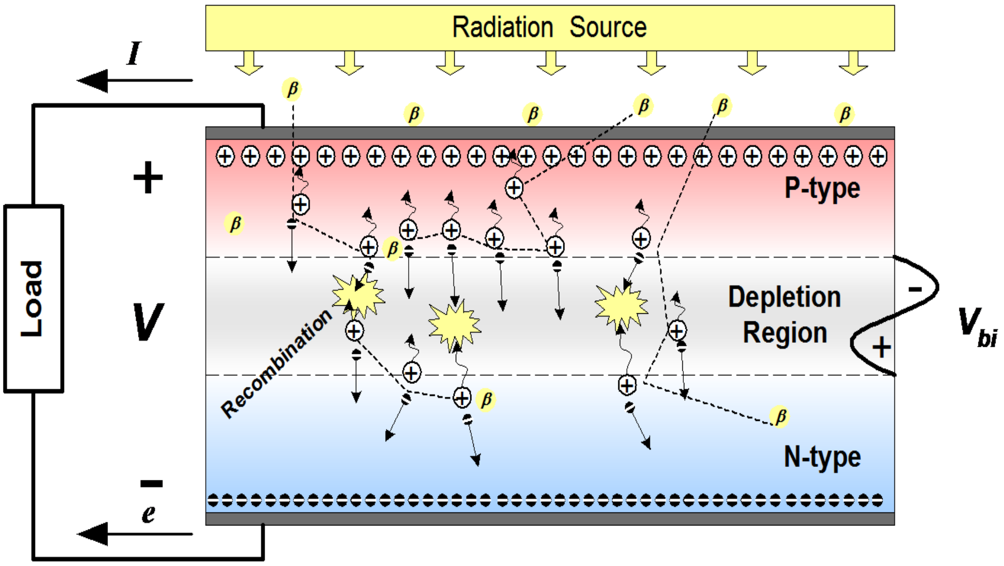

Figure 3. 6: Operating principle of betavoltaic cells (Cabauy et al., 2010)

3.1.5.2 Challenges associated with betavoltaic nuclear battery

Although theoretical efficiency of 5–7% has been estimated, betavoltaics suffer from very modest operational efficiency of roughly 2%. This low efficiency is caused by flaws brought on by long-term beta irradiation, including radiation degradation and semiconductor crystal fracture by high-energy beta particles. Since a betavoltaic's semiconductor serves as the primary energy conversion, its diode semiconductor material quality modifies the betavoltaic's electrical performance. This performance varies depending on temperature. These parameters include intrinsic diffusion length, intrinsic carrier concentration, and mobility (Clarkson et al., 2007). The intrinsic diffusion length primarily impacts the betavoltaic cell's short circuit current and the semiconductor diode's leakage current, which in turn affects the betavoltaic cell's open circuit voltage. In silicon diodes exposed to nickel isotope radiation, Guanguan Wang et al. (2010) conducted experiments to demonstrate that the electrical performance metrics of open circuit voltage, maximum output power, and energy conversion efficiency decrease as temperature rises.

3.1.6 Alphavoltaic nuclear battery

In 1954, the idea of an alphavoltaic battery was put forth (Pfann & Van Roosbroeck, 1954). The sole difference between an alphavoltaic cell and a betavoltaic cell is that the latter uses alpha emitter radioisotopes like Plutonium-238. In contrast, alphavoltaics function in a similar way to betavoltaics and share the very same features. Early research on alphavoltaics reveals that, as betavoltaics, they are similarly hampered by the energetic alpha particles damaging semiconductor materials and leading to a rapid decline in electrical performance over time. As a result, alphavoltaic batteries were not previously commercially successful (Rybicki et al., 1996). Developed by NASA and RIT, alphavoltaic batteries do not experience performance degradation within a short period due to damage to the semiconductor layer caused by the emitted alpha particles.

Alpha voltaic batteries are ideal for micro-electrical mechanical system (MEMS) because they can generate power on the order of microwatts, which is sufficient for many MEMS applications. Because they can be ramped up to higher power levels, alphavoltaic batteries are applicable to various technologies, including power sources for deep space missions. Alphavoltaics are superior prospects for deep space missions because they have two distinct advantages over ordinary electrochemical batteries. They can work over a wide temperature range, and the alpha-emitting materials have half-lives varying from months to years. Alphavoltaic batteries have been proven to function at temperatures as high as 135 ^oC, whereas ordinary electrochemical batteries fail at roughly 40 ^oC.

3.2 Electrochemical batteries

During potential discharge and potential charge, electrochemical batteries transform chemical energy into electricity and electrical energy into electrochemical. Such batteries are employed in spacecraft to provide power during launch, during anomalies needing extra power, during cruises, or during eclipses. Due to its portability, affordability, ease of deployment, and ability to respond almost instantly to input from the battery and output from the network to the battery, electrochemical energy storage in batteries is appealing.

Secondary or rechargeable electrochemical batteries have been extensively used in multiple space applications and different sorts of applications from inner space to outer space missions. This includes rovers, landers, probes, planetary spacecraft, or astronaut equipment, acting as energy storage and power leveling. Space missions require storage units to go through extreme conditions and hazards. As a result, batteries for use in space must be specially designed and tested to guarantee they can survive and function in the circumstances like extreme vacuum pressure; withstand launch parameters (shocks, vibrations, and acceleration). Furthermore, the storage unit should provide adequate energy-to-weight and energy-to-density ratio to have minimum weight and volume. Moreover, outer space exploration batteries should exhibit a minimum of 3000 charge-discharge cycles; meanwhile, planetary probes should have long shelf life superior to 7 years (Halpert et al., 1999). Studies have been conducted on battery systems based on Silver-Zinc, Nickel-Cadmium (NiCd), Nickel-Hydrogen (Ni-H_2), and Lithium-Ion over hundreds of missions and needs (Rahn & Wang, 2013).

Silver-Zinc (Ag-Zn) batteries were the first types of batteries to be used in space, followed by NiCd batteries because of their long cycle life, and thereafter Ni-H_2 was extensively used. The chronology of battery usage is shown in Table 3.2.

Table 3. 2: Chronological list of first use of batteries in space (Halpert et al., 1999)

Launch Date	Spacecraft	Life in Space	Battery/ Fuel Cell Type	
12/6/56	Vanguard	Failed	Zn/HgO	First US Launch
2/1/58	Explorer 1	3.8 Months	Zn/HgO	Van Allen Radiation Belt
3/6/59	Explorer 6	2 years	Cylindrical Ni/Cd	First Earth Photos
3/13/61	IMP 1	3.5 years	Ag/Cd	Non-Magnetic
1/26/62	Ranger 3	Solar Orbit	Ag/Zn	Moon Photos
4/26/62	Ariel I	14 years	Prismatic Ni/Cd	1st in LEO
8/21/62	Gemini	7 days	PEM Fuel Cell	PEM Fuel Cell
8/27/62	Mariner 2	Venus	Ag/Zn	1st Planetary
6/23/63	Syncom-2	N/A	Cylindrical Ni/Cd	1st GEO
5/20/65	Apollo Command Module	Short Life	Ag/Zn	Limited Cycle Life
6/23/66	NTS-2	5 years	Ni/H_2	12 hours Polar
9/23/66	USAF	Classified	Ni/H_2	LEO
9/7/67	Biosatellite 2	3 Months	PEM Fuel Cell	1st Use of Nafion
10/11/68	Apollo 7	11 days	Alkaline Fuel Cell	1st Manned Apollo
2/14/80	Solar Max	8 years	Ni/Cd	Standard Battery
4/12/81	Shuttle (STS-1)	2 days	Alkaline Fuel Cell	1st Shuttle
5/19/83	Intelsat V	14 years	Ni/H_2	GEO
4/4/83	STS-3	Days	Li-BCX	Astronaut Use
4/6/84	LDEF	6 years	Li Cells	Exposure to Space
10/18/89	Galileo	Hours	Li-SO_2	Jupiter Probe
4/25/90	Hubble Space Telescope	In Orbit	Ni/H_2	NASA LEO
6/10/90	Leasat	Orbiting	Super Ni/Cd	GEO
1/25/94	Clementine	5 months	SPV Ni/H_2	Lunar Mapping
1/25/94	Tubsat-B	4 years	2 Cell CPV	Store Messages
5/1995	Centaur	1st Mission	Li-$SOCl_2$	28V, 250 Ah Battery
5/5/96	Iridium-1	Commercial	50 Ah SPV	88 S/C to Date-LEO
11/19/97	Flight Experiment	USAF Experiment	Na/S	7 day Experiment

3.2.1 Lithium-ion battery

Lightweight and compact Li-ion rechargeable batteries are currently found in a wide variety of consumer equipment. Medical equipment, cell phones, and portable electronics all use lithium-ion batteries. A Li-ion battery has an energy and power density between 90 and 190 Wh per kg and 500 and 2000 W per kg, respectively, with high efficiency above 95% and a low self-discharge rate of 5% per month.

Other applications, like electric automobiles and spacecraft, are very interested in the qualities of Li-ion batteries. NASA and the United States of America Air Force (USAF) have created a joint inter-agency effort to develop these for aerospace and aircraft applications. These batteries will be used by NASA on several upcoming space missions, including the Solar Probe, Europa, New Millennium ST4, Mars 2001 Lander, and Mars 2003 Rover. Additionally, there are proposals to switch out the Shuttle's current hydraulic Auxiliary Propulsion Unit (APU) for a 100- to 150-kWh Li-ion battery-powered system. The employment of these cells in aircraft, unmanned aircraft systems (UAVs), and GEO (Geosynchronous Equatorial Orbit) and LEO (Low Earth Orbit) satellites is being considered by the USAF (Tremblay & Dessaint, 2009).

Rechargeable Li-ion batteries are currently the preferred technology for most aircraft applications. Different versions of this technology exist. However, for a long life span (> 5 years) and adequate thermal management, Ni-H_2 batteries are the best technology, with over 60000 depths of discharge and an operation period of above 15 years. However, their high cost and limited operating temperature range have made them unpractical to the profit of Li-ion batteries. Table 3.3 below shows anodes and cathodes employed in Li-ion rechargeable batteries.

Table 3. 3: Materials for the cathode and anode in lithium batteries (Dixit, 2020)

Cathode		Anode	
Composition	**Designation**	**Composition**	**Designation**
Lithium cobalt oxide, $LiCoO_2$	LCO	Meso-carbon micro-bead	MCMB
Lithium iron phosphate, $LiFePO_4$	LFP	Graphite	Gr
Lithium nickel oxide, $LiNi_{0.8}Co_{0.2}O_2$	NCO	Hard carbon	HC
Lithium nickel cobalt aluminium oxide, $LiNi_{0.8}Co_{0.15}Al_{0.05}O_2$	NCA	Silicon (with graphite)	Si
Lithium nickel manganese cobalt oxide	NMC	Lithium metal	Li
Lithium manganese oxide (spinel)	LMO		

Li-ion batteries come in various configurations. They may be specifically tailored for a certain application by selecting the ideal electrode couple and/or changing the cell design to deliver high specific energy, long life, or high power. The properties of Li-ion batteries utilized and intended to be used by NASA in a variety of space missions are displayed in Table 3.4.

Table 3. 4: SOP Li-ion batteries employed in NASA space missions (Surampudi et al., 2017)

Mission	Launch Date	Destination	Battery System
2001 Mars Odyssey	April 2001	Mars	Ni-H_2
COUNTOUR	July 2002	Comet	Ni-Cd
MER-Spirit	June 2003	Mars	Li-ion (NCO)
MER-Opportunity	July 2003	Mars	Li-ion (NCO)
Messenger	August 2004	Mercury	Ni-H_2
Deep Impact	January 2005	Comet	Ni-H_2
Mars Reconnaissance Orbiter	August 2005	Mars	Ni-H_2
New Horizons	January 2006	Pluto	No Battery
Phoenix	August 2007	Mars	Li-ion (NCO)
Dawn	September 2007	Vesta & Ceres	Ni-H_2
Kepler	Mars 2009	Earth Orbit	Li-ion (LCO)
Lunar Reconnaissance Orbiter	June 2009	Moon	Li-ion (LCO)
LCROSS	June 2009	Moon	Li-ion (LCO)
Juno	August 2011	Jupiter	Li-ion (NCO)
GRAIL	September 2011	Moon	Li-ion (NCO)
Mars Science Laboratory	November 2011	Mars	Li-ion (NCO)
LADEE	September 2013	Moon	Li-ion (LCO)
MAVEN	November 2013	Mars	Li-ion (NCO)
OSIRIS-Rex	September 2016	Asteroid	Li-ion
InSight	May 2018	Mars	Li-ion (NCA)
Mars 2020	Summer 2020	Mars	Li-ion (NCA)
Deep Space Climate Observatory (DSCOVR)	February 2015	L-1	Li-ion (LCO)
Magnetospheric Multiscale Satelites (MMS)	Mars 2015	Various Orbits	Li-ion (LCO)
Transiting Exoplanet Survey Satelite (TESS)	December 2017	HEO Orbit	Li-ion (LCO)
James Webb Space Telescope (JWST)	2018	L-2	Li-ion (LCO)
JPSS	2021	LEO	Li-ion (LCO)

3.2.2 Lead-acid batteries

Since the 1970s, solar homes have used lead-acid batteries, also known as the "granddaddy of energy storage," developed by French physicist Gaston Plante in 1859. Although they resemble regular car batteries, they have a higher capacity for discharge and recharge than automobile batteries. The lead-acid battery's chemical energy is stored in the potential difference between the pure lead on the negative side (anode) and the lead oxide (PbO_2) on the positive side when the battery is charged (cathode). The electrolyte in which both electrodes are immersed in aqueous sulfuric acid. The electrical energy generated during lead-acid battery discharge is the result of energy released during the formation of the strong chemical bonds between water molecules (H_2O) from hydrogen ions (H^+) and oxygen ions (O^-) in PbO^2. The most established and least expensive rechargeable battery type is lead-acid. However, it has a shorter lifespan than Li-ion. Lead-acid batteries are less effective at storing energy than other electrochemical batteries. Due to low efficiency, lead-acid batteries cannot charge and discharge as quickly as other energy storage technologies. They are unable to be fully discharged as a result. Therefore, compared to Li-ion batteries, lead-acid batteries need more cells and space.

Lead-acid batteries have several disadvantages, such as relatively poor performance at low and high temperatures, a short lifespan (roughly 3 to 4 years), a minimum depth of discharge (20%), the requirement for routine water maintenance, relatively low energy and power, and the incapability to provide frequent power cycling in a partial state of charge, which may result in an early failure due to sulfation (Ould Amrouche et al., 2016). Lead-acid batteries have nevertheless found use in stand-alone power systems, hospitals, and backup power sources despite their limitations. This is because of their comparably minimal cost.

3.2.3 Nickel-cadmium batteries

One of the most well-known commercially available electrochemical rechargeable batteries is the nickel-cadmium (NiCd) battery. A NiCd battery's positive electrode (cathode) is composed of nickel oxide, the negative electrode (anode) of a cadmium compound, and the electrolyte is potassium hydroxide solution. When a NiCd battery is discharged, chemical energy is transformed into electrical energy, and when it is recharged, electrical energy is transformed back into chemical energy. The NiCad battery may repeatedly cycle since it is rechargeable.

As with any other rechargeable battery system, NiCd batteries work on the premise that electrochemical processes at each electrode are reversible, allowing energy to be stored during charging and released during discharging. When a battery is being charged, electrical energy from an external power source is transferred into chemical energy and stored in the cell as the lower energy $Ni(OH)_2$ is transformed into higher energy NiOOH. The stored chemical energy is released as electrical energy when the NiOOH is changed back into $Ni(OH)_2$ during a discharge reaction.

Compared to other electrochemical batteries like Li-ion and Nickel-Metal-Hydride, NiCd batteries have a lower energy density. But the strong NiCd batteries are incredibly reliable, practical, and affordable. For many electrical and electronic applications that prioritize lower prices while keeping acceptable performance, they continue to be a preferred option.

In terms of the number of charge/discharge cycles, NiCd batteries often outlast other rechargeable batteries like lead-acid batteries. Emergency lighting, cordless and wireless telephones, and other devices all use NiCd batteries. They can supply large surge currents because of their comparatively low internal resistance. They are, therefore, a good option for cordless power tools, camera flash units, remote-controlled electric model cars, boats, and aeroplanes.

3.2.4 Nickel-metal-hydride batteries

A rechargeable battery similar to the nickel-cadmium (NiCd) battery is the nickel-metal hydride (NiMH) battery. The counter electrode in NiMH is the $Ni(OH)_2/NiOOH$ redox pair, just like in NiCd. The NiMH battery, however, uses hydrogen absorbed in a metal hydride in place of Cd. A metal hydride's volumetric hydrogen storage capacity is almost two times that of liquid hydrogen. For an equivalent size, NiMH batteries can hold twice as much energy as NiCd batteries, and their volumetric energy density is similar to that of Li-ion batteries. It is one of the rechargeable batteries with the best environmental performance.

NiMH batteries are distinguished by their energy density, which translates into extended operating hours or a decrease in the battery's required space. Since a typical NiMH battery has almost twice the energy density of a typical NiCd battery while operating at the same voltage, the NiMH battery has established itself as a mainstay in rechargeable batteries. It is strongly recommended for use in many portable electronic devices and applications for electric vehicles. NiMH batteries provide many benefits compared to other secondary battery types, particularly in energy density and life cycle (Ying et al., 2006). Typically, NiMH batteries have a maximum lifespan of five years or less and can be recharged hundreds of times. They may be produced in an almost infinite variety of sizes, ranging from tens of milliampere hours to hundreds of ampere-hours, and they are safe. NiMH batteries are utilized widely in situations where performance and the environment are of utmost concern. The end of the 1980s saw the commercialization of NiMH, which is now widely utilized in consumer electronics and hybrid electric cars (Taniguchi et al., 2001).

3.2.5 Electrochemical batteries versus supercapacitor comparison

Because of its extremely high capacitance, the supercapacitor; also referred to as an ultracapacitor or double-layer capacitor differs from a standard capacitor. An electrochemical reaction is not used in a capacitor; instead, a static charge is used to store energy. The capacitor is charged by applying a voltage difference to the positive and negative plates.

The electrostatic capacitor with a dry separator is the most fundamental of the three different types of capacitors. This traditional capacitor is primarily used for filtering and tuning radio frequencies because of its extremely low capacitance. The capacitance of an electrolytic capacitor is higher than that of an electrostatic capacitor and is measured in microfarads, which are a million times larger than pico-farads. The filtering, buffering, and signal coupling functions of these capacitors employ a wet separator. Like a battery, the electrostatic capacity has a positive and a negative that must be taken into consideration.

The third type, which has a farad rating thousands of times higher than an electrolytic capacitor, is a supercapacitor. A supercapacitor is employed to store energy that frequently goes through high current, rapid charge and discharge cycles.

Using unique electrodes and electrolytes, the supercapacitor has developed into battery technology. The Asymmetric Electrochemical Double Layer Capacitor (AEDLC) uses electrodes that are similar to battery electrodes to achieve a higher energy density than the conventional Electrochemical Double Layer Capacitor (EDLC), but it has a shorter cycle life and other drawbacks that are shared with the battery. Although such advancements are 15 years distant, graphene electrodes offer advances to supercapacitors and batteries (Tahir et al., 2020).

The most popular systems today are based on the electrochemical double-layer capacitor, which is based on carbon, has an organic electrolyte, and is simple to produce. Several different types of electrodes have been attempted (Tahir et al., 2020).

Voltage limitations apply to all capacitors. The supercapacitor is limited to 2.5–2.7 V while the electrostatic capacitor can be engineered to handle high voltages (Scholarly Community Enciclopedia, 2022). Voltages up to 2.8 V are feasible, although they have a shorter service life. Several supercapacitors are connected in series to obtain larger voltages (Scholarly Community Enciclopedia, 2022). The internal resistance rises and the total capacitance decreases with a serial connection. Voltage balancing is necessary for strings longer than three capacitors to avoid any cell from experiencing an overvoltage. There is a similar protection circuit for lithium-ion batteries.

The supercapacitor's specific energy ranges from 1Wh/kg to 30Wh/kg, which is 10–50 times less than Li-ion. Another drawback is the discharge curve. The usable power spectrum is reduced by the supercapacitor's voltage, which declines linearly while the electrochemical battery's voltage remains constant in the usable power spectrum (Battery University, 2021a).

Figures 3.7 and 3.8 show the voltage and current characteristics during a supercapacitor's charge and discharge. Without a full-charge detecting circuit, the voltage rises linearly throughout charging, and the current decreases by default when the capacitor is full. This is accurate when using a constant current supply and a voltage limit that is appropriate for the rated voltage of the capacitor; going above that limit could cause damage to the capacitor.

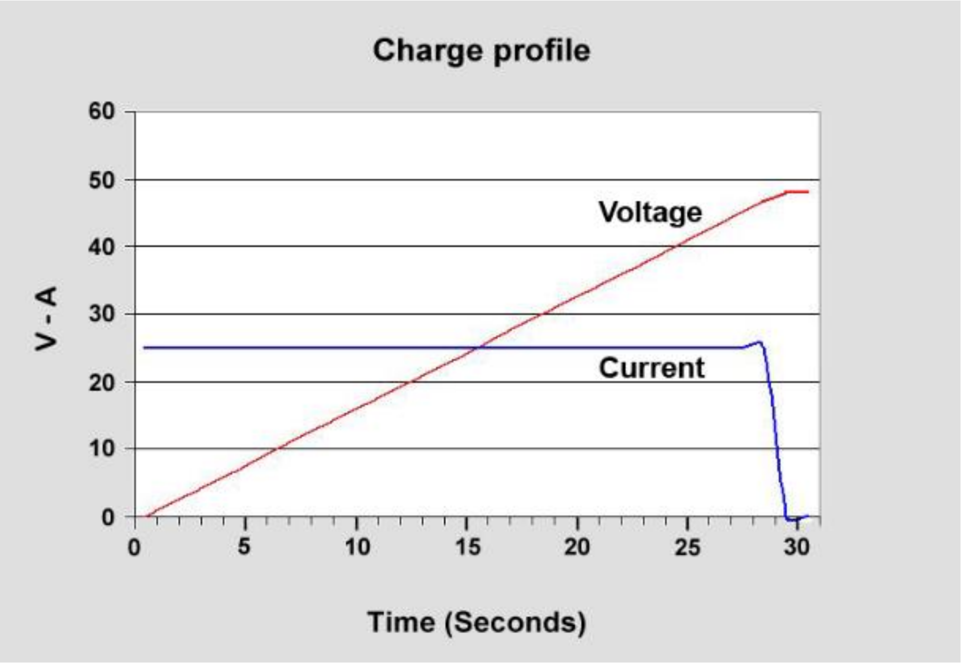

Figure 3. 7: Supercapacitor charge profile (Battery University, 2021a)

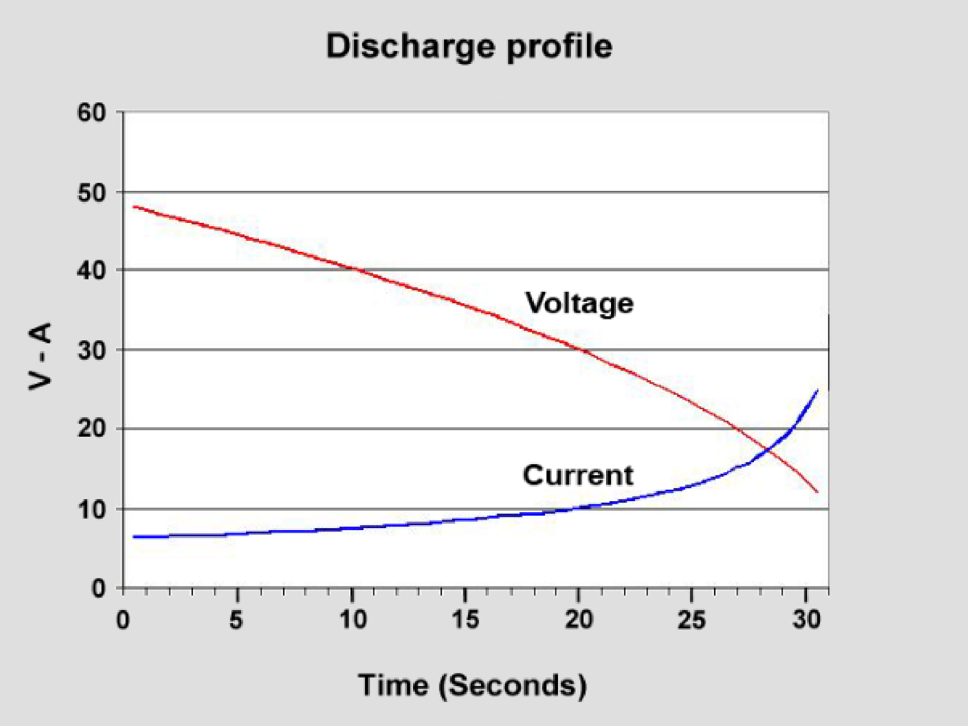

Figure 3. 8: Supercapacitor discharge profile (Battery University, 2021a).

A supercapacitor takes 1 to 10 seconds to charge. The charge characteristic is comparable to that of an electrochemical battery, and the charger's capacity to handle current to a considerable extent limits the charge current. While the topping charge will require more time, the initial charge can be accomplished quickly. When charging an empty supercapacitor, provisions must be taken to limit the inrush current because it will suck up all it can. The current immediately stops flowing when the supercapacitor is fully charged, eliminating the risk of overcharging and the need for full-charge sensing. Table 3.5 illustrates the comparison between a standard Li-ion battery with a supercapacitor.

Table 3. 5: Performance evaluation of Li-ion batteries versus traditional supercapacitors (Battery University, 2021a)

Characteristic	Supercapacitor	Lithium-ion battery
Charge time	1 to 10 seconds	10 to 60 minutes
Cycle life	1 million or 30000 h	500 and higher
Cell voltage	2.3 to 2.75 V	3.6 V nominal
Specific energy (Wh/kg)	5 (typical)	120-240
Specific power (W/kg)	Up to 10000	1000-3000
Service life	10 to 15 years	5 to 10 years
Charge temperature	-40 to 65ºC	0 to 45ºC
Discharge temperature	-40 to 65ºC	-20 to 60ºC
Self-discharge within 30 days	5 to 40 %	5% or less

The number of times the supercapacitor may be charged and drained is practically limitless. When a supercapacitor is cycled, there is less wear and tear than when an electrochemical battery is. The supercapacitor ages better than a battery does. A supercapacitor typically loses 80% of its original capacity in 10 years under normal circumstances (Battery University, 2021a). The life is shortened if greater voltages than required are applied. Batteries cannot match the supercapacitor's tolerance for both hot and cold temperatures.

The organic electrolyte has a role in the fact that the self-discharge of a supercapacitor is significantly higher than that of an electrostatic capacitor and slightly higher than that of an electrochemical battery. Although there are benefits to comparing the supercapacitor to a battery, focusing just on the similarities limits a broader knowledge of this distinct technology.

The operational voltage of a battery is determined by its chemistry; the electrochemical reactions of charge and discharge. In contrast, the capacitor is not electrochemical, and the type of dielectric material employed as a separator between the plates determines the maximum permissible voltage. Some capacitors' capacitance is increased when electrolyte is present. The voltage can increase without restriction until the dielectric fails since the supercapacitor is non-chemical. This frequently takes the shape of a short circuit.

CHAPTER FOUR

MODELING AND SIMULATION OF ELECTROCHEMICAL AND NUCLEAR BATTERIES FOR UTILITY APPLICATIONS

4.1 Introduction

This chapter is dedicated to the study of the behavior of electrochemical and nuclear batteries using modeling and simulation tools to ascertain their performances and drawbacks. Understanding the batteries' behaviours provides insight into application areas.

4.2 Modeling of electrochemical batteries

The study of the behavior of electrochemical batteries is described in two principal ways: the discharging and the charging. Both can be mathematically modeled in MATLAB/Simulink environment.

Four types of batteries: Lithium-Ion (Li-ion), lead-acid, Nickel Cadmium (NiCd), and Nickel-Metal-Hybride (NiMH) batteries under consideration are the most preferred in the field of space applications due to their capacity to recharge and their power density. The behavior of these batteries can be defined by two sets of equations for discharging and charging, respectively.

4.2.1 Governing equations

The equations presented in Table 4.1 below have been purposefully developed for use in the SimPowerSystems environment in Simulink (Tremblay & Dessaint, 2009) so that the model exhibits real behavior during charge and discharge. They are derived from the Shepherd model describing the battery electrochemical behavior using the terminal voltage, open circuit voltage, internal resistance, discharge current, and the state of charge (Shepherd, 1965).

Table 4. 1: Model equation summary (Mathworks, 2008)

Battery	Discharge	Charge
Li-ion	$V_{batt} = E_o - K\frac{Q}{Q-it}(it+i^*) + Ae^{-Bit} - R.i$	$V_{batt} = E_o - K\frac{Q}{it-0.1Q}(i^*) - K\frac{Q}{Q-it}(it) + Ae^{-Bit} - R.i$
Lead-acid	$V_{batt} = E_o - K\frac{Q}{Q-it}(it+i^*) + e^t - R.i$	$V_{batt} = E_o - K\frac{Q}{it-0.1Q}(i^*) - K\frac{Q}{Q-it}(it) + e^t - R.i$
NiCd	$V_{batt} = E_o - K\frac{Q}{Q-it}(it+i^*) + e^t - R.i$	$V_{batt} = E_o - K\frac{Q}{\lvert it\rvert-0.1Q}(i^*) - K\frac{Q}{Q-it}(it) + e^t - R.i$
NiMH	$V_{batt} = E_o - K\frac{Q}{Q-it}(it+i^*) + e^t - R.i$	$V_{batt} = E_o - K\frac{Q}{\lvert it\rvert-0.1Q}(i^*) - K\frac{Q}{Q-it}(it) + e^t - R.i$

4.2.2 Modeling system and parameters

The battery modeling system is represented by a power source and an internal resistance R. The battery voltage E_{batt} depends on the current, i (positive during charge and negative during discharge). The Shepherd model of battery discharge equation is based essentially on three very important parameters: internal resistance, polarization coefficient, and initial drop of potential at the beginning of a cell discharge. Considering firstly the R-int model circuit consisting of a power source and an internal resistance R in series, it is possible to write:

$$U_t = U_{OCV} - R.i \tag{4.1}$$

Where U_t, R, i and U_{OCV} are the terminal voltage, the internal resistance, the current and the open circuit voltage, respectively.

According to Shepherd, another parameter that has to be considered is the polarization coefficient K of the electrodes. Taking the polarization coefficient into consideration, equation one becomes:

$$U_t = U_{OCV} - K\left(\frac{Q}{Q-it}\right).i - R.i \tag{4.2}$$

where Q is the amount of active material in electrodes and measured in coulombs.
Lastly, the parameter which Shepherd considered is an initial drop of potential at the beginning of a cell discharge obtained experimentally, which is not included in Equation 4.2. Therefore, another term has to be added to correct the behavior described by this equation, obtained experimentally. The variable $Ae^{-BQ^{-1}.i.t}$; with A and B being "empirical constant" exhibiting good estimation of initial voltage drop in

what can be called the exponential area. Incorporating the exponential function, equation 2 becomes:

$$U_t = U_{OCV} - K\left(\frac{Q}{Q-it}\right).i - R.i + Ae^{-BQ^{-1}.i.t} \qquad (4.3)$$

The diagram in Figure 4.1 depicts the battery discharge model.

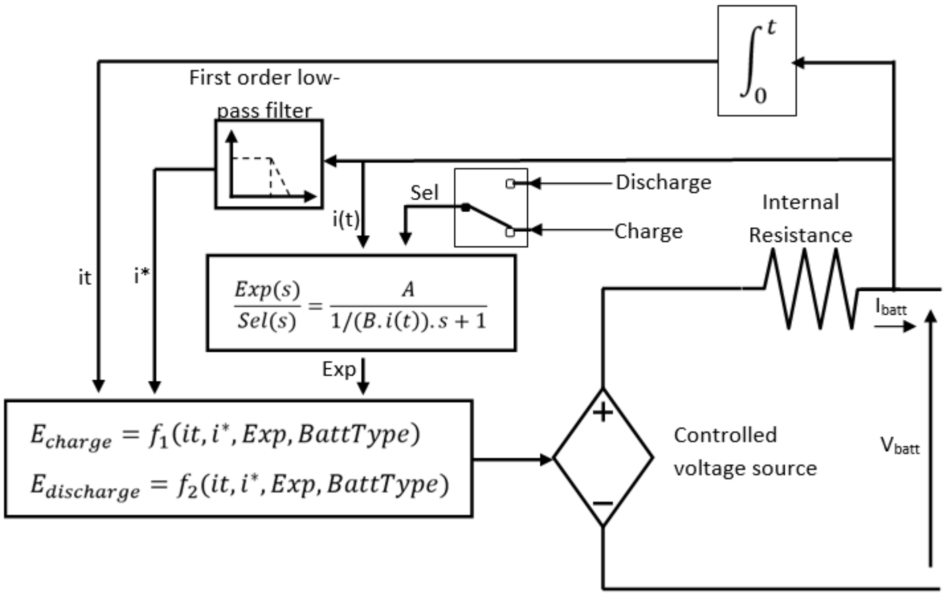

Figure 4. 1: Battery discharge model (Mathworks, 2008)

The parameters are represented in Table 4.2.

Table 4. 2: Battery Parameters (Tremblay & Dessaint, 2009)

	Type of batteries			
Parameters	**Lead-acid** 2V 4 Ah	**NiCd** 1.2 V 2.3 Ah	**Li-ion** 3.3 V 2.3 Ah	**NiMH** 1.2 V 6.5 Ah
E_0 (V)	2	1.2705	3.366	1.2816
R (Ω)	0.04	0.003	0.01	0.002
K (Ω or V/Ah)	0.047	0.0037	0.0076	0.0014
A (V)	0.83	0.127	0.26422	0.111
B (Ah)$^{-1}$	125	4.98	26.5487	2.3077

4.2.3 Simulink models of electrochemical batteries

The following section describes the design of the Matlab/Simulink model of the discharge and charge behaviors of the four batteries under consideration: Li-ion, NiCd, NiMH, and lead-acid, based on the equations in Table 4.1.

- **Li-ion model**

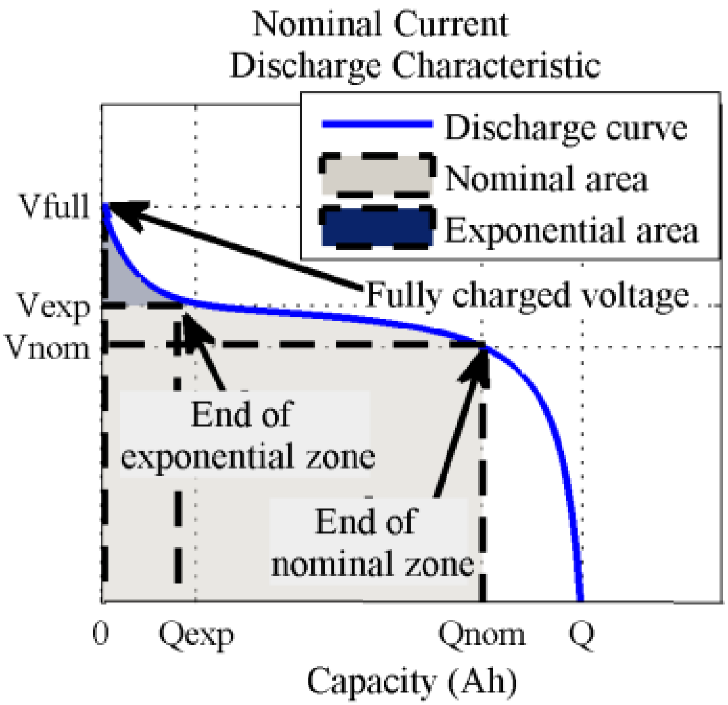

Figure 4. 2: Discharge behaviour at nominal current (Tremblay & Dessaint, 2009)

The discharge characteristic of most batteries could be illustrated as shown in Figure 4.2 above. According to Tremblay & Dessaint (2009), the discharging model battery of the open circuit voltage (OCV) with regards to the state of charge (SoC) could be best represented since it adds a polarisation voltage variable to better describe the OCV behavior; and polarisation resistance is changed compared to Shepherd equation above since it is a filtered current to minimize error and expressed as $K\frac{Q}{Q-it}$ The proposed equation is:

$$V_{batt} = E_0 - K\frac{Q}{Q-it}it - Ri + Ae^{-Bit} - K\frac{Q}{Q-it}i^* \tag{4.4}$$

where V_{batt} is the terminal voltage (V), E_0 is the fully charged battery voltage (V), R is the internal resistance (Ω), i and i^* are current (A) and filtered current (A), respectively, Q is the battery capacity or the actual battery charge (Ah), K is the polarisation constant/resistance (V/Ah), A is the exponential zone amplitude (V), and B is the exponential zone time constant inverse $(Ah)^{-1}$.

The filtered current i^* flowing through the polarisation resistance solves the control loop for the simulation in Simulink. It also helps to describe the nonlinearity between the OCV and SoC. The use of this equation in Li-ion battery retains the same exponential zone expressed by Ae^{-Bit}.

The discharge model of the Li-ion is represented in Figure 4.3, and it is made of 6 critical parts. Block 2 is the electrical representation of the battery with a controlled source voltage, an internal resistance $R_{1,}$ and a load resistance R_2. The current block at 4 takes the current value and integrates it calculating the charge being drawn over time, and in block 5, there is a filtration that filters the current going through the circuit. Meanwhile, on block 3 are located the different constant values determined in the previous section. These blocks are transferred into block 1, which is the modeling of the discharge equation; in the blue line, it is possible to see that the output voltage at block 1 or discharge voltage is then connected back to the controlled voltage source response.

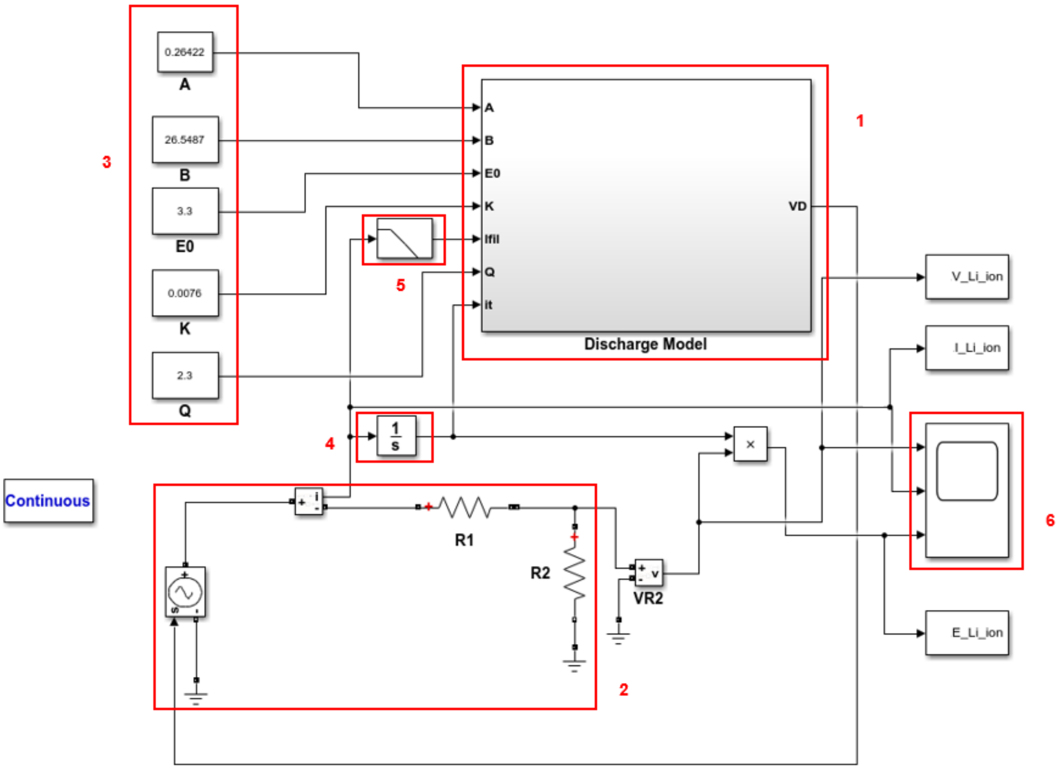

Figure 4. 3: Simulink discharge model

Meanwhile, the discharge model subsystem (block 1) is represented in Figure 4.4 below, and it is made up of block 7, 8 and 9, representing the exponential zone of the discharge curve. The battery charge and, in addition, filtered current and the polarisation resistance, respectively. All are being fed to the output (discharge) voltage V_D.

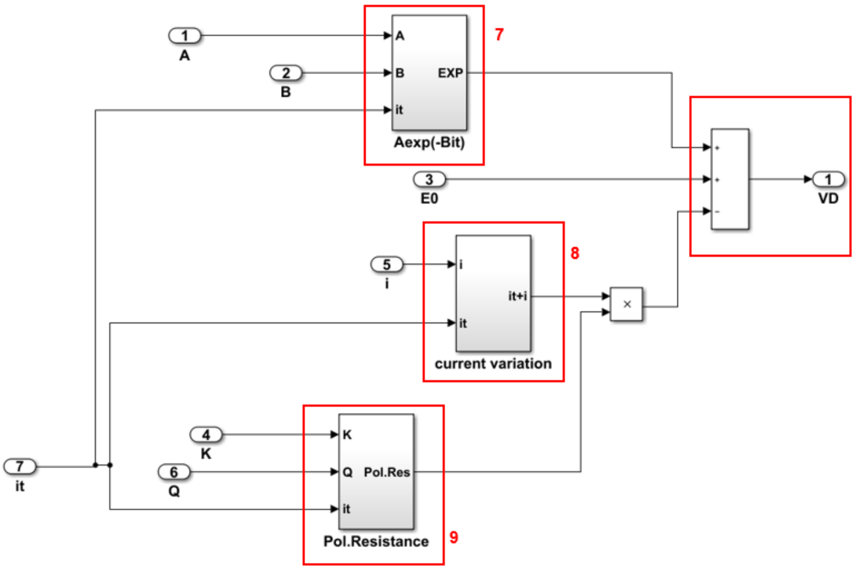

Figure 4. 4: Discharge model function

Inside the exponential subsystem (block 7), it could be seen that signal B is multiplied by the battery actual charge *it* and brought to the exponent power, then multiplied by the signal *A* to result in the exponential value Exp (see Figure 4.5).

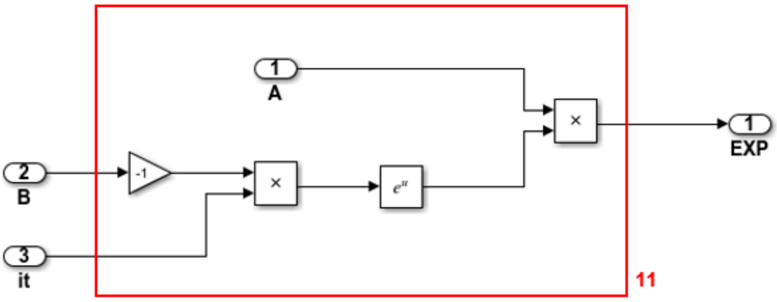

Figure 4. 5: Exponential zone voltage $Ae^{-B.it}$

The Li-ion battery discharge behavior is relative to the polarization resistance $\frac{Q}{Q-it}$, which, when multiplied by *it,* produces the polarization voltage created by the ionization of the electrodes; and responsible for side effects such as electric current converted into heat and self-discharge. While when the pole resistance is multiplied by the filtered current, it evaluates the amount of voltage produced by unused active material. Therefore, Figure 4.6, for simplicity, add the actual charge and current, which is then multiplied by the polarization resistance modeled as shown in Figure 4.7.

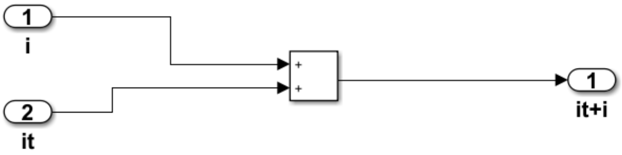

Figure 4. 6: Variable discharge current

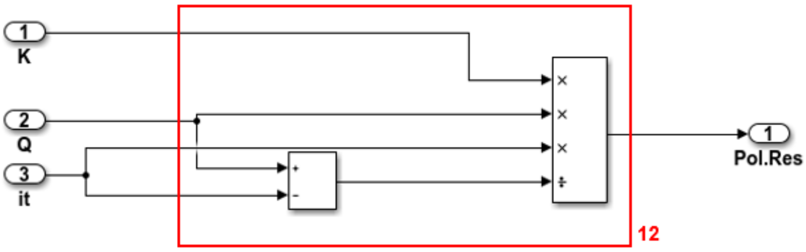

Figure 4. 7: Polarization resistance

The system characteristics of a charging battery in Figure 4.8 exhibit very different behavior; especially the end of charge (EOC).

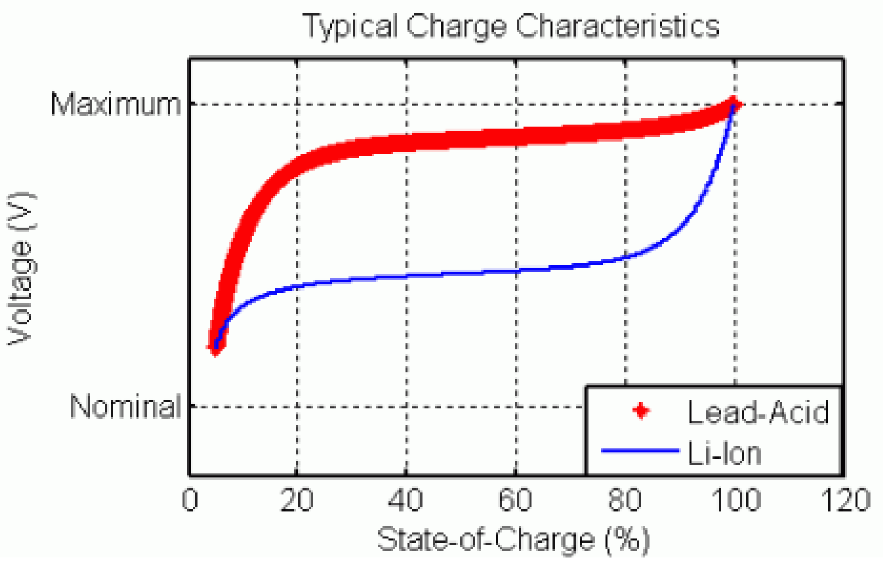

Figure 4. 8: Battery charging behavior (Tremblay & Dessaint, 2009)

- **Li-ion and lead-acid model**

These two types of batteries exhibit similar EOC with a sudden voltage increase when the battery gets fully charged. This is demonstrated by the polarisation variable resistance that increases considerably when the battery charge (it) decreases and reaches 0. Another consideration is that at full charge, the polarization is infinite when the actual charge (it) is about 10% less than the battery charge Q (Rynkiewicz, 1999). Thus the polarisation equation can be written as:

$$Pole - resistance = K\frac{Q}{it-0.1Q} \tag{4.5}$$

Thus the Li-ion charge behavior is exhibited using the following equation:

$$V_{batt} = E_0 - K\frac{Q}{it-0.1Q}(i^*) - K\frac{Q}{Q-it}(it) + Ae^{-Bit} - R.i \tag{4.6}$$

We can see that the battery's voltage source (battery) receives the charge voltage signal V_C (blue line) is connected in parallel with another constant power source (block 5) while the internal resistance R_1 which is connected in series with the constant power source (block 5) is to facilitate the running of the Simulink model depicted by Figure 4.9.

In charging mode, the creation of ions in the electrolyte rebuilds both electrodes to their initial state, restoring the battery's energy with a negative current flowing through the battery. This negative current then passes through the integrator at block 3 and filter at block 4. At block 2, we could find the battery parameters previously determined, which are fed to the charge model in block 1.

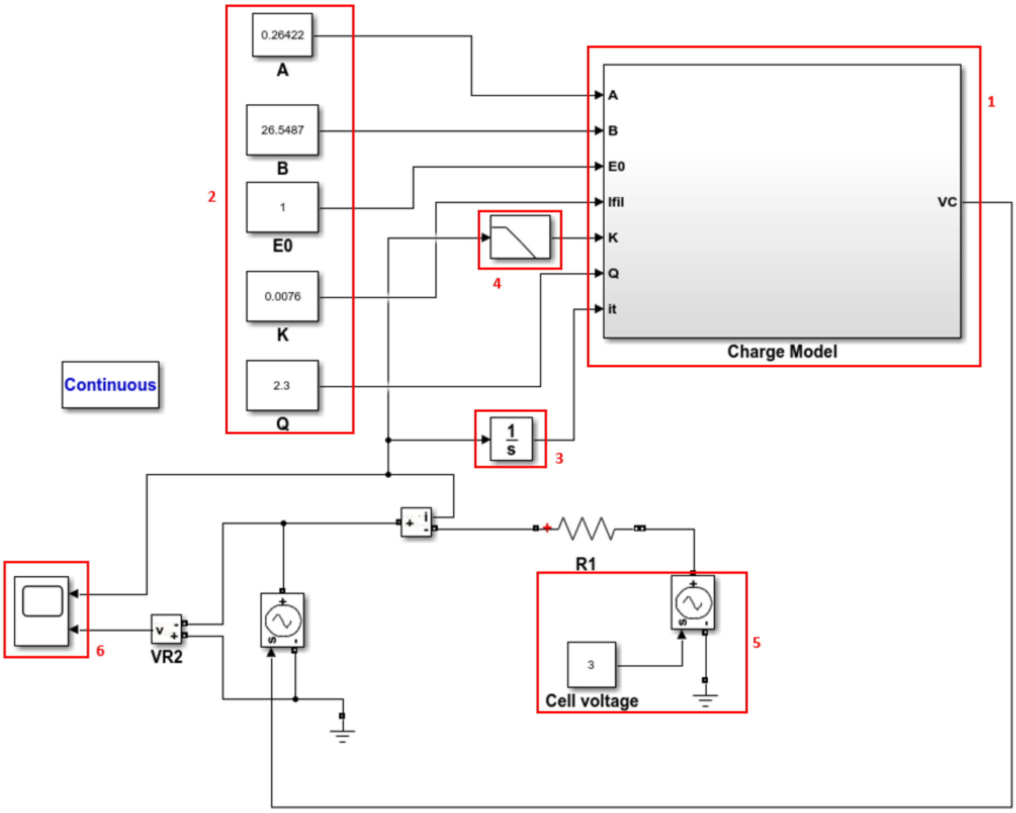

Figure 4. 9: Battery charge Simulink model

Figure 4.10 is the content of the charge model sub-system. It is divided with blocks 7, 8, and 9 that represent the exponential voltage zone, the polarization resistance, and polarization voltage, respectively, connected to the appropriate sign relative to the charge equations developed above. And on block 10 the output is the charging voltage V_C fed back to the controlled source.

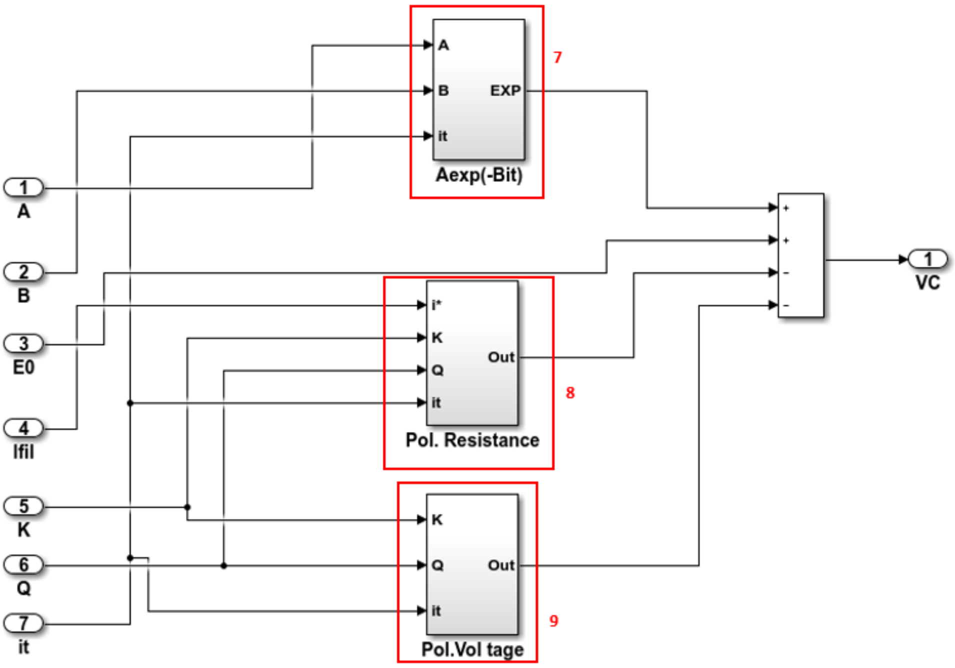

Figure 4. 10: Charge model sub-system

Figure 4.11 represents the sub-system of the exponential zone voltage. Again we see that signal *B* is multiplied by -1 and the actual charge *it,* thereafter, the exponent value is multiplied by signal *A.*

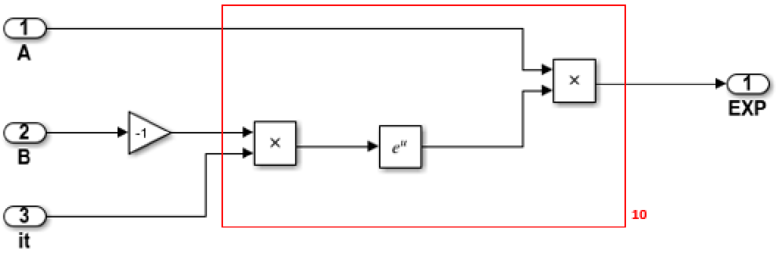

Figure 4. 11: Exponential zone voltage Ae$^{-B.it}$

Figure 4.12 represents the polarization resistance created during charge (block 8 shown in Figure 4.10). It takes all parameters and arranges them in the way of the charging equation stated above.

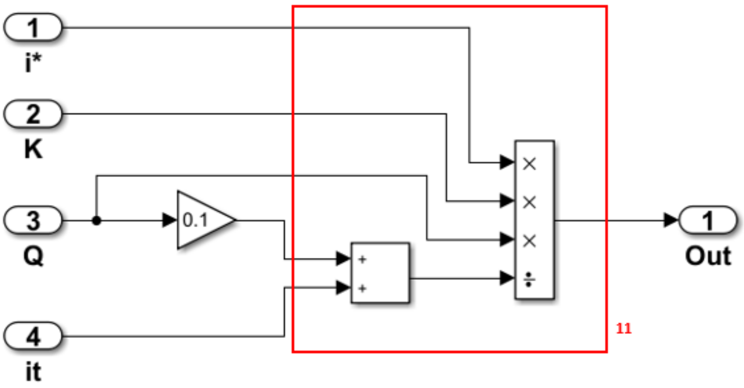

Figure 4. 12: Polarisation resistance

Finally, Figure 4.13 represents the polarization voltage sub-system (block 9 of Figure 4.10) is shown below. With *K* multiplying the inverse of the value of inactive material $\frac{Q}{Q-it}$.

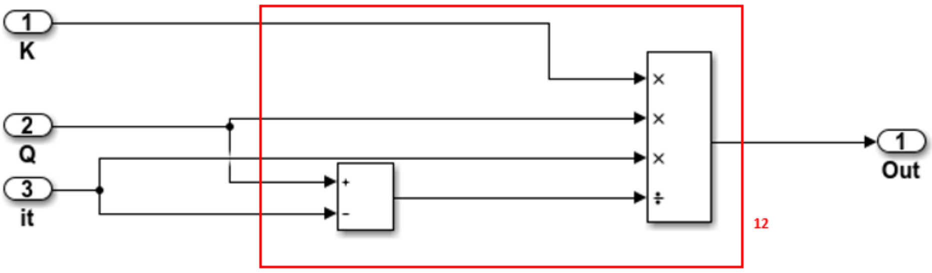

Figure 4. 13: Polarisation voltage

Although the battery needs to be simulated under some real-life conditions, thus it is necessary to model a charge and discharge system when there is a need to study the number of life cycles the battery can endure. The combination of battery charge and discharge could be seen in Figure 4.13 to simulate the battery behavior when being discharged and charged successively, assuming a constant current flow through it.

Block 1 contains the Li-ion battery parameters, which are then connected to the inputs of the battery discharge and charge model in block 2 (note that both sub-systems have the same type of equations as described above). Each of the two sub-systems is then connected to one of the controlled voltage sources in block 4, the blue lines representing the discharge signal and the light-green representing the battery charge signal. Finally, these two voltage-relays connections are then connected in parallel. It could be seen that the controlled voltages are connected in series with a relay, one at block 5 and the other at block 6, which are then arranged in parallel. It is observable that the relay of block 5 is connected to the discharge signal; meanwhile, the relay at block 6 is connected to the charge signal. Furthermore, the charge signal is also connected to two other relays in block 7, which, when activated, close circuitry to the controlled voltage source with charge model input.

Similarly, the other two relays on block 8 are connected to the discharge signal. When relays get closed, it connects the load resistance to the controlled voltage source, receiving the discharge voltage output. Thus, this configuration makes the voltage connected to exhibit discharge behavior when discharge relays are closed; but displays charge behavior when the relays connected to the charge signal are closed.

The activation of the relays is done after the passing of the signals contained in the Simulink function block (block 9 in Figure 4.14). The Matlab code contained in this function is indicated in Code 4.1 which takes for input the actual charge *it,* the actual battery voltage V_B and while it gives the following output: the *discharge voltage, charge voltage, and state of charge* of the battery. Thus, when the simulation is launched with the assumption that the battery is fully charged, the code calculates the SoC (state of charge) and sets the discharge bit to 1 and the charging bit to 0; which means that the relays connected to the load resistance and voltage source connected to the discharge model sub-system are first activated.

The first **if** condition in the code checks for the SoC percentage so that if it is above 80% (i.e. when fully charged), it activates the discharge relay and turns off the charge relay. While the second **if** condition verifies if the SoC is below 30%, where if the condition is met, then the relays change polarities to activate the charge relay and deactivate the discharge relay.

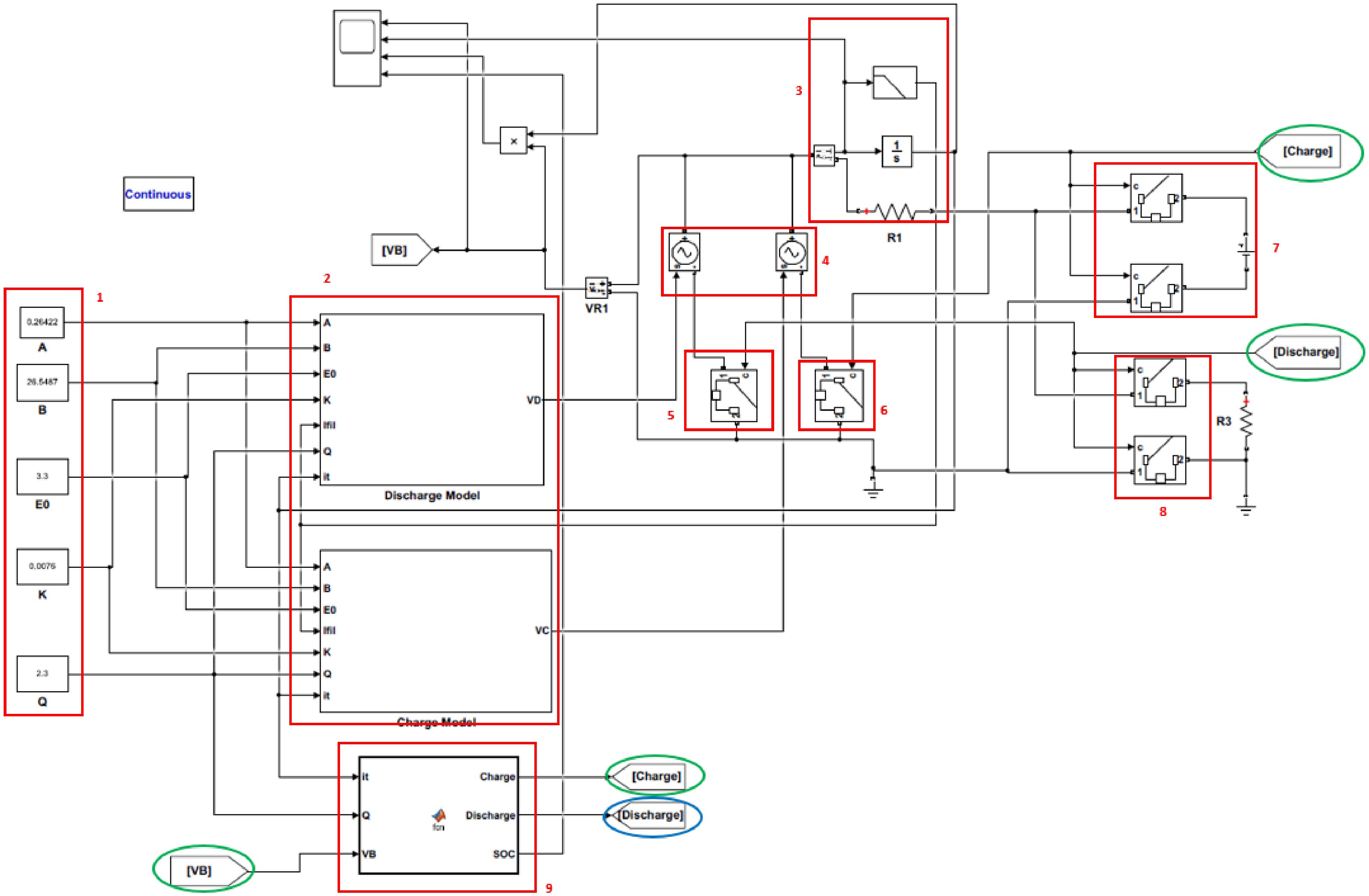

Figure 4. 14: Lithium-ion battery charge-discharge model

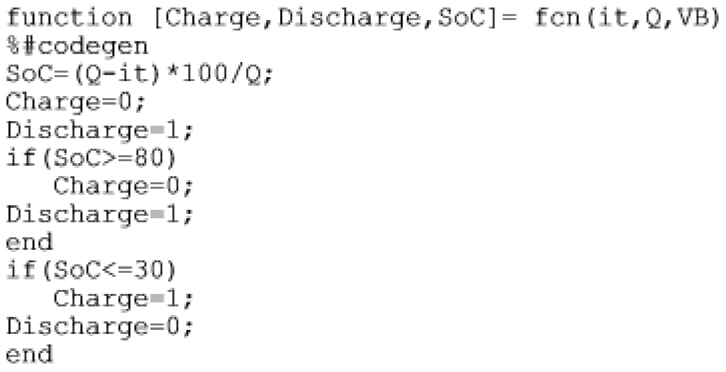

```
function [Charge,Discharge,SoC]= fcn(it,Q,VB)
%#codegen
SoC=(Q-it)*100/Q;
Charge=0;
Discharge=1;
if(SoC>=80)
    Charge=0;
Discharge=1;
end
if(SoC<=30)
    Charge=1;
Discharge=0;
end
```

Code 4. 1: Function Code controlling battery charge-discharge behavior

The three other types of batteries, NiCd, NiMH, and lead-acid, present some hysteresis behavior between charge and discharge (Rynkiewicz,1999; Feng et al,2008), as seen in Figure 4.15 below.

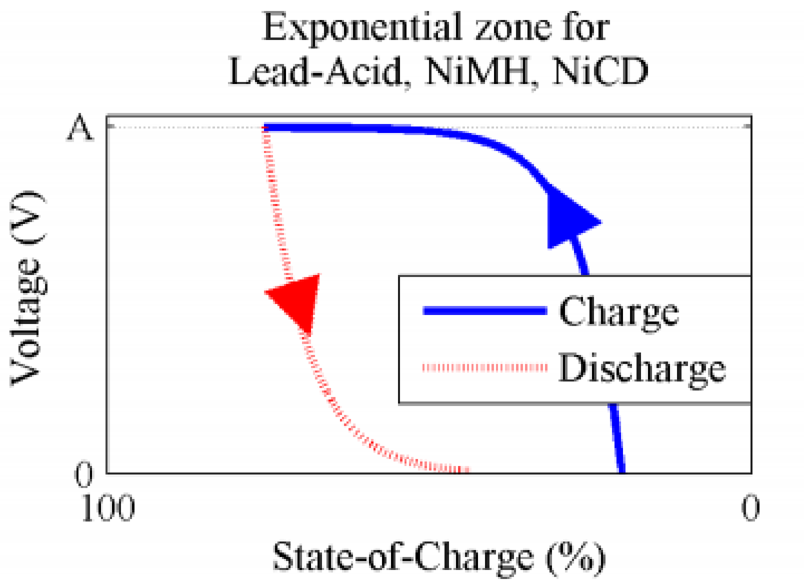

Figure 4. 15: Battery hysteresis phenomenon in charge behavior (Tremblay & Dessaint, 2009)

The hysteresis phenomenon in the three batteries under consideration: NiCd, NiMH, and lead-acid, can be described by the equation:

$$\dot{e^t} = B.|i(t)|\left(-e^t + A.u(t)\right) \tag{4.7}$$

Where e^t, $i(t)$, $u(t)$ are the exponential zone voltage (V), the battery current (A), *and* the charge or discharge mode, respectively. *u*(t) = 0 when discharged and *u*(t) = 1 when charged.

It could be seen that a new component |*i*(t)| needs to be added to the Simulink model to calculate the value of e^t. Thus the equation of discharge of these three types of batteries can be expressed by:

$$V_{batt} = E_0 - K\frac{Q}{Q-it}(it) + K\frac{Q}{Q-it}(i^*) + e^t - R.i \tag{4.8}$$

where e^t is the integral of the hysteresis phenomenon derived above.

The Matlab/Simulink models of the discharge behavior of the three batteries under consideration are represented in Figure 4.16. However, it is clear that it contains all of the blocks as of those present in the Li-ion discharge model previously except for block 2 and the battery parameter of block 1 that have been determined before.

The discharge model sub-system shown in Figure 4.17 is composed of block 1, 2, and 3 representing the hysteresis, the current variation, and polarization, respectively. The hysteresis equation at block 1 is represented by Figure 4.18. It is arranged to solve the differential equation of $\dot{\mathrm{Exp}}(\mathrm{t})$ using a feedback loop of $Exp(t)$ and integrating the result.

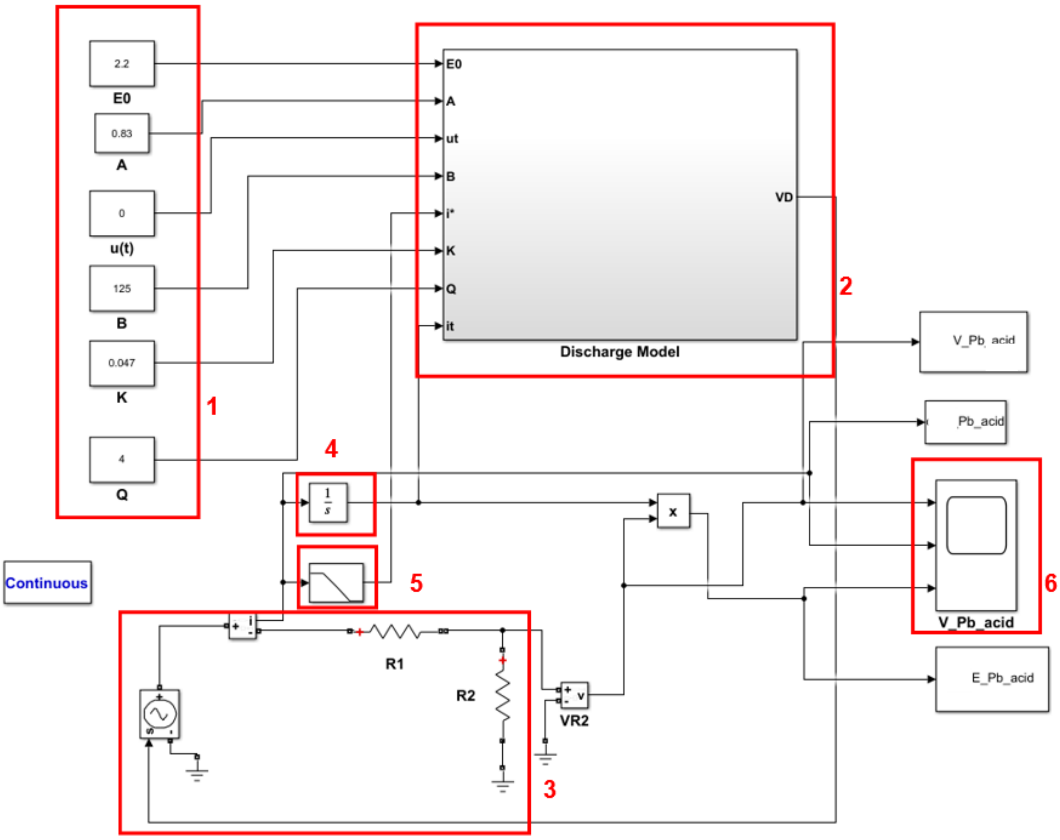

Figure 4. 16: NiCd, NiMH, Lead-Acid battery discharge model

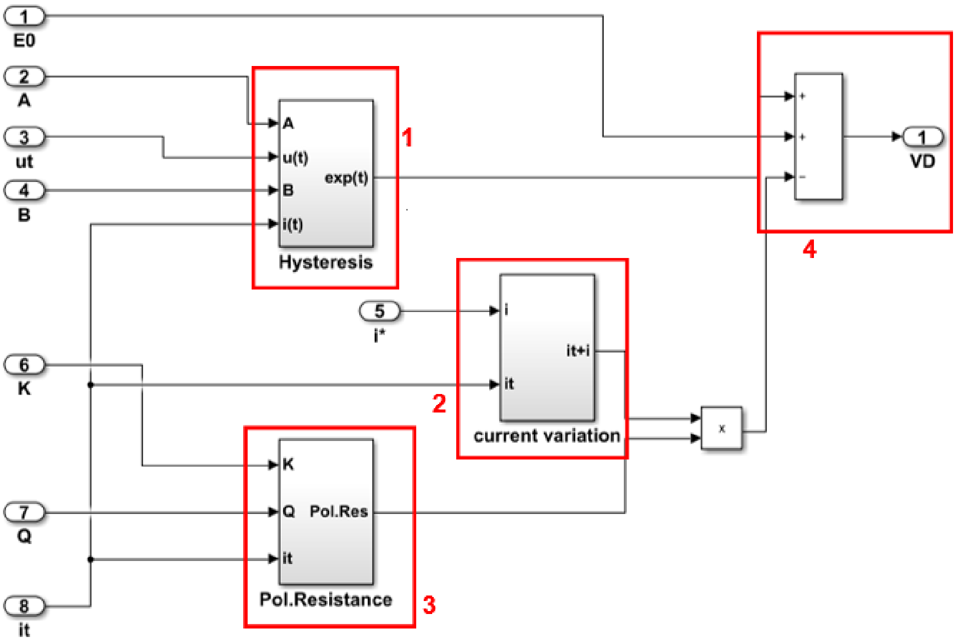

Figure 4. 17: Discharge model Sub-system (with hysteresis)

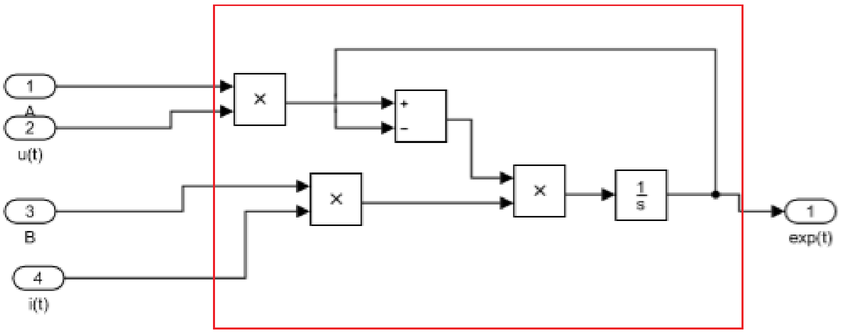

Figure 4. 18: Hysteresis phenomenon model

The modeling expression of the current variation and polarization resistance of block 2 and variable current block 3, respectively (Figure 4.19 and Figure 4.20) are similar to the expression developed for the Li-Ion battery.

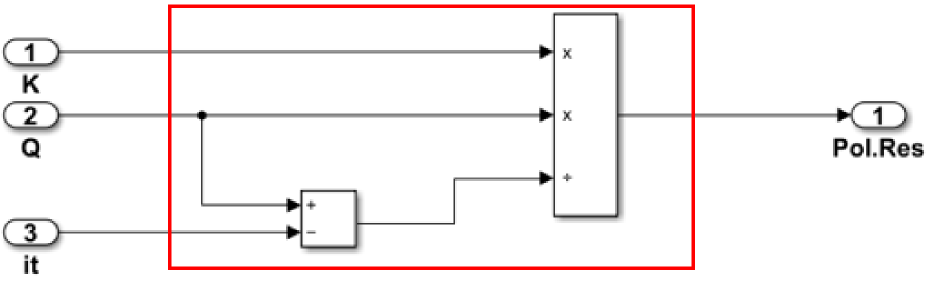

Figure 4. 19: Polarisation resistance

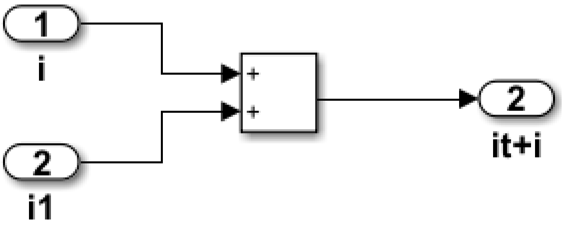

Figure 4. 20: Variable Current

The charging model (equation) for NiCd and NiMH models have EOC characterized by a slight drop in voltage (about 5 mV per cell) just after the full charge is reached, and it is important to model a battery charger to control the voltage drop so as to ensure that further charging should not take place. The battery charger is modeled by changing the polarisation resistance and using the absolute value of the actual charge |it|. This is because when the battery is fully charged and the voltage drop occurs, the value of (it<0) becomes negative. The use of the absolute value thus decreases the polarization resistance when the battery is overcharged. The polarization resistance can be expressed as:

$$Pol.resistance = K\frac{Q}{|it|-0.1Q} \tag{4.9}$$

where $Pol.resistance$ is the polarization resistance

Therefore, the charge equation of Ni-Cd, NiMH, and lead-acid batteries is:

$$V_{batt} = E_0 - K\frac{Q}{|it|-0.1Q}(i^*) - K\frac{Q}{Q-it}(it) + e^t - R.i \tag{4.10}$$

The design presented in Figure 4.21 shows the approach taken to model the battery voltage (Equation 4.10) into Simulink, which is similar to what was previously done for Li-ion battery; noting that the charge model requires a battery connected to the controlled source model and flowing electricity through it (represented by block 3). Furthermore, the charge model contains the actual charge it, after integrating the value of i (block 4) and the filtered current (block 5); and the current *i* (blue signal), which is added in order to compute Exp(t) in the sub-system.

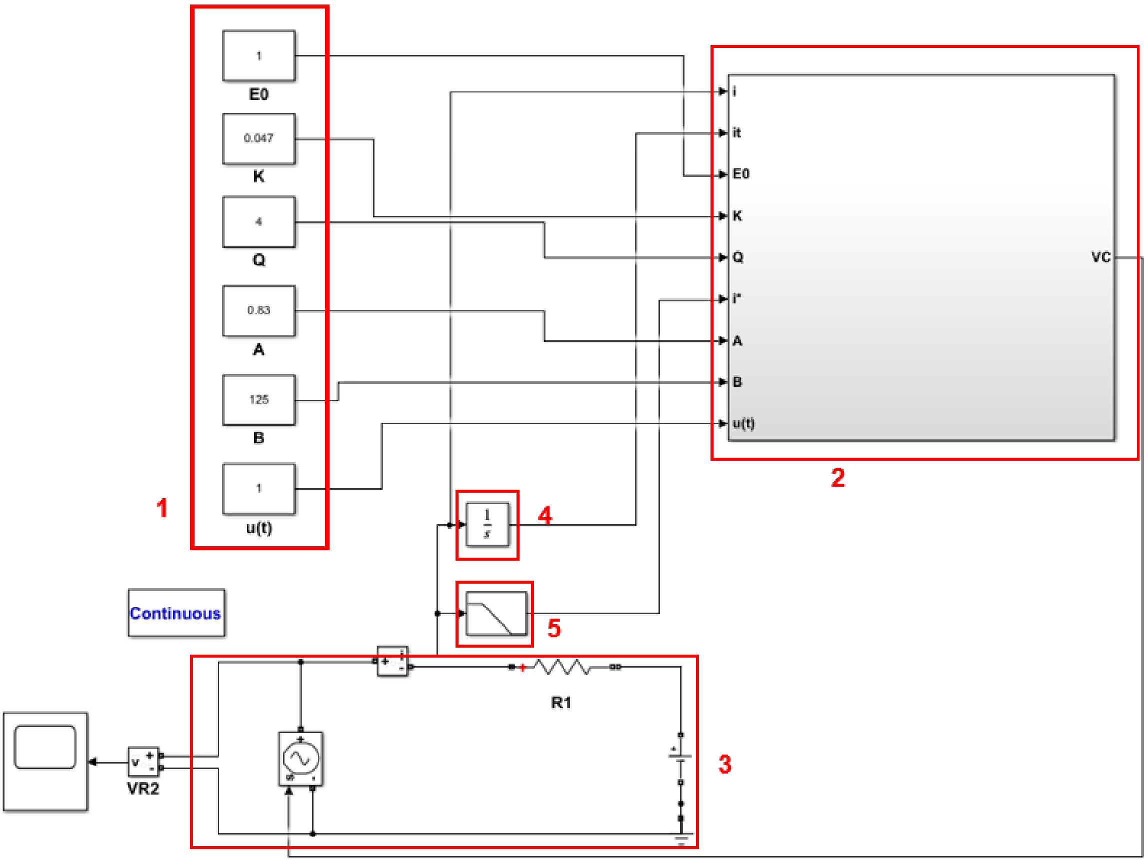

Figure 4. 21: Charging model (with hysteresis)

Figure 4.22 shows the content of the charge model sub-system with the polarisation resistance at block 9 and polarisation voltage at block 8, which are similar to these before. Although the hysteresis sub-system at block 7, further developed in Figure 4.23 shows how the absolute value of the current is used in the model in order to determine the value of *Exp(t).* Figure 4.24 and Figure 4.25 are sub-systems of polarization voltage and polarization resistance, respectively.

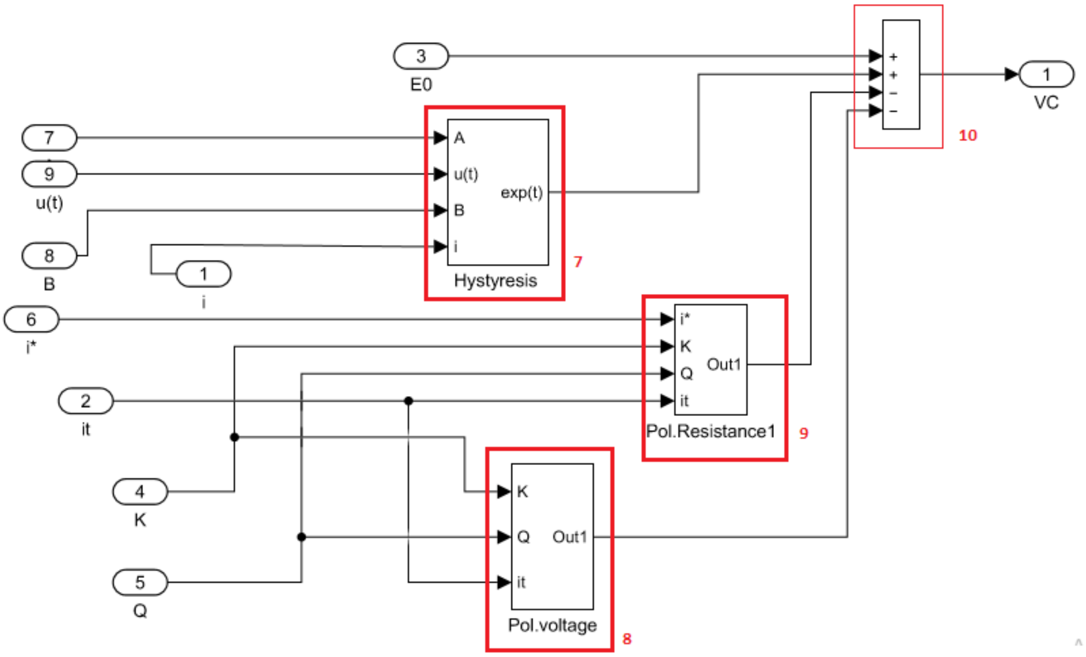

Figure 4. 22: Charge model sub-system (hysteresis)

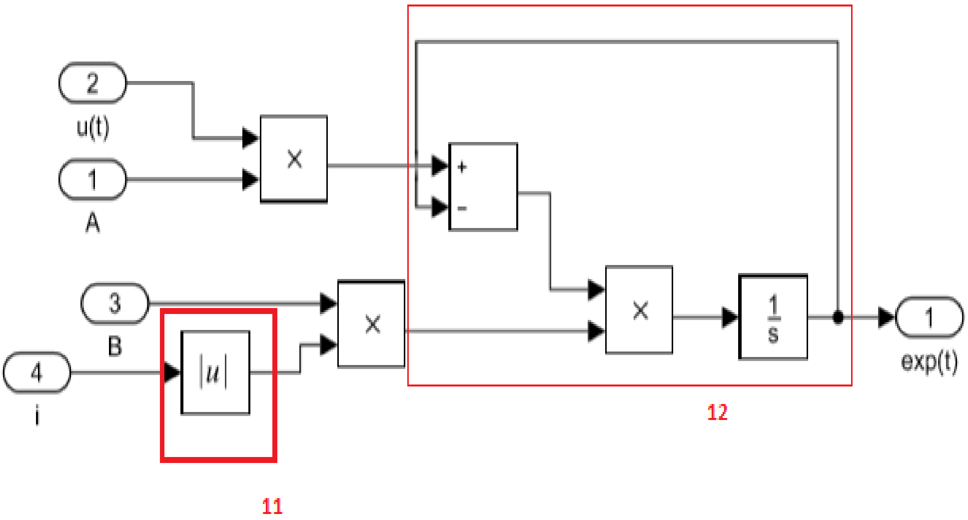

Figure 4. 23: Exp(t) voltage value model

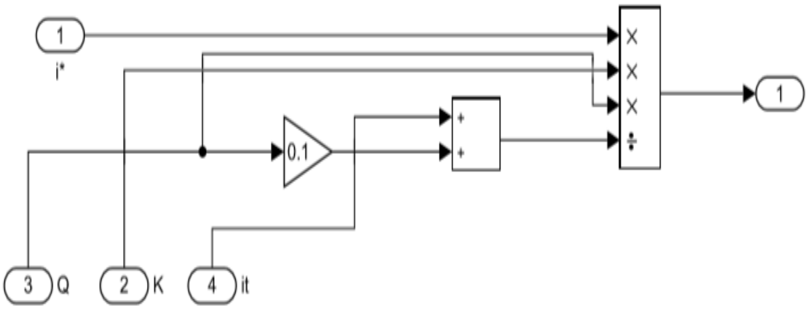

Figure 4. 24: Polarisation Resistance

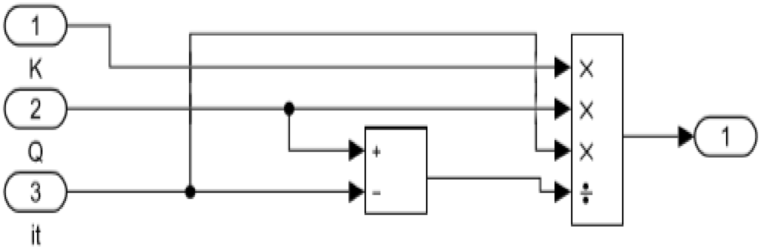

Figure 4. 25: Polarisation Voltage

For the purpose of studying the life cycle of the battery, it is also possible to develop a charge-discharge system as developed in previous sections (see Figure 4.26), which uses a Matlab function that activates the port connected to relays, switching between discharge or charge behavior according to the value of the state of charge (SoC). The program used in the Matlab function is shown in Code 4.2.

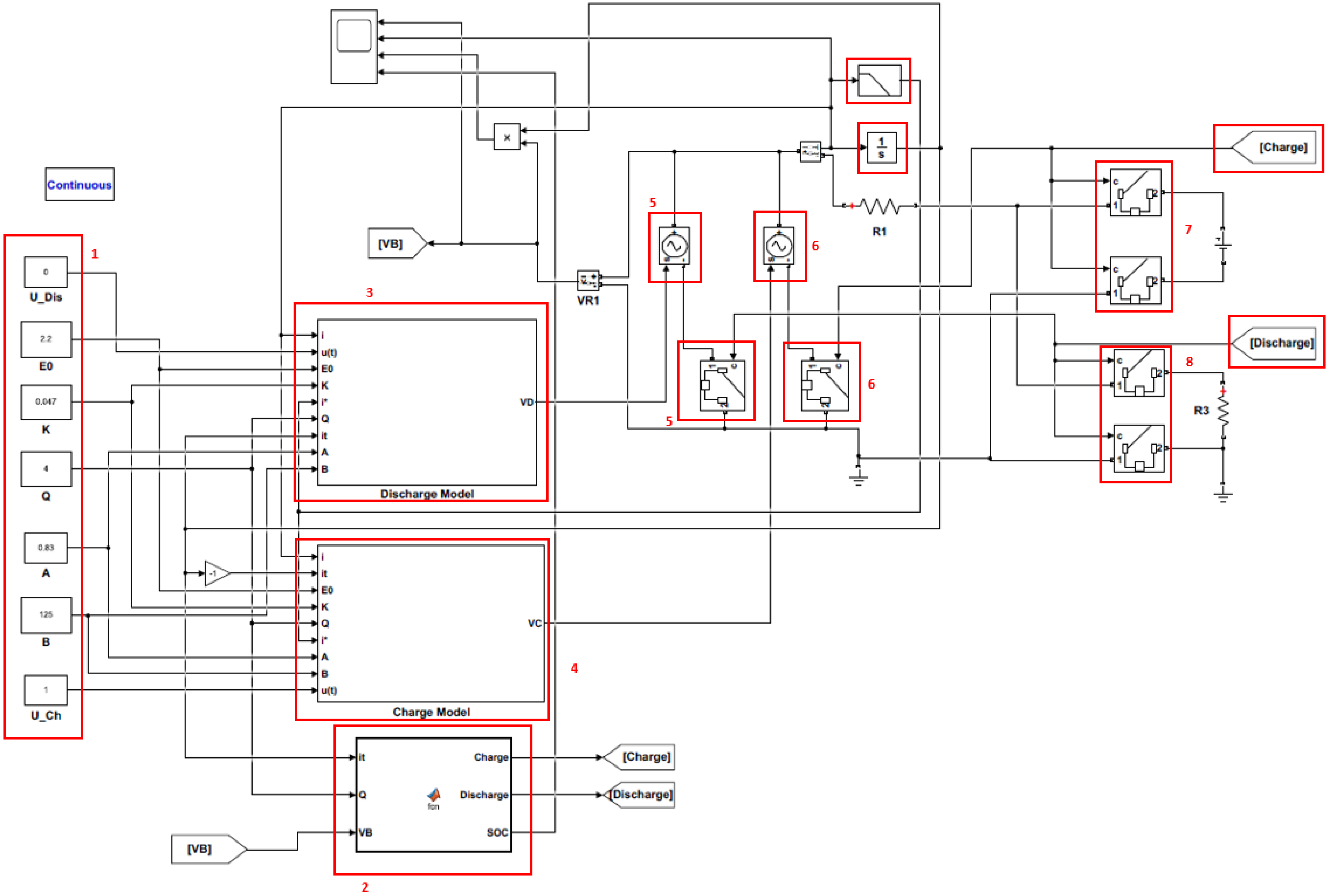

Figure 4. 26: NiCD, NiMH, lead-acid charge-discharge model

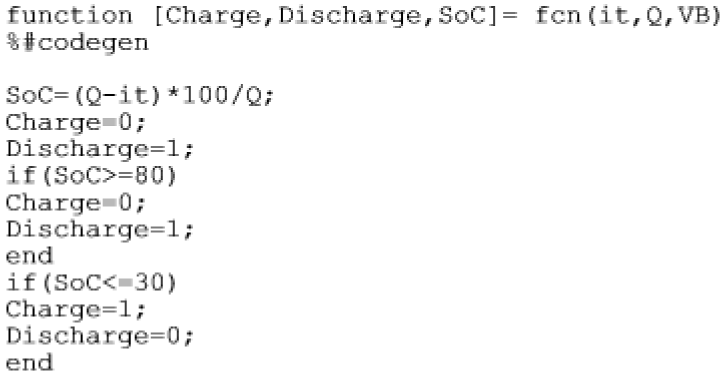

```
function [Charge,Discharge,SoC]= fcn(it,Q,VB)
%#codegen

SoC=(Q-it)*100/Q;
Charge=0;
Discharge=1;
if(SoC>=80)
Charge=0;
Discharge=1;
end
if(SoC<=30)
Charge=1;
Discharge=0;
end
```

Code 4. 2: Function code controlling the battery behavior

4.2.4 Simulation and discussion of results

This section examines the behavior of discharge under different *C-rate* since this investigation aims to develop accurate systems of control over battery discharge. Batteries can be considered multi-input and multi-output systems; under this consideration, the primary input is the delivered current to the battery, and the primary output is the voltage output (or sometimes temperatures, ionic concentrations within cells). Indeed, when the battery is connected to a load, an amount of current is being drawn slowly and thereby discharging the battery until there is a need to recharge it.

A battery stores energy in the form of electrochemical constituents, and it releases it. However, the energy tends to deplete over a certain amount of time. As elaborated in section 3.2.5, electrochemical batteries exhibit better advantages than other types of energy storage units, such as supercapacitor that has a linear discharge behavior, and compressed air that has inverse power output to that of electrochemical batteries with higher power at the beginning. However, rechargeable batteries may experience damaging stress overload occurring during extended discharge, affecting/directly lowering the battery longevity. Whereas overcharge of the battery results in saturated voltage; consequently, in such conditions, most energy input goes lost in the form of heat or physical effect on the battery.

It is also important to state that a discharge-charge cycle is not meant to fully discharge the battery being used. The 80% depth-of-discharge (DoD) method is frequently used by manufacturers to grade batteries because batteries are rarely entirely depleted. Thus, only 80% of the energy that is available is used, leaving the remaining 20% in reserve (Tremblay & Dessaint, 2009).

Batteries specifications are usually rated using the voltage and charge Q also taken as C-rates. Thus, a fully charged battery with a charge of 5 Ah as its specified charge Q will, at 0.5 ^{o}C, have a charge of 2.5 A operating for 2 hours. While at 0.2 ^{o}C it will exhibit 1A for 5 hours.

The benchmark result below presents the discharge behaviour of the four types of batteries modeled in the previous section and analyses their performances. To perform the analysis, a cell of Li-ion, NiCd, and NiMH has been connected to loads withdrawing an amount of about 1.5A.

- **Battery cell voltage (V)**

The plot in Figure 4.27 obtained from simulation in Matlab/Simulink shows the behavior of the four different types of batteries. The results show that the Li-ion battery (red line) discharges first (at approximately 1 hr 40 min of usage) and followed by the NiCd battery (at approximately 2 hrs 25 min of usage), then the lead-acid battery (at approximately 4 hrs of usage) and lastly NiMH (at about 4 hrs 20 min of usage) which shows the best performance in the time taken to reach full discharge.

The plot in Figure 4.28 supports the fact that when a battery is connected to a load, the current will be drawn from the battery and hence the need for charging. The above plot shows that the Li-ion and NiCd batteries have a sharp drop in current, and they do not deliver the required amount of current for a long period, while NiMH battery shows satisfactory results by delivering a constant current to the load for a longer period.

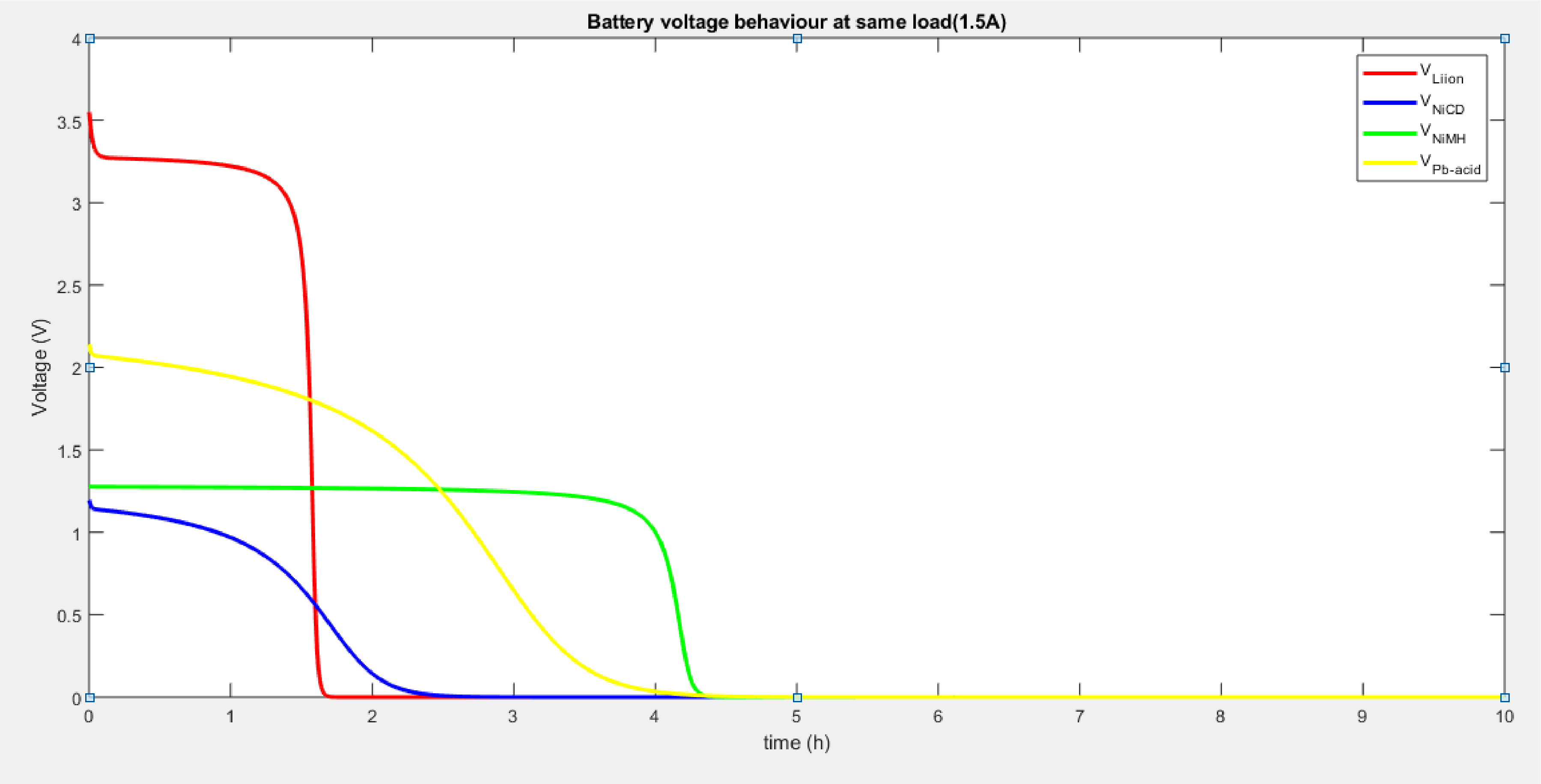

Figure 4. 27: Batteries discharge voltage comparison at 1.5A

- **Battery cell charge (Ah)**

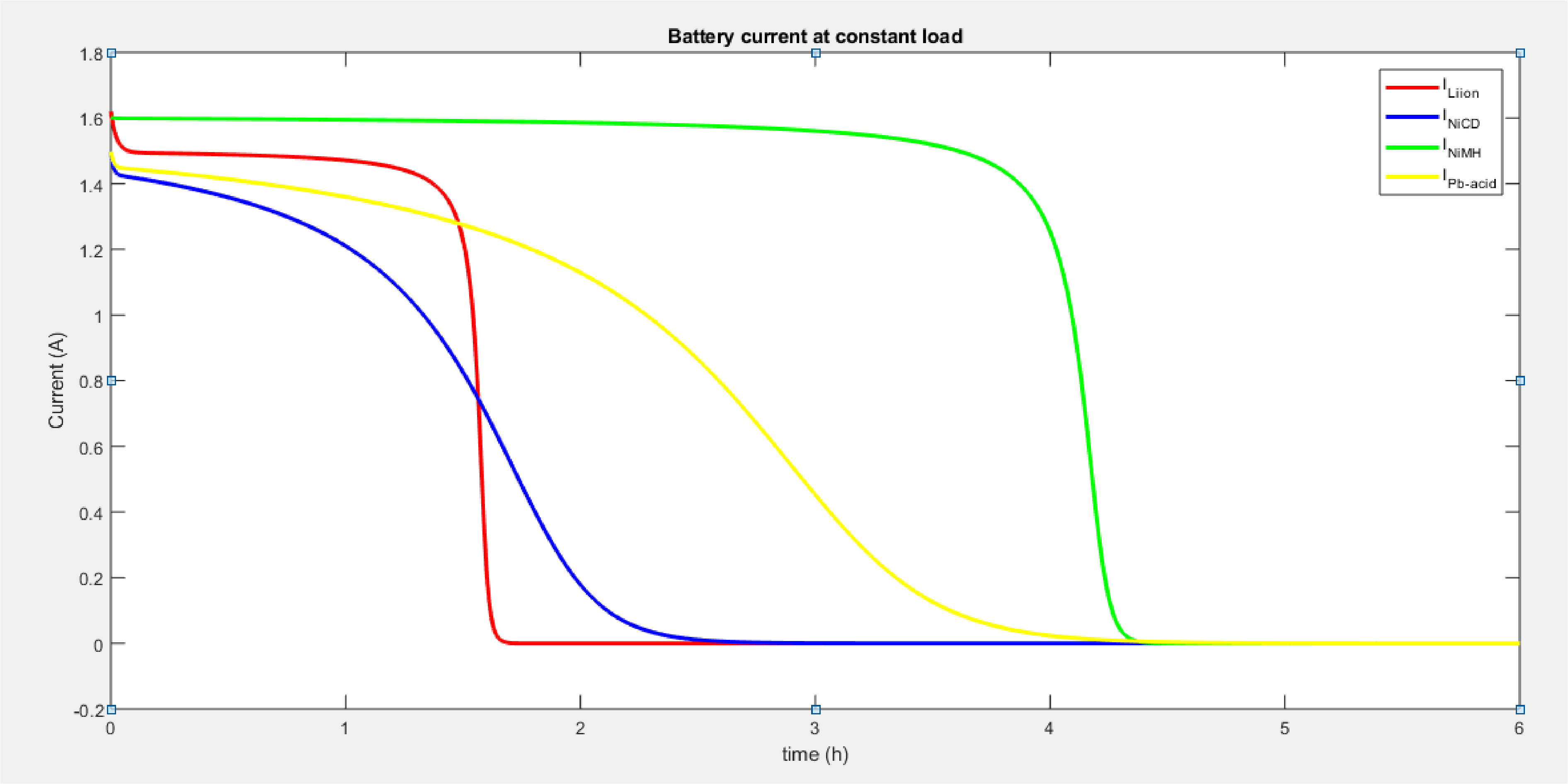

Figure 4. 28: Batteries discharge capacity comparison at 1.5A

- **Battery cell power (W)**

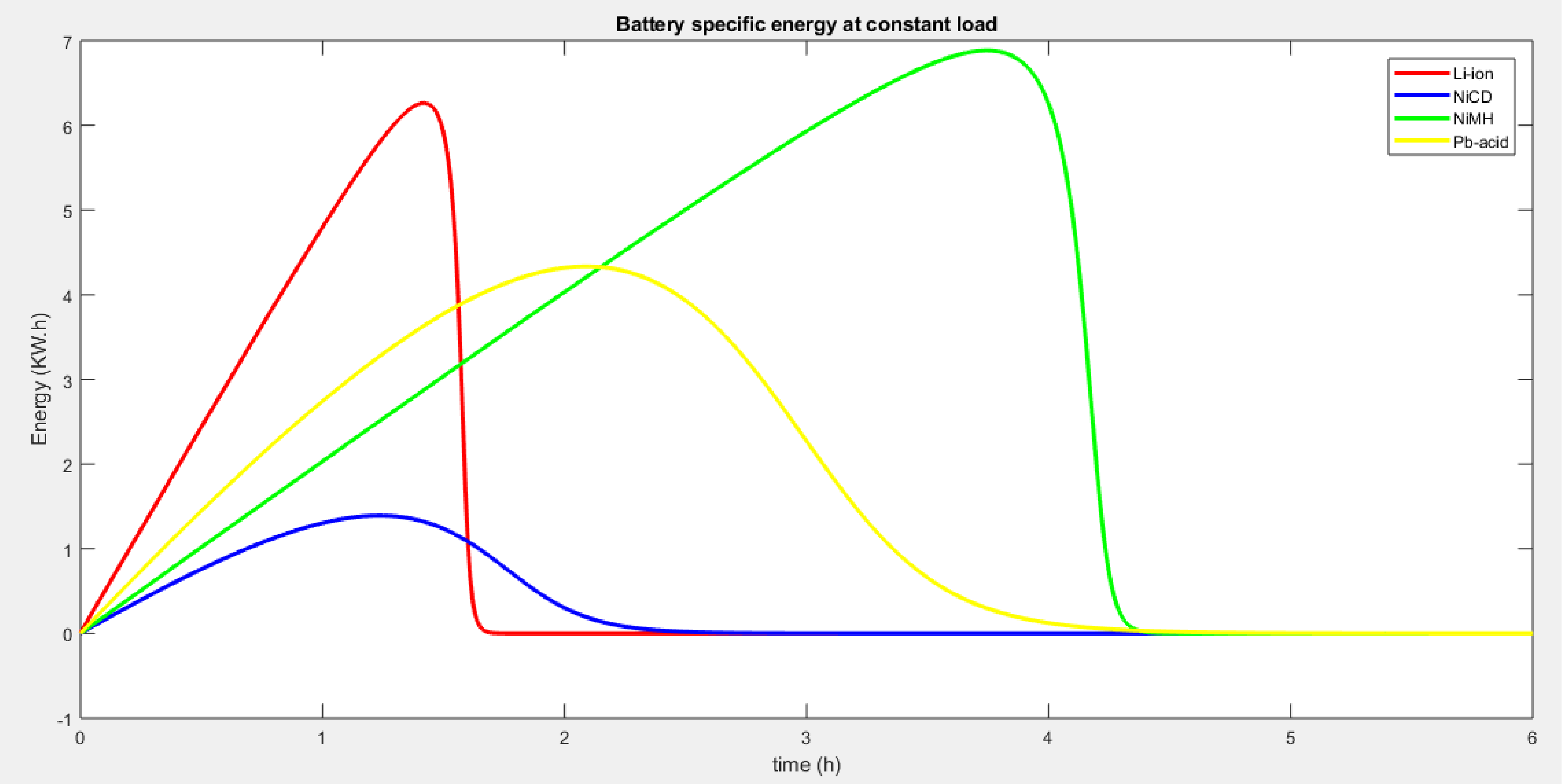

Figure 4. 29: Batteries discharge power comparison of the same load

The power plot in Figure 4.29 expresses a very important property of batteries, which is the power delivered. We can see that Li-ion and NiMH batteries deliver nearly 6W, which is about twice the value of the power delivered by lead-acid and NiCd batteries.

Table 4. 3: Rechargeable battery specification (Battery University, 2021b)

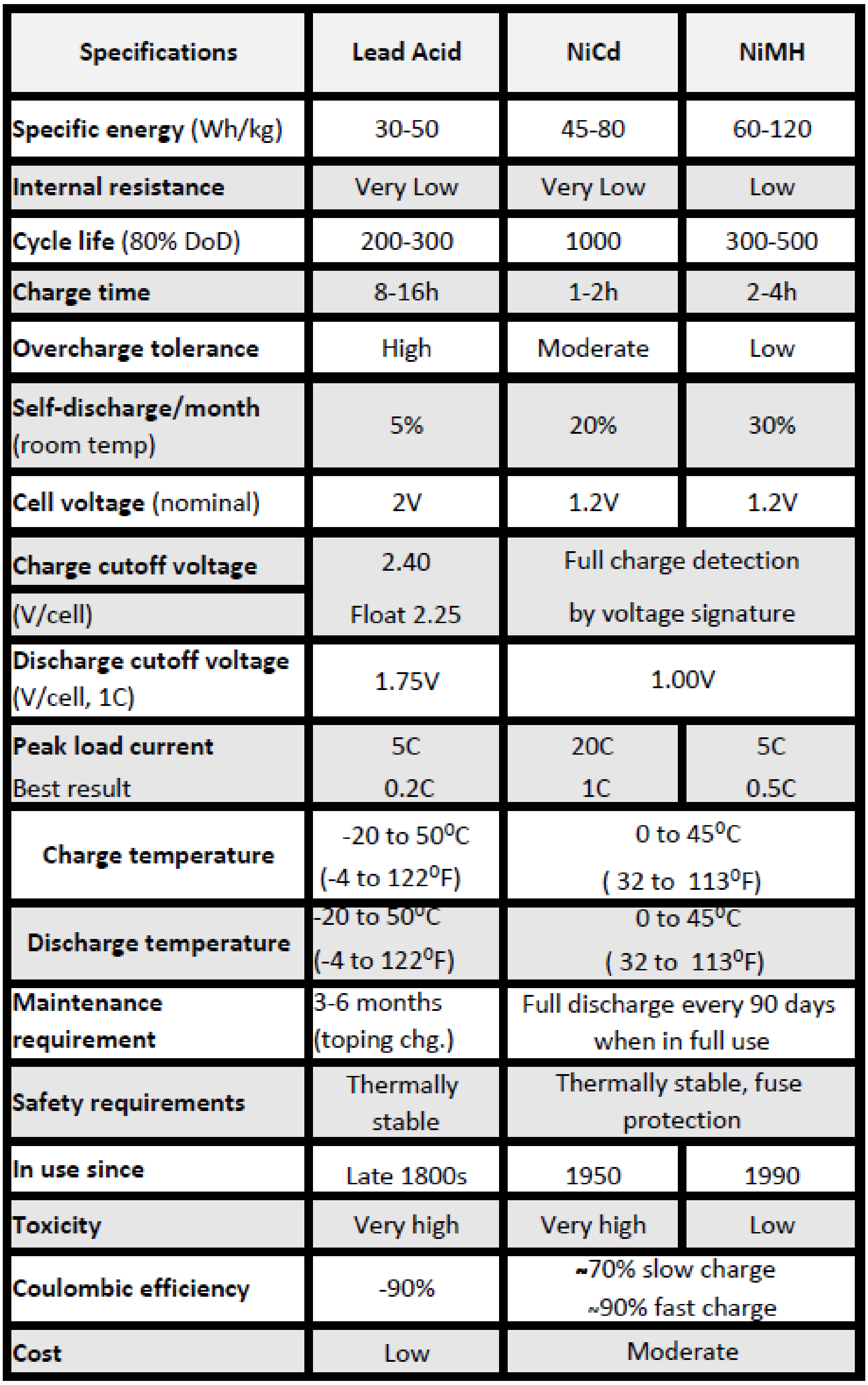

Specifications	**Lead Acid**	**NiCd**	**NiMH**
Specific energy (Wh/kg)	30-50	45-80	60-120
Internal resistance	Very Low	Very Low	Low
Cycle life (80% DoD)	200-300	1000	300-500
Charge time	8-16h	1-2h	2-4h
Overcharge tolerance	High	Moderate	Low
Self-discharge/month (room temp)	5%	20%	30%
Cell voltage (nominal)	2V	1.2V	1.2V
Charge cutoff voltage (V/cell)	2.40 Float 2.25	Full charge detection by voltage signature	
Discharge cutoff voltage (V/cell, 1C)	1.75V	1.00V	
Peak load current Best result	5C 0.2C	20C 1C	5C 0.5C
Charge temperature	-20 to 50^{0}C (-4 to 122^{0}F)	0 to 45^{0}C (32 to 113^{0}F)	
Discharge temperature	-20 to 50^{0}C (-4 to 122^{0}F)	0 to 45^{0}C (32 to 113^{0}F)	
Maintenance requirement	3-6 months (toping chg.)	Full discharge every 90 days when in full use	
Safety requirements	Thermally stable	Thermally stable, fuse protection	
In use since	Late 1800s	1950	1990
Toxicity	Very high	Very high	Low
Coulombic efficiency	-90%	~70% slow charge ~90% fast charge	
Cost	Low	Moderate	

Following the above plots, it could be concluded that when one cell of each type of the batteries is being discharged at the same C-rate, the NiMH battery takes a longer time and delivers more power density, followed by Li-ion, then lead-acid, and lastly NiCd. Therefore, among the four types of batteries studied and in terms of performance, the NiMH battery is the most suitable. This conclusion could be supported by Table 4.3, where it could be seen that the NiMH and Li-ion have about the same specific energy, close to 100 Wh/kg.

4.3 Modeling of nuclear battery

The modeling of RTG modules have been developed to simulate their behavior and study their performances in order to improve design and optimization. The proposed Simulink model of the radioisotope thermoelectric energy source (RTG) is based on the work of Tsai & Lin (2010) and is subject to the following assumptions (Tsai & Lin, 2010):

- Steady-state radioisotope thermoelectric module (the temperature distribution of the air gap is the same as the thermoelectric elements; hence heat transfer of the thermoelectric device can be treated as approximately one-dimensional heat transfer)
- Identical configurations of the p-type and n-type thermoelectric element (equal lengths, widths, thicknesses)
- Materials with a similar thermal coefficient of expansion must be chosen for the thermoelectric elements because different materials will bring about thermal expansion mismatch of the materials, which will lead to severe stress, leading to the degradation and breaking of the contacts between the thermoelectric elements (p-type and n-type semiconductors) and the ceramic substrate. In situations in which utilization of similar materials is not possible, the thermoelectric module must be designed to minimize thermal stresses
- thermoelectric elements are connected electrically in series and thermally in parallel
- the material properties (Seebeck coefficient, thermal conductivity, and electrical conductivity) of the thermoelectric elements are temperature dependent
- Uniform heat from the heat source
- Radioisotope thermoelectric module is thermal insulation packaged; hence the heat leakage through the lateral surface is negligible

4.3.1 Governing equations

RTGs modeling heavily relies on four types of energy processes occurring, Thermal conduction, Joule heating, Peltier effect, and Seebeck effect. The additional Thompson effect, which is described by the Thompson coefficient

$$r = dS/dT \tag{4.11}$$

is comparatively very small and therefore negligible.

Thermal conduction (or Fourier process) related to thermal conductivity ***K_i*** is expressed by:

$$Q_{th} = -dT.K_{th} \tag{4.12}$$

And the Joule heating effect causing heat dissipation in a resistive element, expressed by:

$$Q_J = I^2 \times R \tag{4.13}$$

Finally, the Peltier effect occurring during current flow through the junction of two dissimilar materials is given by:

$$Q_P = S.I.T_A \tag{4.14}$$

The load delivered by the Thermocouple can be expressed by:

$$Q_h = SIT_H - 0.5RI^2 - K_{th}.dT \tag{4.15}$$

and the Figure of Merit is given by:

$$Z = \frac{S^2}{R.K_{th}} \tag{4.16}$$

The formulas used for modeling are summarised in Table 4.4. It is worth mentioning that RTGs manufacturers will often provide the (hot temperature) T_H, (cold temperature) T_C, (matched power) Wm, (matched voltage) Wm, and (maximum efficiency) η_{max}.

Table 4. 4: RTG modeling parameters (Tsai & Lin, 2010)

Seebeck Coefficient, S (V/K)	$S = V_{max}/T_H$ $S = 2V_m/\Delta T$
Figure of Merit, Z (K^{-1})	$Z = S^2/R_{K_{th}}$ $Z = (m_{opt}^2 - 1)/T_{ave}$
Figure of merit, Z (matched load efficiency)	$Z = 4\eta_{TEG}^{m}/[\Delta T - \eta_{TEG}^{m}(1.5T_H + 0.5T_C]$
Thermal Conductivity, K_{th} (W/K)	$K_{th} = S^2/RZ$
Resistance, R (Ω)	$R = V_{max}(1 - \Delta T_{max}/T_H)/I_{max}$ $R_{th} = V_{max}I_{max}(T_H - \Delta T_{max})/(2T_H\Delta T_{max})$ $R = R_L = V_m^2/W_m$
Current I (A)	$I = S\Delta T/[(1+m)R]$ m (resistance ratio between the load and internal resistance)
Matched load current I_m	$I_m = S\Delta T/2R$
Thermal efficiency η_{th}	$\eta_{th} = I^2R_L/Q_H$ $\eta_{th} = mZ\Delta T/\{(1+m)^2 + Z[(m+0.5)T_H + 0.5T_C\}$
Max Thermal Efficiency	$\eta_{th}^{max} = (m_{opt} - 1)(\Delta T/T_H)/(m_{opt} + T_C/T_H)$
Matched load efficiency	$\eta_{th.m} = Z\Delta T/[4 + Z(1.5T_H + 0.5T_C)$
m	$m_{opt} = (1 + ZT_{ave})^{0.5}$ $m_{opt} = (\Delta T + \eta_{th}^{max}T_C)/(\Delta T - \eta_{th}^{max}T_H$ $T_{ave} = 0.5(T_H + T_C)$
Short-Circuit current	$I_{SC} = 2I_m = 2\,W_m/V_m$
Output Voltage	$V = -R(I - I_{SC})$

4.3.2 Modeling system and parameters

Through the configuration dialog of RTGs contained in Table 4.5, one can calculate the model parameters: S, R, K_{th}, and Z. The output characteristics of I–V and I–W for the TEM can then be plotted. The TEM has maximum power output with the matched load of R_L = R.

The Simulink model created in Figure 4.30 represents the formula arrangement describing the operation of the RTE module. Using this Simulink model and the manufacturers data for HZ-20 module which has the following parameters: T_H = 230C, T_C = 30C, W_m = 19 W, V_m = 2.38 W, and η_{max} = 4.5%.

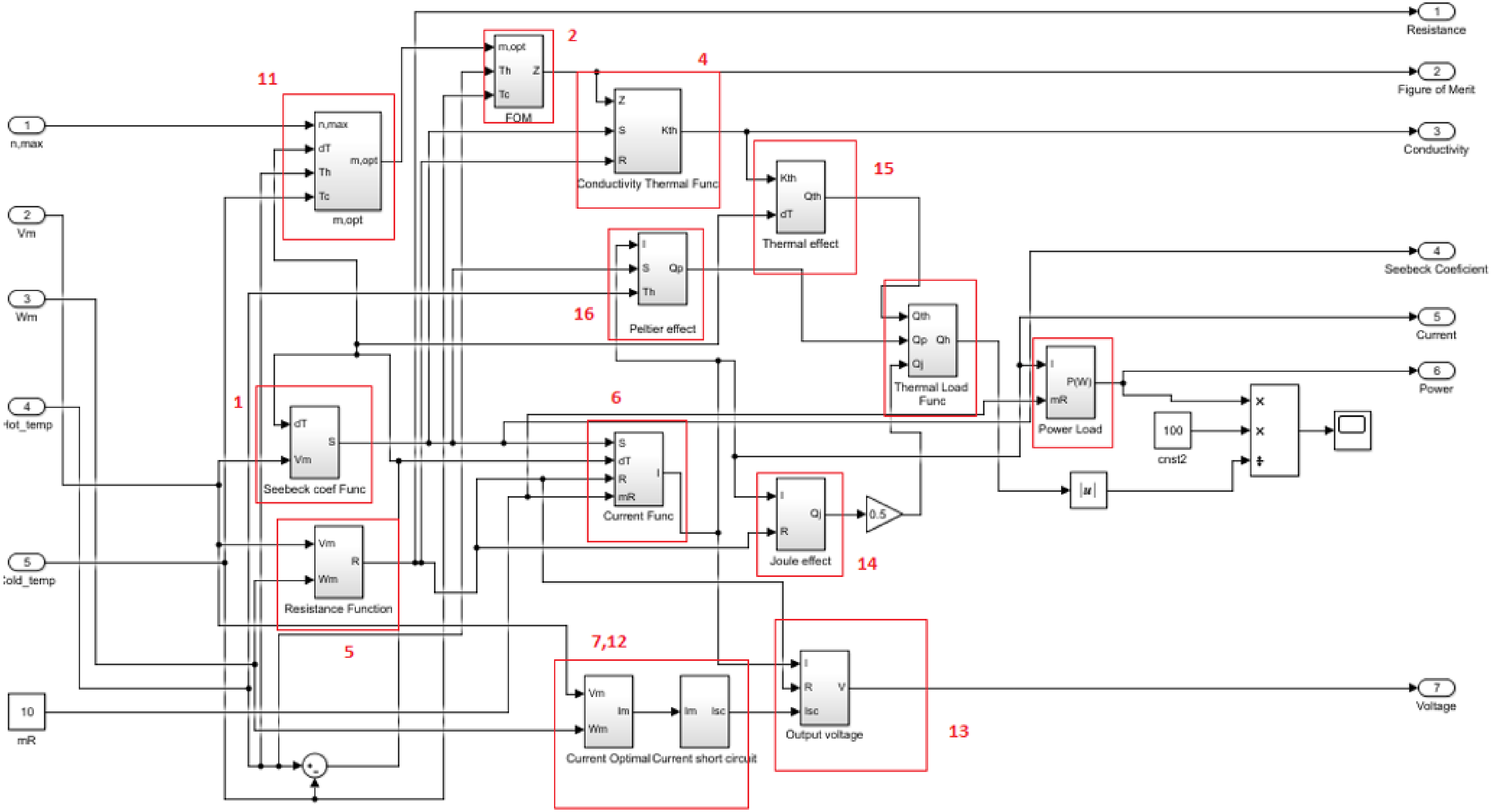

Figure 4. 30: RTG Simulink model

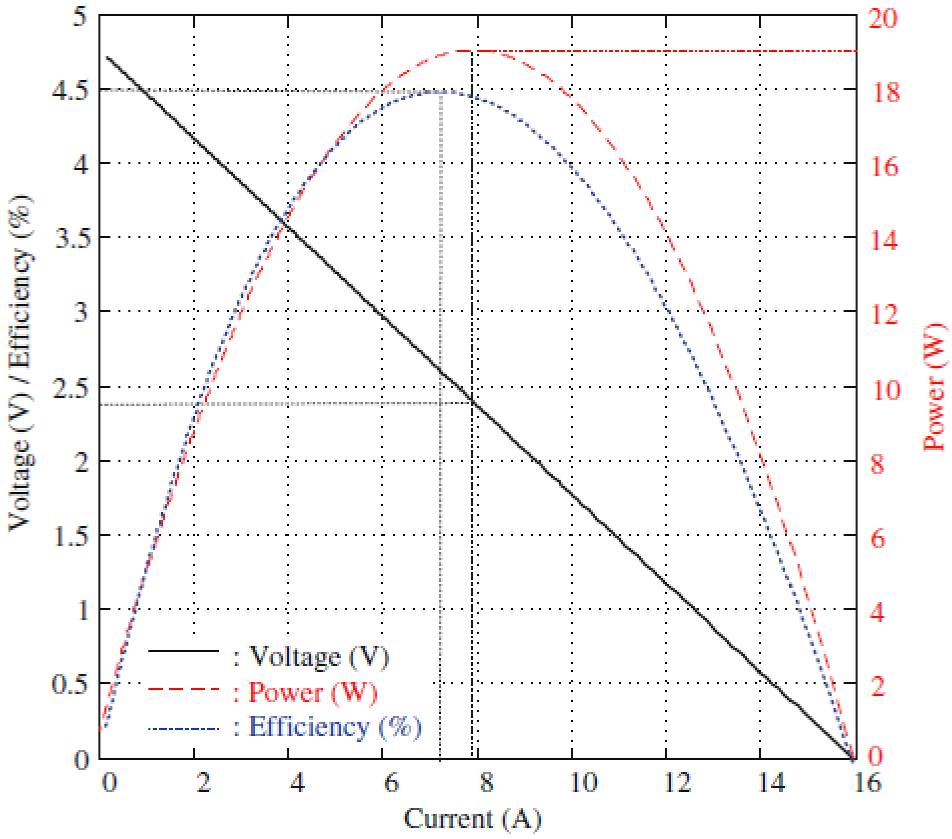

Figure 4. 31: I-V and I-W output characteristics (Tsai & Lin, 2010)

4.3.3 Simulink model of nuclear batteries

Considering a typical RTG, Multi-Mission Radioisotope Thermoelectric Generator (MMRTG) used in the 2011 Mars Science Laboratory mission as a power source with characteristics given in Table 4.5.

Table 4. 5: MMRTG manufacturer characteristics (Holgate et al., 2015)

Design parameters	MMRTG	Enhanced MMRTG
No. of GPHS bricks	8	8
TE materials	PbTe(TAGS 85, PbSnTe)	n-SKD/p-SKD
No. of couples	768	768
Design-point Q_{HS}	1984 W_{Th} @ BOL	TBD
TE hot-side temp	525^{o}C	600^{o}C
TE cold-side temp	100-200^{o}C	100-200^{o}C
BOL power (W_{E})	~120	~145-170
Est. EOL (14 years) power	60	~90-105
BOL system efficiency	6.0%	7.6-8.3%
Specific power (W_{E} kg^{-1})	2.8	~3.6-4.2
Containment system	Argon overpressure	Argon overpressure
Mission usage	Multi-mission	Multi-mission
Addressed program	MSL and Mars 2020	Europe

- Efficiency (Thermal to Electrical conversion): 6.3%
- Thermal Power: 2000W
- Electrical power:110W
- Specific power: 2.8 We/Kg
- Output voltage: 28-32 V dc
- Hot-side temperature: 525ºC (798.15K)
- Cold-side temperature: 100-200ºC

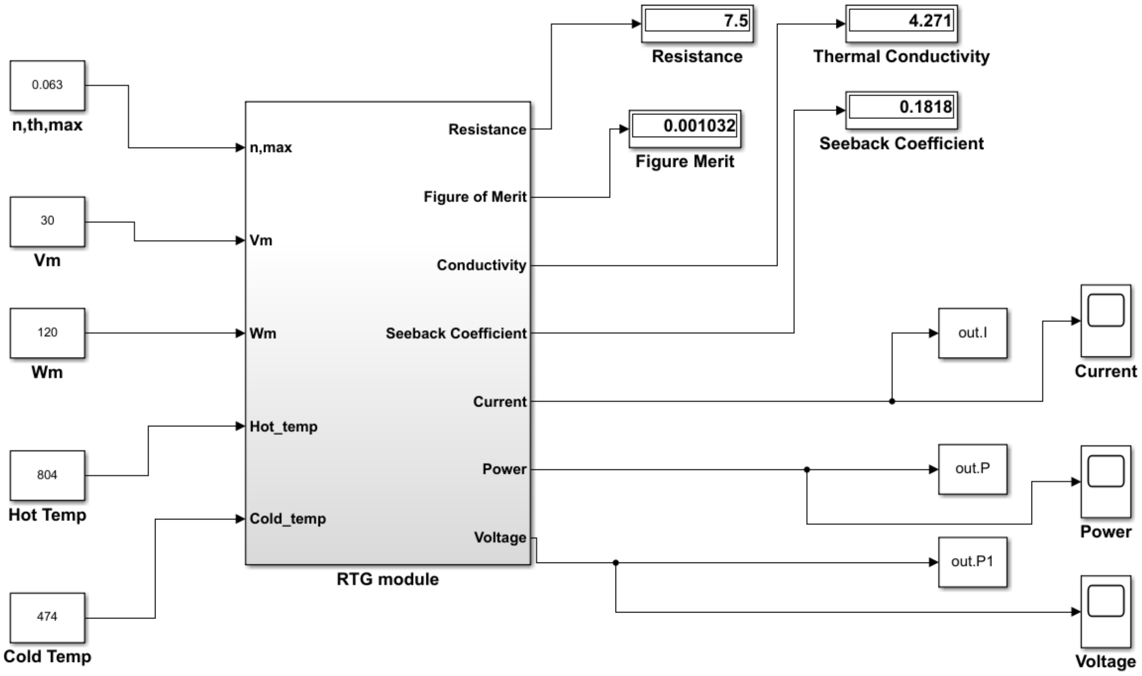

Figure 4. 32: MMRTG Simulink model

4.3.4 Simulation and discussion of results

Replacing these parameters in the Simulink model previously described and presented in Figure 4.32, the plot of the voltage versus current (Figure 4.33) and plot of power versus current (Figure 4.34) are obtained. The other variables obtained and necessary to the description of the MMRTG behavior are:

- Figure of merit, Z: 0.001032 Z^{-1}
- Seebeck coefficient, S: 0.1818 V/K
- Thermal Conductivity, K_{th}: 4.271 W/K
- Resistance, R: 7.5Ω

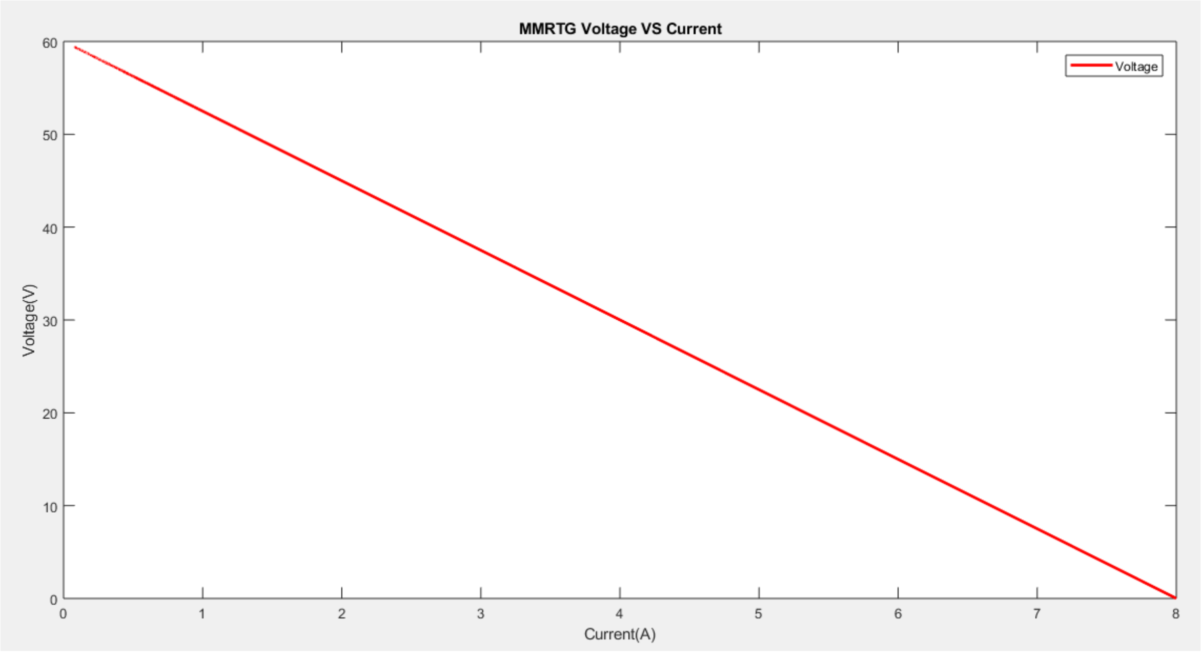

Figure 4. 33: MMRTG voltage vs. current

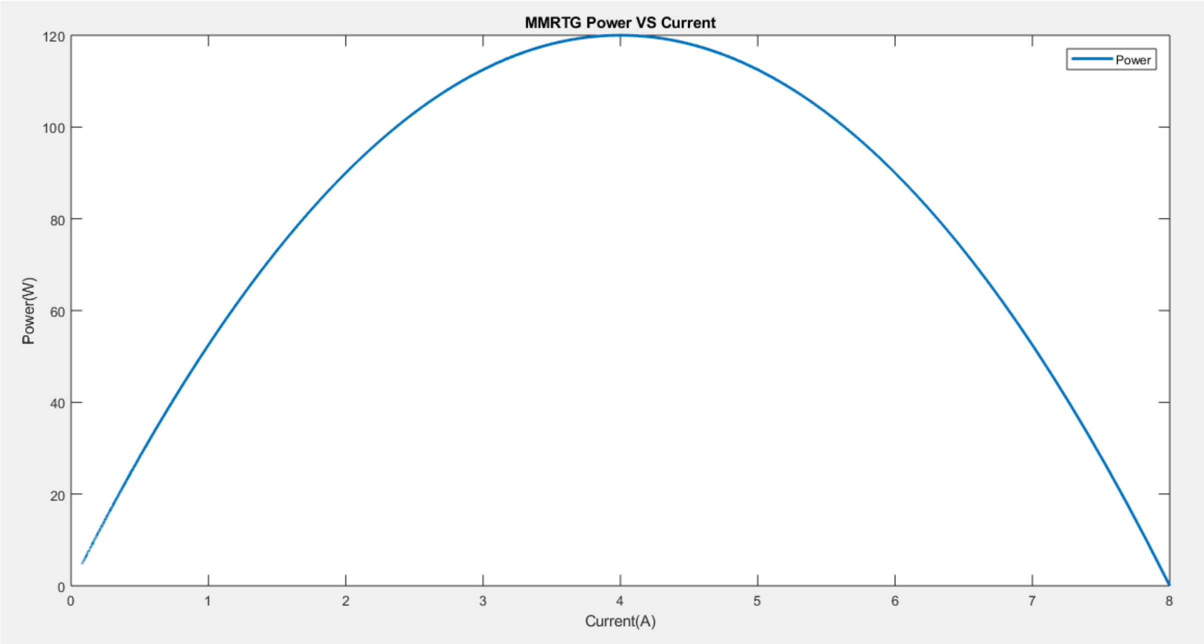

Figure 4. 34: MMRTG power vs. current

We can observe that the maximum efficiency of 6.3% can be obtained when the current I is at 4.2 A, thus the value of the load resistance is obtained by calculating the *m* ratio, which can be deduced in the two following methods:

- Using current I=4.2A:

$$I = \frac{S \times \Delta T}{(1+m)R}$$

$$m = \frac{S \times \Delta T}{I \times R} - 1$$

$$m = \frac{0.1818 \times (525 - 200)}{4 \times 7.5} - 1$$

$$m = 1$$

Consequently, the load resistance is: *mR=0.88×7.5=6.6* Ω or m=8 Ω (this value has to be put on the Simulink model.

- Using the standard formula: $m = \sqrt{(1 + ZT_{ave})}$

$$m = \sqrt{\left(1 + Z \times 0.5(T_H + T_C)\right)}$$

$$m = \sqrt{\left(1 + 0.001032 \times 0.5(804 + 474)\right)}$$

$$m = 1.3$$

Resulting in a load resistance of *mR=1.3×7.5≅10* Ω.

Figures 4.33 and 4.34 are comparatively similar to Figure 4.31, therefore, validating the model implemented.

CHAPTER FIVE
MODELLING AND SIMULATION OF HYBRID BATTERY SYSTEM

5.1 Introduction

Space exploration missions might require several years before accomplishing the objectives they are sent to do, but still shall be nevertheless continuously powered. This is to ensure the control of navigation and communication; therefore, it is necessary to have a long-life power source accompanied by an energy storage unit capable of storing the excess energy. Moreover, a single power source system usually has to feed or absorb power peaks to or from the load; this mixed operation can be disadvantageous, resulting in an overweight energy source with a shorter life span. Furthermore, some situations might require additional power. Meanwhile, a single source system only provides average power, ensuring the basic function of the spacecraft. The use of batteries in spacecraft has been mainly for load leveling and supply considerable power for some period of time. Such situations can be solved by adding a rechargeable battery supplying power during periods of high demands (Fakham et al., 2011; Becherif, 2006). Thus, combining an electrochemical battery with a radioisotope thermoelectric energy source to create a hybrid power source would create an energy source that could be highly efficient and reliable.

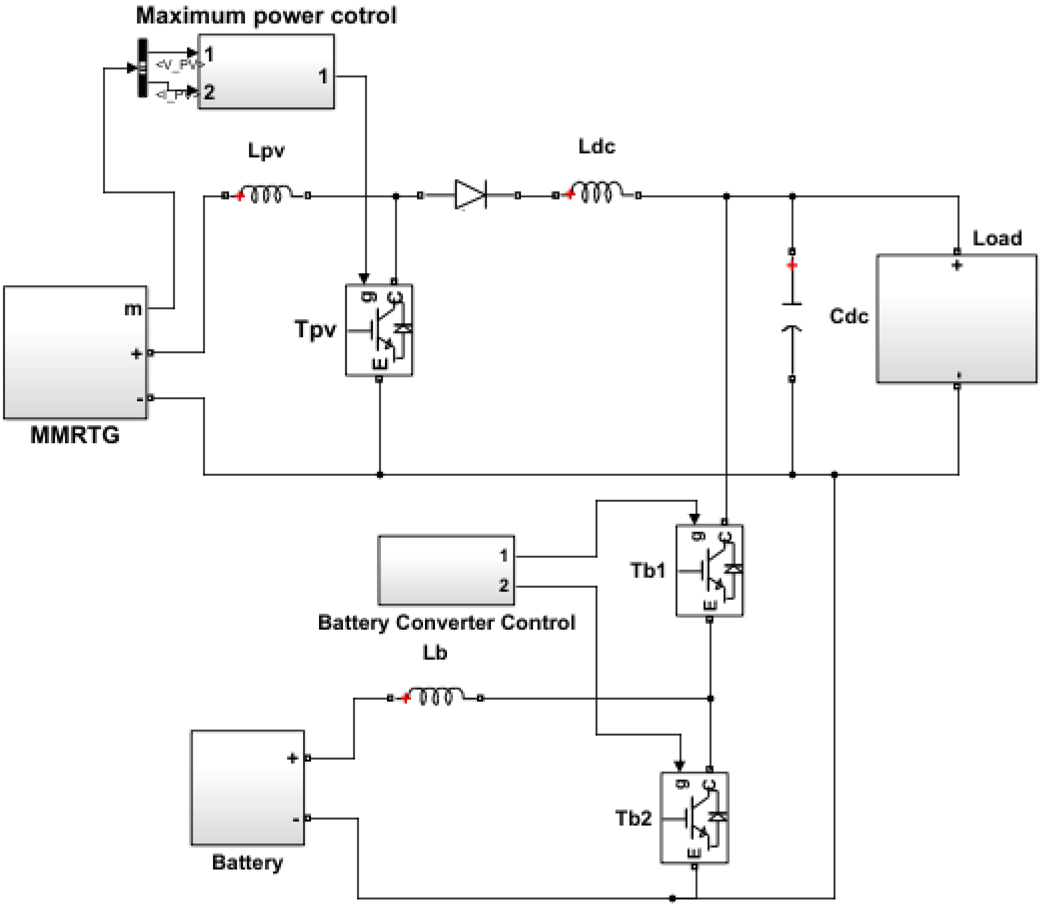

Figure 5. 1: Hybrid energy source system configuration

A typical hybrid system shown in Figure 5.1 combines a radioisotope thermoelectric energy source (MMRTG in this instance), an electrochemical battery (Li-ion), and complementary components: a DC-DC boost converter, a half-bridge converter, and a load.

The choice of Li-ion battery over other electrochemical batteries previously studied (Li-ion, lead-acid, NiCd, and NiMH) is because of their relative advantages. Li-ion batteries provide important weight and volume benefits (three- to four-fold), good low-temperature performance, low self-discharge, high energy density, and high W/h efficiency compared with other electrochemical batteries (Ratnakumar et al., 2004; Marsh et al., 2001). The current Li-ion batteries used for most of the NASA-JPL missions were developed by a NASA consortium including Yardney Technical Products (YTP), Jet Propulsion Laboratory (JPL), USAF-WPAFB, and NASA-Glenn Research Centre (GRC).

Currently, there are two different kinds of Li-ion batteries in use: those built with small-capacity cylindrical Li-ion cells and those made with large-capacity prismatic or cylindrical Li-ion cells. On the Mars Exploratory Rovers (MER) missions, large-capacity prismatic Li-ion cell batteries were a key enabler. The MER missions have been supported by this battery for nearly 13 years on Mars, significantly longer than the intended design life of 90 days. On several planetary missions, including Juno (2005), Phoenix (2007), Grail (2011), and MSL, JPL has utilized such batteries (produced by Yardney) with large-capacity Li-ion cells (2011). Additionally, several Surface Mounted Device (SMD) applications, including Kepler (2009), Aquarius (2011), NuStar, and others, have used batteries (produced by ABSL/Enersys) with compact cylindrical Li-ion cells (Sony). On the Europa Clipper, comparable batteries with E-One Moli 18650 cells are expected.

The disadvantages of Li-ion batteries outweigh their benefits since they have low specific energies (100Wh per kg) and poor energy densities (< 200Wh per l). Other drawbacks of Li-ion batteries include their poor abuse tolerance (during accidental overcharge/over-discharge and short circuit as well as incompatibility with conventional planetary protection techniques), limited resilience to high-temperature exposure (>60°C), limited low-temperature operational capability (<−30°C), and limited resilience to low-temperature exposure.

After the development phase, NASA launched two Mars missions christened MER missions in January 2004, namely “spirit’ and “opportunity,” consisting of two rovers designed to operate for 90 Martian solar days and explore 600 m of Mars surface. “Spirit” rovers operated for nearly seven years until 2011; meanwhile, the “opportunity” rovers drove for over 4900 Martian solar days and explored nearly 45km of the mars surface. These missions, which set the stage for the Li-ion battery, can be explained by the battery long life characteristics and solar arrays on the system. Such performances are due to the ability of the Li-ion battery to provide sufficient energy at launch and during surface operations, resist and control altitude adjustment during the cruise and exhibit adequate life cycle characteristics (Smart et al., 2007; Smart et al., 2010)

To achieve such satisfactory healthy and operational characteristics, extensive tests were run on individual cells and the battery over a range of temperature of -20°C to +20°C; estimation of the life cycle of the battery when fully discharged under different temperatures; evaluation of the self-discharge and storage; even study of battery behavior at 55% SoC under mission conditions of operations. The 4.2V, 8Ah Li-ion cell from Yardney technology produced well over 10Ah and around 126 Wh/kg under the right conditions (see Figure 5.2).

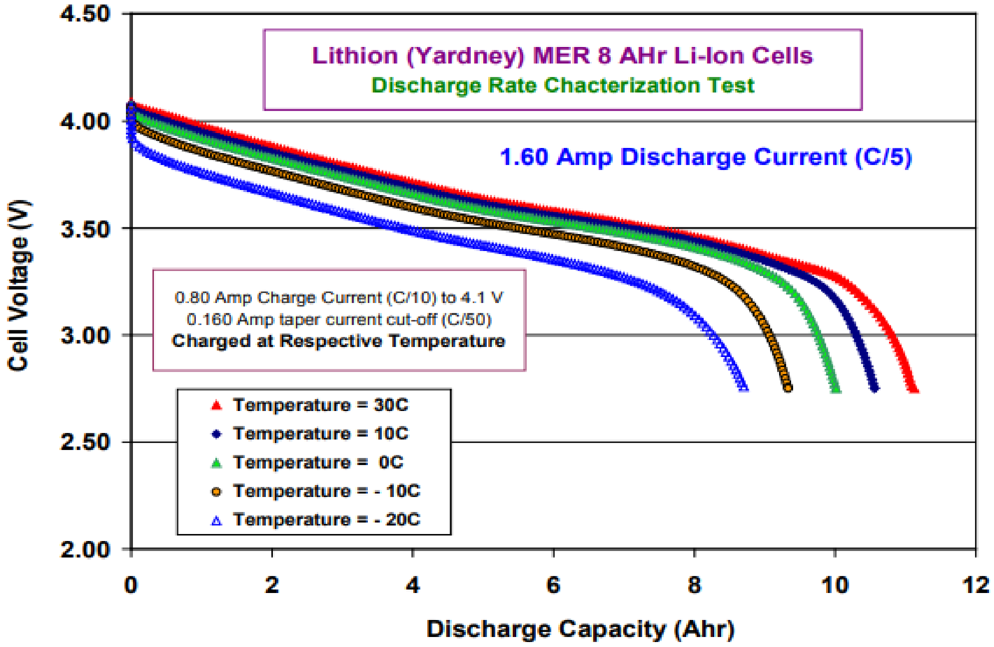

Figure 5. 2: 4.2V, 8Ah Li-Ion cell from Yardney technology (Smart et al., 2009)

The excellent performance of the MER mission in 2003 encouraged NASA to further the development of a new battery for their Mars Science Laboratory (MSL) mission in 2011. The “Curiosity” rover landed on Mars on August 06, 2012, with the objective to study the planet ability to support microbial life; because of the requirements of the mission necessity 687 Martian Solar days instead of 90 in the previous missions. The battery used for the mission was two 8-cell strings of 43Ah prismatic cell manufactured by EaglePicher-Yardney Division. Similarly, extensive ground testings were run on the battery cells under various ranges of conditions, including charge-discharge cycle rate testing, life cycle estimation under extensive full discharge and simulation of battery under Mars surface operation. By and large, the Li-ion batteries had exhibited excellent results in NASA missions The datasheet in Table 5.1 from Yardney manufacturer (Eaglepicher Technologies, 2019) gives us information regarding the battery specifications.

Table 5. 1: Yardney Space Li-ion battery Specification (Eaglepicher Technologies, 2019)

Specifications	
Part Number	LP 33450
Nominal Cell Weight	1.27 kg
Dimensions	See details om back
Voltage Range	3.0 to 4.1 V
Nominal Voltage	3.6 V
Nominal Capacity	4Ah at C/5 at 20^{o}C (68^{o}F)
Energy Density	378 Wh/L
Specific Energy	153 Wh/kg
Discharge Rates	Max constant current 200 A
	Max pulse current (<1 sec.) 400A
Nominal Cell Impedance	2 mΩ at 20^{o}C (68^{o}F)
Cycle Life (80% capacity measured at 0.5C discharge current at 20^{O}C (68^{O}F)	>2000 at 100% DOD
Standard Charging Method	Constant current 21.5A (0.5C) to 4.1V
	Constant voltage 4.1V to 0.86 (C/50)
Operating Temperature	-20 to 60^{o}C (-4 to 140^{o}F)
Storage Temperature	-40^{o}C to +60^{o}C (-40 to 140^{o}F)

A Simulink model of the 43 Ah cell battery is shown in Figure 5.3 to compare the experimental result from the manufacturer and the proposed model. The simulation is conducted assuming that the current drawn from the battery is constant and occurring under normal operating temperature. The internal resistance of the cell experiences an IR voltage drop when current flows through it. This IR voltage drop lowers the terminal voltage of the cell during discharge and raises the voltage required to charge the cell, lowering both the cell's effective capacity and charge/discharge efficiency. The lower voltage discharge curves at high C rates are explained by the higher internal voltage drops that are caused by higher discharge rates. Additionally, we can observe sudden changes in the discharge characteristics in Figure 5.3. these changes are dependent on both the C rates and the selected Simulink solver. At a high C rate (C and C/2), we can observe high sudden changes, whereas, at a low c rate (C/5), the change decreases significantly. On the other hand, the solver is selected as a compromise between the accuracy of the results and the speed of the simulation.

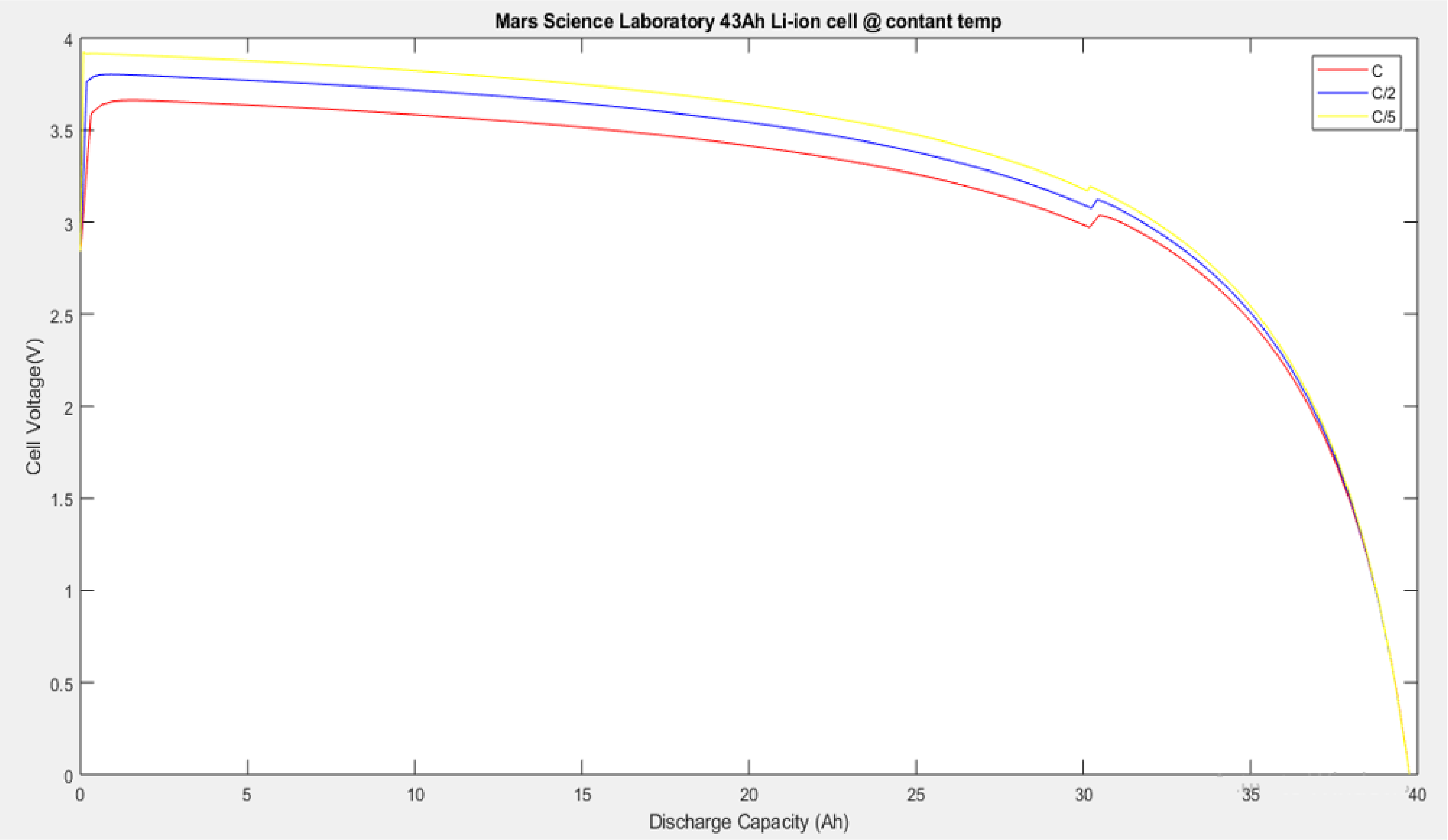

Figure 5. 3: Simulink discharge behavior of Yardney Li-ion battery

It could be seen that there is a considerable difference in the discharge of the battery behavior at the same discharge C-rate. The difference between the Simulink simulation and the real-life experiment could be ascribed to the effect of temperature on the battery.

Table 5. 2: Recent mission that used Li-ion battery as storage (Surampudi et al., 2017)

Mission	Launch date	Destination	Battery System
2001 Mars Odyssey	April 2001	Mars	Ni-H_2
COUNTOUR	July 2002	Comet	Ni-Cd
MER-Spirit	June 2003	Mars	Li-ion (NCO)
MER-Opportunity	July 2003	Mars	Li-ion (NCO)
Messenger	August 2004	Mercury	Ni-H_2
Deep Impact	January 2005	Comet	Ni-H_2
Mars Reconnaissance Orbiter	August 2005	Mars	Ni-H_2
New Horizons	January 2006	Pluto	No Battery
Phoenix	August 2007	Mars	Li-ion (NCO)
Dawn	September 2007	Vesta & Ceres	Ni-H_2
Kepler	March 2009	Earth Orbit	Li-ion (LCO)
Lunar Reconnaissance Orbiter	June 2009	Moon	Li-ion (LCO)
LCROSS	June 2009	Moon	Li-ion (LCO)
Juni	August 2011	Jupiter	Li-ion (NCO)
GRAIL	September 2001	Moon	Li-ion (NCO)
Mars Science Laboratory	November 2011	Mars	Li-ion (NCO)
LADEE	September 2013	Moon	Li-ion (LCO)
MAVEN	November 2013	Mars	Li-ion (NCO)
OSIRIS-REx	September 2016	Asteroid	Li-ion
InSight	May 2018	Mars	Li-ion (NCA)
Mars 2020	Summer 2020	Mars	Li-ion (NCA)
Deep Space Climate Observatory (DSCOVR)	February 2015	L-1	Li-ion (LCO)
Magnetospheric Multiscale Satellites (MMS)	March 2015	Various Orbits	Li-ion (LCO)
Transiting Exoplanet Survey Satellite (TESS)	December 2017	HEO Orbit	Li-ion (NCO)
James Webb Space Telescope (JWST)	2018	L-2	Li-ion (LCO)
JPSS2	2021	LEO	Li-ion (LCO)

Despite its benefits, Li-ion batteries have downsides, including low-specific energy. The 8s2p Li-ion batteries (2 parallel, 8 Li-ion cells), designed by Yardney Industries, were used by the MSL rover. They had an 80 Ah capacity and could provide up to 28 V. Large-capacity Li-ion batteries have been employed for planetary applications by leveraging the "legacy" MCMB-$LiNiCoO_2$ chemistry developed for the MER program and produced by YTP. This legacy cell chemistry has been used on missions such as Juno (2005), Phoenix (2007), Grail (2011), and MSL, as shown in Table 5.2. (2011).

Table 5. 3: Li-Ion battery used in MSL curiosity–yellow (Surampudi et al., 2017)

Technology	**NCO Li-ion**	**NCO Li-ion**	**NCO Li-ion**	**NCO Li-ion**	**NCO Li-ion**
Mission	MER-Rover	Juno	Phoenix	Grail	MSL Curiosity
Launch Date	6/10/2003	8/5/2005	9/4/2007	9/10/2011	11/26/2011
Battery Configuration	8s2p	8s2p	8s2p	8sp1	8s2p
Battery Vendor	Yardney	Yardney	Yardney	Yardney	Yardney
Cell Size or Model	NCP-8-1	NCP-55-2	NCP-25-1	NCP 25-1	NCP 43-1
Capacity (Ah) Voltage Range	16/20	110/120	50/62	50/62	86/92
Operating Voltage Range	24-32.8 V	24-32.8 V	24-32.8 V	24-32.8 V	24-32.8 V
Battery Mass (kg)	7.12	34.90	17.80	9.25	26.50
Specific Energy (Wh/kg)	90	110	105	100	104
Operating Temperature Range (ºC)	20º to 30º	15º to 25º	-20º to 30º	0º to 30º	-20º to 30º
Cycle Life to date	>4500	<50	<200	1500	>1500

Table 5.3 highlights the type of battery used for the MSL “Curiosity” mission. The 8s2p battery built for the need of the MSL mission can be considered the most recent advancement in the development of energy sources for space exploration. The modeling presented in Figure 5.4 studies the discharge voltage by the Li-ion battery. The study will be conducted in order to determine the value of charge and voltage at 100% SoC. Thus, we attached any load values (block 2) to the Li-ion battery flight battery (block 1).

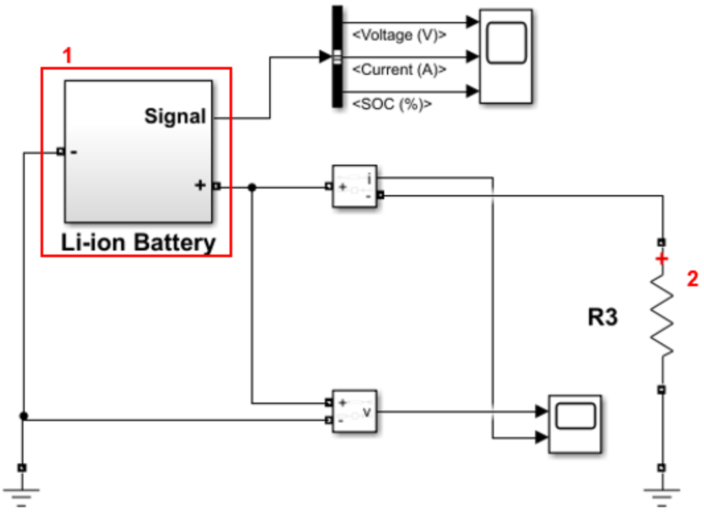

Figure 5. 4: Simulink model of Yardney battery for discharge testing

The Simulink model presented in Figure 5.5 is similar to the charge-discharge system developed in the previous discussion of Li-ion batteries. It could be observed that there are two sets of 16 voltages sources, one exhibiting the charge and the other showing the discharge. However, the particularity of the system comes from the fact that there are two sets of 8 cells in parallel. One set is linked to the discharge function (block 1), while the other is joined to the charge model. It should be noted that each battery cell (controlled voltage block) is connected to the same charge/discharge output.

Figure 5.6 illustrates the behaviour of the Li-ion battery discharge used for developing the hybrid system.

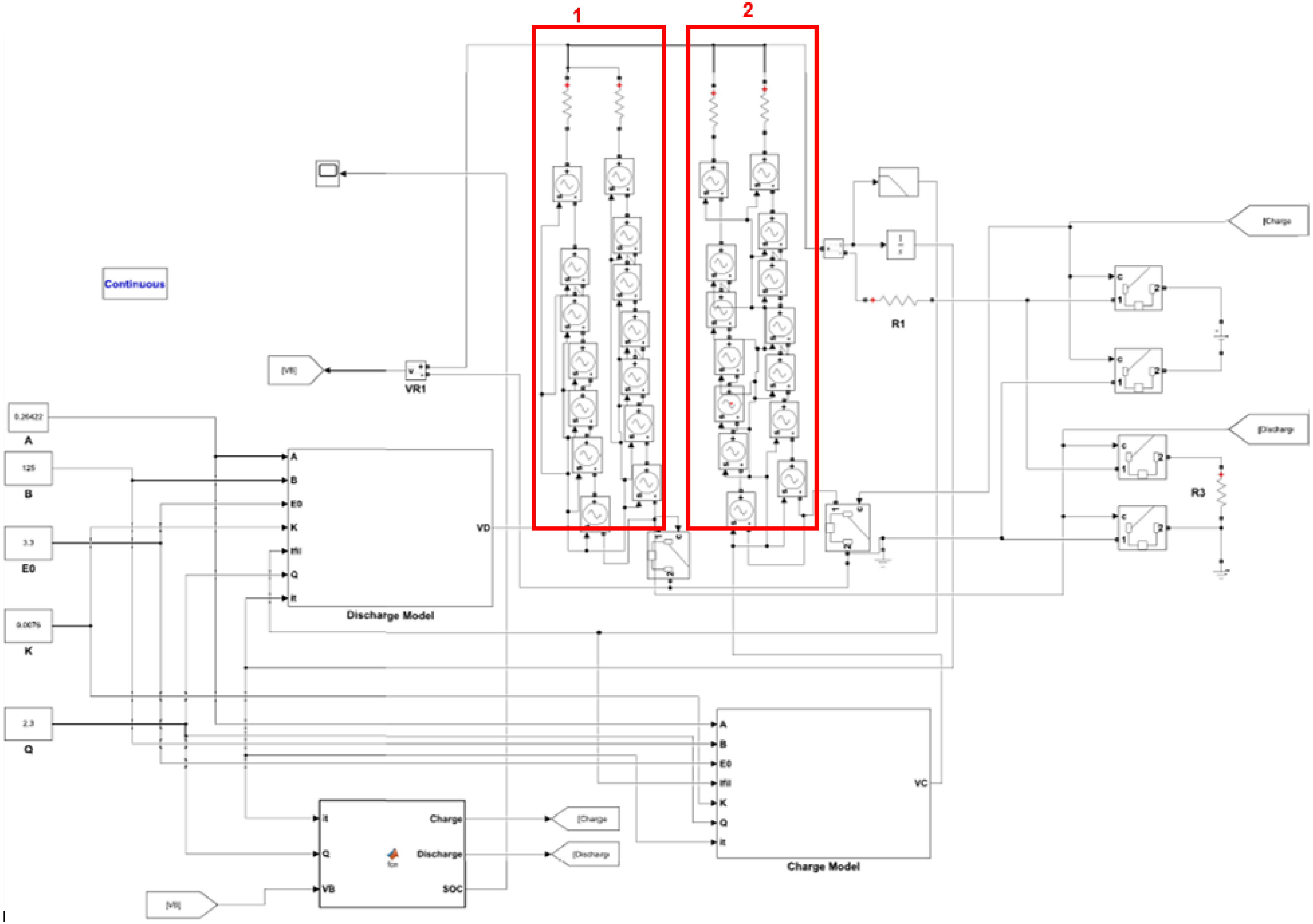

Figure 5. 5: Simulink model of the 8s2p battery used in the 2011 MSL mission

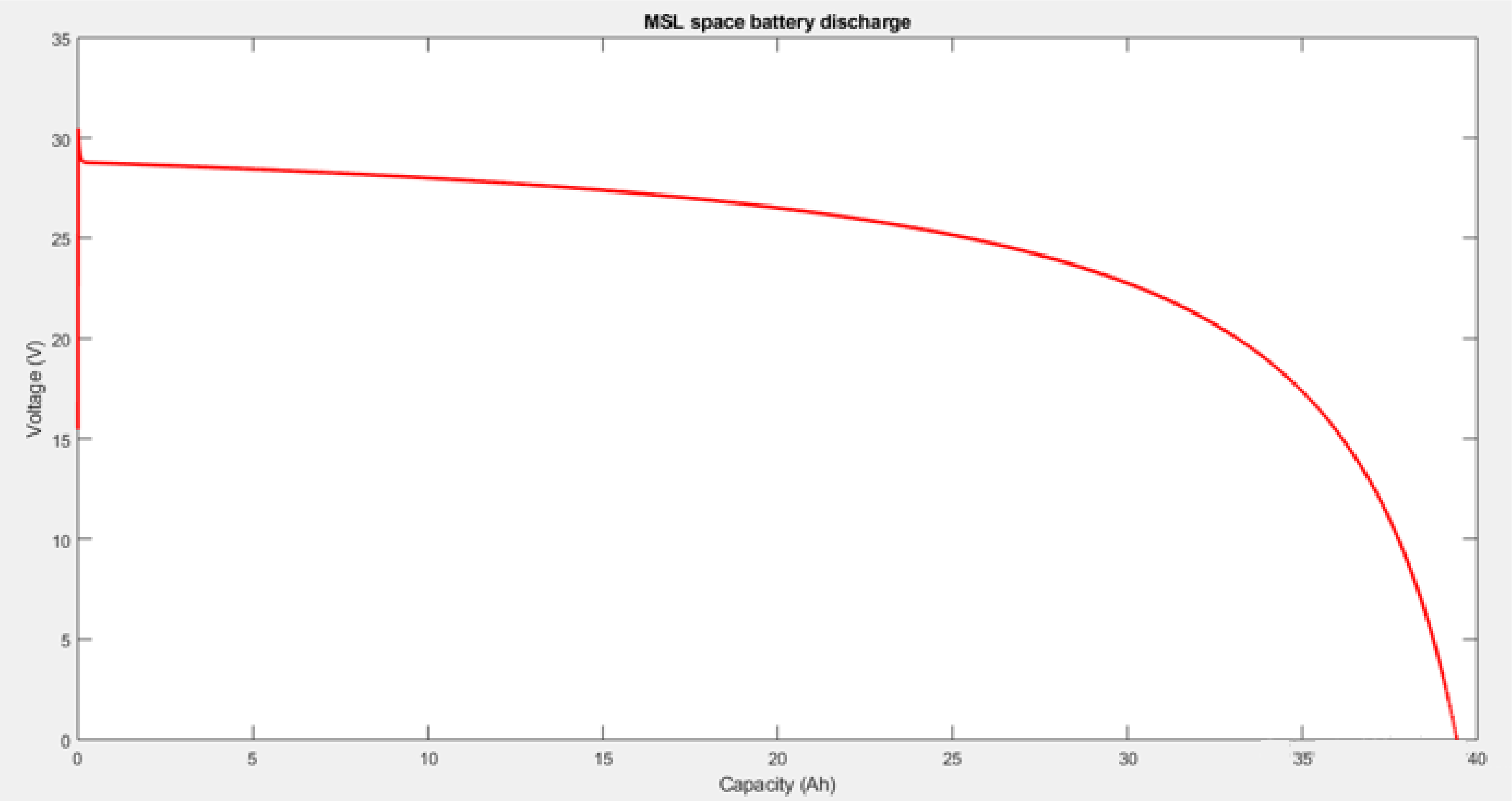

Figure 5. 6: Yardney Li-ion battery discharge behavior in 8s2p arrangement

5.2 Auxiliary components

In addition to the electrochemical battery and radioactive energy source, the hybrid energy source also includes the boost converter, half-bridge converter, and electric motor.

5.2.1 Boost converter unit

The boost converter for the hybrid system would enhance the voltage to be delivered by the RTE to the load.

The boost converter inductance and capacitance values are obtained based on Equations 5.1, 5.2 and 5.3:

- RTE voltage (determined previously): V_s=V_{RTE}= 34.25 V
- The approximate load voltage: V_{Load} = 60 V
- The frequency: *f=25000Hz*
- Voltage ripple is not superior to 1%
- The load resistance: 1Ω

Thus, the duty cycle,

$$\mathrm{D} = 1 - \frac{\mathrm{V_S}}{\mathrm{V_O}} = 1 - \frac{34.25}{60} = 0.43\text{; thus, D=43\%} \tag{5.1}$$

The minimum inductance value,

$$\mathrm{L_{min}} = \frac{\mathrm{D}(1-\mathrm{D}^2)\mathrm{R}}{2\times\mathrm{f}} = \frac{0.43(1-0.43^2)\times1}{2\times25000} = 7\times10^{-6}\ \mathrm{H} = 7\mu\mathrm{H} \tag{5.2}$$

The capacitance,

$$\mathrm{C} \geq \frac{\mathrm{D}}{\mathrm{R}\left(\frac{\Delta\mathrm{V_o}}{\mathrm{V_o}}\right)\times\mathrm{f}} = \frac{0.43}{1(0.01)\times25000} = 1.72\times10^{-3}\mathrm{F} => \mathrm{C} \geq 1.72\mathrm{mF} \tag{5.3}$$

5.2.2 Half-bridge converter unit

Half bridge bidirectional DC-DC converters are employed in systems where boost operation is required in one direction and buck in another, making it an ideal converter device to control the flow of power through the battery.

The half-bridge parameters during the boost mode operation are obtained as follows:

- $\mathrm{D} = 1 - \frac{\mathrm{V_S}}{\mathrm{V_O}} = 1 - \frac{30}{70} = 0.57$ (5.4)
- $\mathrm{L_{min}} = \frac{\mathrm{D}(1-\mathrm{D}^2)\mathrm{R}}{2\times\mathrm{f}} = \frac{0.63(1-0.63^2)\times1}{2\times25000} = 7.7\times10^{-6}\ \mathrm{H} = 7.7\mu\mathrm{H}$ (5.5)
- $\mathrm{C_1} \geq \frac{\mathrm{D}}{\mathrm{R}\left(\frac{\Delta\mathrm{V_o}}{\mathrm{V_o}}\right)\times\mathrm{f}} = \frac{0.5}{1(0.01)\times25000} = 2.3\times10^{-3}\mathrm{F} => \mathrm{C_1} \geq 2.3\mathrm{mF}$ (5.6)

The value of C_1 (parallel to the load) must be superior to 2 mF and the minimum value for the half-bridge to operate in boost mode is about 7.5 mH.

In buck mode, the voltage from the boost converter at the output of RTE is lowered in order to recharge the battery; we can thus assume that the input voltage V_s= 60V and the output voltage V_o =30V.

- RTE voltage (determined previously): V_s=60
- The Load voltage shall be around: V_o=$V_{battery}$= 30 V
- The frequency *f=25000Hz*
- Voltage ripple is not superior to 1%

The half-bridge converter parameters in the buck mode operation are as follows:

- $D = \frac{V_o}{V_S} = \frac{30}{60} = 0.5$ (5.7)
- $L_{min} = \frac{(1-D)R}{2\times f} = \frac{(1-0.5)\times 1}{2\times 25000} = 1 \times 10^{-5}\ H = 10\mu H$ (5.8)
- $C_2 = \frac{1-D}{8L\left(\frac{\Delta V_o}{V_o}\right)\times f^2} = \frac{1-0.5}{8\times 10^{-5}(0.01)\times 25000^2} = 1 \times 10^{-3} F => C_2 = 1mF$ (5.9)

The values calculated of inductance and capacitance in the two modes allow us to emit an approximation of their values so that the half-bridge works in both modes without any disturbance.

Estimation rated L_{min} = *10* μH in buck mode and L_{min} = *7.5* μH in boost mode. Thus, we could take the value of *L=15* μH.

The capacitor in the battery can be $C_2 = 2.3mF$, and the load capacitor can be taken $C_1 = 5mF$.

5.2.3 Electric motor

The DC motor parameters are given in Table 5.4

Table 5. 4: Motor parameters (Kushwah & Patra, 2014)

Description	Value
Armature Resistance R_a (Ω)	1
Armature Inductance L_a (H)	0.5
Moment of Inertia J (Kgm^{2}S^{-2})	0.01
Friction Coefficient B	0.1
Torque Constant K_t	0.01
EMF constant	0.01

5.3 Hybrid system command strategy

The Li-ion battery's function is to provide the extra power needed by the load during transient states and to recover the energy produced by losses; the RTG module's function is to supply power to the load (Meskani & Haddi, 2019; Miao et al., 2017). Power exchange in the storage element is managed using the following three procedures:

- Charging the battery: with the RTG powering the battery.
- Unload mode: when the battery and the RTG provide power to the load
- Recovery mode: when the load provides power to the battery

5.4 Simulink model

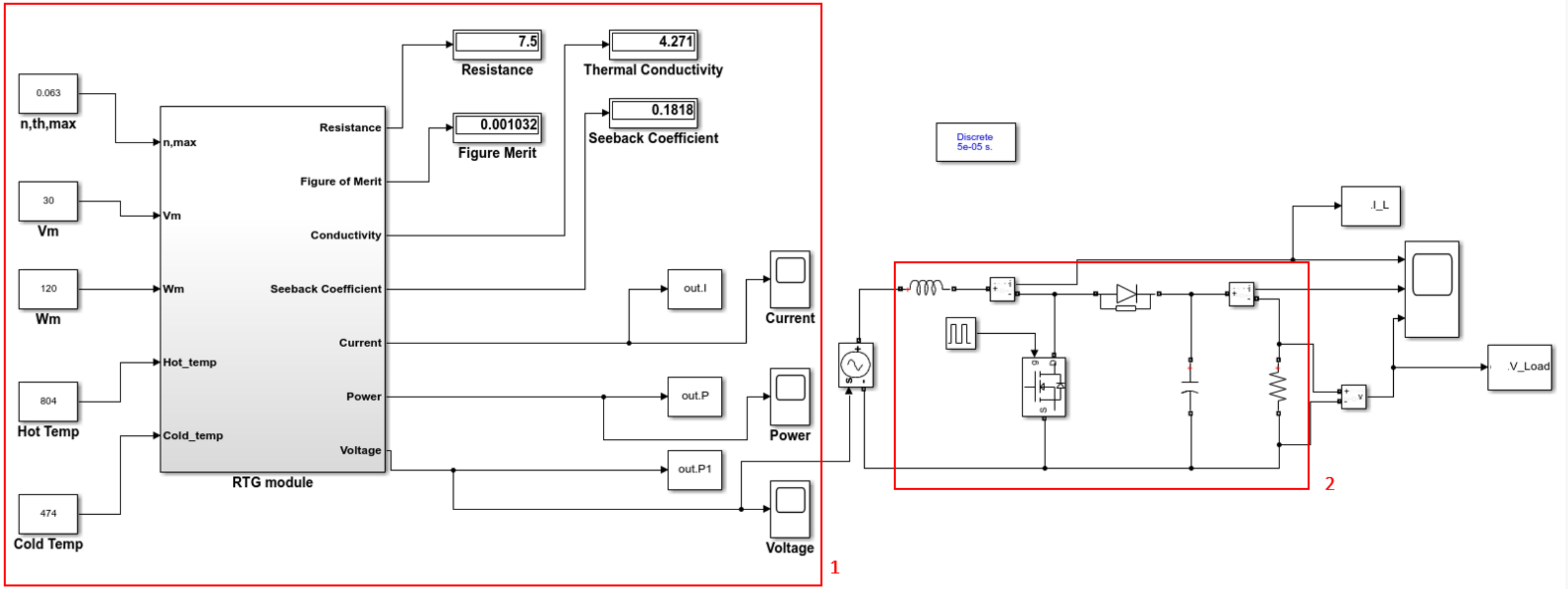

Figure 5. 7: MMRTG-Boost converter system

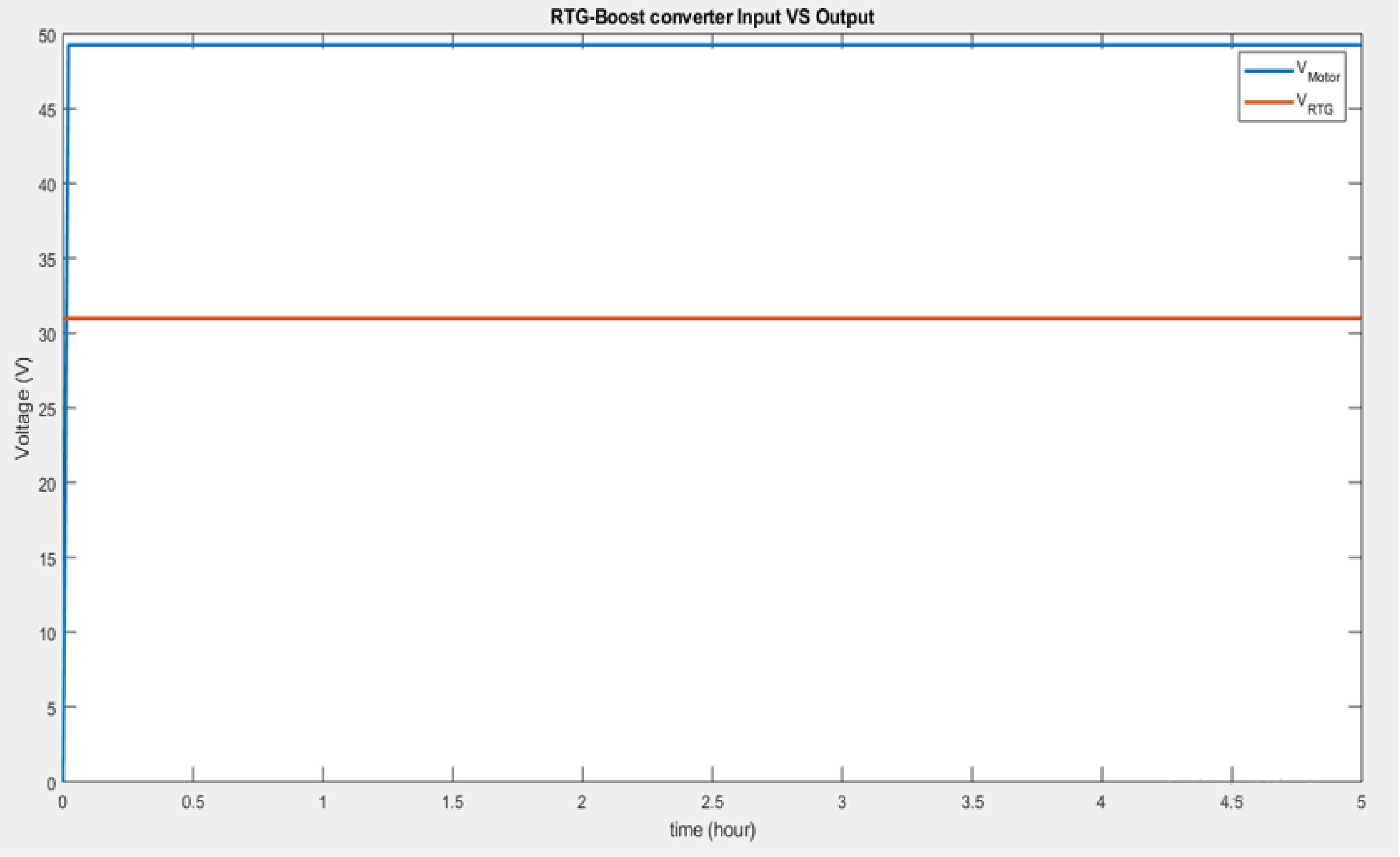

Figure 5. 8: RTG voltage and load voltage

Figure 5.7 displays the system Simulink model connecting the MMRTG to a boost converter, and the voltage at the load is presented in Figure 5.8. It could be observed that while the voltage of the MMRTG is slightly above 30 V, the output voltage as a result of the incorporation of the booster is approximately 48 V which is close to the expected value of 60 V.

The Simulink model of the system is shown in Figure 5.9 for the system to operate in boost mode. During this mode, the duty cycle is controlled by the MOSFET Q2 provided by the signal P while the signal S is connected to MOSFET Q1, turning it off. It is also important to note that the duty cycle set in the Duty Cycle generator must have a percent equal to or superior to 50%. We obtain the result in Figure 5.10 with a load resistance of 1 Ω, where it can be observed that during mode 1 (boost mode) the battery voltage is increased from 25 V to nearly 40 V. Note that there is some marginal error between the value calculated and the value displayed by the simulator; this could be explained by the non-ideal behavior of MOSFET and other voltage ripples in the circuit.

The Simulink design of the motor mixes both mechanical and electrical blocks. The electrical blocks, including the armature resistance, R, and the armature inductance, L, are shown in Figure 5.11 and Figure 5.12, respectively. Meanwhile, the mechanical parts concerned are the inertia, J of the shaft, and the damping resistance in the shaft. The motor under consideration would be based on the physical parameter in Table 5.4.

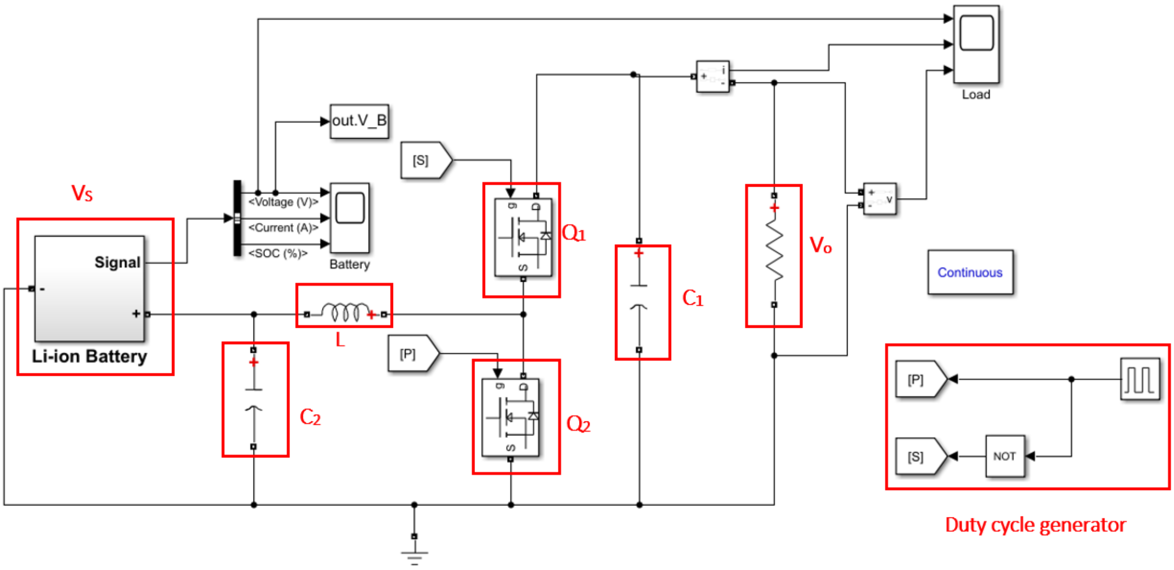

Figure 5. 9: Battery half-bridge converter system

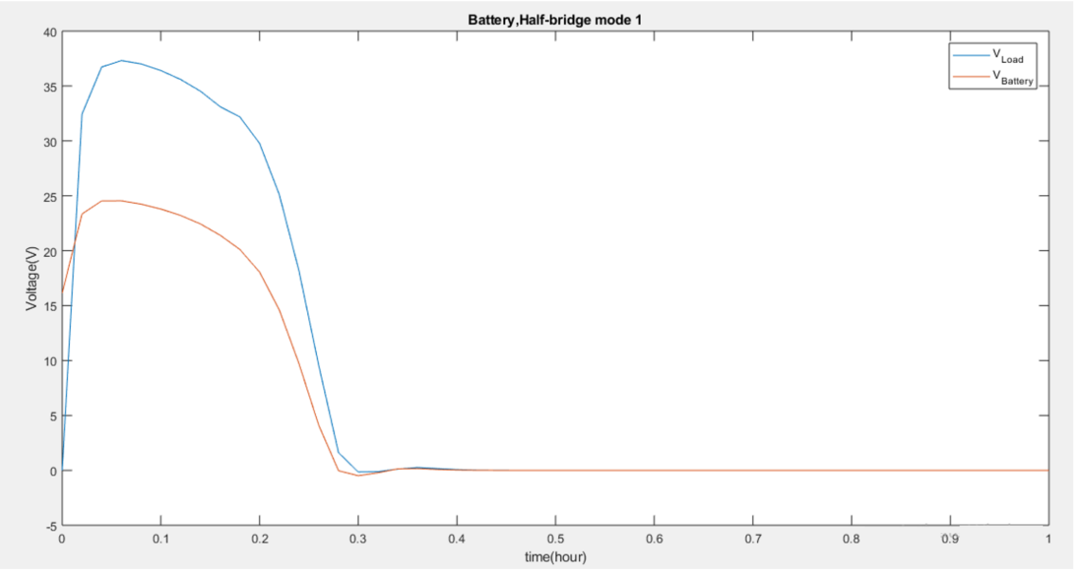

Figure 5. 10: Battery half-bridge (operating in boost mode) voltage output

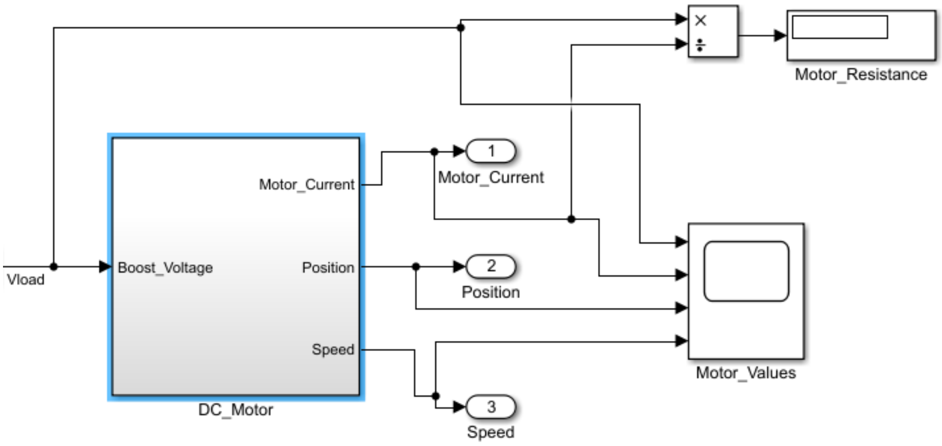

Figure 5. 11: Motor Simulink system

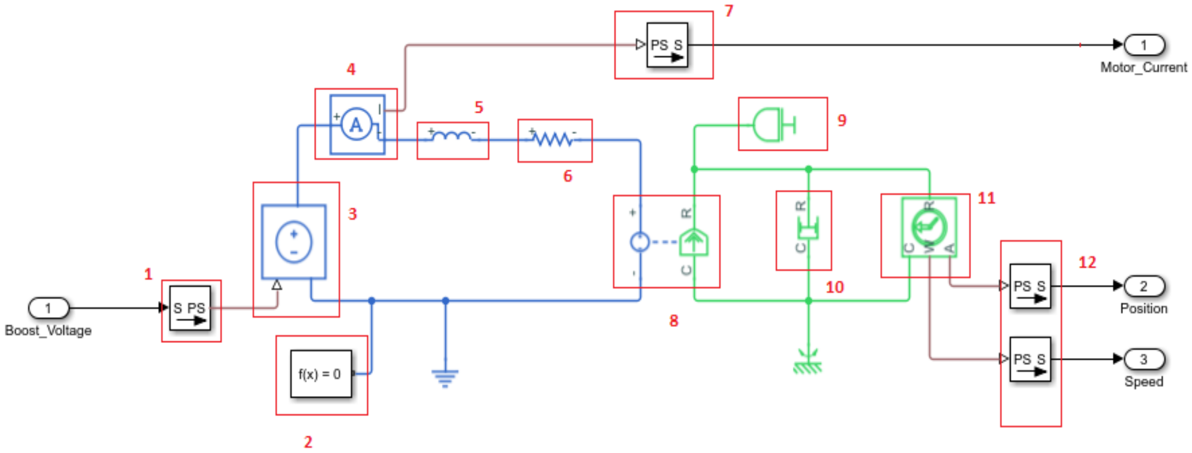

Figure 5. 12: Motor Simulink sub-system

./

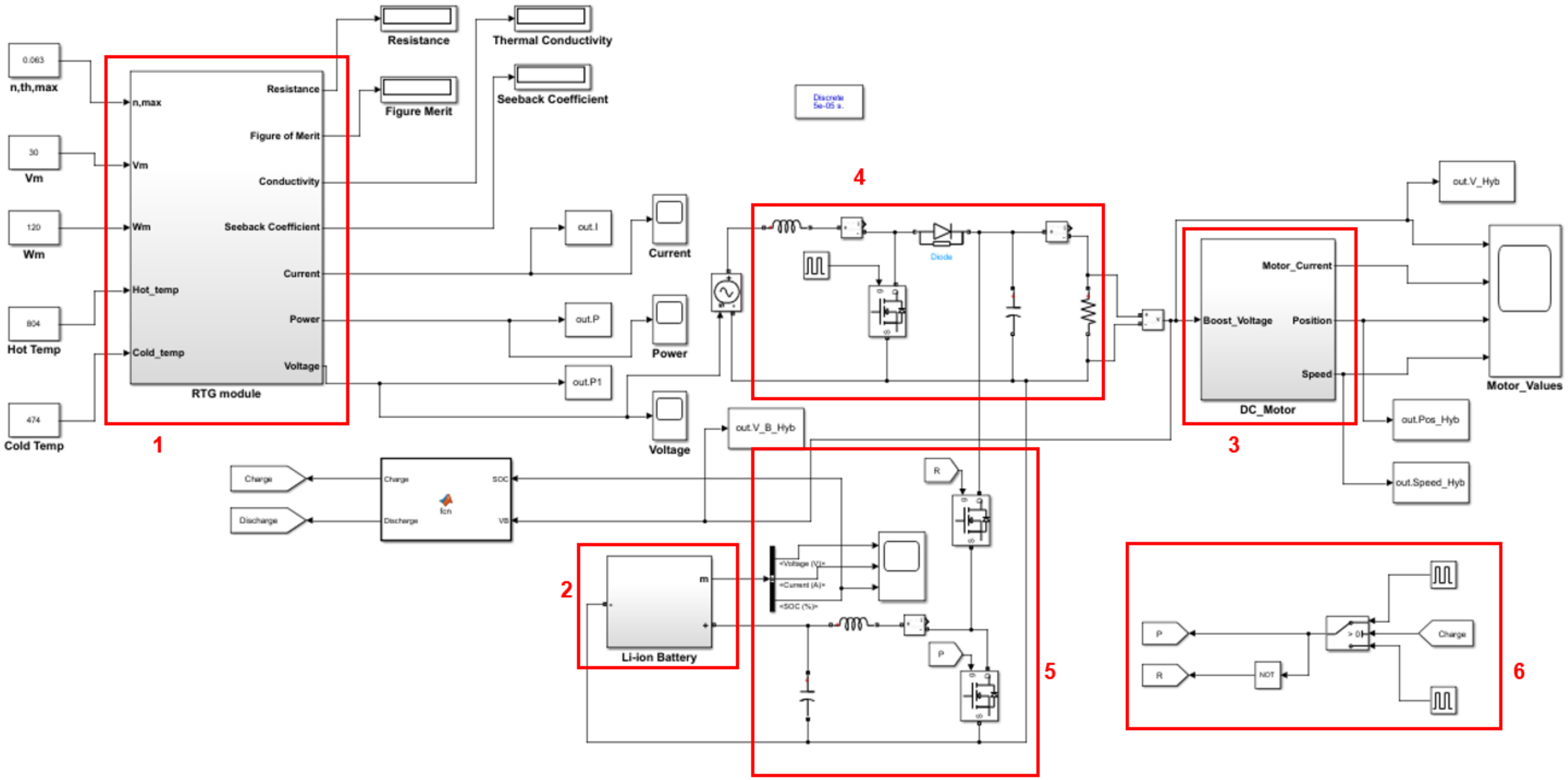

Figure 5. 13: Hybrid system Simulink model

The hybrid system represented in Figure 5.13 is being controlled by the pulse generated in block 6. In this block, the charge pulse is transferred to the MOSFET if the charge signal is superior to 0, while the pulse will be sent to the MOSFET if the charge signal is equal to zero.

The code shown in Code 5.1 is responsible for the charge-discharge cycle of the battery by controlling the voltage at the output so that if the motor voltage is superior to 50 V, the battery SoC is below 30%. The output voltage should be used to power back the battery. The same thing should happen if the output voltage is below 50 V, meaning that the battery cannot give supplementary power to the output and needs an emergency recharge.

```
function [Charge,Discharge]= fcn(SoC,VB)

%#codegen
Charge=0;
Discharge=1;

if(VB>60)
    Charge=0;
    Discharge=1;
end

if(VB>50 && SoC<30)
    Charge=1;
    Discharge=0;
end

if(VB<50)
    Charge=1;
    Discharge=0;
end
```

Code 5. 1: Function code controlling charge-discharge behavior of the hybrid system

The hybrid system relies on two MOSFET switches turning ON & OFF at different pulses at a duty cycle D. This setup is important mainly because a change in the duty cycle changes the power flow of the system. In other words, when the duty cycle D is inferior or superior to a pre-set value, the bidirectional DC-DC converter either charges or discharges the battery..

5.5 Simulation and discussion of results

Running the simulation in Matlab/Simulink gives the result in Figure 5.14. It could be seen that the voltage at the output reaches a maximum value of 60 V when the battery voltage discharges, but when the output voltage drops to 40 V, it is due to an increase in the battery voltage during charging. Therefore, the system, if subjected to appropriate development and the right conditions, is capable of power leveling (supply additional power), battery charging, and recovery mode.

Figure 5.15 shows that the current through the motor increases considerably during battery discharge and decreases when the battery charges. It could be seen that the current ripples are unstable. Thus, the system might operate on high power demand but only for a limited amount of time.

Analysing Figure 5.15 it can be observed that during the transient regime, the initial current is zero when the motor is connected to the output terminals of the boost converter and it takes some time for it to attain the nominal current because of the inductance in the armature circuit. The motor reaches its steady state once the current settles around 47 A which is its final value. However, this current is subjected to ripples, making the final value of the current to oscillate between 45 and 50 A. These ripples originate from the output of the boost converter as the motor receives its supply from it. When the inductor of the converter is storing energy, the output voltage decreases, and it rises when the energy is released.

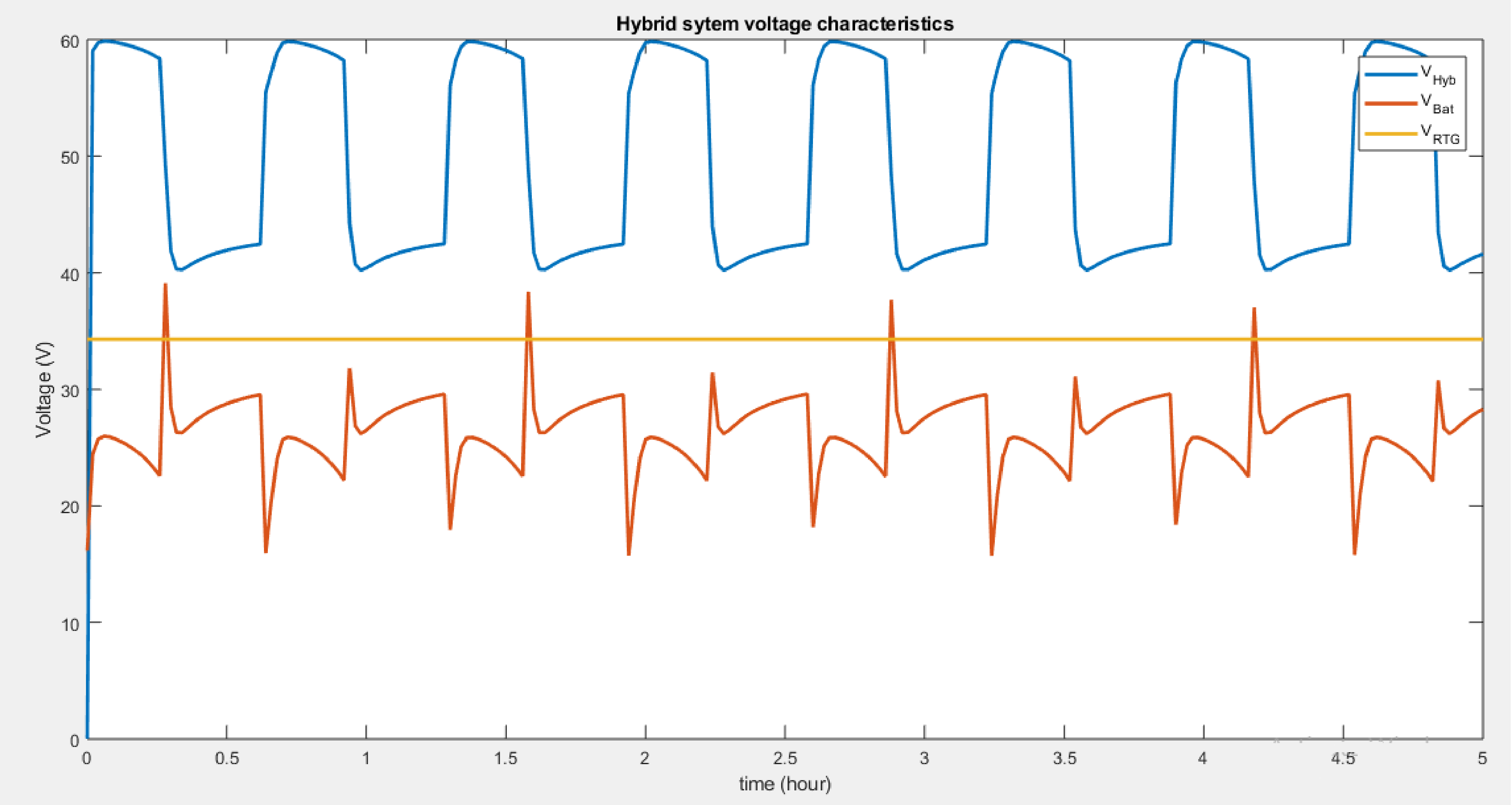

.

Figure 5. 14: Hybrid system output voltage

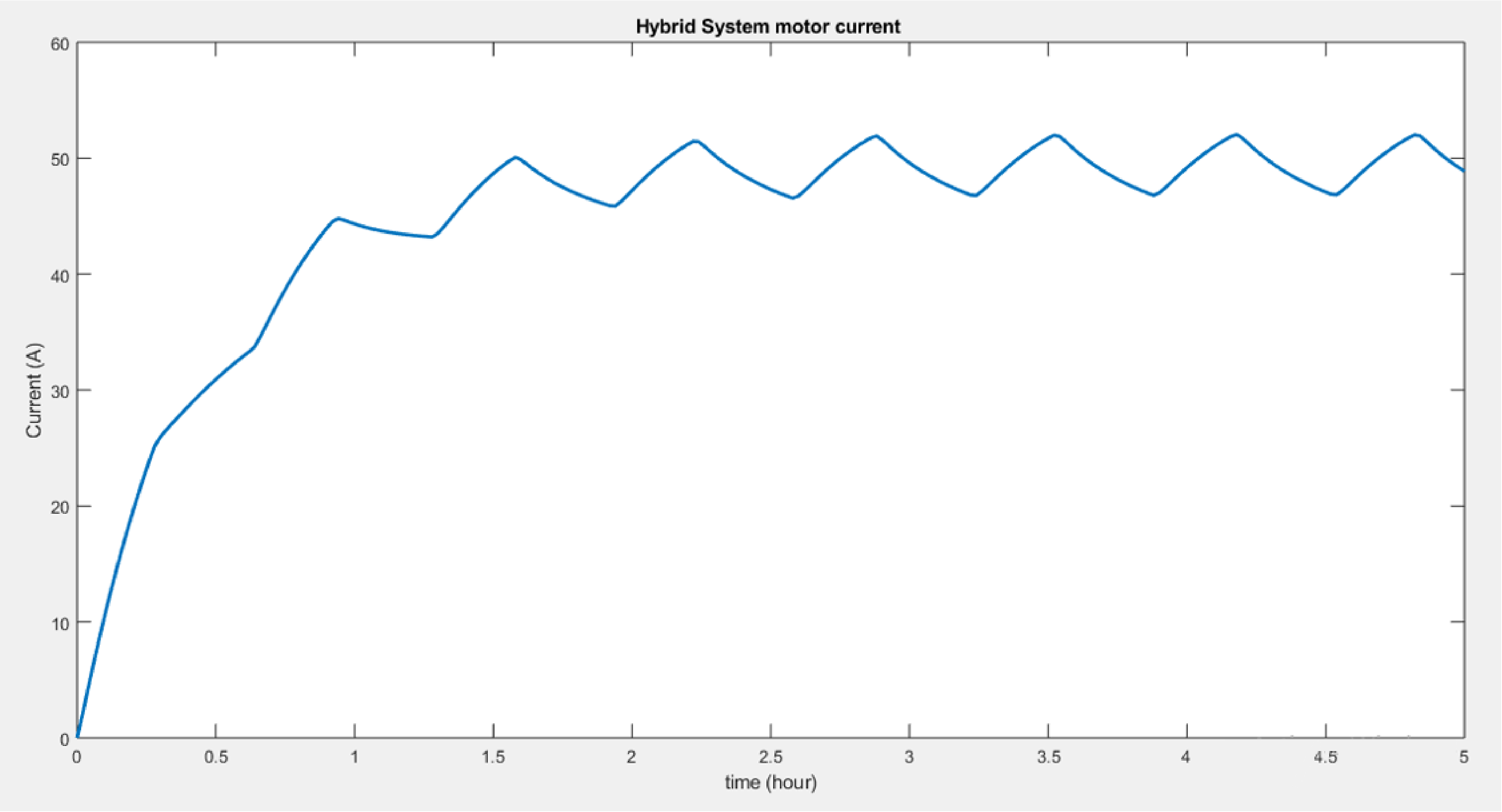

Figure 5. 15: Motor current when powered by the hybrid system

The power plot in Figure 5.16 shows that the rather unstable power behavior from the battery does not affect the power stability of the motor. Thus the arrangement of the hybrid system provides a viable and relatively stable power at its output, regardless of the input power behavior.

The above hybrid system, however, can be compared to the result obtained from a single supply RTG connected to the motor (Figure 5.8). The comparison presented in Figure 5.17 shows that the constant voltage of 48 V boosted from the RTG single system is inferior to that of the voltage delivered by the hybrid system when charged by the battery of 60 V.

Therefore, the hybrid system is capable of delivering better performance when additional power is needed, recharging the battery if necessary, and it can also solely rely on the MMRTG power, making it more advantageous.

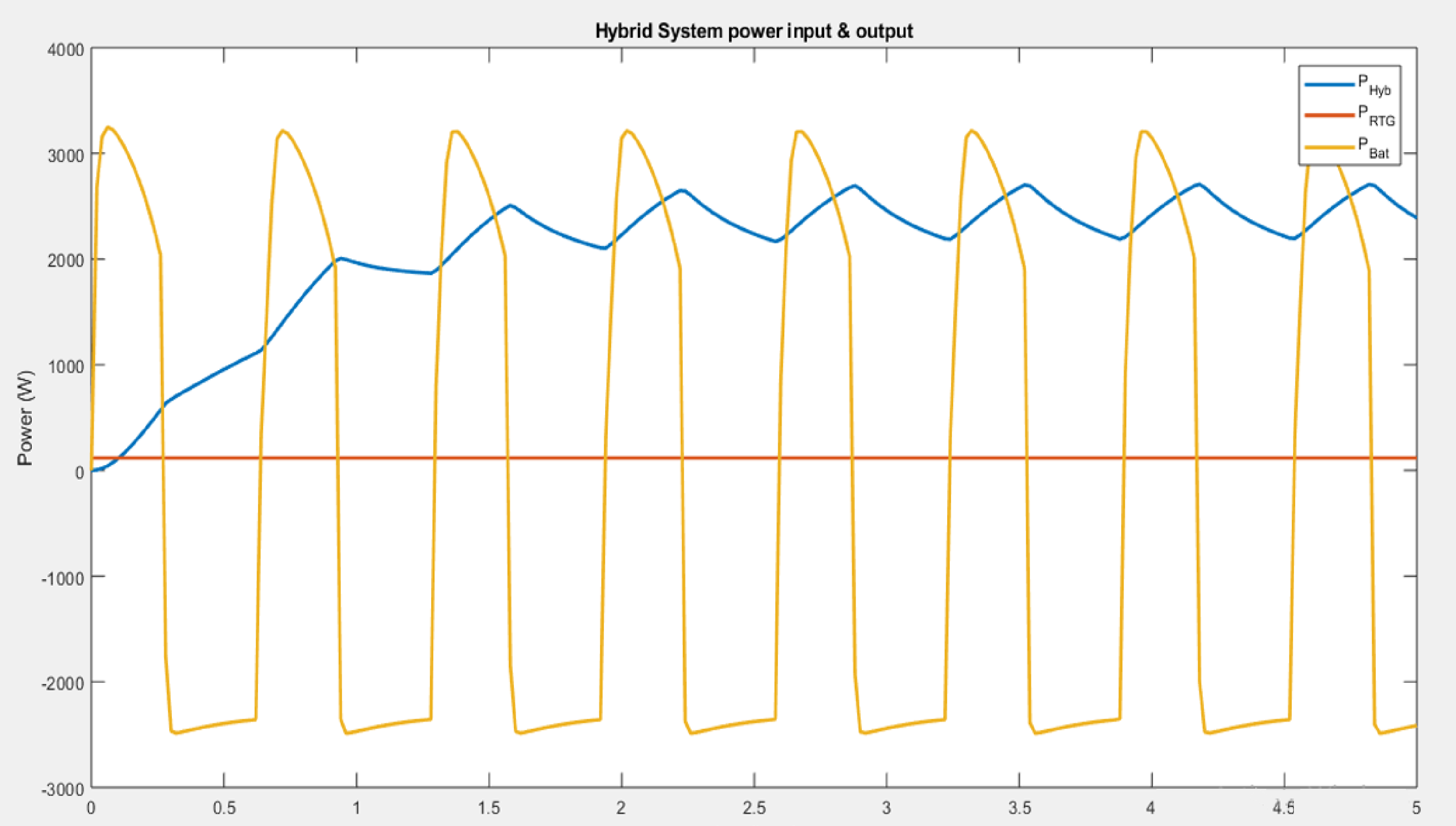

Figure 5. 16: Hybrid system power input and output

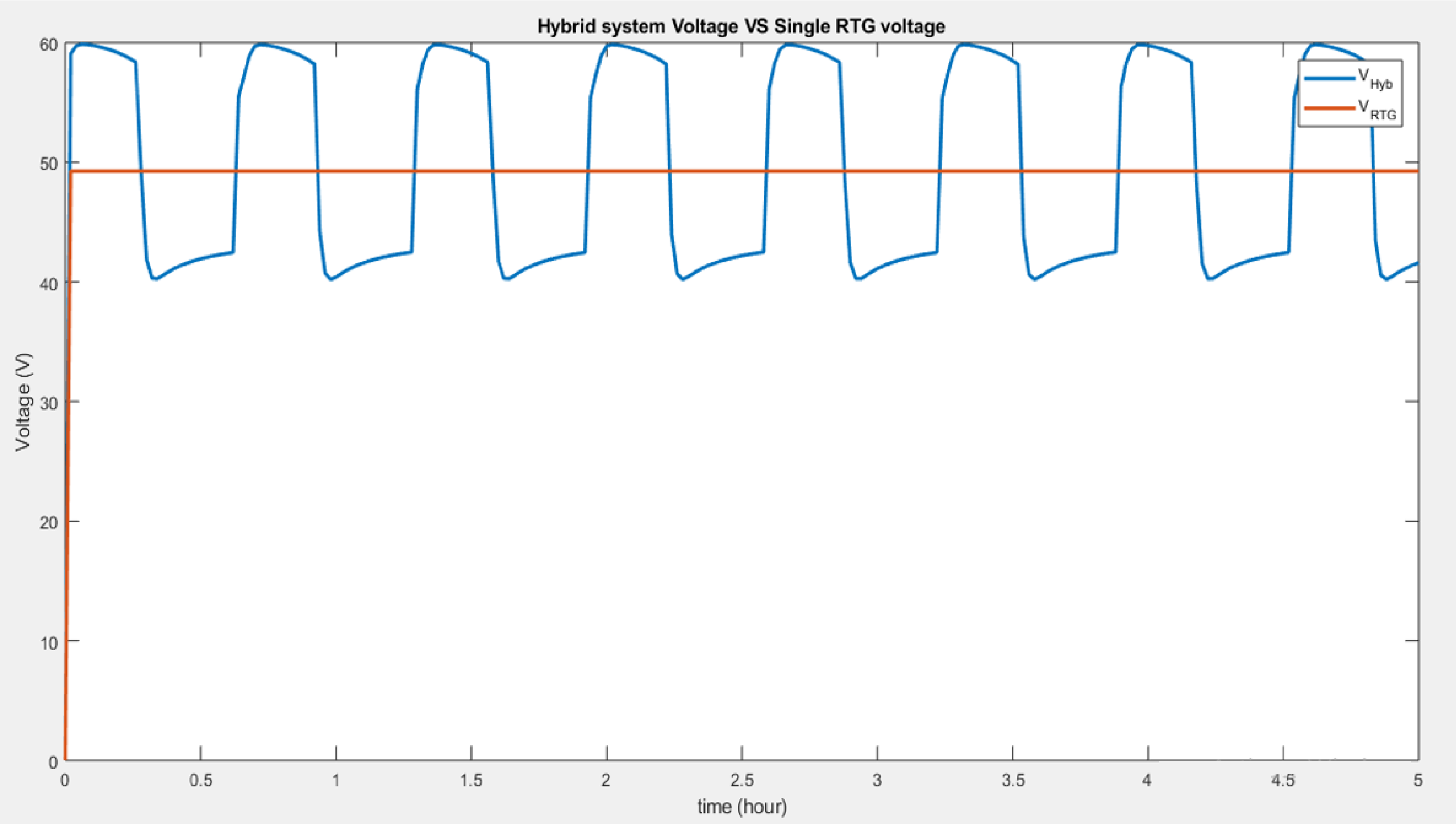

Figure 5. 17: Load voltage: hybrid system versus single power source (RTG only)

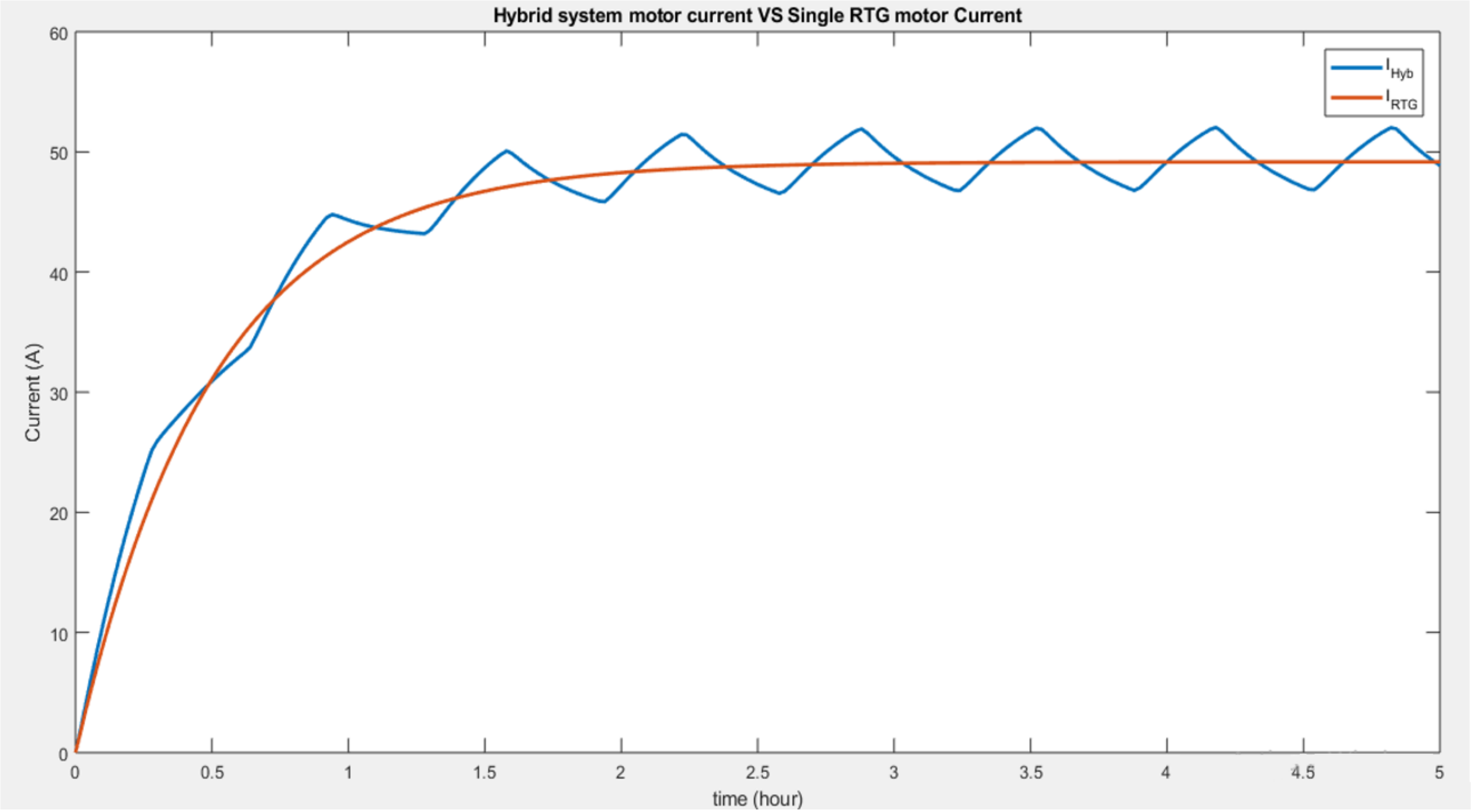

Figure 5. 18: Motor current: hybrid system versus single power source (RTG only)

Figure 5.18 suggests that the current through the motor is higher when the motor is connected to the hybrid system than when powered by a single RTG. While figure 5.19 indicates that the power of the hybrid system is superior to this of the RTG system during battery discharge and slightly inferior to the nominal power when the battery is charging.

We can see the motor behavior in Figure 5.20, which shows that the torque of the motor under the hybrid system is above this of the single RTG. But this can be explained by the constant current through the armature in a single supply, while the hybrid system in the simulation conditions switches between charging and discharging successively. However, in better simulation conditions, the system should charge and then run on RTG power and only use battery power in case of considerable power demands. The same comment can be said for the velocity in Figure 5.21.

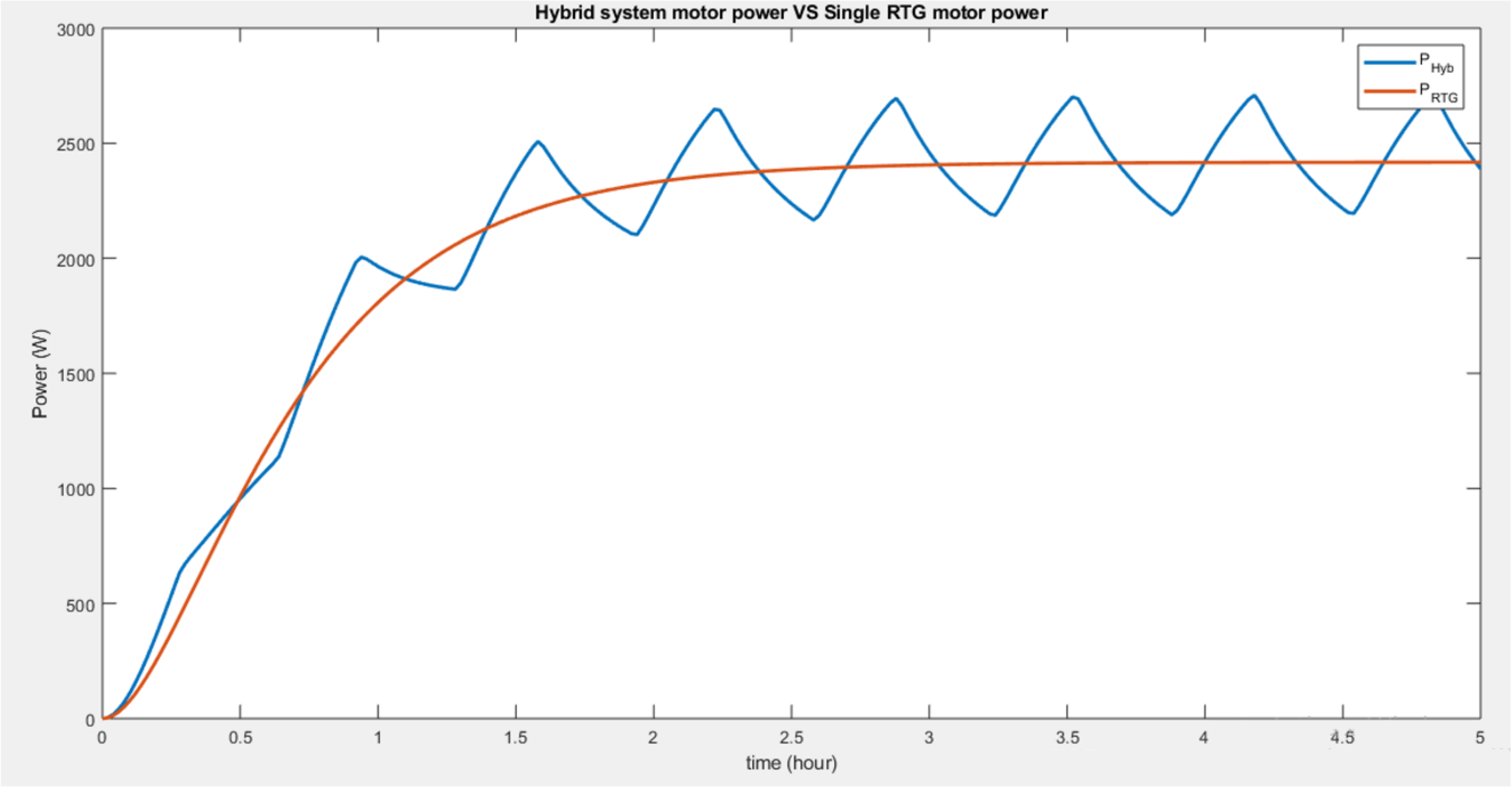

Figure 5. 19: Load power: hybrid system versus single power source (RTG only)

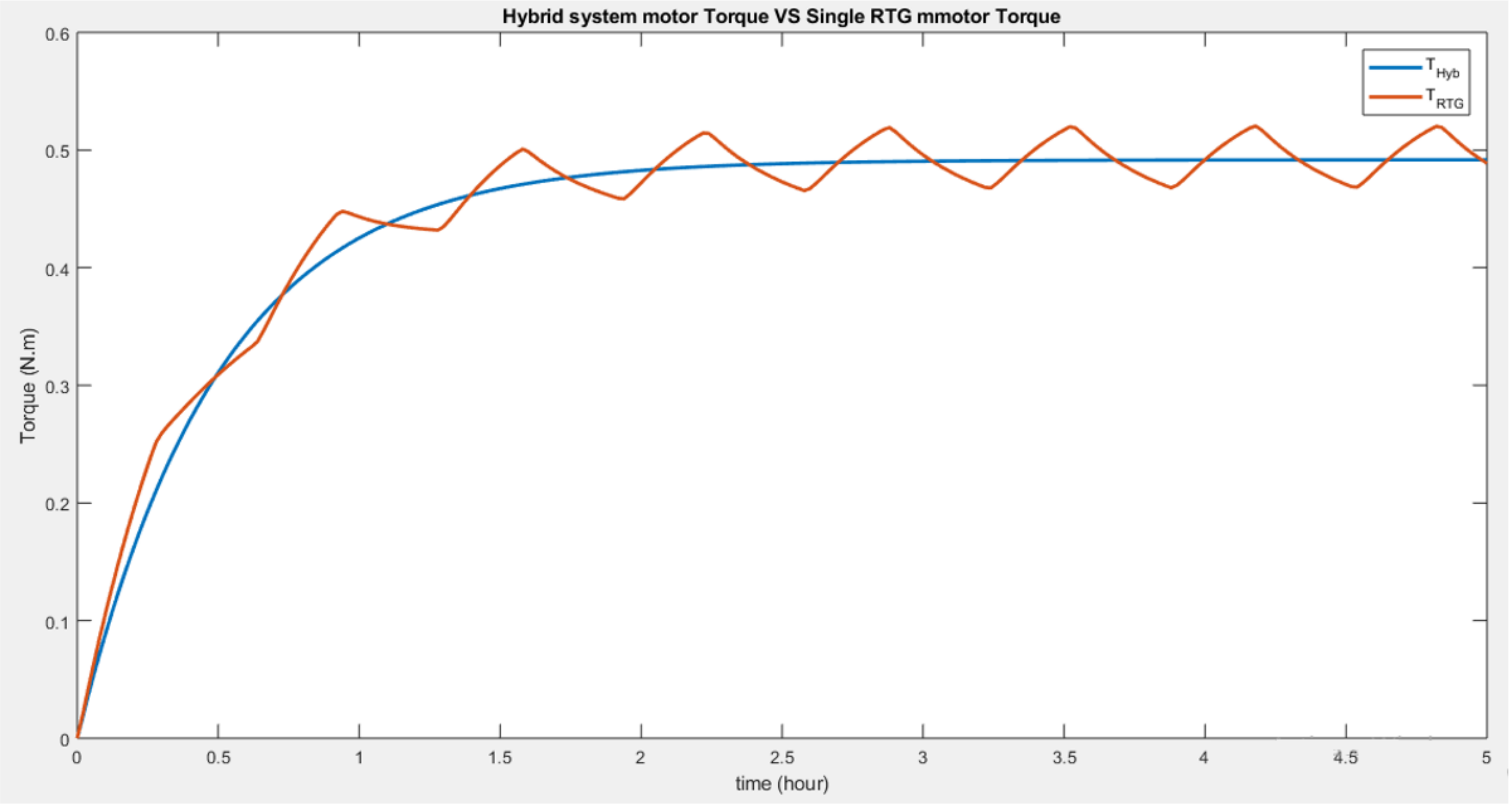

Figure 5. 20: Torque: hybrid system(red) versus of single RTG supply(blue)

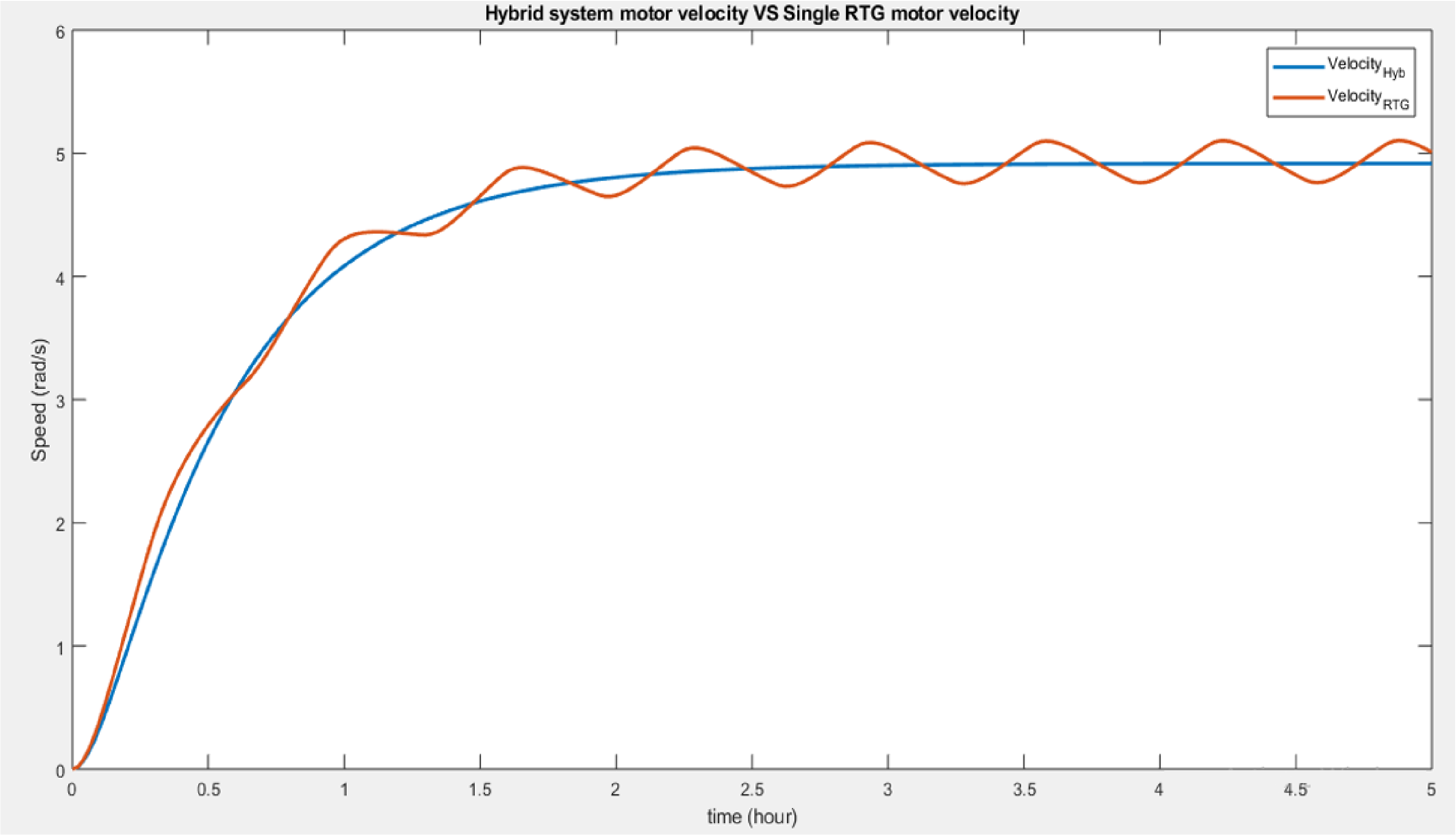

Figure 5. 21: Torque: hybrid system(red) versus single RTG supply(blue)

Consequently, the hybrid system exhibits better voltage management to ensure the long life of the battery. Furthermore, an inconvenient condition of solely relying on the RTG-powered system is the fact that energy depletes by nearly 4% per year, making the power less efficient in the course of a long operating time. This issue can be overcome by the supplementary power coming from the Li-ion battery.

5.6 Hybrid system with PI controller

The implementation of the hybrid system with PI control is presented in Figure 5.22. The system is used to control the motor speed and stabilize it to a value of 5 rad.s^{-1}.

A closer look at the model of Figure 5.23 shows the PI controller gain value used where we could see two branches of PI being implemented. One controls the charging behavior of the system with PI control. Meanwhile, the other controls the discharge behavior of the system with PI control. This arrangement is also known as the battery management system controlling the hybrid battery.

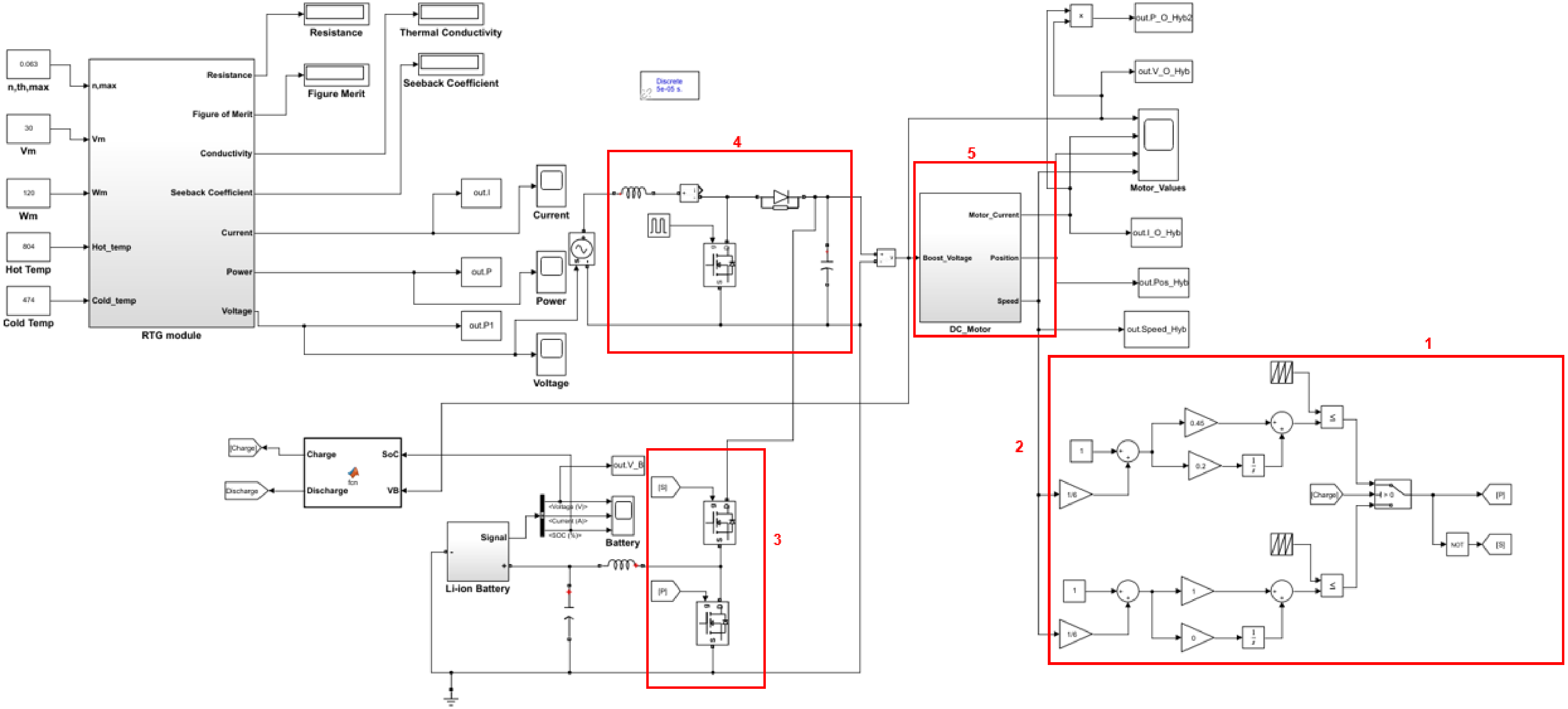

Figure 5. 22: Hybrid system with PI controller

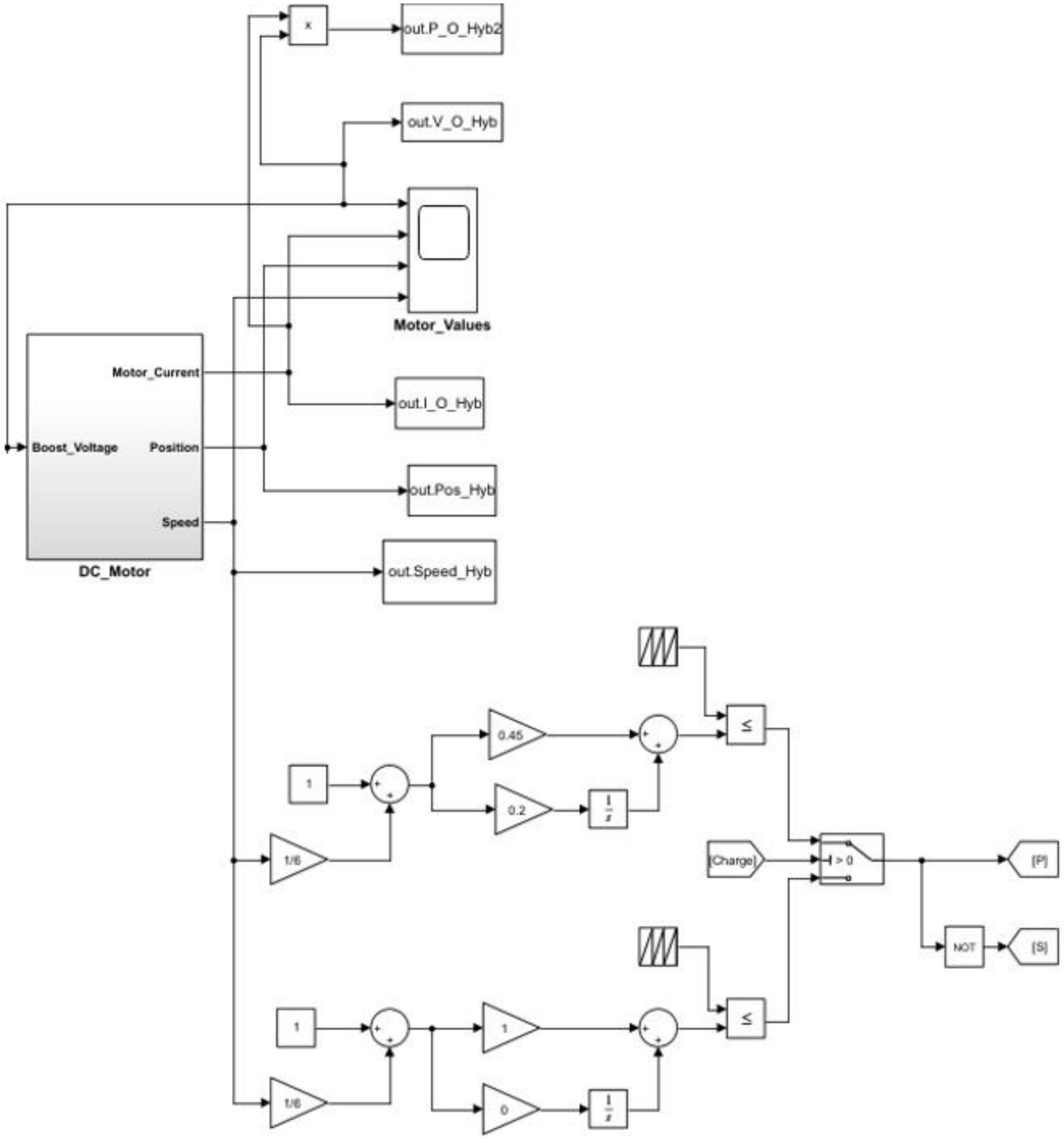

Figure 5. 23: PI controller gain value

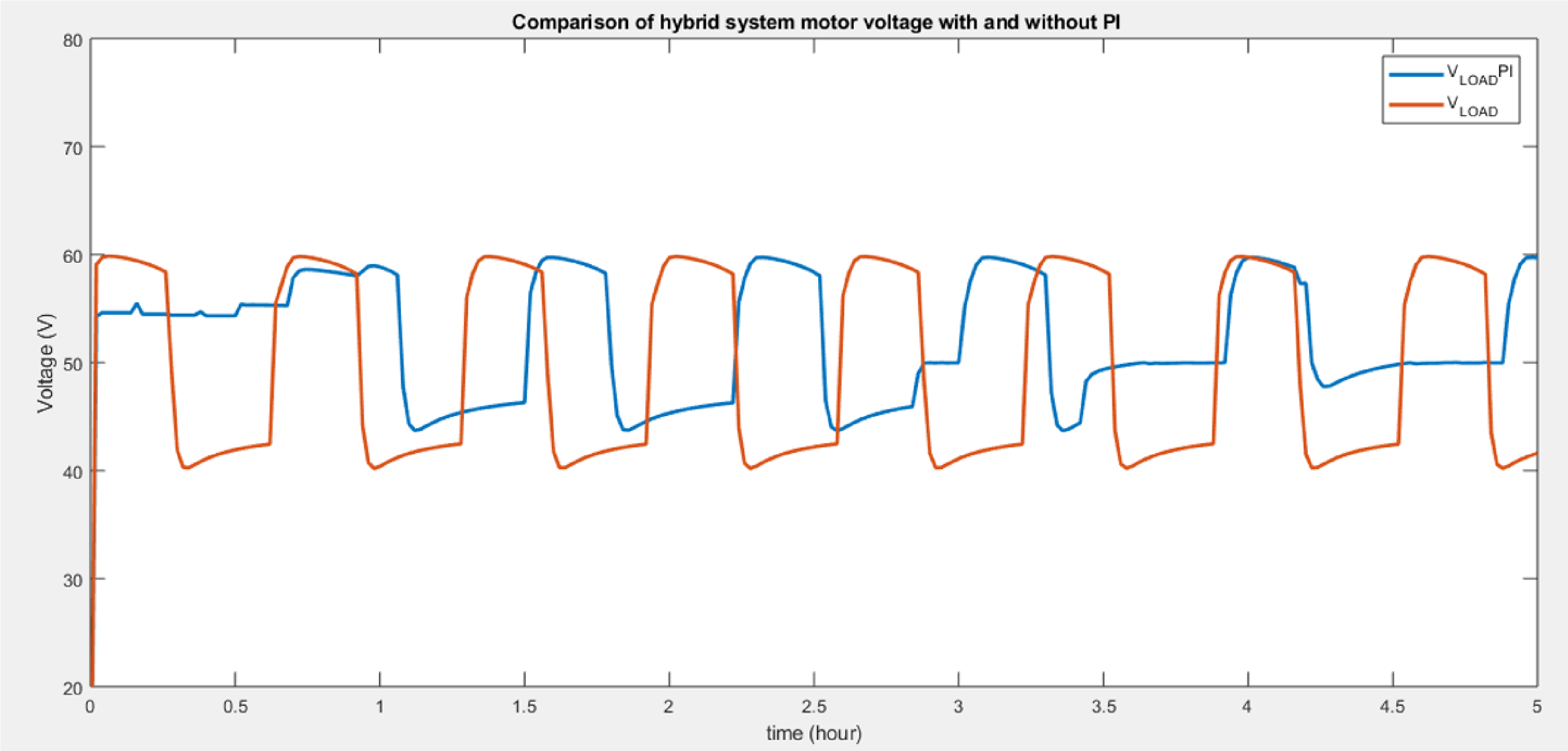

Figure 5. 24: Load voltage comparison with the Hybrid system with PI control(blue) and without PI control

The plot in Figure 5.24 of the voltage behavior of the charge-discharge cycle of the hybrid system with and without PI control shows that the load voltage of the hybrid system with PI control tends to charge and discharge less than the non-controlled battery system. Furthermore, the voltage of the system when charging the battery does not fall as low as 40 V when PI controlled is implemented but only falls to 50 V.

This is due to the fact that the peak voltage from the battery is used at first when the system stabilizes (peak demand of energy), and then the system requires less battery assistance. Indeed Figure 5.25 shows that after 3 hours of running, the system speed starts reaching the value set on the controller and presents less ripple. Figure 5.26, which compares the battery behavior with PI control and without PI control, shows that the battery undergoes less charge-discharge period but still delivers much better performance than the hybrid system without PI control. The SoC tends to have a larger period, meaning that the discharge occurs over a more extended period. Thus the fed additional power lasts longer.

Therefore, implementing a battery system management (PI control) guarantees a better functioning of the system, which could positively affect the life of the battery by increasing the period of the life cycle.

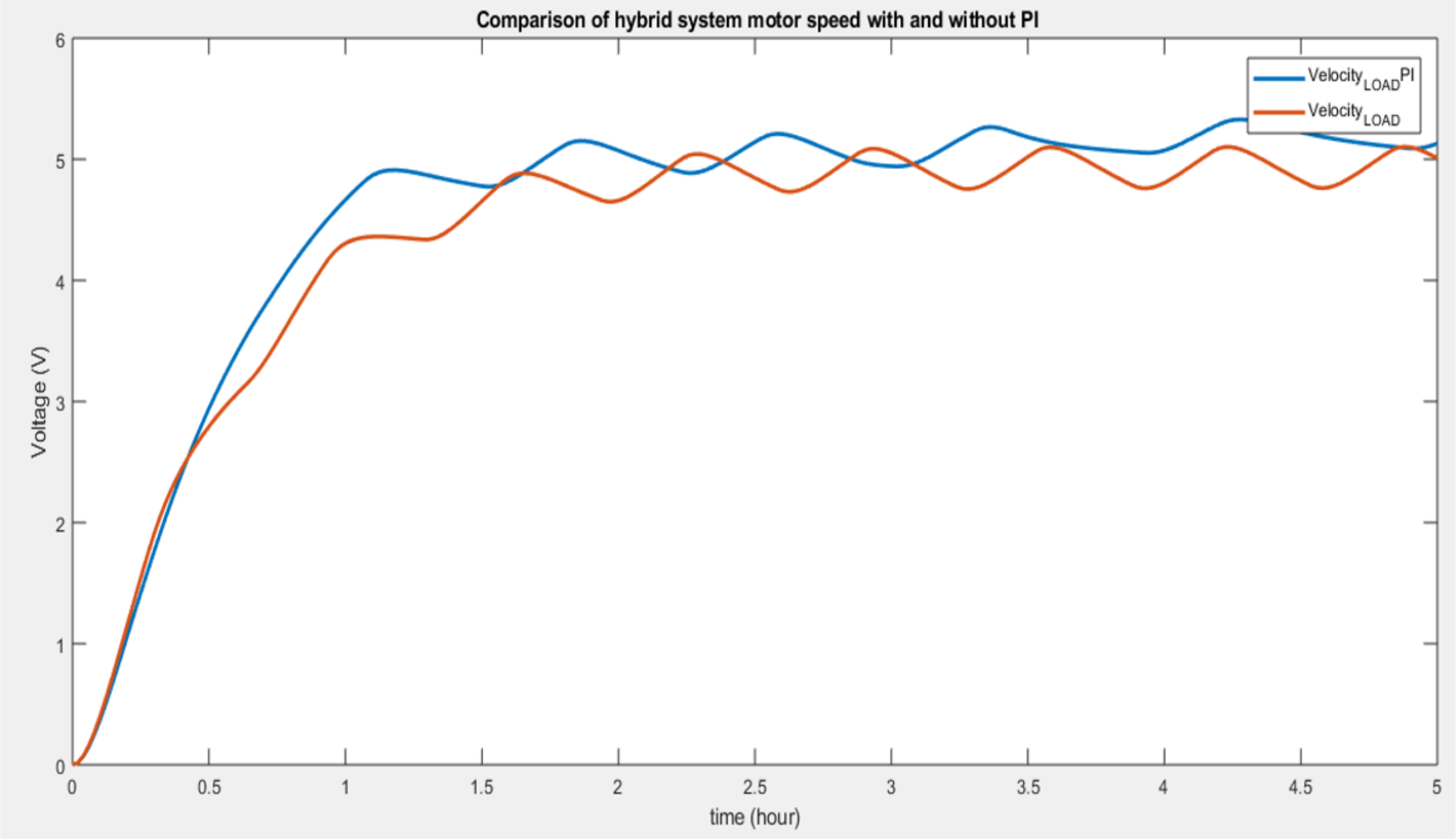

Figure 5. 25: Motor speed of hybrid system: with PI control (blue) and without PI control (red)

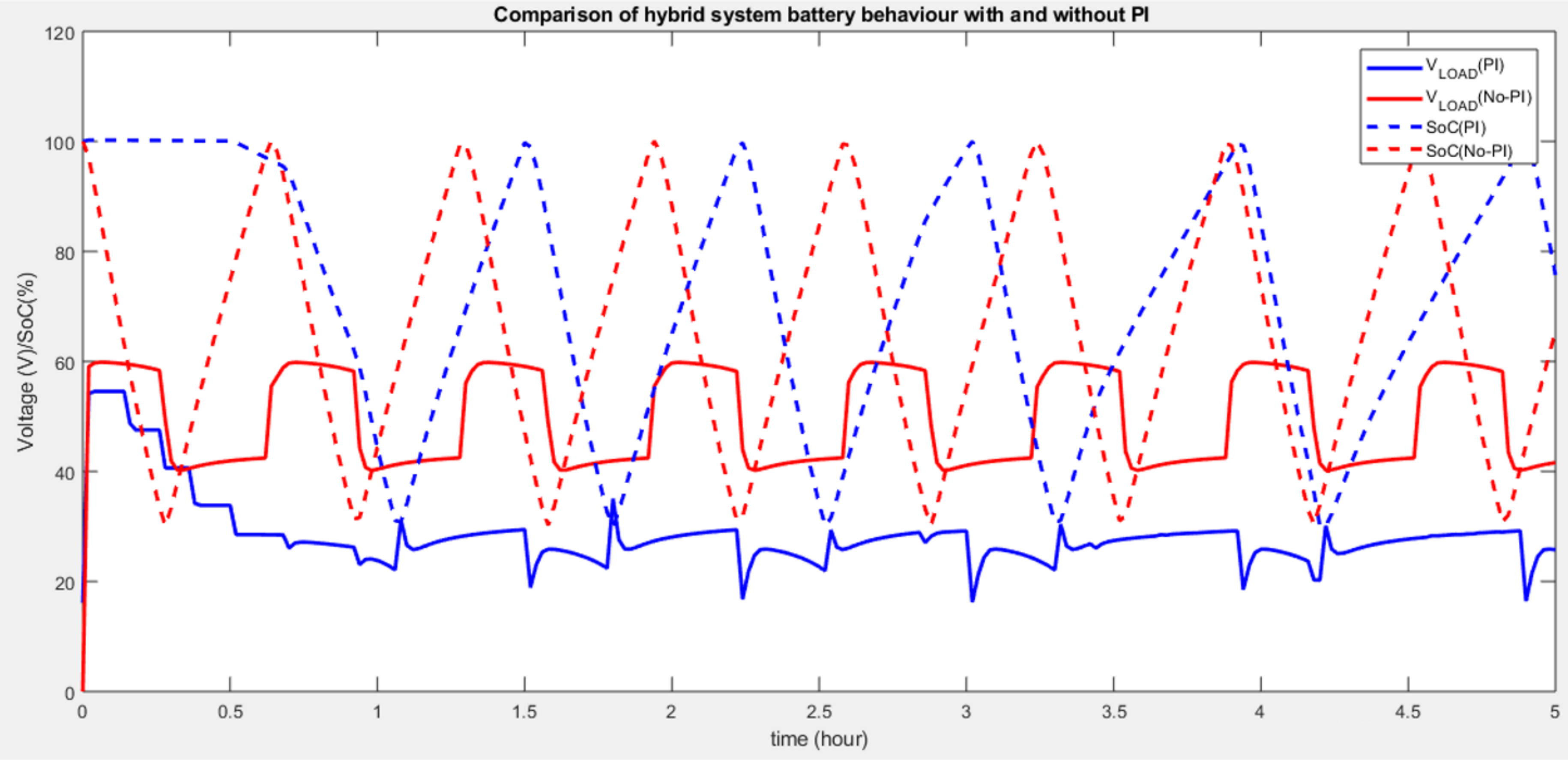

Figure 5. 26: Battery voltage and SOC with PI implementation vs. simple hybrid system

5.7 Electrical characteristics and validation of the hybrid battery system

The previous section focused on designing and approving the behaviour of the hybrid system and guide an output comparison between a single-powered system (only RTG) and a hybrid system without an elaborated controller and studied/analysed the estimated outputs to the load.

This section explores the power characteristics of the hybrid system under different load conditions, throughout the three important phases of system usage: charging mode (main source powers the battery) unload mode (where the battery and main source provide power to the DC motor) and main power mode (RTG powers the load on its own). Therefore, this section will analyze the discharge behavior of the hybrid system with a PI controller; and will also focus on studying the motor behavior.

5.7.1 Hybrid battery system characteristics with different load resistance

The resistance load is an important variable of the DC boost converter and DC-DC bi-directional converter because varying the load resistance may affect the value at the output. The resistance values that would be used to conduct our study are $R_1 = 1\Omega$, $R_2 = 3\Omega$, and $R_3 = 7\Omega$. The simulation happens at a nominal duty cycle of 70%.

Figure 5.27 shows the Simulink configuration for the system under consideration, and the results obtained during the complete discharge of the battery at different loads are depicted in Figures 5.28, 5.29, and 5.30.

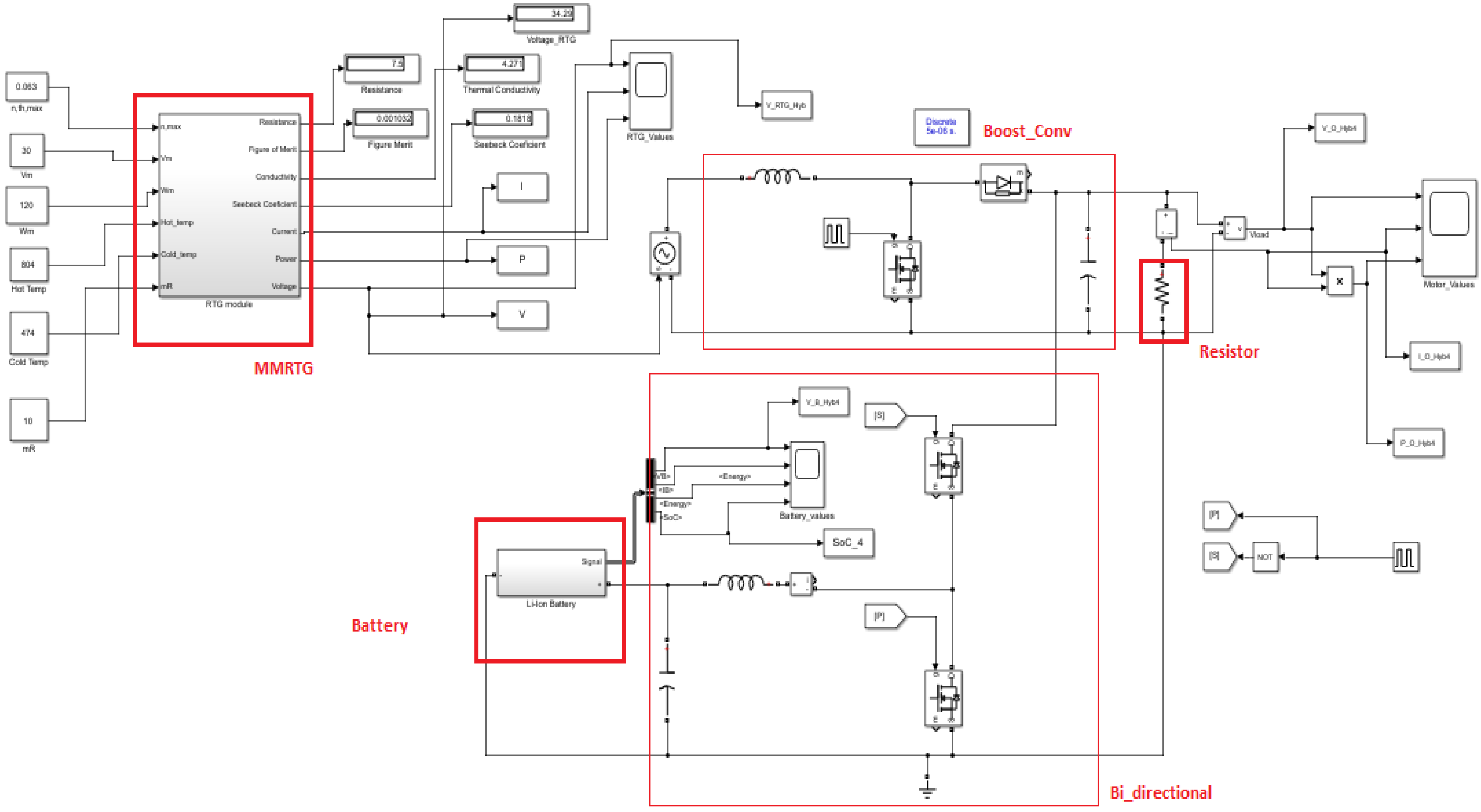

Figure 5. 27: Hybrid system

5.7.2 Voltage comparison at different load resistances

The voltage plot presented in Figure 5.28 shows that the load voltage tends to be superior at a higher resistance; indeed, the hybrid system exhibits the highest output voltage of 95 V when a load of 7 Ω is connected; meanwhile, the smallest load of 1 Ω only provides a voltage of 60 V during discharge. It is also interesting to see that the higher load, has the tendency to increase the battery discharge life, from about half an hour (30 minutes) up to an hour when operated at 1 Ω and 7 Ω, respectively.

Moreover, it could be observed that even after that the battery-fed discharge voltage period has flattened out, the constant voltage out of the hybrid system is only the voltage produced by the boost converter coming from the RTG.

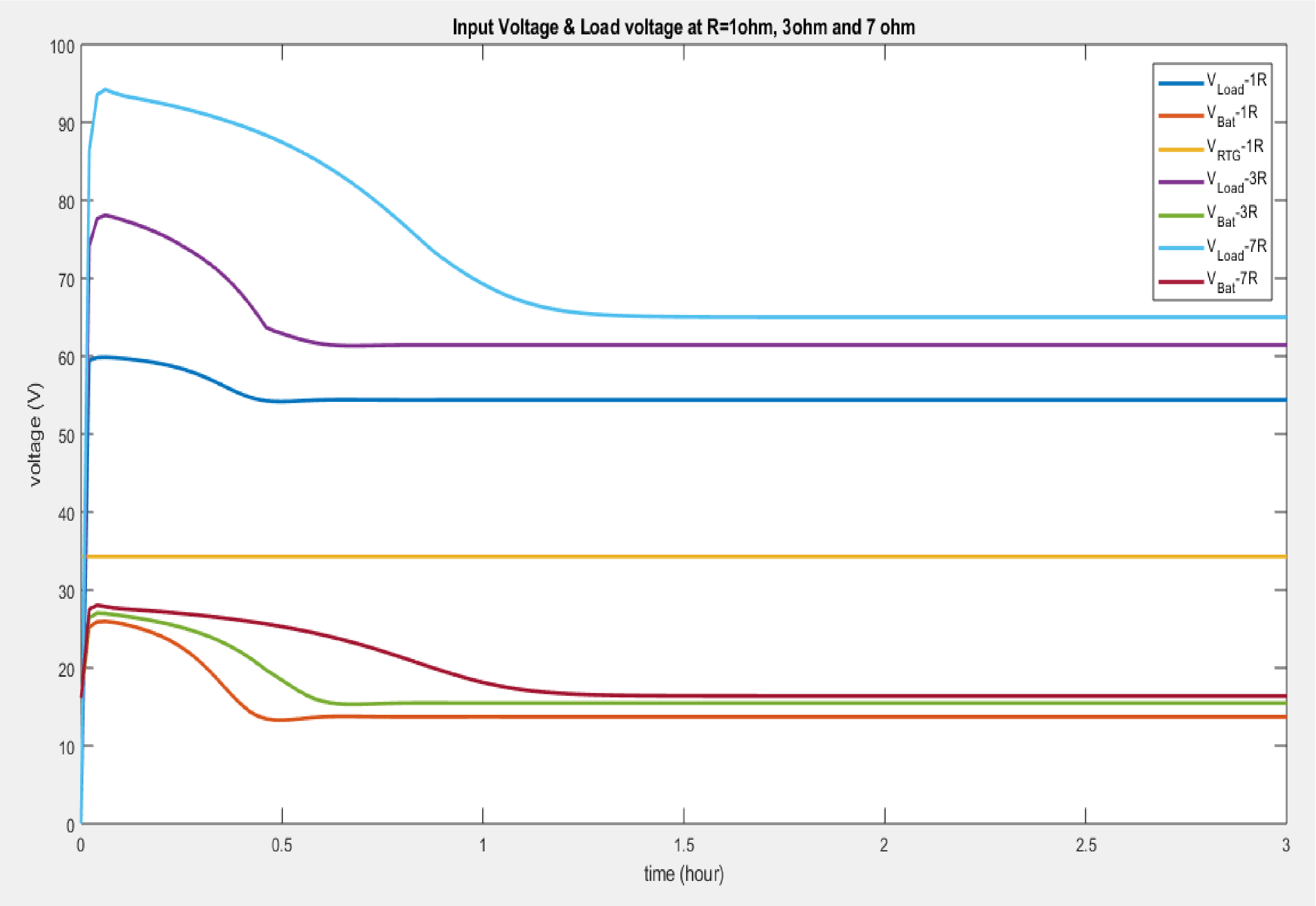

Figure 5. 28: Voltage characteristics under different resistance values

5.7.3 Current comparison at different load resistances

In contrast, Figure 5.29 shows that the current through the 1 Ω resistance turns out to be at its highest during discharge. Meanwhile, this 7 Ω resistor shows the smallest amount of current.

5.7.4 Power comparison at different load resistances

Without a doubt, the most promising result is that of the power (Figure 5.30) under the conditions described above. It could be observed that the highest peak of power is obtained at the lowest load resistance of 1 Ω at 3500 W, followed by the mid-range resistance of 3 Ω at 2000 W and the highest resistance of 7 Ω at 1250 W. It could also be seen that the peak in power entirely comes from the battery power, which turned out to be superior to the output power only in the 1 Ω load, while in other types of load; the output power is lower than that of the battery.

It is evident that the peak in power takes a considerable time to fade during the discharge period regarding the amount of resistance R; indeed, the more resistance, the longer the power supplied to the load remains at a peak.

The result of the test conducted by varying the load resistance shows that the lower the resistance, the better the power at the output. Even though it has the inconveniency of operating at peaks for a shorter period, the short operating time is a minor issue since the battery is to be recharged during operation and is required to be used for maximum power delivery.

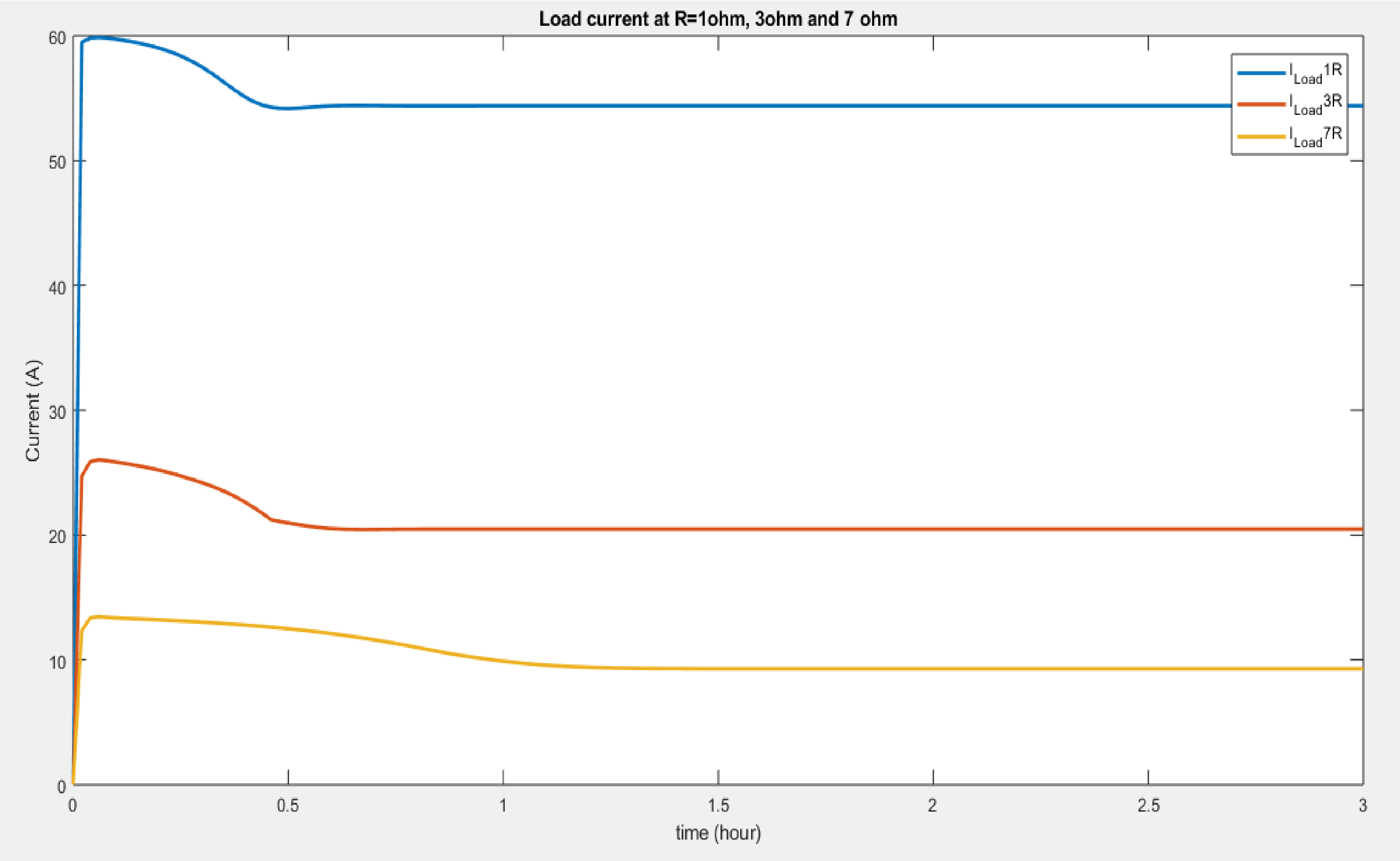

Figure 5. 29: Load current under different resistance values

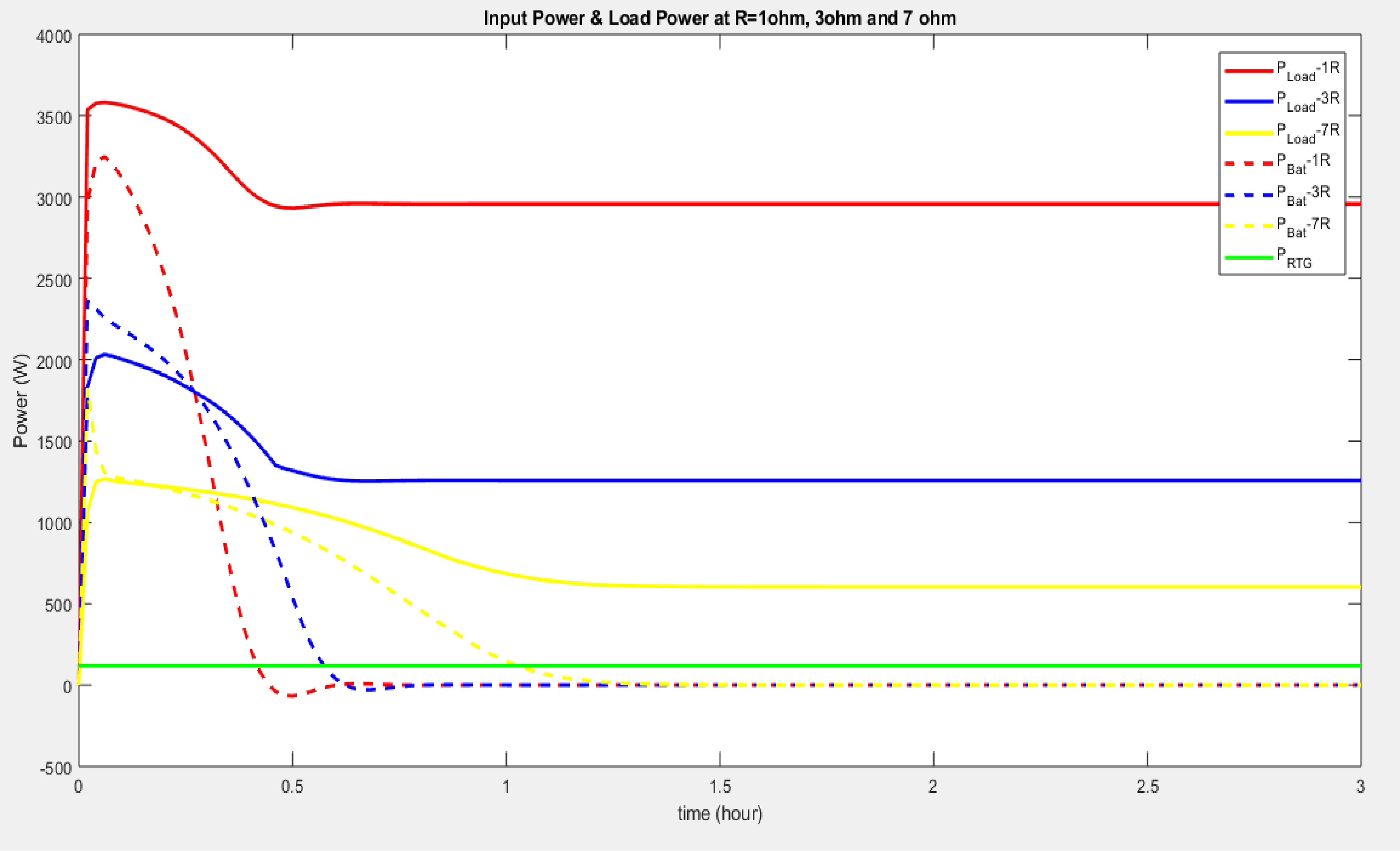

Figure 5. 30: Power input versus power output at different load resistance

5.8 Motor performance

This section compares the DC motor behavior when connected to the load analyzed in the previous section.

5.8.1 Electrical performance of DC motor

- **Voltage**

Comparing Figure 5.31 and Figure 5.28, which are similar, it is evident that the voltage is superior at the largest resistance, reaches a higher peak at 7 Ω load, and tends to decrease as the resistance decreases.

- **Current**

Meanwhile, the current fed to the motor is higher as the resistance decreases (Figure 5.32), with a value of 50 A at 1 Ω down to only 10 A when operated at 7 Ω. Thus, the motor performance is highly affected by the variation of the value of resistance. Thus, the considerable amount of current fed to the motor is responsible for the fast discharge of the voltage at the output.

- **Power**

Lastly, the power delivered to the motor is at the highest value with a higher load, and this power gets lower when the resistance of the boost converter is changed to a lower value (Figure 5.33). Since at 7 Ω, the output power may reach a value around 600 W at the motor, this value is only 2500 W under 1 Ω. Moreover, it could be noticed that the battery power offers a better discharge period with a low peak at a higher resistance. The discharge period decreases but the power peak value increases.

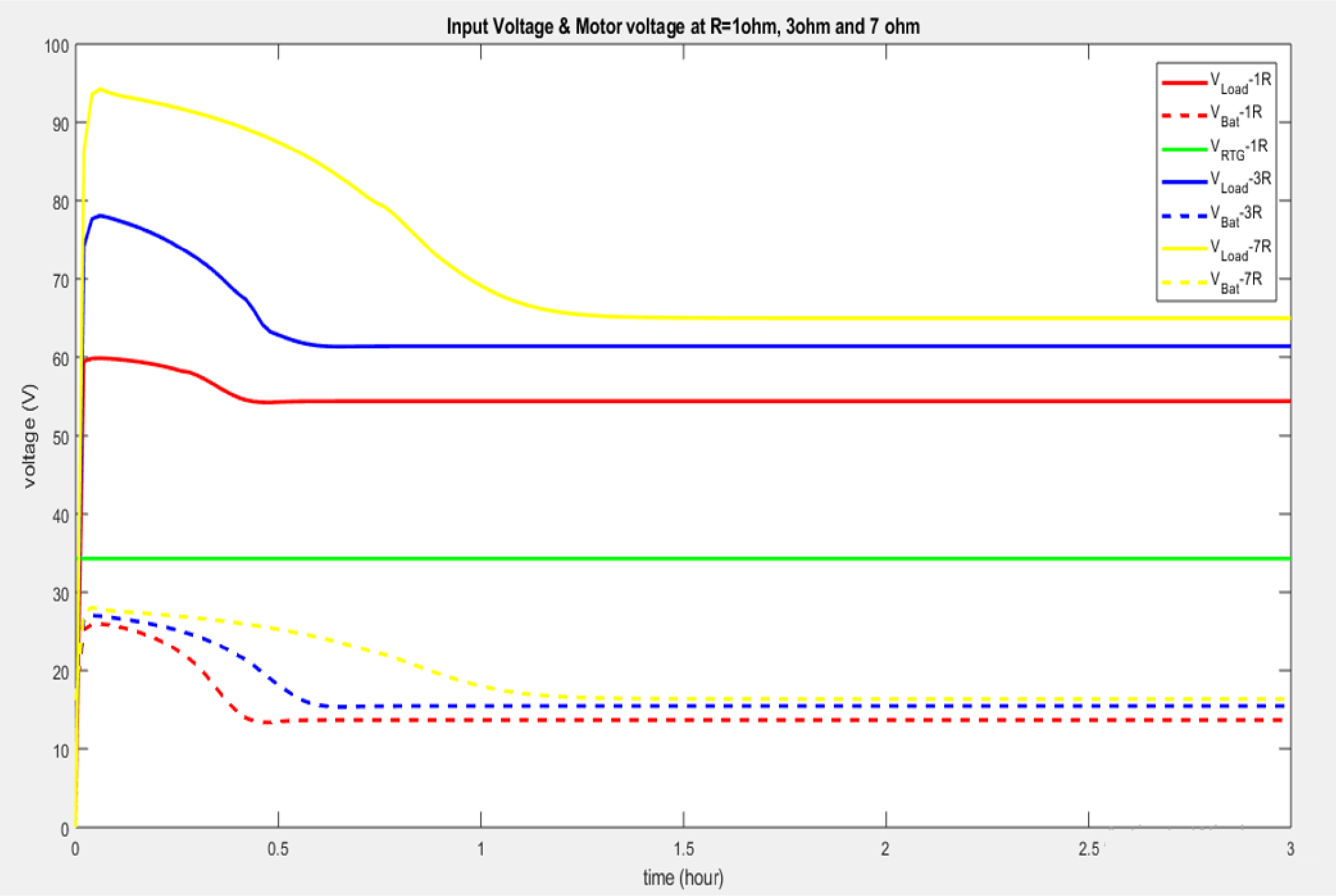

Figure 5. 31: Motor Voltage and battery voltage when connected to load of different values

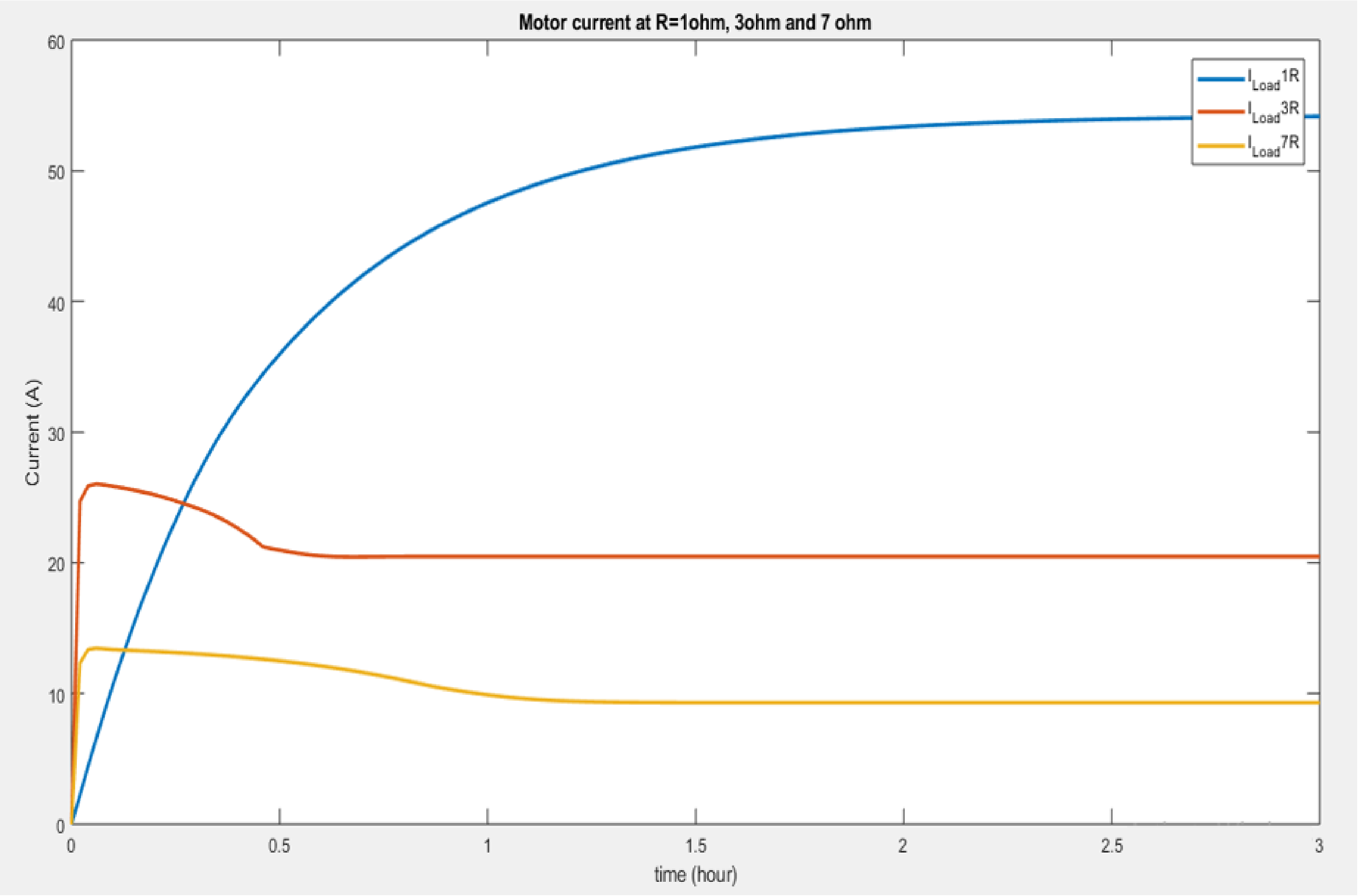

Figure 5. 32: Motor current when connected to load of different values

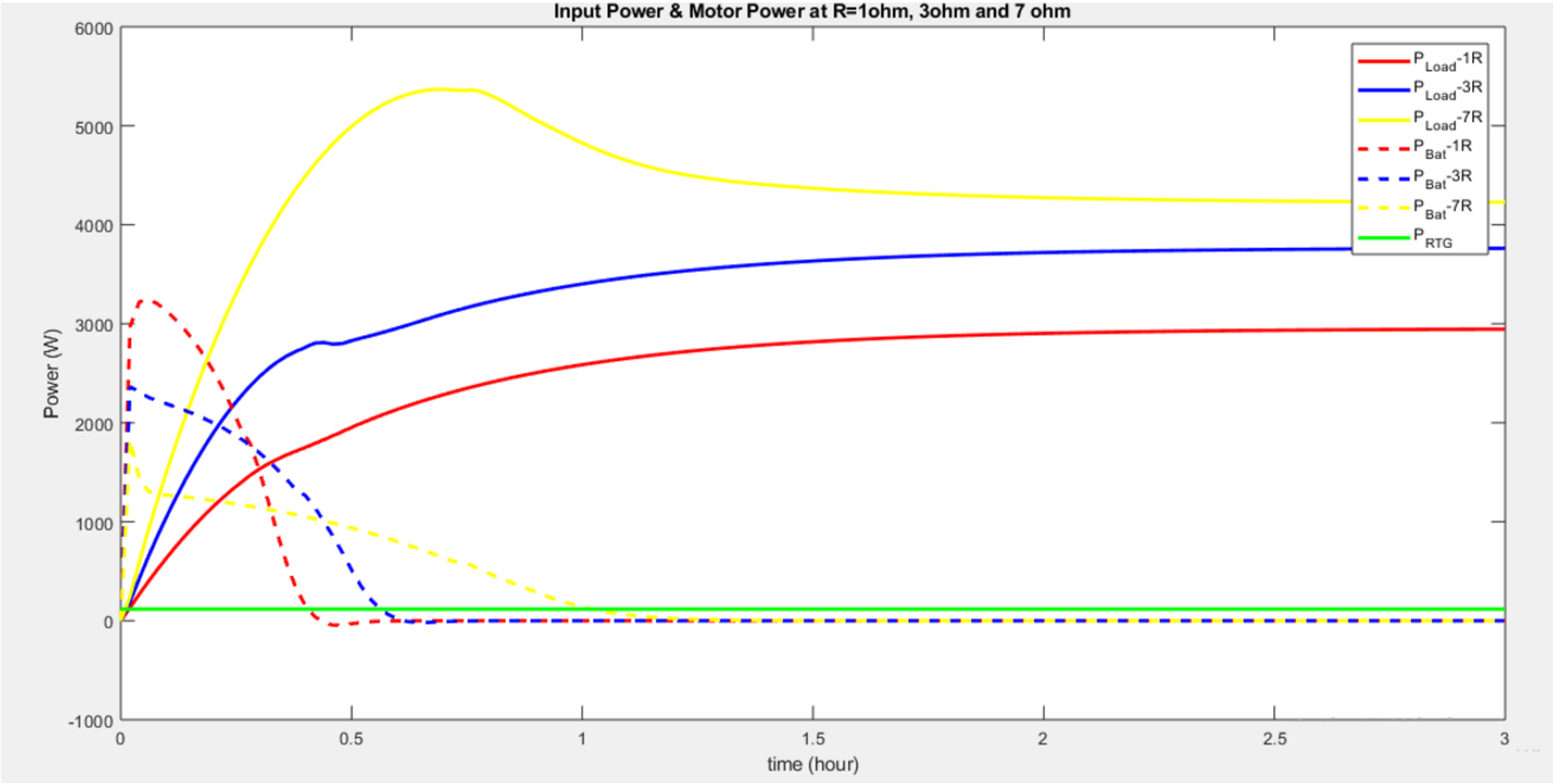

Figure 5. 33: Motor power and battery power when connected to load of different values

5.8.2 Mechanical performance of DC motor

The motor speed versus current plot in Figure 5.34 shows that the best performance is achieved by the motor attached to the 1 Ω resistor. In contrast, the motor connected at the 7 Ω resistor shows the poorest speed even though it has the highest amount of power. On the other hand, the torque of the motor gives a very different result from that of the speed, as it could be observed that the motor with the highest power (7 Ω) also exhibits higher torque. In contrast, the 1 Ω load that produced the highest speed has the lowest amount of torque (Figure 5.35).

Therefore, the load resistance may vary to find the right compromise between power, voltage, and current regarding how much torque or speed is needed for a particular application.

5.9 DC motor performance for charge-discharge state of hybrid battery

The Simulink model used will be similar to the one used in section 5.8.2, corresponding to the system monitored using a PI controller. The investigation would therefore consist of monitoring how well will the system voltage output and motor speed responds. This is to verify the system's efficiency in controlling voltage spikes and its ability to be implemented in different systems without many difficulties.

Figure 5.22 represents the Simulink model of the hybrid system with a PI controller incorporated. This PI controller compares the actual motor speed (divided by a max value 6), subtracted to a reference value of 1. The result is fed into the PI control, which then compares the controlled signal to a saw shapes signal. It should be noted that two PI control units have been created, one for charge and the other for discharge.

Furthermore, the charge model makes use of a K_P and K_i so that the charging behavior occurs faster and eliminates unnecessary overcharging. Meanwhile, the discharge PI controller does not have a K_i variable since the discharge is required to happen over a longer period.

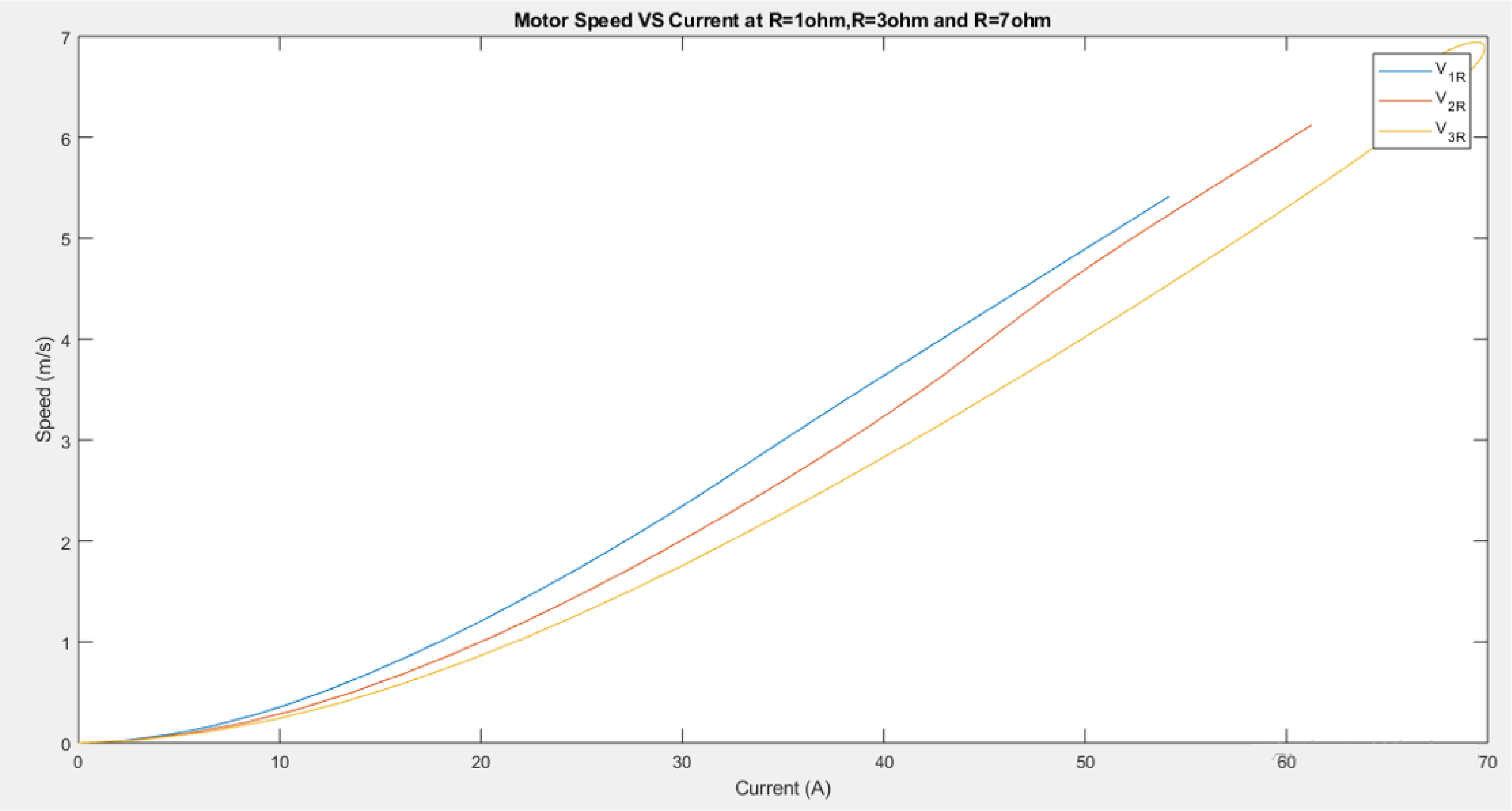

Figure 5. 34: Motor Speed vs. current at different load resistance

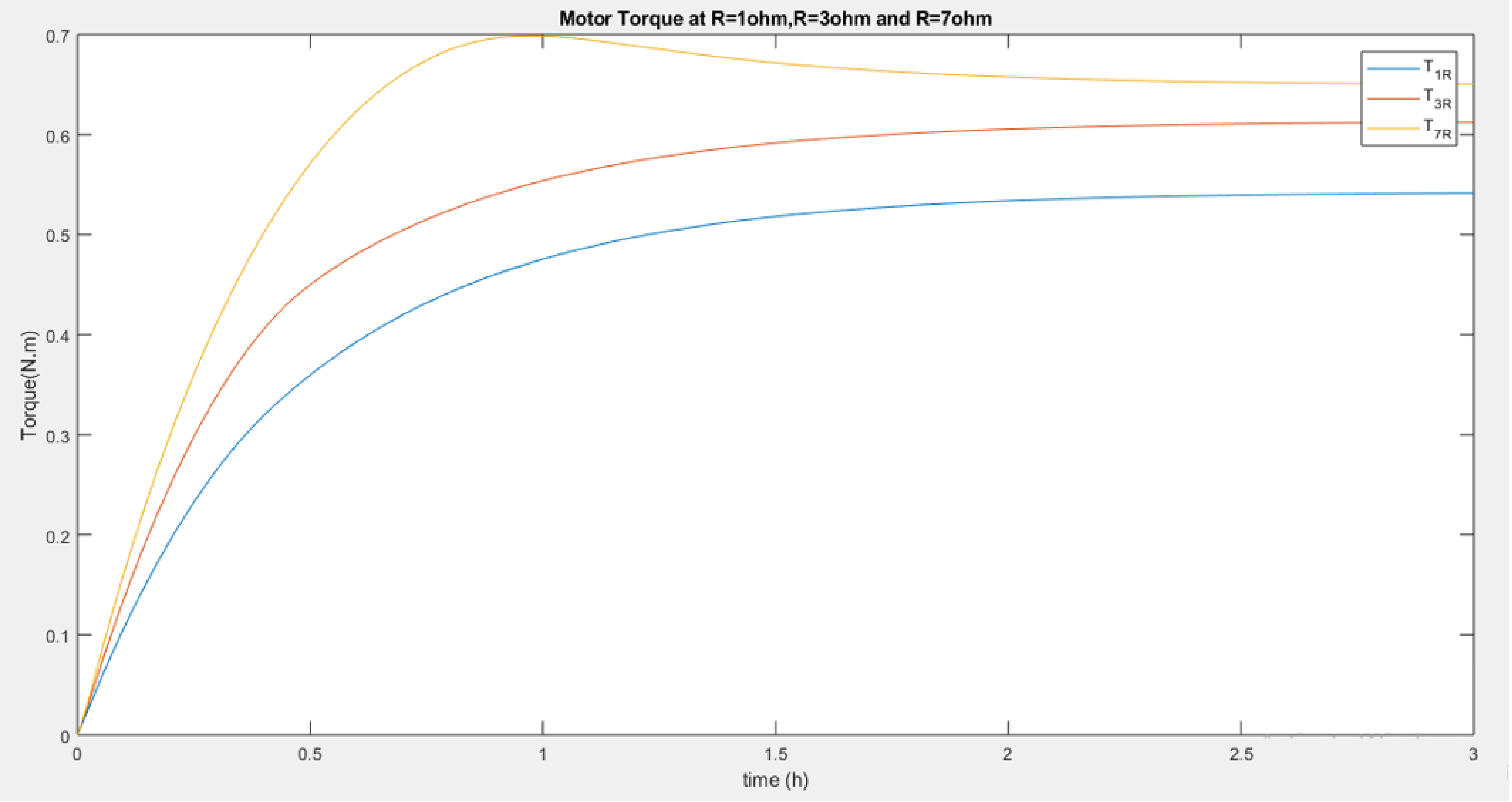

Figure 5. 35: Motor torques at different load resistance

5.10 Discussion of results

The plot of Figure 5.36 shows the battery charge-discharge cycle of the hybrid system incorporating the PI controller. Here we can see that the state of the charge period tends to increase after 2.5 hours, meaning the battery takes longer to charge and discharge, putting less strain on the battery because the system is about to stabilize. Thus, such behavior will, in the long term, affect the battery life in the long term.

The output voltage of the hybrid system decreases when the SoC is increasing, which means that the power from the RTG and load are used to recharge the battery. Once the battery is fully recovered, the system now uses the battery voltage in order to provide power to the load, increasing the load voltage up to 60 V. The battery voltage plot in green shows a varying voltage that charges over a period of 30 min and discharges after only 15 min. Thus, the discharge period occurs at a faster rate than the charge.

The current plot in Figure 5.37 shows a rather stable motor current regardless of the variable battery current, which characterizes the charge-discharge cycle of the battery. While the power plot in Figure 5.38 shows that the hybrid system power over during charge and discharge does not vary considerably. In other words, the motor will receive enough power to run its most basic needs during charge and receive excess power during discharge and critical periods.

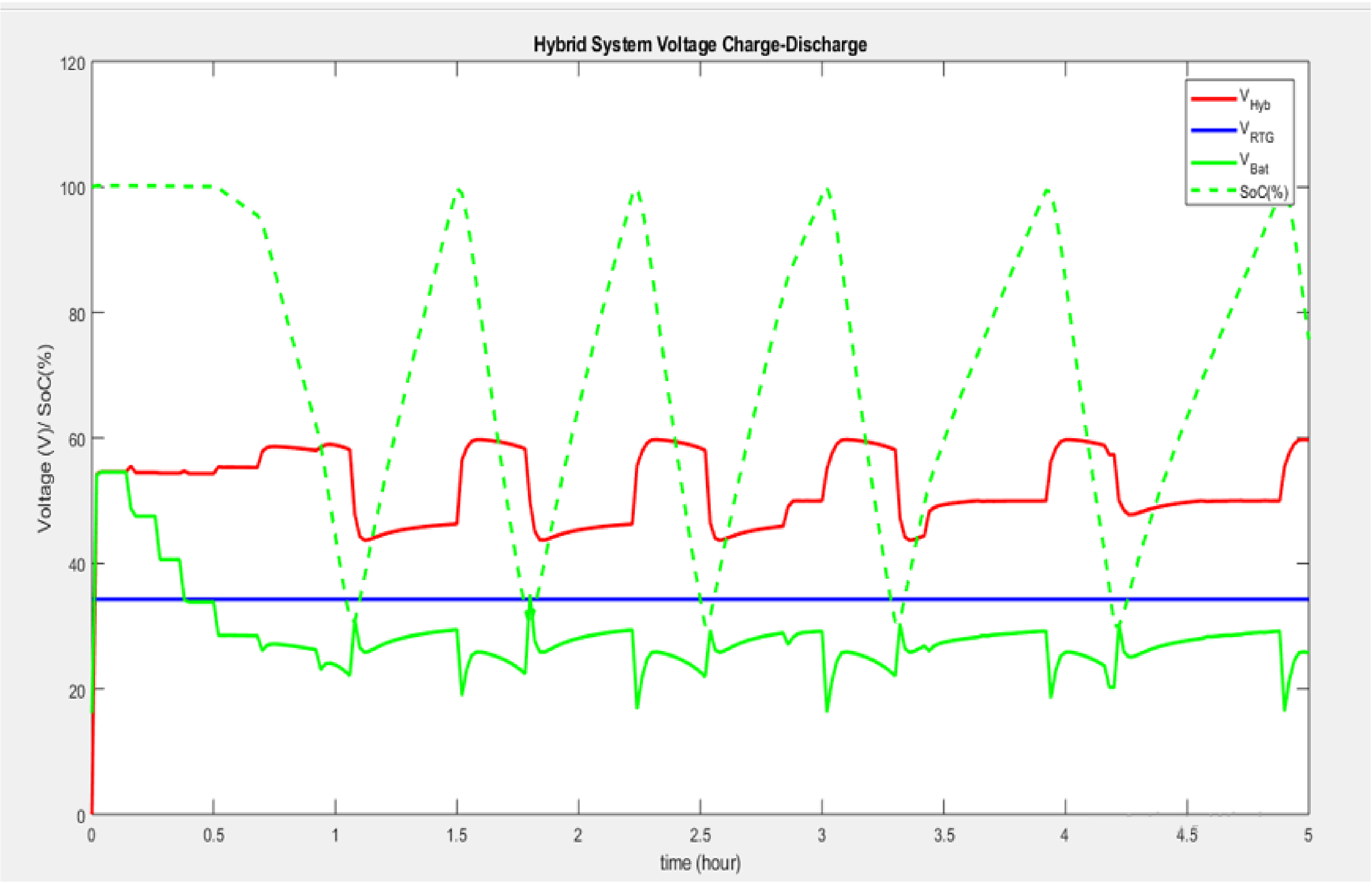

Figure 5. 36: Hybrid system (red) charge-discharge cycle incorporating the PI controller

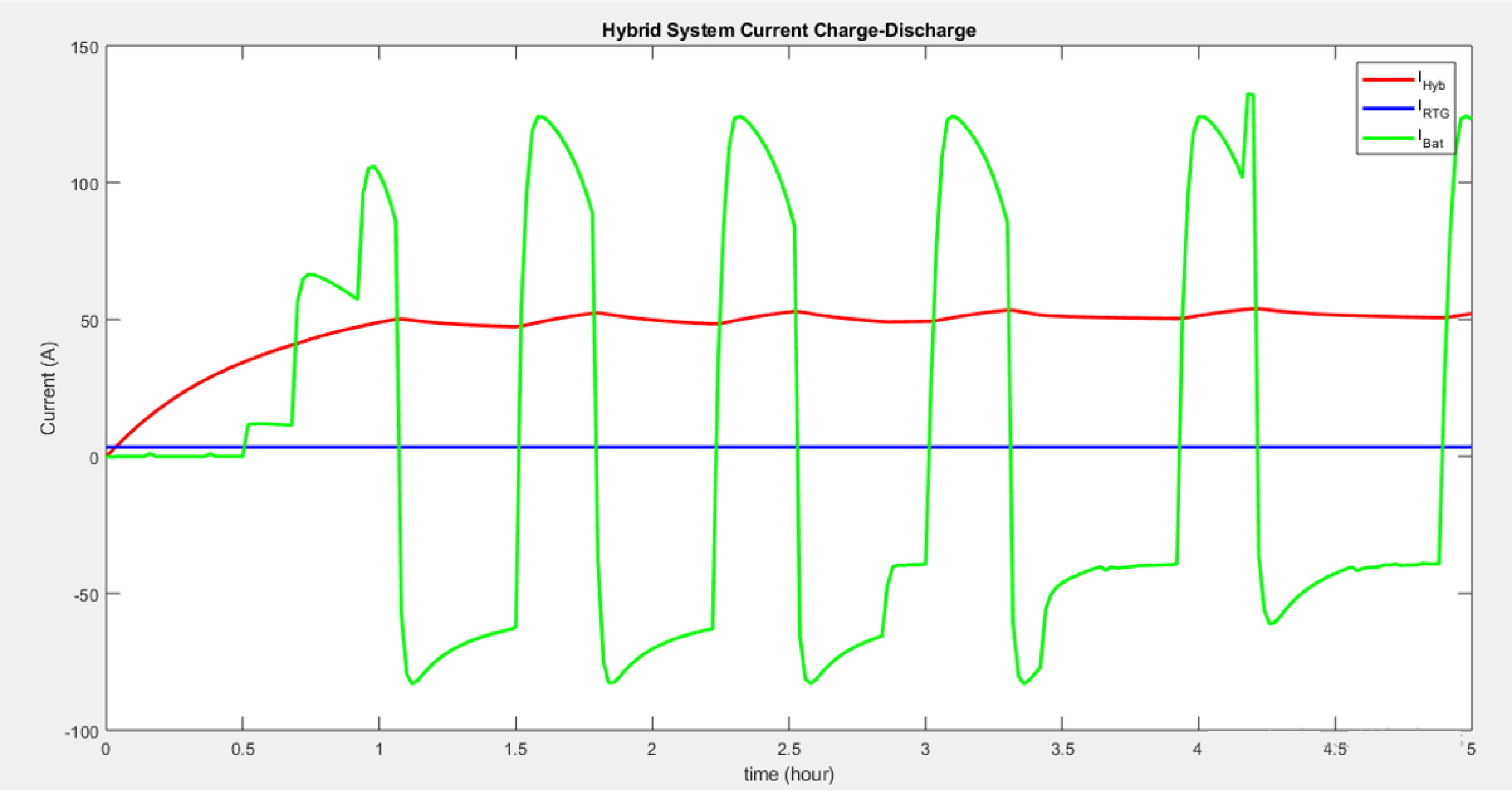

Figure 5. 37: Hybrid system current during charge-discharge cycle incorporating the PI controller

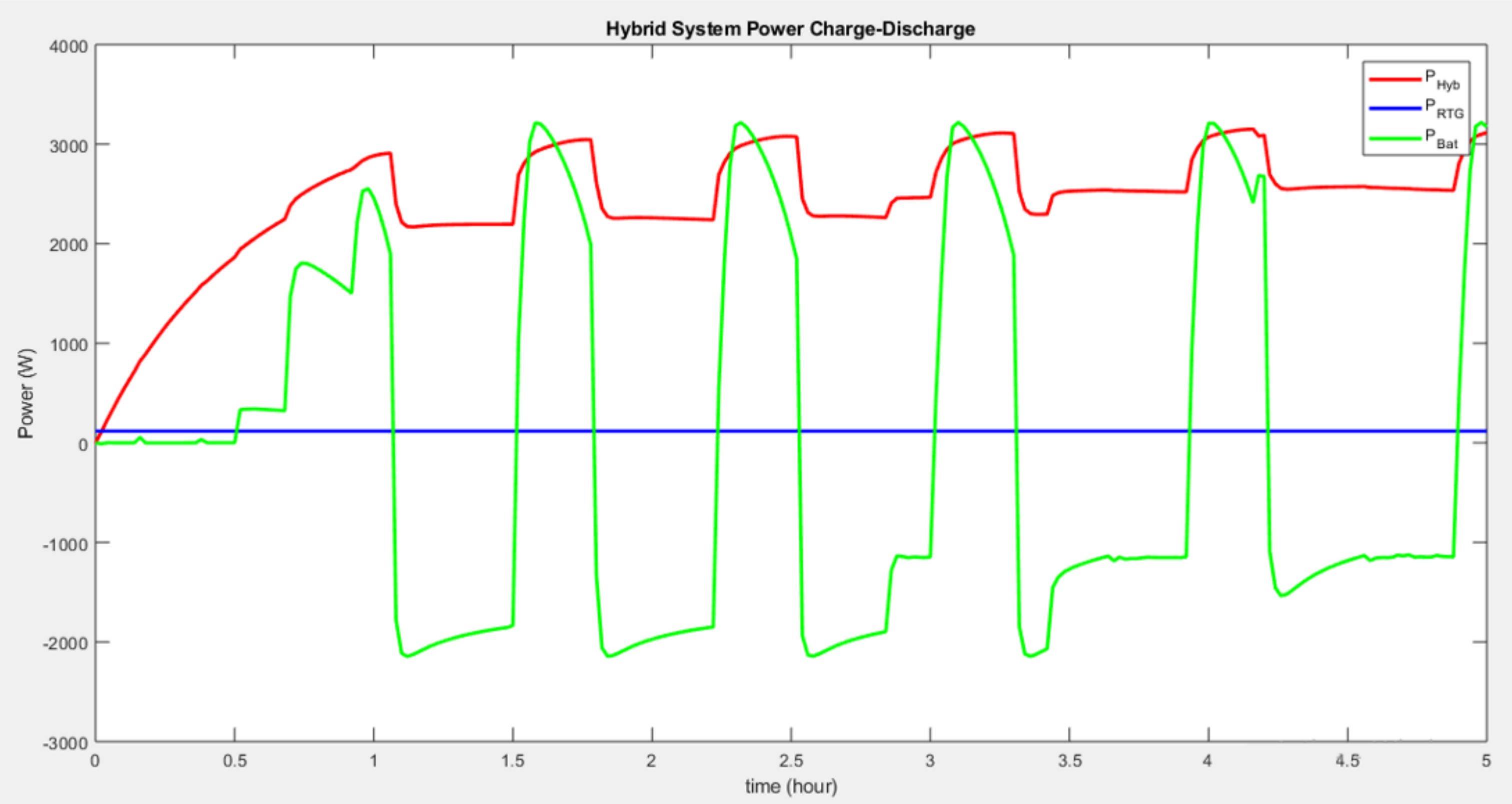

Figure 5. 38: Comparison of power charge and discharge

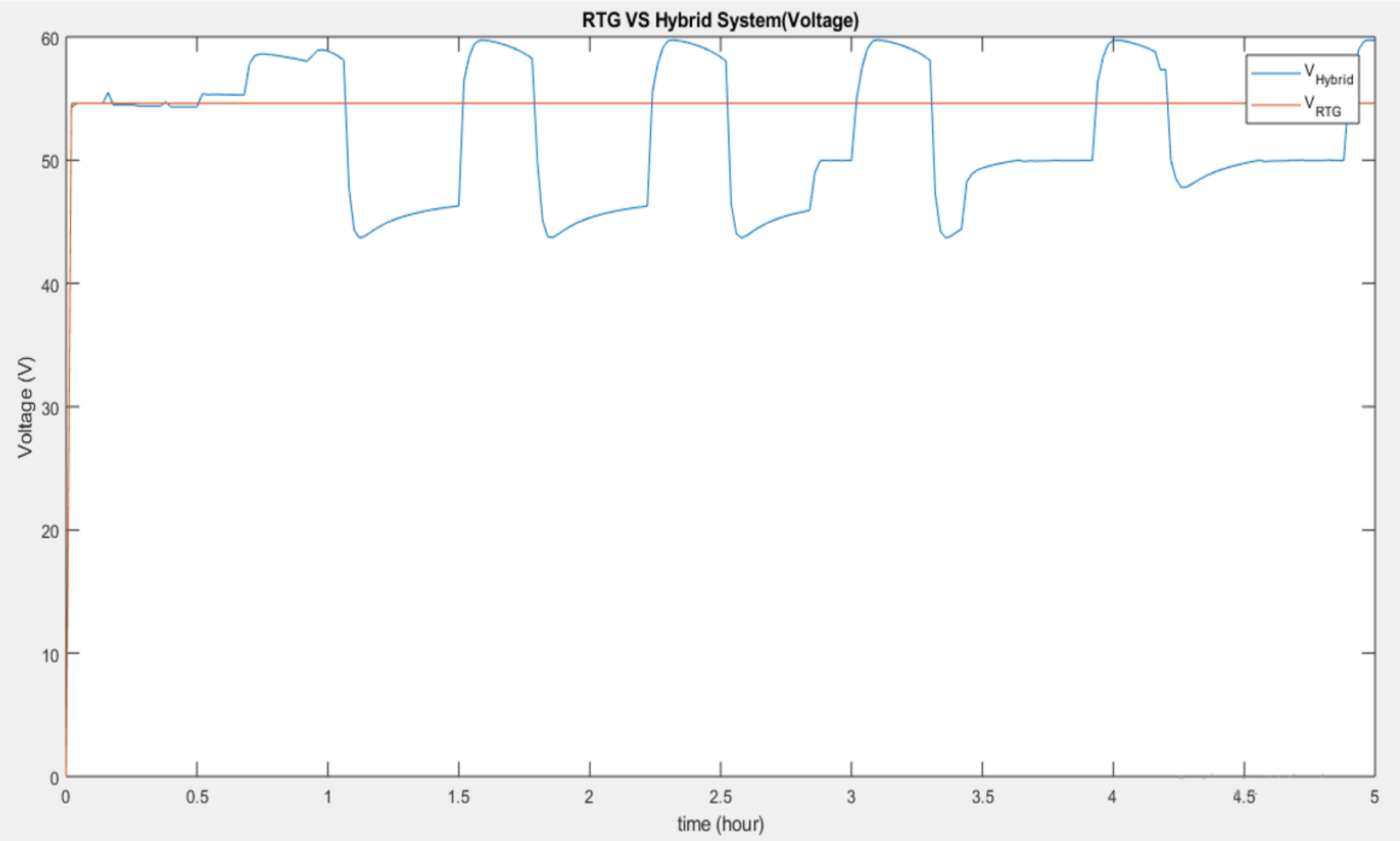

Figure 5. 39: Comparison of voltage: hybrid source vs. RTG source

A comparison of the voltage output from the hybrid system with PI control against a single source RTG system in Figure 5.39 shows that not only is the hybrid system capable of delivering more voltage during battery discharge, but it could also deliver voltage at a lesser frequency than the non-PI hybrid system which can eventually lead to less strain put within the battery.

The motor behavior shown in Figure 5.40 shows that the motor speed in a hybrid energy source system with PI control is very close to the behavior of a single energy source system. This behavior could be considered to be a satisfactory result since in the simulation condition, the motor is being powered by the battery at first and has to lower its fed power in order to recharge the battery.

Meanwhile, in real-life conditions, the system would rely on RTG power solely and only requires hybrid battery power for extreme conditions. Thus, these result shows how efficient a hybrid system would react.

This investigation has shown the importance of developing a viable and efficient battery management system that will be capable of controlling and monitoring the charge-discharge cycle of the battery. It is also important to note that even though the simulations were done under continuous charge and discharge, the hybrid system does not have to operate in such a way in real life. In other words, the application which makes use of the hybrid system might as well discharge the battery and rely on the RTG power before recharging again prior to a period of need for additional power.

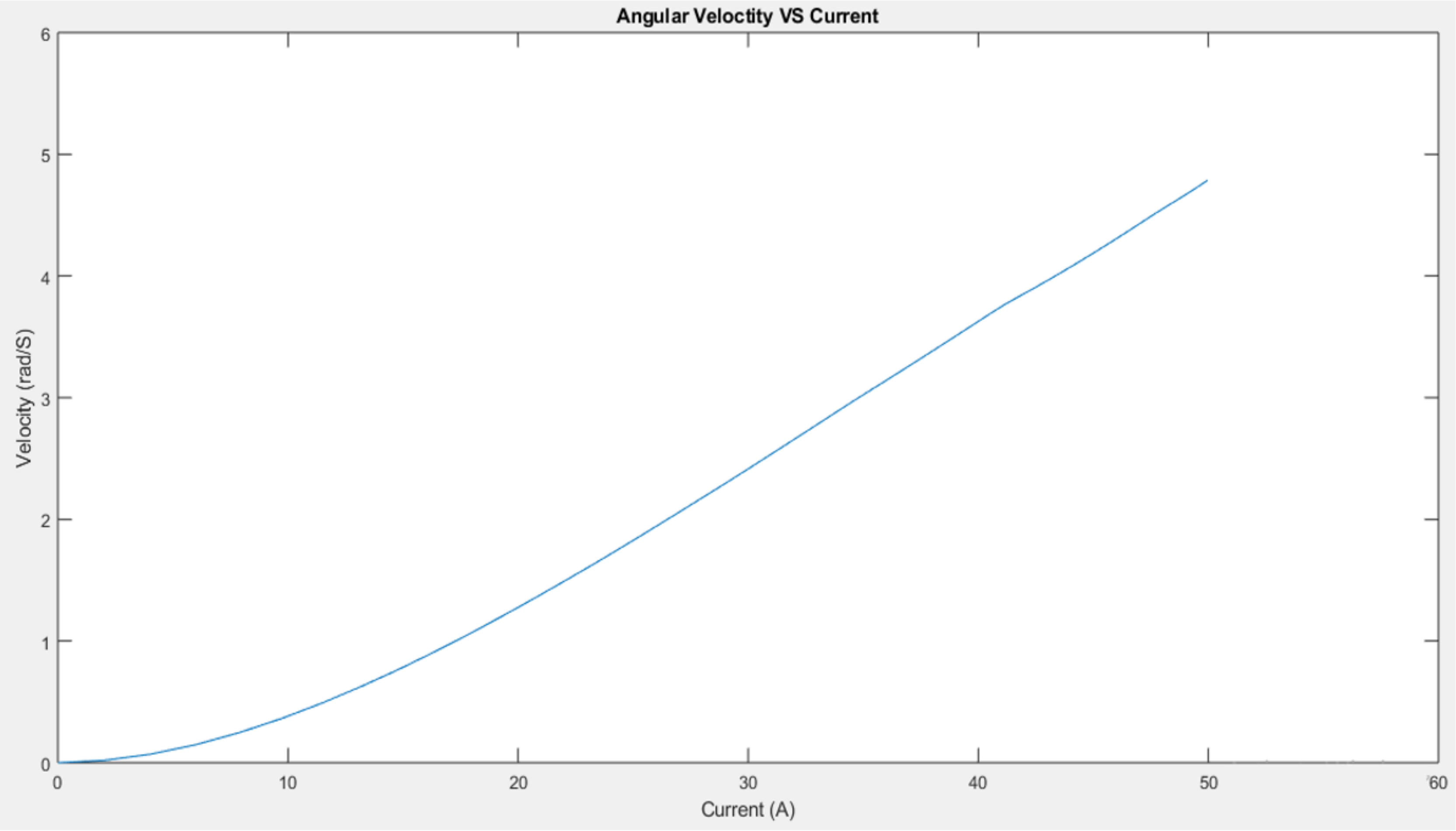

Figure 5. 40: Hybrid energy source speed vs. current

5.11 Effects of temperatures on battery

The performance of a battery is affected by the temperature (either low or high) under which they operate as it affects the internal chemical reaction. At low temperatures, ionic diffusion and migration from one electrode to the other can be difficult, causing side effects in the long-term whilst high-temperature operations might make the battery deliver better performance, with long-term side reactions such as corrosion and thermal run-away. The case study of Li-ion batteries that have been found to have operating temperatures ranging from 20°C and 60°C are considered in this section. Jaguemont & Jow (2018) established that a Li-ion battery will show signs of defect at a temperature under 10°C (Jaguemont et al., 2016). The low temperature also has effects on the SoC. It was found that the Soc of a Li-ion battery operating at 10°C decreased considerably by 23% in comparison with a battery operating at the ambient temperature of 20°C. The main source of this degradation is due to the electrolyte's property, which increases its viscosity and reduces the ionic conductivity. Consequently, raising the internal resistance to the migration of ions in the solution.

Low temperature resists the charge transfer, thereby adversely affecting the battery kinetics. Gao et al (2008) reported that the charge transfer resistance of a battery operating at 10°C is twice higher than the battery operating at the ambient temperature (Gao & Tang, 2008).

In addition, low temperature affects the battery electrodes through a phenomenon known as lithium plating (Petzl et al., 2015), which triggers the polarization of the anode, thereby creating residual lithium ions that get deposited on the surface of the electrodes with the overall effect reduction in the capacities of the battery (Gunawardhana et al., 2011).

On the other hand, high temperature due to heat generation yields improved performance. However, exposure of batteries to high temperatures over a long period of time will produce a negative impact. Indeed, heat generation is a very critical factor that needs to be understood.

5.11.1 Heat generation

Heat generation is associated with chemical reactions and charge transfer occurring during the charging and discharging of the battery (Xiao & Choe, 2013). The heat generation could be due to entropy changes or entropic heat, ohmic heating, or enthalpy changes. Entropy changes are generated during the reversible chemical reactions, while the ohmic heating process is due to resistance in the electrolyte and electrode, preventing the transportation of charges. Enthalpy change is due to an irreversible process in the cathodes primarily due to ion diffusion.

The entropy change in the electrodes is related to the change of the electrode potential with temperature $\frac{\mathrm{dE}}{\mathrm{dT}}$ varying with the SoC (Liu et al., 2017), while some heat generation in Li-ion batteries is due to ohmic, reversible, and irreversible heat (Fang et al., 2010). An expression of heat generation by Li-ion battery developed by Newman et al., 2003 is given by (Newman et al., 2003):

$$\mathrm{Q_{gen}} = (\mathrm{E_0(T)} - \mathrm{V_{batt}(T)})\,\mathrm{I} + \frac{\mathrm{dE}}{\mathrm{dT}}\mathrm{IT} \qquad (5.10)$$

The complexity of a battery operating at high temperatures creates the creation of an exothermic reaction within a poorly manufactured battery. Consequently, releasing more heat which in turn increases the battery internal temperature in an uncontrolled manner and could eventually lead to fire and/or explosion should the heat safety limit be exceeded. Even though the understanding of thermal runaway in Li-ion batteries is important to the design of thermal management systems, their study requires advanced laboratory techniques such as X-ray tomography (Finegan et al., 2015).

5.11.2 Thermal model and energy balance

This section deals with the equations and parameters used to model the thermal behavior of Li-ion batteries. It suffices to state that, indeed, the different chemical reactions release heat that depends on the temperature of the battery. A first approximation of battery temperature is uniform throughout the cell at T(t). Thus, the conservation of energy allows determining the temperature changes with time using the following lumped parameters equation (Murashko et al., 2013).

$$\mathrm{mC_p}\frac{\partial \mathrm{T}}{\partial \mathrm{t}} = -\mathrm{q_n} + \mathrm{Q_{gen}} = -\mathrm{hA_s}(\mathrm{T_{surf}} - \mathrm{T_{amb}}) + \mathrm{Q_{gen}} \qquad (5.11)$$

where:

- C_P is the thermal capacitance or heat capacity
- m is the mass of the battery cell
- h is the heat transfer coefficient
- A_s is the surface area of the battery
- T_{surf} is the surface temperature
- T_{amb} is the ambient temperature

From Equation 5.11, it could be deduced that:

$$\frac{\partial T}{\partial t} = -\frac{hA_s(T_{surf}-T_{amb})}{mC_p} + \frac{Q_{gen}}{mC_p}$$

$$=> \frac{\partial T}{\partial t} = -\frac{(T_{surf}-T_{amb})}{\frac{mC_p}{hA_s}} + \frac{Q_{gen}\frac{1}{hA_s}}{\frac{mC_p}{hA_s}} \qquad (5.12)$$

The lumped capacitance method defines the convection thermal resistance R_{th} as:

$$R_{th} = \frac{1}{hA_s} \qquad (5.13)$$

While the thermal time constant t_c is defined as:

$$t_c = \frac{mC_p}{hA_s} \qquad (5.14)$$

Thus, we have:

$$\frac{\partial T}{\partial t} = -\frac{(T_{surf}-T_{amb})}{t_c} + \frac{Q_{gen}R_{th}}{t_c}$$

$$=> t_c\,\frac{\partial T}{\partial t} = -T_{surf} + T_{amb} + Q_{gen}R_{th} \qquad (5.15)$$

Using Laplace transform on Equation 15, we have:

$$L[t_c\frac{\partial T}{\partial t}] = L[-T_{surf} + T_{amb} + Q_{gen}R_{th}] \qquad (5.16)$$

Since $\frac{\partial T}{\partial t} = \frac{\partial T_{surf}}{\partial t}$, Equation 16 could be re-arranged as:

$$ST(S) \times t_c \;= -T_{surf}(S) + T_{amb} + Q_{gen}R_{th} \qquad (5.17)$$

$$=> ST(S) \times t_c + T(S) = T_a + Q_{gen}R_{th}$$

$$=> T(S)[S \times t_c + 1] \;= T_a + Q_{gen}R_{th}$$

$$=> T(S) = \frac{Q_{gen}R_{th}+T_a}{S\times t_c+1} \qquad (5.18)$$

Invoking the Inverse Laplace transform on Equation 5.18, the equation of the cell or internal temperature, T, at any given time t could be expressed as:

$$T(t) = L^{-1}\left[\frac{Q_{gen}R_{th}+T_a}{St_c+1}\right] \tag{5.19}$$

Using the data in Table 5.6, the parameters R_{th}, t_c, C_P and h in a single cell can be determined.

From Table 5.5 we have:

- Mass of a battery cell, m=1.27 kg
- The heat capacity of the cell, $C_p = \frac{\text{Energy density}\left(\frac{Wh}{Kg}\right)}{\text{Temperature(K)}} = \frac{153\ (\text{at } 20^0C)}{293\ (\text{at } 20^0C)} = 0.522\,\frac{Wh}{Kg.K}$
- The area A_S of the battery (using manufacturer dimension) is given by:

  $A_S = (165.5\times106.7)\ mm^2 = 0.0177\ m^2$
- The heat transfer coefficient *h* (estimated value),

$$h = \frac{\text{power(from previous simulation)}}{\text{battery area } \times \text{temperature}} = \frac{35\ W}{293\ K \times 0.283\ m^2} = 0.422\,\frac{W}{m^2.K}$$

Therefore, the convection thermal resistance of the battery is obtained as:

$$R_{th} = \frac{1}{h \times A_s} = \frac{1}{0.0177 \times 0.422}$$

$$=> R_{th} = 133.88\ (K.W^{-1})$$

Consequently, the thermal time constant is obtained as:

$$t_c = \frac{m \times C_p}{h \times A_s} = \frac{1.27 \times 0.522}{0.422 \times 0.0177}$$

$$=> t_c = 88.754\ h$$

Table 5. 5: Specification for Li-ion battery LP33450

Specifications	
Part Number	LP33450
Nominal Cell Weight	1.27 kg
Dimensions	See details on back
Voltage Range	3.0 to 4.1V
Nominal Voltage	3.6V
Nominal Capacity	43Ah at C/5 at 20ºC (68ºF)
Energy Density	378 Wh/L
Specific Energy	153 Wh/kg
Discharge Rates	Max constant current 200A
	Max pulse current (<1 sec) 400A
Nominal Cell Impedance	2mΩ at 20ºC (68ºF)
Cycle Life (80% capacity measured at 0.5C discharge current at 20ºC (68ºF))	>2000 at 100% DOD
Standard Charging Method	Constant current 21.5A (0.5C) to 4.1V
	Constant voltage 4.1V to 0.86A (C/50)
Operating Temperature	-20 to 60ºC (-4 to 140ºF)
Storage Temperature	-40 to 60ºC (-40 to 140ºF)

Battery cell parameters such as kinetic rate constants and transport properties (resistance, viscosity, etc.) depend on temperature T. Consequently, most of the electrochemical properties controlling the battery performance can be described by the parameter, $K_{A,}$ referred to as the rate constant (specific reaction rate). This parameter depends on the temperature. According to Fogler (2006), the Arrhenius equation is given by (Fogler, 2006)`:

$$K_A(T) = Ae^{-\frac{E}{RT}} \tag{5.20}$$

Where:

- A is the frequency factor or pre-exponential factor
- E is the activation energy J per mol or cal per mol
- R is the universal gas constant = 8.314 J per mol.
- T is the absolute temperature K

Equation 5.20 could be re-written as:

$$\ln\,[K_A(T)] = \ln\,[Ae^{-\frac{E}{RT}}]$$

$$=> \ln\,[K_A(T)] = \ln[A] + \ln\,[e^{-\frac{E}{RT}}]$$

$$=> \ln\,[K_A(T)] = \ln[A] - \frac{E}{RT}$$

$$=> \ln\,[\mathrm{K_A(T)}] = -\frac{\mathrm{E}}{\mathrm{R}}\left(\frac{1}{\mathrm{T}}\right) + \ln[\mathrm{A}] \qquad (5.21)$$

A linear equation is generally expressed as:

$$\mathrm{Y = mX + B} \qquad (5.22)$$

Comparing equations 5.21 and 5.22, we could have:

$\mathrm{Y} = \ln[\mathrm{K_A(T)}]$, $\mathrm{m} = -\frac{\mathrm{E}}{\mathrm{R}}$, $\mathrm{X} = \left(\frac{1}{\mathrm{T}}\right)$ and $\mathrm{B} = \ln[\mathrm{A}]$

$$\mathrm{m} = -\frac{\mathrm{E}}{\mathrm{R}} = \frac{\ln\,(\mathrm{K_2}) - \ln\,(\mathrm{K_1})}{\frac{1}{\mathrm{T_2}} - \frac{1}{\mathrm{T_1}}}$$

Therefore,

$$\mathrm{Ln}(\mathrm{K_2}) = -\frac{\mathrm{E}}{\mathrm{R}}\left(\frac{1}{\mathrm{T_2}} - \frac{1}{\mathrm{T_1}}\right) + \ln\,(\mathrm{K_1})$$

$$=> \mathrm{K_2} = \mathrm{e}^{\left[-\frac{\mathrm{E}}{\mathrm{R}}\left(\frac{1}{\mathrm{T_2}} - \frac{1}{\mathrm{T_1}}\right) + \ln(\mathrm{K_1})\right]}$$

$$=> \mathrm{K_2} = \mathrm{e}^{\ln(\mathrm{K_1})}\,\mathrm{e}^{\left[-\frac{\mathrm{E}}{\mathrm{R}}(\mathrm{T_2} - \mathrm{T_1})\right]}$$

$$=> \mathrm{K_2} = \mathrm{K_1}\mathrm{e}^{\left[-\frac{\mathrm{E}}{\mathrm{R}}\left(\frac{1}{\mathrm{T_2}} - \frac{1}{\mathrm{T_1}}\right)\right]} \qquad (5.23)$$

5.11.3 Modeling

Tremblay et al (2009) established a set of equations describing the behavior of Li-ion batteries, as represented below (Tremblay & Dessaint, 2009). Equation 5.24 and Equation 5.25, respectively, indicate the behavior of batteries during discharge and charge conditions, with great accuracies under different C-rate.

$$\mathrm{V_{batt}} = \mathrm{E_0} - \mathrm{K}\frac{\mathrm{Q}}{\mathrm{Q-it}}(\mathrm{it} + \mathrm{i^*}) + \mathrm{A}e^{-Bit} \qquad (5.24)$$

$$\mathrm{V_{batt}} = \mathrm{E_0} - \mathrm{K}\frac{\mathrm{Q}}{\mathrm{it-0.1Q}}(\mathrm{i^*}) - \mathrm{K}\frac{\mathrm{Q}}{\mathrm{Q-it}}(\mathrm{it}) + \mathrm{A}e^{-Bit} \qquad (5.25)$$

Where,

- $\mathrm{V_{batt}}$ represents the battery voltage expressed in Volt
- $\mathrm{E_0}$ represents the constant voltage expressed in Volt
- K represents the polarization resistance expressed in Ohm
- Q represents the maximum battery capacity in Ampere-hour
- i represents the battery current in Ampere
- it represents the extracted battery capacity in Ampere-hour
- $\mathrm{i^*}$ is the low-frequency current dynamics in Ampere

- A is the exponential voltage in Volt
- B is the exponential capacity in Ampere per hour

The parameters of equations 5.26 and 5.27, especially polarisation resistance K and internal resistance R, depend on the temperature of the cell or internal temperature. These two parameters behave at a reaction rate that can be described using the Arrhenius equation. The battery capacity Q and voltage E_0 have a linear relationship with temperature and thus do not need to be incorporated in the Arrhenius equation.

Masih-Tehrani et al., (2017) proposed a modified set of equations that consider the battery's temperature by making each parameter temperature dependent (Masih-Tehrani & Yahyaei, 2017). Therefore, equations 24 and 25 can be expressed respectively as equations 26 and 27:

$$V_{batt}(T) = E_0(T) - K(T)\frac{Q(T_a)}{Q(-it}(it + i^*) + Ae^{-Bit} - R(T). \quad (5.26)$$

$$V_{batt}(T) = E_0(T) - K(T)\frac{Q(T_a)}{it - 0.1Q(T_a)}(i^*) - K(T)\frac{Q(T_a)}{Q(T_a) - it}(it) + Ae^{-Bit} - R(T).i \quad (5.27)$$

Where:

- R is the internal resistance (Ω)
- $E_0(T) = E_0^{ref} + \frac{\partial E}{\partial T}(T - T_{ref})$
- $Q(T_a) = Q_{Ta} + \frac{\partial Q}{\partial T}(T_a - T_{ref})$
- $K(T) = K_{Tref} \times e^{\left[\alpha\left(\frac{1}{T} - \frac{1}{T_{ref}}\right)\right]}$
- $R(T) = R_{Tref} \times e^{\left[\beta\left(\frac{1}{T} - \frac{1}{T_{ref}}\right)\right]}$
- T_{ref} is the nominal ambient temperature (K)
- T is the cell temperature or internal temperature (K)
- T_a is the ambient temperature (K)
- $\frac{E}{T}$ is the reversible voltage temperature coefficient (V/K)
- $\frac{\Delta Q}{\Delta T}$ is the Maximum capacity temperature coefficient (Ah/K)
- α is the Arrhenius rate constant for polarization resistance
- β is the Arrhenius rate constant for internal resistance

5.11.4 Design and simulation

MSL mission space battery LP 33450 (3.6V, 43Ah) is utilized, and the simulation is performed using the Matlab/Simulink environment. The values of relevant parameters are extracted from Table 5.5 and the experimental data in Figure 5.41.

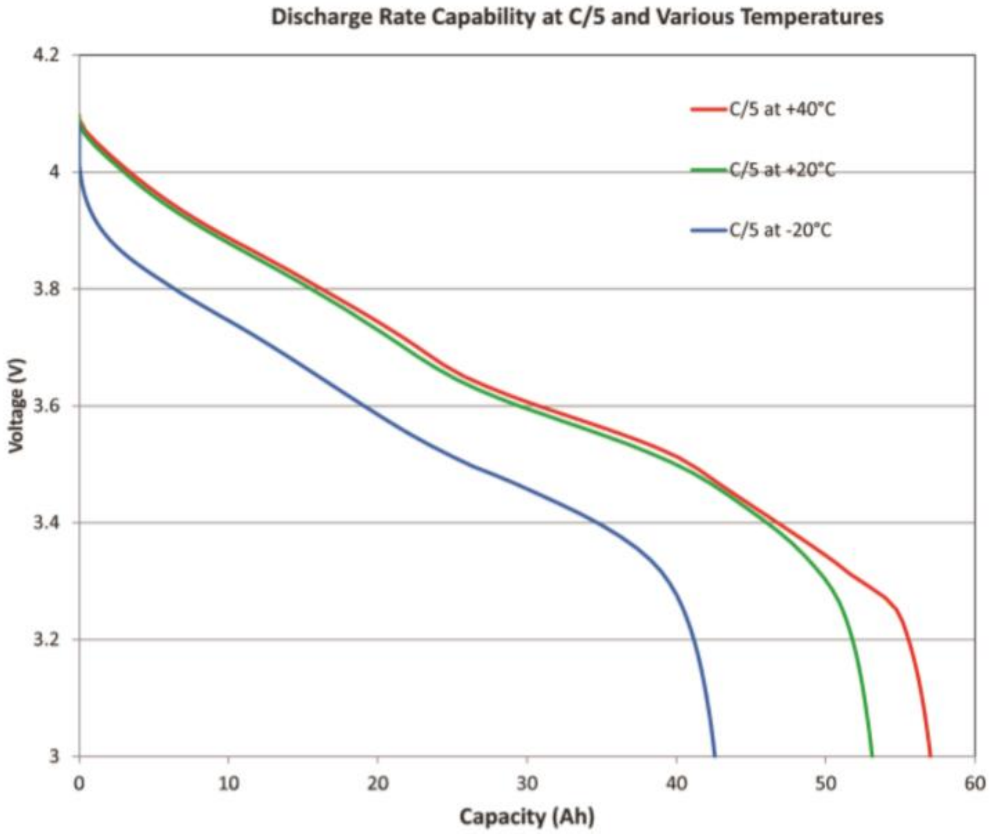

Figure 5. 41: Experimental data of LP-33450 space battery (Eaglepicher Technologies, 2019)

- **Determination of the battery parameters at different temperatures**

Tremblay et al., (2009) established that polarization resistance can be expressed as (Tremblay & Dessaint, 2009):

$$\mathrm{K} = \frac{\left(\mathrm{E_{full}} - \mathrm{E_{nom}} + \mathrm{A}\left(e^{(-\mathrm{B.Q_{nom}})-1} - 1\right)\right) \times (\mathrm{Q} - \mathrm{Q_{nom}})}{\mathrm{Q_{nom}} \times \mathrm{i}} \tag{5.28}$$

Where the actual value of voltage in a fully charged battery, $\mathrm{E_{full}}$ is given by:

$$\mathrm{E_{full}} = \mathrm{E_0} - \mathrm{R.i} + \mathrm{A}$$

$$=> \mathrm{R} = \frac{\mathrm{E_0} - \mathrm{E_{full}} + \mathrm{A}}{\mathrm{i}} \tag{5.29}$$

- **At the temperature of $T_1 = -20^oC$**

  From the manufacturer datasheet and experimental data, the following values could be extracted:

  $A = E_{full} - E_{exp} = 4 - 3.77 = 0.23V$
  $E_0 = 3.82$ V
  Q = 42.5 Ah
  $V_{exp} = 3.55$ V
  $Q_{exp} = 9$ Ah
  $B = \frac{3}{9.85} = 0.305$ Ah^{-1}
  $V_{nom} = 3.54$ V
  $Q_{nom} = 25.6$ Ah

  Therefore, the polarization resistance is obtained as:

$$K_1 = \frac{\left(4 - 3.77 + 0.23\left(e^{(-0.305\times25.6)} - 1\right)\right) \times (42.5 - 25.6)}{25.6 \times 8.6}$$
$$= 0.0161\Omega$$

  While the internal resistance is obtained as:

$$R_1 = \frac{E_0 - E_{full} + A}{i} = \frac{3.82 - 4 + 0.23}{8.6}$$
$$= 0.01\ \Omega$$

- **At temperature of $T_2 = 20^oC$**

  From the manufacturer datasheet and experimental data, the following values could be extracted:
  $A = E_{full} - E_{exp} = 4.1 - 3.88 = 0.22$ V
  $E_0 = 3.89$ V
  Q = 52.5 Ah
  $V_{exp} = 3.88$ V
  $Q_{exp} = 10.2$ Ah
  $B = \frac{3}{10.2} = 0.294$ Ah^{-1}
  $V_{nom} = 3.6$ V
  $Q_{nom} = 29.7$ Ah

Therefore, the polarization resistance is obtained as:

$$\mathrm{K_2} = \frac{\left(4.1 - 3.6 + 0.22(e^{(-0.294\times 29.7)} \ - 1)\right) \times (52.5 - 29.7)}{29.7 \times 8.6}$$

$$= 0.0249\ \Omega$$

While the internal resistance is obtained as:

$$\mathrm{R_2} = \frac{\mathrm{E_0 - E_{full} + A}}{\mathrm{i}} = \frac{3.89 - 4.1 + 0.22}{8.6}$$

$$= 0.002\ \Omega$$

- **At temperature of T_3 = 40°C**

From the manufacturer datasheet and experimental data, the following values could be extracted:

$A = E_{full} - E_{exp} = 4.1 - 3.89 = 0.21$ V

$E_0 = 3.9$ V

Q = 58 Ah

$V_{exp} = 3.89$ V

$Q_{exp} = 9.7$ Ah

$B = \frac{3}{9.7} = 0.309\ \mathrm{Ah^{-1}}$

$V_{nom} = 3.64$ V

$Q_{nom} = 27.5$ Ah

Therefore, the polarisation resistance is obtained as:

$$\mathrm{K_3} = \frac{\left(4.1 - 3.64 + 0.21 \ \ (e^{(-0.309\times 27.5)} \ - 1)\right) \times (58 - 27.5)}{27.5 \times 8.6}$$

$$= 0.0322\ \Omega$$

While the internal resistance is obtained as:

$$\mathrm{R_3} = \frac{\mathrm{E_0 - E_{full} + A}}{\mathrm{i}} = \frac{3.9 - 4.1 + 0.21}{8.6}$$

$$= 0.00116\ \Omega$$

From the above calculations, it could be seen that the polarization resistance K increases with temperature, and this is due to the resistance to charge transfer due to irreversible and reversible processes. On the other hand, the battery's internal resistance tends to be higher at lower temperatures, which could be attributed to physical factors like an increase in the electrolyte viscosity and lack of ions distributions between electrodes.

- **Arrhenius rate constant for polarization α using values of K.**

The modified Arrhenius, $\ln\left[\mathrm{K_A(T)}\right] = -\frac{\mathrm{E}}{\mathrm{R}}\left(\frac{1}{\mathrm{T}}\right) + \ln[\mathrm{A}]$ could be given in the form Y= αX + B, in which α is the Arrhenius rate constant for polarization.

Making use of the values obtained in the previous section, as given in Table 5.6, the relationship between K and T using MS Excel is shown in Figure 5.42.

Table 5. 6: Relationship between polarization resistance and temperature

	K(Ω)	ln(K)	1/T (K^{-1})
T1 = 253K (−20°C)	0,0161	−4,12894	0,003953
T2 = 293K (20°C)	0,0214	−3,69289	0,003413
T3 = 313K (40°C)	0,0322	−3,43579	0,003195

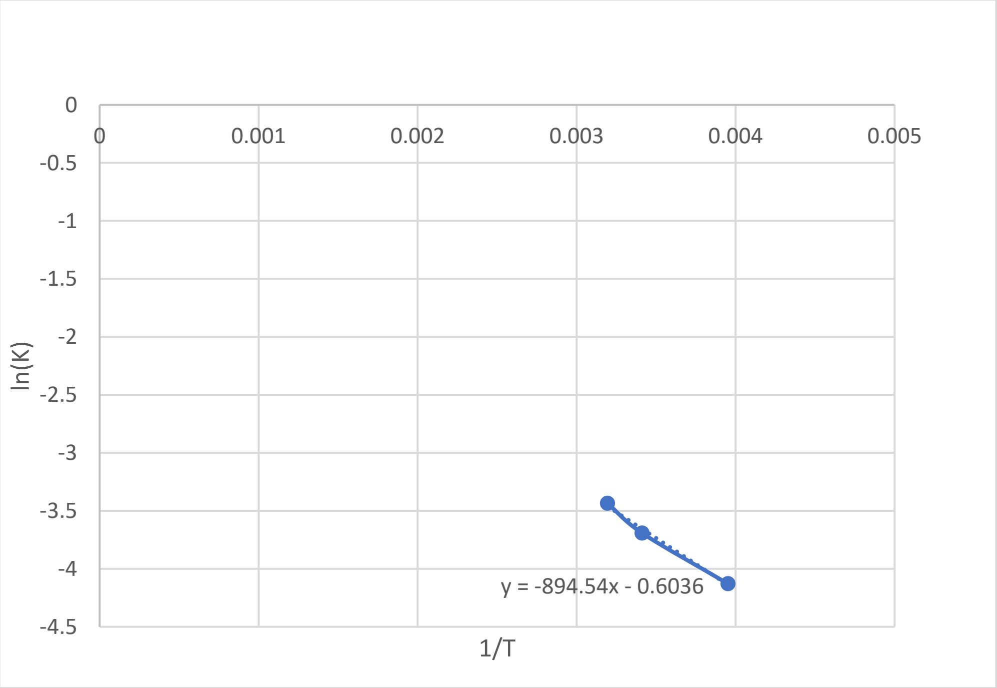

Figure 5. 42: Variation of the polarization resistance with temperature

From Figure 5.42, we have an equation in the form of:

$$\mathrm{Y} = -894.54\mathrm{X} - 0.6036 = \alpha\mathrm{X} + \mathrm{B} \tag{5.30}$$

Therefore, $\alpha = -\frac{\mathrm{E}}{\mathrm{R}} = -894.54$

We also have ln (A) = B = -0.6036 => A = 0.547

Consequently, the Arrhenius equation of polarization resistance with respect to temperature is:

$$\mathrm{K(T)} = 0.547 \times \mathrm{e}^{-894.54\left(\frac{1}{\mathrm{T}}\right)} \tag{5.31}$$

- **Arrhenius rate constant for internal resistance β using values of R.**

Like the polarization resistance K, the internal resistance R also depends on temperature, and its variable can also be found using the Arrhenius equation. The Arrhenius equation with relation to the internal resistance is of the form:

$\ln\,[\mathrm{R_A(T)}] = -\frac{\mathrm{E}}{\mathrm{R}}\left(\frac{1}{\mathrm{T}}\right) + \ln[\mathrm{A}]$ which could be written in the form Y= βX + B, in which β is the Arrhenius rate constant for internal resistance.

Making use of the values obtained in the previous section, as given in Table 5.7, the relationship between R and T using MS Excel is shown in Figure 5.43.

Table 5. 7: Relationship between internal resistance and temperature

	R(Ω)	ln(R)	1/T (K^{-1})
T1 = 253K (–20ºC)	0,010	-4,60517	0,003953
T2 = 293K (20ºC)	0,002	-6,21461	0,003413
T3 = 313K (40ºC)	0,00116	-6,75934	0,003195

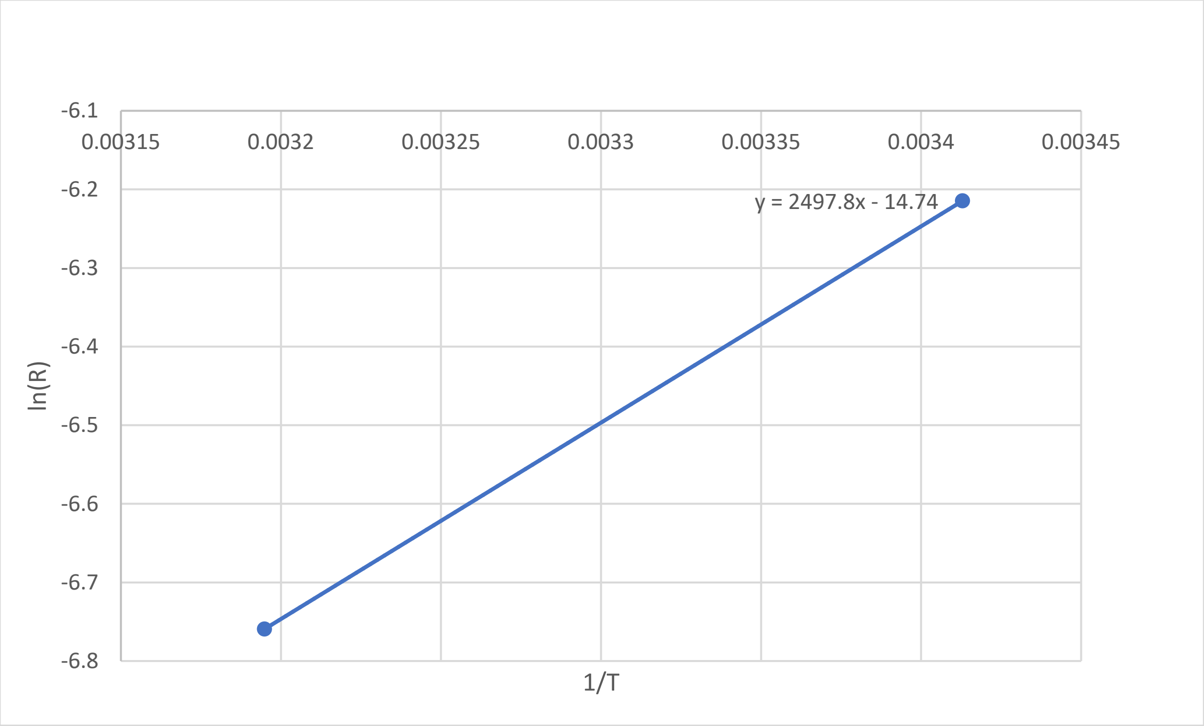

Figure 5. 43: Relationship between the internal resistance and temperature

Following the graph (Figure 5.44), the equation describing the relationship between internal resistance R and the cell temperature T is expressed as:

$$\mathrm{Y} = 2497.8\mathrm{X} - 14.74 = \beta\mathrm{X} + \mathrm{C} \qquad (5.32)$$

Therefore $\beta = -\frac{\mathrm{E}}{\mathrm{R}} = 2497.8$

We also have ln(A) = C = -14.74 => A=3.967×10^{-7}

Consequently, the Arrhenius equation of internal resistance with respect to temperature is:

$$\mathrm{R(T)} = 3.967 \times 10^{-7} \times e^{2497.8\left(\frac{1}{T}\right)} \qquad (5.33)$$

- **Reversible voltage temperature coefficient $\frac{\Delta \mathrm{E}}{\Delta \mathrm{T}}$ (V/K)**

In contrast to α and β, the reversible voltage temperature coefficient is a parameter independent of the chemistry and the chemical reactions. Consequently, it does not require the use of the Arrhenius equation. The trend of constant voltage in relation to temperature is given in Table 5.8.

Table 5. 8: Relationship between constant voltage and temperature

T	E_0
T1 = 253K(−20°C)	3,66
T2 = 293K (20°C)	3,89
T3 = 313K (40°C)	3,9

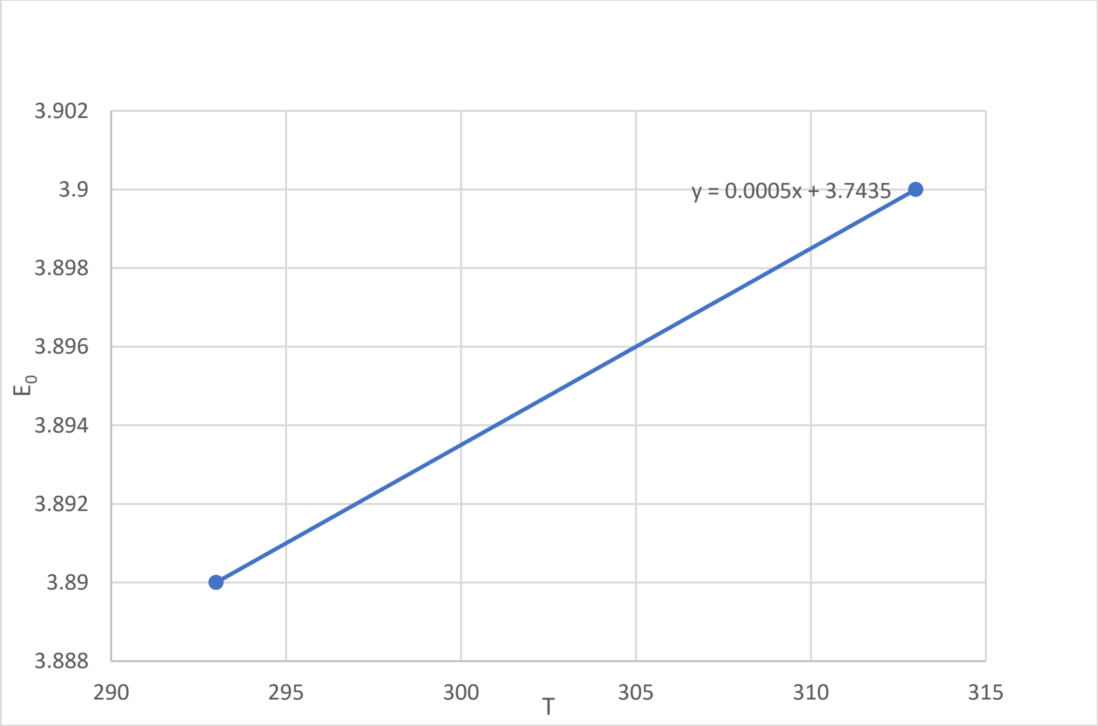

Figure 5. 44: Variation of voltage with temperature

Following the graph (Figure 5.44), the equation which describes the relationship between voltage E_0 and the cell temperature T is expressed as:

$$Y = 0.0005X + 3.7435 \tag{5.34}$$

The reversible voltage temperature coefficient $\frac{\Delta E}{\Delta T}$ is given by the slope of the graph. Therefore,

$$\frac{\Delta E}{\Delta T} = \frac{E_0(T) - E_0^{ref}}{T - T_{ref}} = 0.005$$

$$=> E_0(T) = (T - T_{ref})\frac{\Delta E}{\Delta T} + E_0^{ref}$$

$$=> E_0(T) = (T - T_{ref}) \times 0.005 + E_0^{ref} \tag{5.35}$$

From the datasheet, it could be assumed that T_{ref} = 200°C = 293 K and $E_0^{ref} = 3.89$ V.

Therefore,

$$E_0(T) = (T - 293) \times 0.005 + 3.89$$

- **Maximum capacity temperature coefficient $\frac{\Delta Q}{\Delta T}$ (Ah/K)**

Like the voltage temperature coefficient, this parameter shall not be determined using the Arrhenius equation since it is a derivative of maximum capacity with regards to temperature. The trend of maximum capacity in relation to temperature is given in Table 5.9.

Table 5. 9: Relationship between maximum capacity and temperature

T	Q
T1 = 253K (–20ºC)	42
T2 = 293K (20ºC)	52,5
T3 = 313K (40ºC)	58

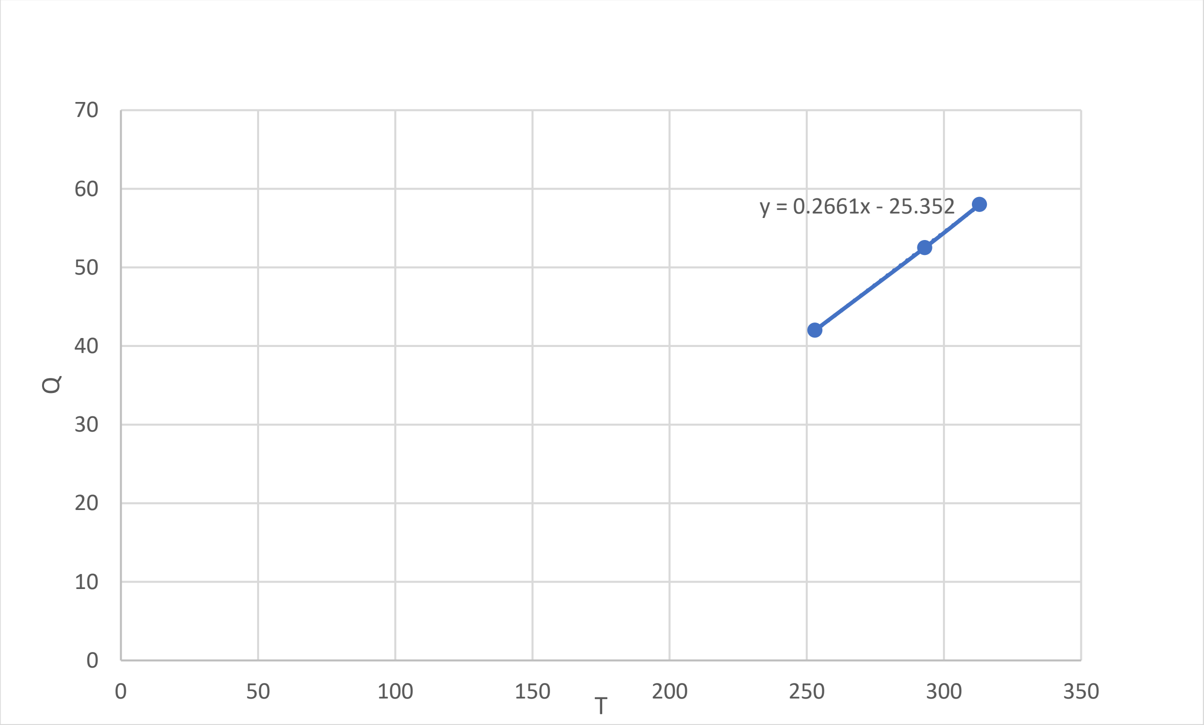

Figure 5. 45: Variation of maximum capacity with temperature

Following the graph (Figure 5.45), the equation which describes the relationship between maximum capacity Q and the cell temperature T is expressed as:

$$Y = 0.2661X - 25.352 \tag{5.36}$$

The maximum capacity temperature coefficient $\frac{\Delta Q}{\Delta T}$ is given by the slope of the graph.

Therefore,

$$\frac{\Delta Q}{\Delta T} = \frac{Q(T_a) - Q_{Ta}}{T_a - T_{ref}} = 0.2661$$

$$=> Q(T_a) = (T_a - T_{ref})\frac{\Delta Q}{\Delta T} + Q_{Ta}$$

$$=> Q(T_a) = (T_a - T_{ref}) \times 0.2661 + Q_{Ta} \tag{5.37}$$

The laboratory results obtained from the datasheet can allow for the assumptions that T_{ref} = 20^0C= 293 K, Q_{Ta}= 52.5 Ah. T_a can be any prevailing environment temperature. Therefore,

$$Q(T_a) = (T_a - 293) \times 0.2661 + 52.5 \tag{5.38}$$

The modeling of the single cell battery LP 33450, where the rated voltage is 3.6 V and the rated capacity is 43 Ah needs to implement the parameters developed in the previous section. Each of the parameters is dependent on the cell temperature T of the battery except for the battery charge $Q(T_a)$, which is dependent on the ambient temperature.

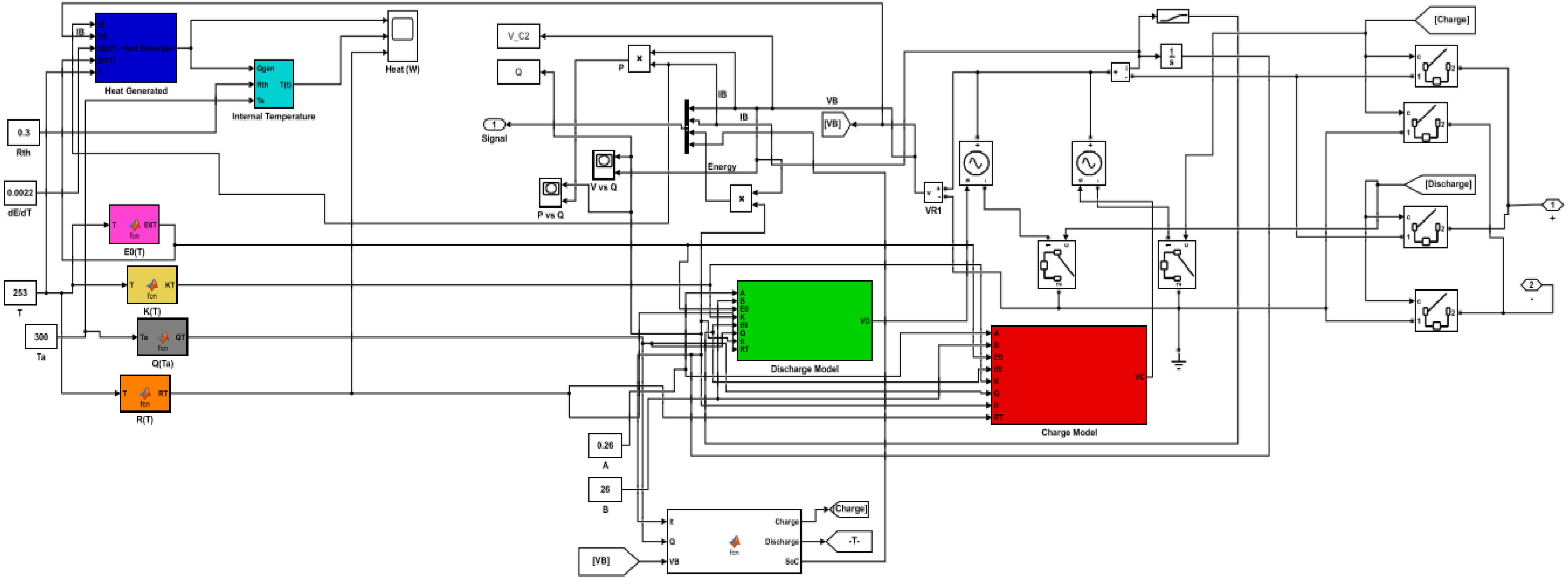

Figure 5. 46: Integration of temperature-dependent parameters

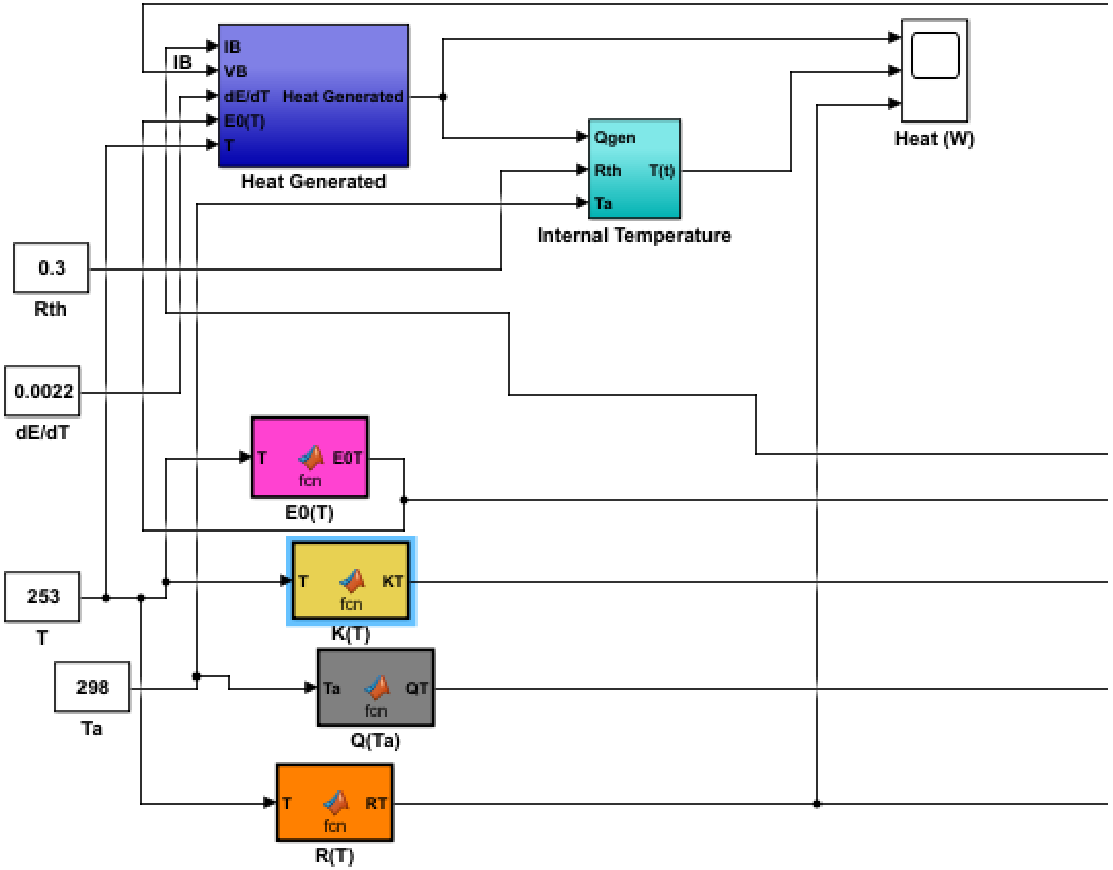

Figure 5. 47: Integration of temperature-dependent R and K

The models to be implemented for the simulation of the battery are similar to those implemented in the study of the behavior of the battery charging and discharging but with modifications to allow the varying temperature parameter as expressed in equations 17 and 18.

$$\mathrm{V_{batt}(T)} = \mathrm{E_0(T)} - \mathrm{K(T)}\frac{\mathrm{Q(T_a)}}{\mathrm{Q(-it}}(\mathrm{it} + \mathrm{i}^*) + Ae^{-\mathrm{Bit}} - \mathrm{R(T).\,i} \qquad (5.42)$$

$$\mathrm{V_{batt}(T)} = \mathrm{E_0(T)} - \mathrm{K(T)}\frac{\mathrm{Q(T_a)}}{\mathrm{it-0.1Q(T_a)}}(\mathrm{i}^*) - \mathrm{K(T)}\frac{\mathrm{Q(T_a)}}{\mathrm{Q(T_a)-it}}(\mathrm{it}) + Ae^{-\mathrm{Bit}} - \mathrm{R(T).\,i} \quad (5.43)$$

The modified discharge model in which the integrated temperature-dependent resistance, R(T), green background, is shown in Figure 5.46. It suffices to state that the Simulink environment does not allow users to input variable values into a physical resistor. Therefore, the value of R(T) had to be incorporated into the modeling equation.

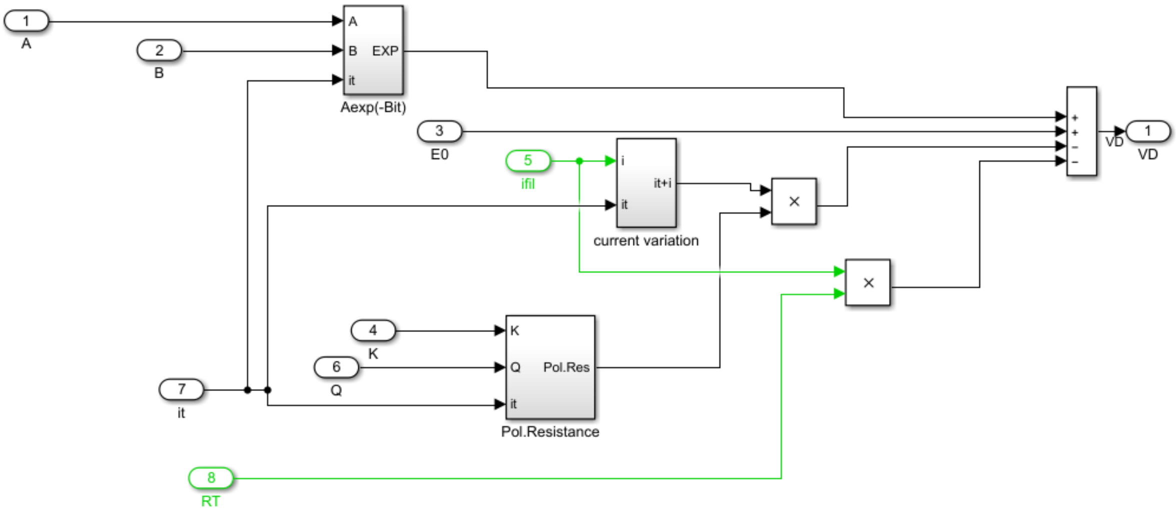

Figure 5. 48: Integration of Arrhenius function (discharge)

Like the discharge behavior, the model for the charging behavior also had to be updated by adding the same value R(T) in the modeling equation. Again, since the Simulink environment does not allow users to enter variable resistance into a resistor, the value of the battery's internal resistance must be added to the charging behavior modeling equation.

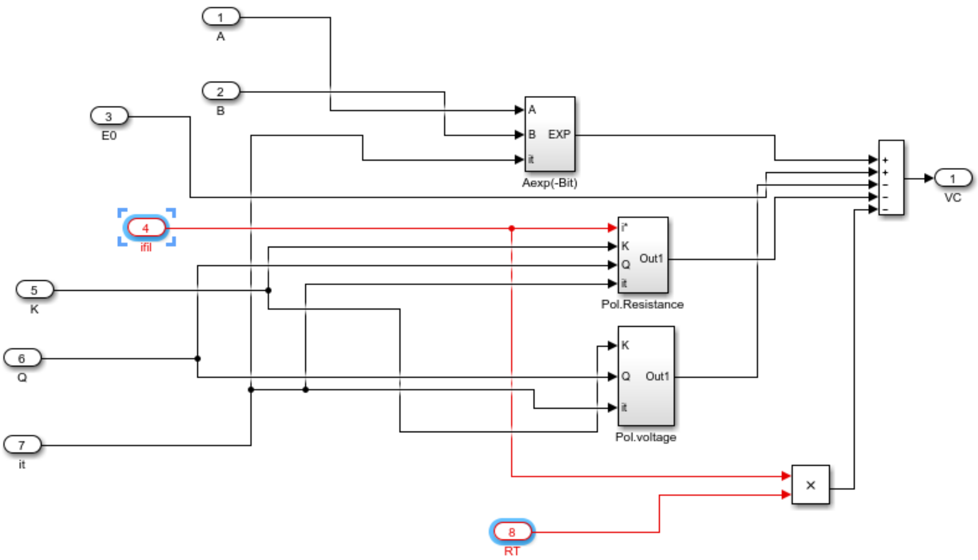

Figure 5. 49: Integration of Arrhenius function (charge)

Furthermore, as illustrated in Figure 5.46, parameters R(T) and K(T) that depend on the Arrhenius equations have also been added and are connected to the charging and discharging model. The internal resistance model equation R(T) has been modeled using the Matlab function block (orange background). Similarly, the polarization resistance K(T) has been modeled using the Matlab function block (yellow background). These functions are, as stated before, expressions of the Arrhenius equation for the development rate with regard to temperature.

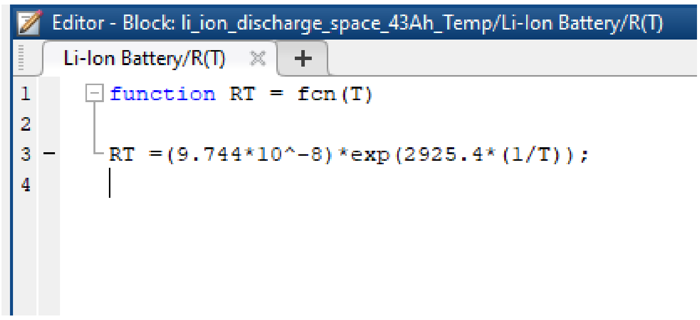

```
function RT = fcn(T)

RT =(9.744*10^-8)*exp(2925.4*(1/T));
```

Figure 5. 50: Function for temperature-dependent internal resistance

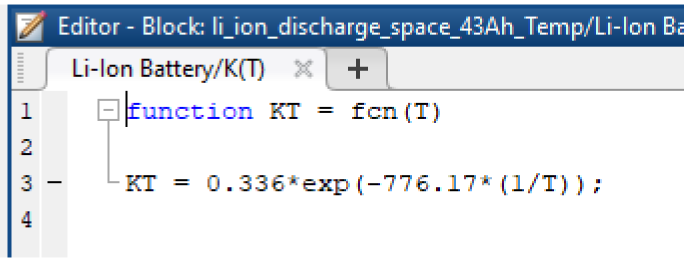

```
function KT = fcn(T)

KT = 0.336*exp(-776.17*(1/T));
```

Figure 5. 51: Function for temperature-dependent polarization resistance

Furthermore, the other battery parameters, E0(T) and Q(Ta) which are independent of the Arrhenius equation are defined using Matlab functions in Figure 5.50 and Figure 5.51, respectively.

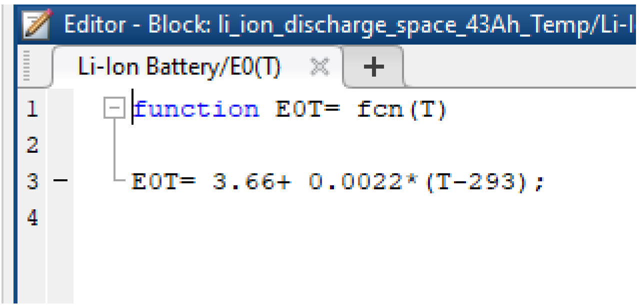

```
function E0T= fcn(T)

E0T= 3.66+ 0.0022*(T-293);

```

Figure 5. 52: Function for voltage

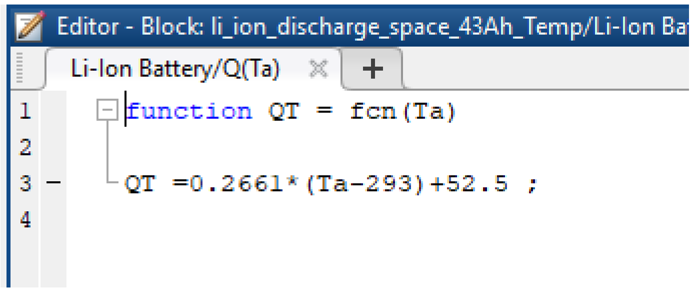

```
function QT = fcn(Ta)

QT =0.2661*(Ta-293)+52.5 ;

```

Figure 5. 53: Function for maximum capacity

The remaining parameters are the equation of internal temperature with respect to time T(t) and the heat generated. They are modeled accordingly, as depicted in Figure 5.54 and Figure 5.55, respectively.

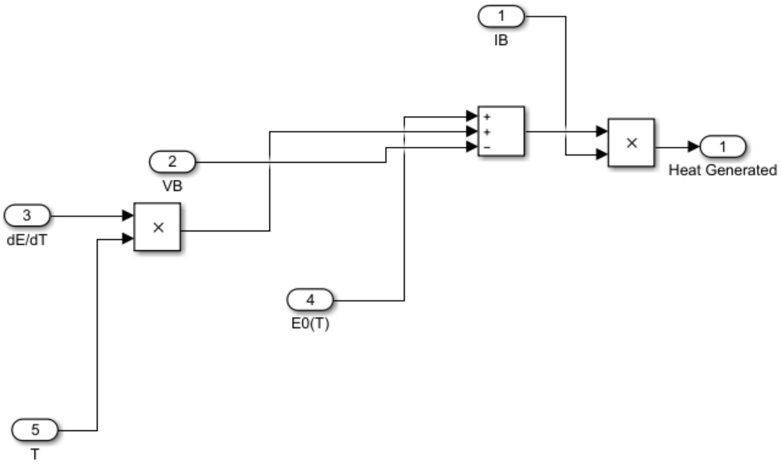

Figure 5. 54: Representation of internal temperature with respect to time

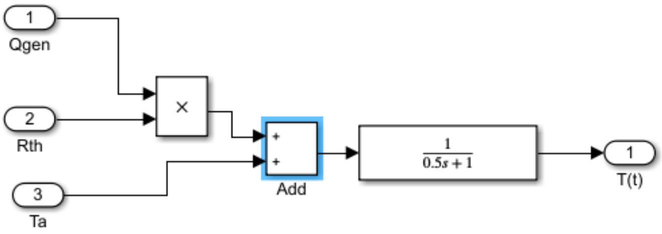

Figure 5. 55: Representation of heat generated with respect to time

5.11.5 Discussion of results

- **Single-cell**

Figure 5.56 shows the behaviour of the battery voltage and capacity at different ambient temperatures of T_a = 40°C (313 °K); T_a = 20°C (293 °K) and T_a = –20°C (253 °K). From the graphs, it could be seen that the performance of the battery decreases as the operating (ambient) temperature decreases. Therefore, the model developed for the temperature effect on the battery has been validated.

Figure 5.57 shows the behaviors of the internal temperature change. It could be seen that at higher operating maximum capacity, the internal temperature of the battery tends to increase dramatically. Likewise, an increase in ambient temperature results in an increase in the internal temperature of the battery.

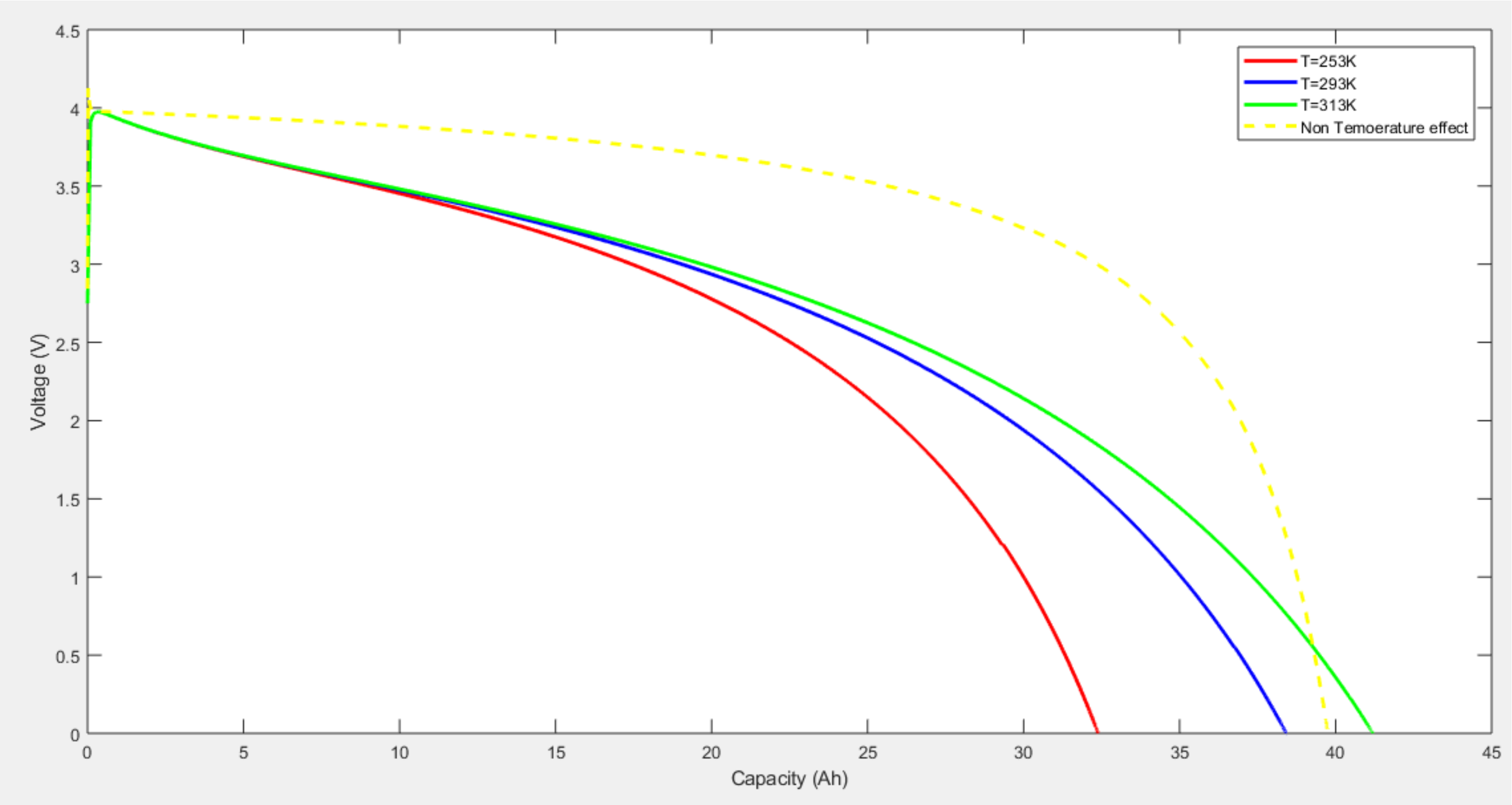

Figure 5. 56: Battery voltage and capacity at different ambient temperatures

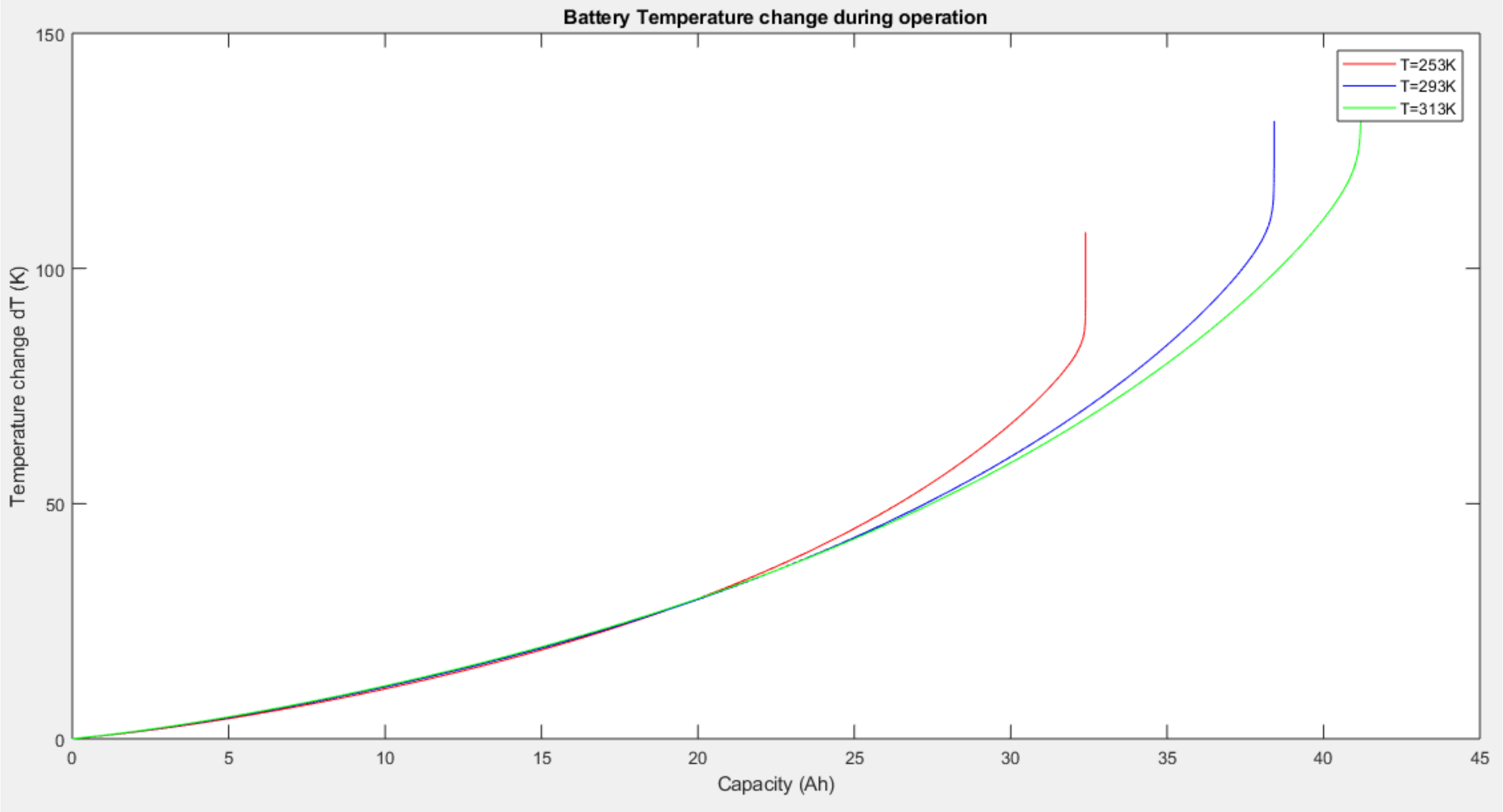

Figure 5. 57: Battery temperature change and capacity at different ambient temperatures

- **Multiple cells at different temperatures**

The MSL battery considered contains two eight-series cells arranged in parallel (8s2p). The choice of the MSL battery, which is used in space for the powering of the rover vehicle, is because such a battery will have to operate in rough conditions and extreme temperatures. To allow for comparison, the battery is connected to a load that draws an amount of constant current (I) of 8.6 A.

The behaviors of 8s2p space batteries are shown in figures 5.58 and 5.59. Comparing Figure 5.56 with Figure 5.58 and Figure 5.57 with Figure 5.59, it could be seen that the responses of the single and multiple cells follow the same pattern, i.e., the performances of the batteries decrease with the decrease in temperature and that the higher the maximum operating capacity, the higher the internal temperature of the battery. In addition, the internal temperature of the battery rises as the outside temperature rises.

This likeness in responses could be adduced to the fact that the temperature emitted (heat generation) by a single cell is the same throughout the 8s2p space battery and that the accumulated temperature of the 8s2p space battery is in addition to the temperatures of the individual cells that make up the 8s2p space battery.

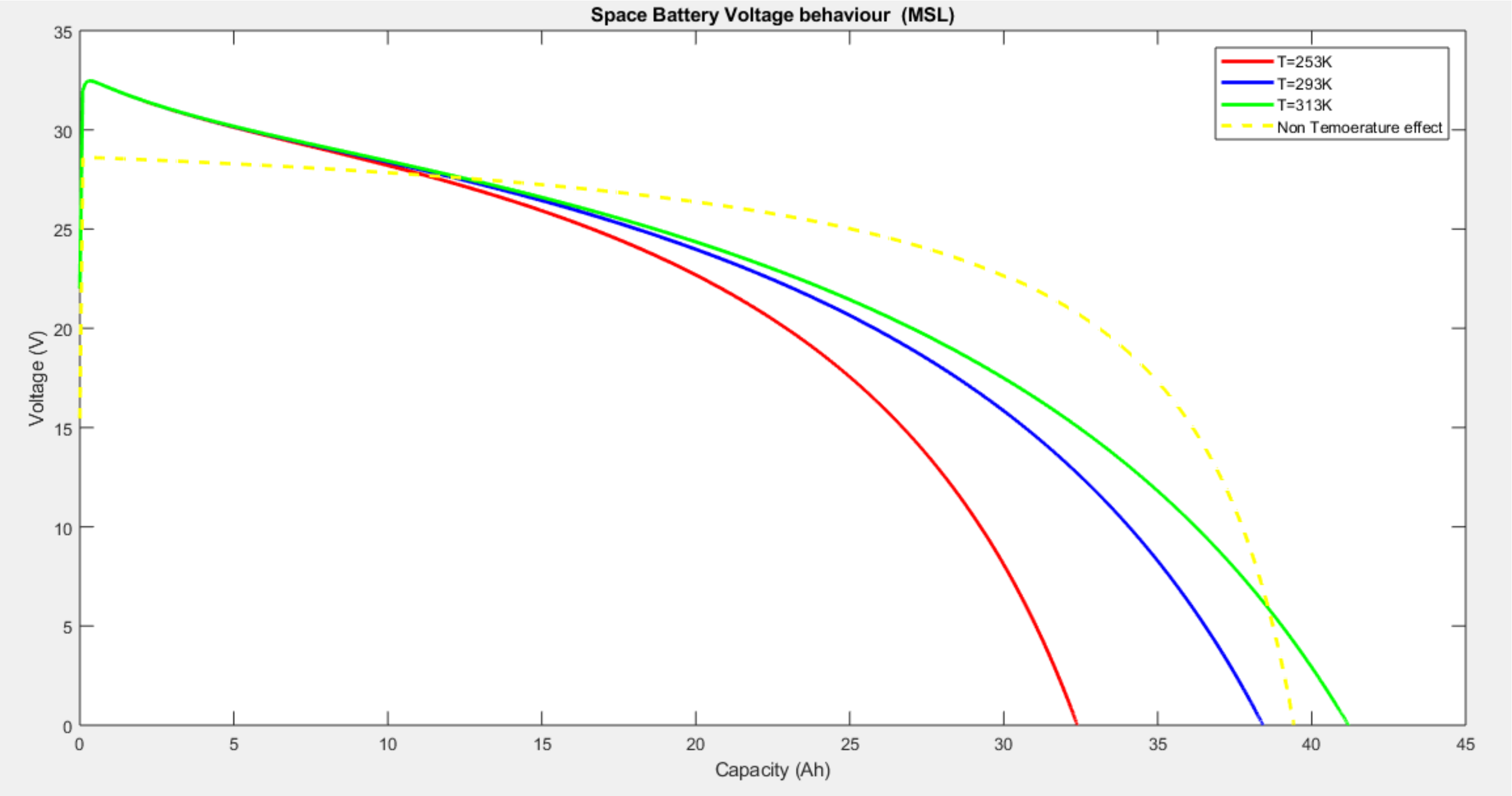

Figure 5. 58: Space battery voltage and capacity at different ambient temperatures

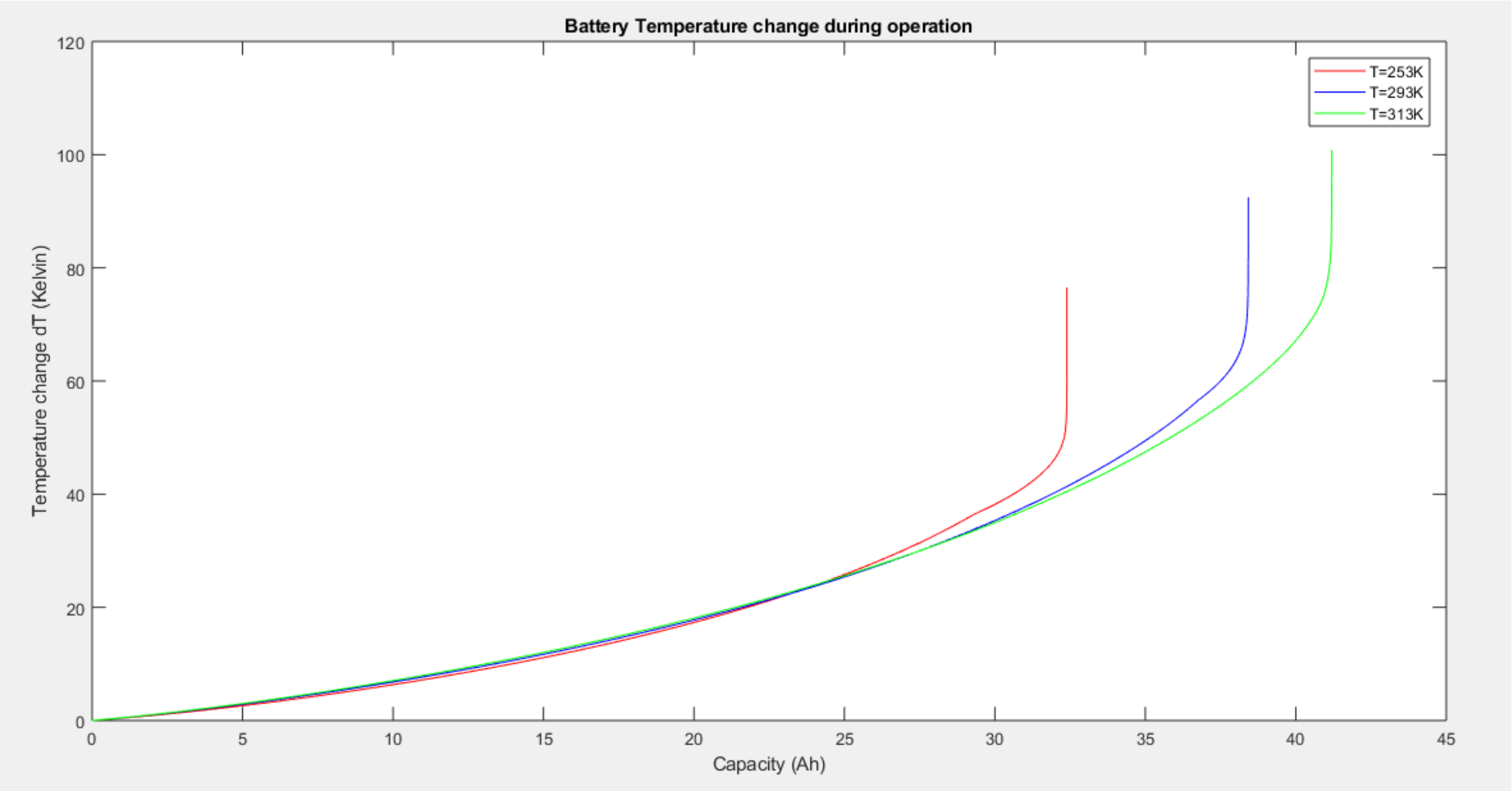

Figure 5. 59: Space battery temperature change and capacity at different ambient temperatures

- **Hybrid battery system behavior at different ambient temperatures**

Figure 5.60 and Figure 5.61 show the charge and discharge cycles of batteries at three different ambient temperatures (253 °K, 293 °K, and 313 °K). It is evident that throughout the 5 hours of operations, the battery tends to charge and discharge more often at a lower temperature (253 °K) than at a higher temperature (293 °K). This is because the charge delivered by the battery at a low temperature is poor. Consequently, more charge-discharge is needed to compensate for the load of the hybrid system. The hybrid battery system operates optimally at high temperatures.

As shown in Figure 5.62 and Figure 5.64, at the same temperature, the output voltage of a hybrid battery is higher than a single battery, but it is interesting to note that a change in temperature does not affect the output voltages of the hybrid battery. It could be seen that the hybrid system output voltage at temperature T =253 °K (Figure 5.62) and the hybrid system output voltage at T=293 °K (Figure 5.63) are relatively equal. However, it could be observed that the power cycle (when the hybrid voltage is at maximum) is wider, and it takes a long time before dropping. Also, the number of charge-discharge cycles is less at high temperatures than at low temperatures.

Indeed, a charge-discharge cycle refers to charging a battery and discharging it into a load. Charge-discharge cycles are also used to describe the lifespan of a battery. Since all chemical reactions are affected by temperature and because batteries rely on chemical reactions to generate power, the change in temperature affects the battery power. Batteries operate best at room temperature. The capacity and expected life of a battery can fluctuate with a small temperature change. Because of a reduction in internal resistance and an increase in chemical metabolism, batteries' capacities rise as the temperature rises. However, if such conditions persist for a long duration, the expected life of the battery shortens.

These results should not be overlooked in the design of an appropriate Battery Management System. By and large, while the performance of a battery improves as temperature increases, it should be noted that prolonged exposure to high temperatures could shorten the battery's life span.

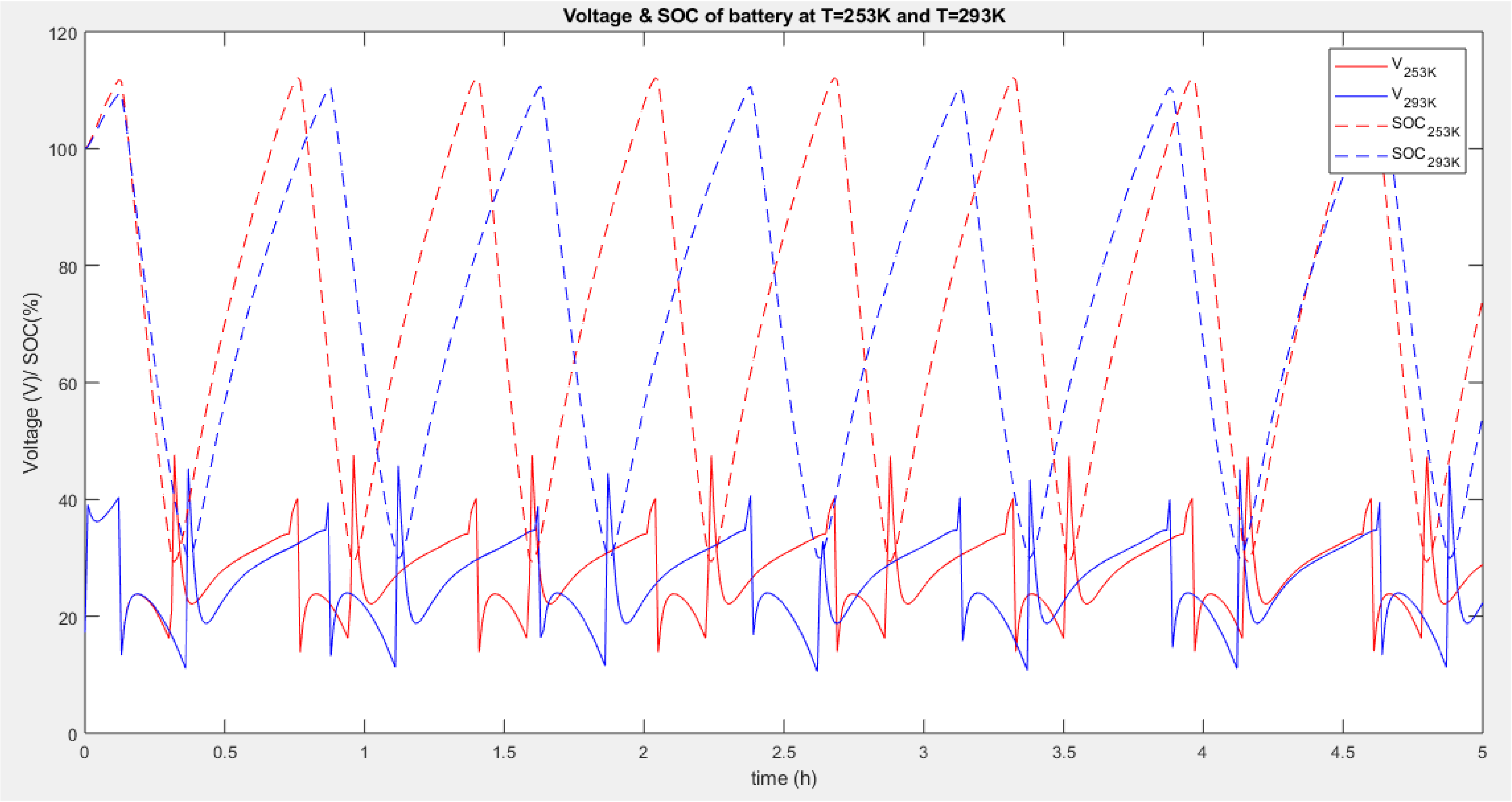

Figure 5. 60: Performances of hybrid batteries at different temperatures (253K & 293K)

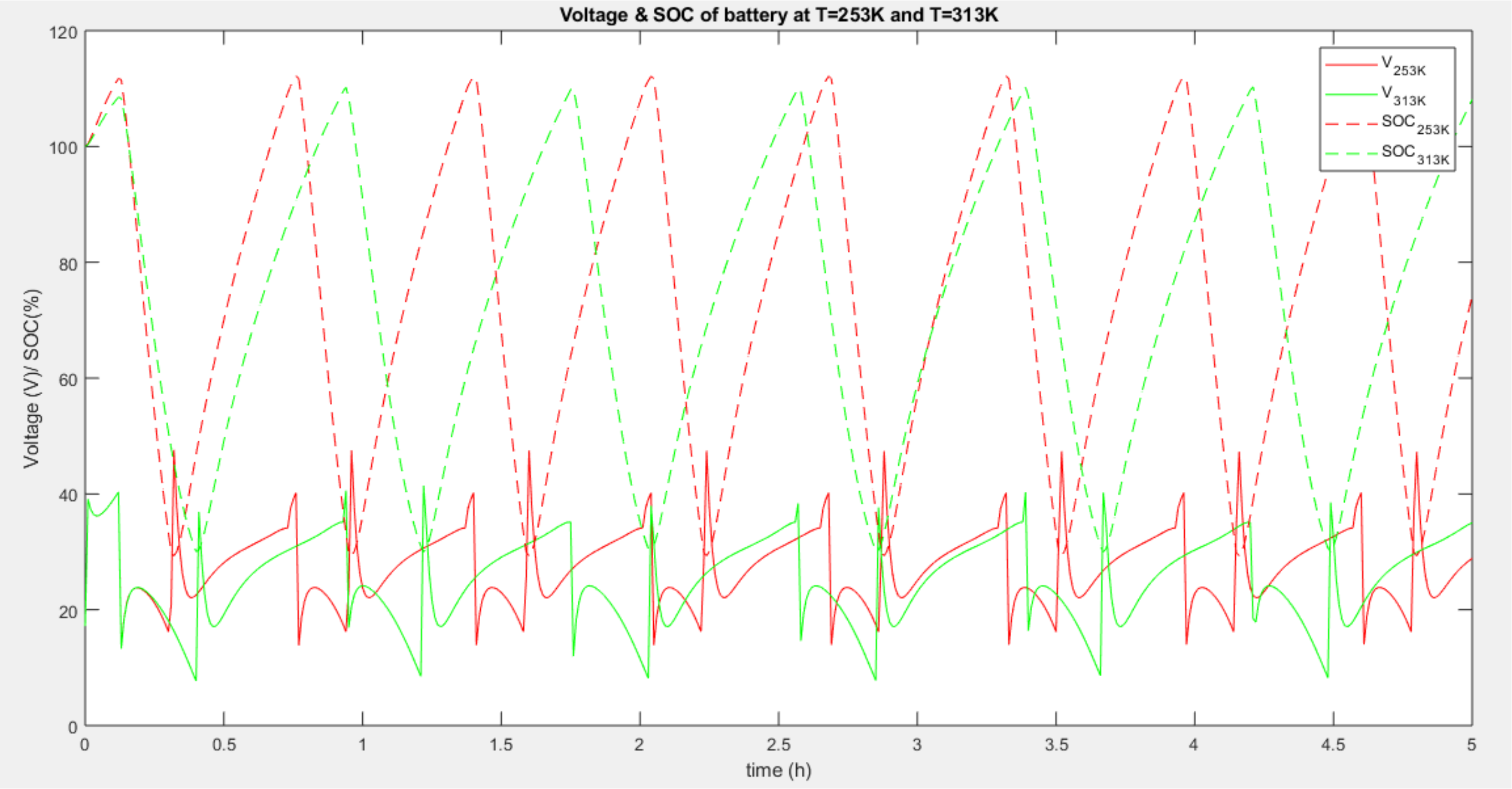

Figure 5. 61: performances of hybrid batteries at different temperatures (253K & 313K)

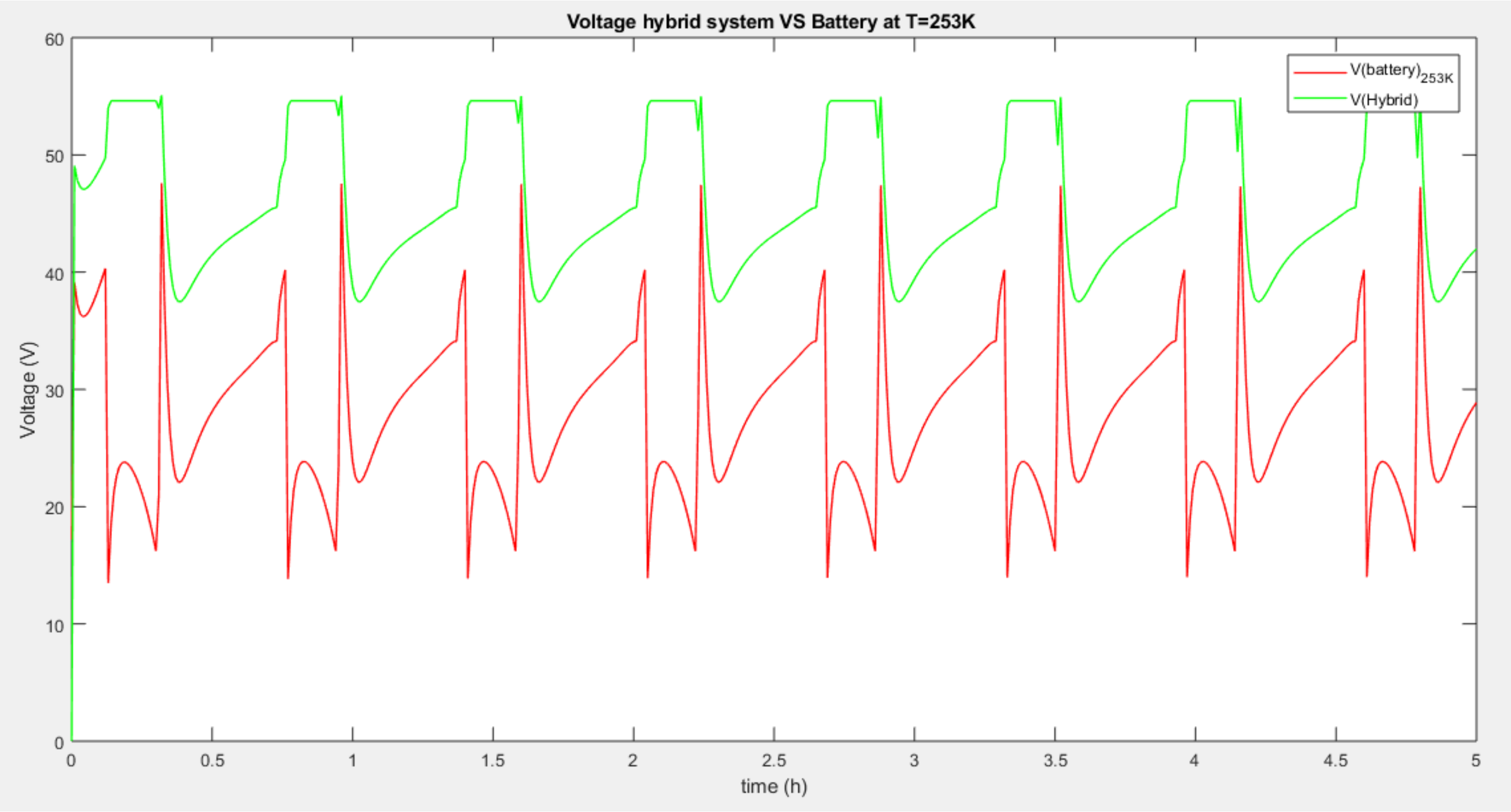

Figure 5. 62: Comparison of single and hybrid battery (253K)

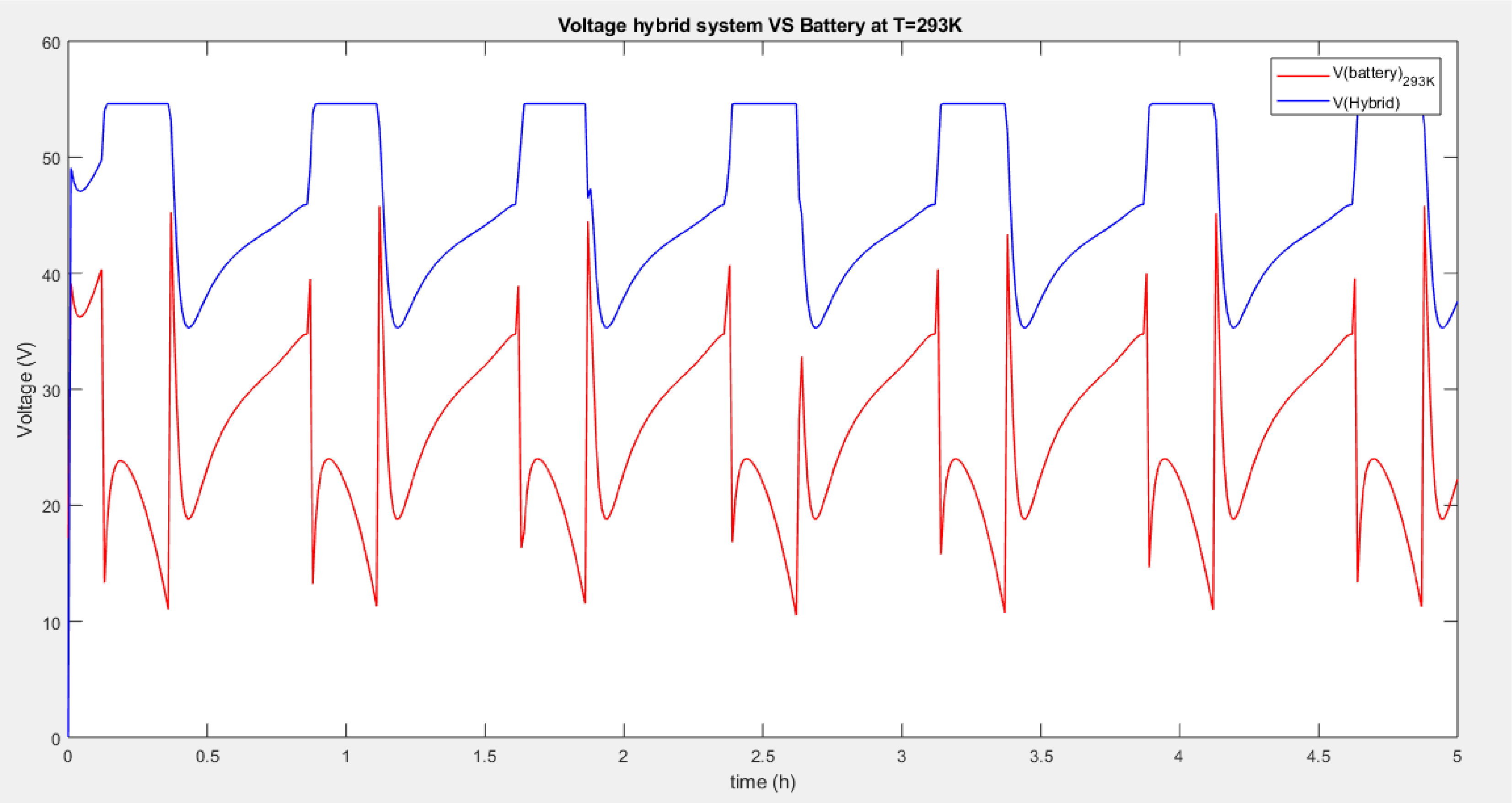

Figure 5. 63: Comparison of single and hybrid battery (293K)

CHAPTER SIX
CONCLUSIONS AND RECOMMENDATIONS

6.1 Conclusions

The earth and its environment have historically provided good things to humanity, including fertile land, clean air, water, and energy sources. Thanks to technological innovation, we can now use energy more efficiently to achieve our goals. Since energy has been essential to human existence and growth, human dependence on it is associated with his survival. Energy availability is necessary for both economic and technical development. Growing environmental and economic costs are associated with producing enough electrical energy to meet the needs of a growing global population and a considerable continuous depletion of natural energy resources. The current energy issue and the inherent limitations connected with the dependency on energy from fossil fuels must be solved to maintain the sustainability of the non-endangered planet for future generations.

It has become imperative to develop cleaner, safer, and renewable energy systems due to the rising concern over the continuous use of fossil fuels for generating electrical energy and the need to reduce dependence on this energy source significantly. A growing number of studies are being conducted on solar, wind, and other non-renewable energy sources due to improved technology that uses them in real-world applications.

Industrial and human activity release large amounts of waste heat into the environment. Using this waste heat to produce electrical energy will go a long way toward resolving the current global energy crisis and reducing the environmental risks connected with producing electrical energy from fossil fuels.

On the other hand, the demand for small-scale energy sources with high energy density, portability, and durability has significantly increased in recent years. These energy sources are essential for micro-scale devices used in autonomous systems applications, such as sensors for toxic gas and inaccessible locations for environmental monitoring or in hermetic environments such as extreme heat, cold, or corrosive conditions. The current electrochemical batteries employed in those autonomous systems are afflicted by low energy density, short life, undesirable maintenance requirements for recharging or replacement, and the disposal of unnecessary batteries, which pose a risk to the environment. Micro-scale devices are therefore very interested in finding a more effective and reliable energy source to replace the extensively utilized electrochemical batteries in autonomous systems.

Harnessing radiation energy from underutilized radioactive energy sources to generate electrical energy represents an excellent alternative to power micro-scale devices used in autonomous systems applications in toxic, inaccessible, harsh and hermetic environments.

Therefore, the main objective of this research was to take advantage of the abundantly available radioactive energy sources to develop compact, longer-lasting, high-energy density, and light energy sources. The investigation explored creating a hybrid energy system using these radioisotope energy sources in conjunction with the existing electrochemical batteries.

Apart from the introductory and the conclusive chapters, the rest of the study can be summarized as follows:

Chapter two provided a literature survey on energy sources for autonomous systems such as space exploration, satellite activities, structural health monitoring, and terrestrial monitoring in harsh and inaccessible environments. These energy sources include electrochemical batteries, solar panels, fuel cells, and thermoelectric generators. The chapter starts by providing each energy source's relative strengths and weaknesses while focusing on thermoelectric generators' performance characteristics and specific applications

Chapter three dealt with a review of nuclear and electrochemical batteries. The chapter began by focusing on nuclear batteries, devices that convert radiation energy emitted by the natural decay of radioactive isotopes to electricity. The types of nuclear batteries, such as thermoelectric, thermophotovoltaic, thermionic, AMTEC, betavoltaic, alphavoltaic, optoelectric, etc., and their characteristics, were presented. Lastly, this chapter focused on electrochemical batteries such as lithium-ion, lead-acid, nickel-cadmium, and nickel metal hybrid by concentrating on their technical characteristics and applications.

Chapter four was dedicated to the modeling and simulation of nuclear and electrochemical batteries for utility applications by focusing on the behavior of electrochemical and nuclear batteries using modelling and simulation tools to ascertain their performances and drawbacks.

Lastly, chapter five dealt with the modelling, simulation, and discussion of the results of the adopted hybrid battery system combining an electrochemical battery with a radioisotope thermoelectric energy source.

The adopted hybrid system was modeled and simulated using the Simulink environment. Overall, the simulation of the developed system showed satisfactory results, such as delivering additional powers and the ability to recover energy or power peaks. It was also revealed that integrating a proportional-integral controller into the hybrid system enhanced the ability of the system to stabilize its charge-discharge cycle, thereby ensuring less stress on the battery and, eventually, extending the battery's lifespan.

Several other simulations were conducted to assess the performance of the adopted system at different operating temperatures considering first a single cell, then multiple cells, and lastly, the hybrid battery system. Regarding the single cell, it could be seen that the performance of the battery decreased as the operating (ambient) temperature decreased. In addition, the battery's internal temperature increased dramatically at higher operating maximum capacity. Similarly, an increase in ambient temperature results in an increase in the internal temperature of the battery.

On the other hand, the simulation of multiple cells revealed that the responses followed the same pattern as the single cell response. The performance of the batteries decreased with the decrease in temperature, and the higher the maximum operating capacity, the higher the internal temperature of the battery. In addition, the internal temperature of the battery rises as the outside temperature rises. This likeness in responses could be adduced to the fact that the temperature emitted (heat generation) by a single cell is the same throughout the 8s2p space battery and that the accumulated temperature of the 8s2p space battery is in addition to the temperatures of the individual cells that make up the 8s2p space battery.

The simulation of the hybrid battery system's performance assessed the developed system's behavior for five hours of operation under different operating temperatures. It was revealed that the battery tended to charge and discharge more often at a lower temperature of 253 ^{o}K than at a higher temperature of 293 ^{o}K. That was because the charge delivered by the battery at a low temperature was poor. To compensate for the issue, more charge-discharge processes were required. Hence, it was shown that the hybrid battery system operated optimally at high temperatures.

On the other hand, the results showed that at the same temperature, the output voltage of a hybrid battery was higher than a single battery, and a temperature change had no effect on the output voltages of the hybrid battery. It was also noticeable that the system output voltages at 253 ^oK and 293 ^oK were relatively equal. However, the power cycle when the hybrid voltage is at the maximum was wider and took a long time before dropping.

Although the results revealed that the performance of a battery improved as temperature increased, prolonged exposure to high temperatures could shorten a battery's life span. The effects of temperature on batteries are significant and, therefore, should not be overlooked in designing an appropriate Battery Management System.

In summary, this investigation's findings showed that the study's objective was attained as simulation results revealed that the developed hybrid battery system could perform excellently.

6.2 Recommendations

In the system modeled, to prevent constant charge-discharge, especially when unnecessary, a proper battery management system that relies not only on the use of the PID tuning method needs to be developed.

Further investigation will focus on developing a test bench to validate the simulation results with measured experimental values.

With the rising cost of petroleum-based products and the need to continue to mitigate the adverse effects of greenhouse gases, further work in adapting hybrid energy to electric power vehicles is recommended. The hybrid system investigated was based on a DC motor. It would be of utmost interest to take the investigation further to other applications.

REFERENCES

Alexander, R. & McKinley, L.E. 2006. *Deep geological disposal of radioactive waste - An international perspective*. Academic Press Elsevier.

Bass, J.C. 1999. Thermoelectric generator. , (19).

Battery University. 2021a. BU-209: How does a Supercapacitor Work? https://batteryuniversity.com/article/bu-209-how-does-a-supercapacitor-work 8 November 2022.

Battery University. 2021b. Comparison Table of Secondary Batteries. *Battery University*. https://batteryuniversity.com/article/bu-107-comparison-table-of-secondary-batteries.

Becherif, M. 2006. *Passivity-based control of hybrid sources: Fuel cell and battery*. IFAC. http://dx.doi.org/10.3182/20060829-3-NL-2908.00101.

Bennett, G.L. & Skrabek, E.A. 1996. Power performance of U.S. space radioisotope thermoelectric generators. In *International Conference on Thermoelectrics, ICT,*. IEEE: 357–364.

Bitnar, B. 2003. Silicon, germanium and silicon/germanium photocells for thermophotovoltaics applications. *Semiconductor Science and Technology*, 18(5).

Cabauy, P., Olsen, L., Elkind, B. & Adams, T. 2010. Micropower Betavoltaic Hybrid Sources. In *44th Power Sources Conference*. Las Vegas: 14–17.

Carmo, J.P., Antunes, J., Silva, M.F., Ribeiro, J.F., Goncalves, L.M. & Correia, J.H. 2011. Characterization of thermoelectric generators by measuring the load-dependence behavior. *Measurement: Journal of the International Measurement Confederation*, 44(10): 2194–2199. http://dx.doi.org/10.1016/j.measurement.2011.07.015.

Cataldo, R.L. & Bennett, G.L. 2016. Space radioisotope power systems and applications: Past, present and future, Radioisotopes. In *Applications in Physical Sciences*. IEEE, WILEY: 225–240. https://www.intechopen.com/books/advanced-biometric-technologies/liveness-detection-in-biometrics.

CATRENE. 2009. *Energy Autonomous Systems: Future Trends in Devices, Technology, and Systems*.

Chou, S.K., Yang, W.M., Chua, K.J., Li, J. & Zhang, K.L. 2011. Development of micro power generators - A review. *Applied Energy*, 88(1): 1–16.

Clarkson, J.P., Sun, W., Hirschman, K.D., Gadeken, L.L. & Fauchet, P.M. 2007. Betavoltaic and photovoltaic energy conversion in three-dimensional macroporous silicon diodes. *Physica Status Solidi (A)*, 204(5): 1536–1540.

Coutts, T.J. 1997. Thermophotovoltaic principles, potential, and problems. In *AIP Conference Proceedings 404*. 217–234.

Dixit, A. 2020. Cathode Materials for Lithium Ion Batteries (LIBs): A Review on Materials related aspects towards High Energy Density LIBs. , (November). http://arxiv.org/abs/2008.10896.

Duggirala, R., Li, H., Pappu, A.M., Z., F., A., A. & A., L. 2004. Radioisotope micropower generator for CMOS self-powered sensor microsystems. In *Power MEMS 2004*. Kyoto: 133–136.

Eaglepicher Technologies. 2019. 6Ah Space Cell High energy , long cycle life and low maintenance lithium- ion cell for demanding applications 6Ah Space Cell. https://www.eaglepicher.com/sites/default/files/LP 33450 43Ah Space Cell 0319.pdf.

El-Genk, M.S., Saber, H.H. & Caillat, T. 2003. Efficient segmented thermoelectric unicouples for space power applications. *Energy Conversion and Management*, 44(11): 1755–1772.

Fakham, H., Lu, D. & Francois, B. 2011. Power control design of a battery charger in a hybrid active PV generator for load-following applications. *IEEE Transactions on Industrial Electronics*, 58(1): 85–94.

Fang, W., Kwon, O.J. & Wang, C.-Y. 2010. Electrochemical–thermal modeling of automotive Li-ion batteries and experimental validation using a three-electrode cell. *International Journal of Energy Research*, 34: 107–115.

Finegan, D.P., Scheel, M., Robinson, J.B., Tjaden, B., Hunt, I., Mason, T.J., Millichamp, J., Di Michiel, M., Offer, G.J., Hinds, G., Brett, D.J.L. & Shearing, P.R. 2015. In-operando high-speed tomography of lithium-ion batteries during thermal runaway. *Nature Communications*, 6: 1–10.

Fogler, H.S. 2006. *Elements of Chemical Reaction Engineering*. 4th ed. Prentice Hall PTR.

Gao, F. & Tang, Z. 2008. Kinetic behavior of LiFePO4/C cathode material for lithium-ion batteries. *Electrochimica Acta*, 53(15): 5071–5075.

Ghamaty, S., Bass, J.C. & Elsner, N.B. 2003. Quantum well thermoelectric devices and applications. In *22nd International Conference on Thermoelectrics, ICT,*. La Grande

Motte: IEEE: 563–566.

Gospodarczyk, M.M. 2022. Amid Global Crises, Nuclear Power Provides Energy Security with Increased Electricity Generation in 2021. *IAEA Department of Nuclear Energy*. https://www.iaea.org/newscenter/news/amid-global-crises-nuclear-power-provides-energy-security-with-increased-electricity-generation-in-2021 8 November 2022.

Guazzoni, G. & Mathews, S. 2004. Thermophotovoltaic generation of electricity. In *AIP proceedings of the 6th Conference on Thermophotovoltaic generation of Electricity, TPV6*. Freiburg.

Gulian, A., Wood, K., Fritz, G., Gyulamiryan, A., Nikogosyan, V., Giordano, N., Jacobs, T. & Van Vechten, D. 2000. X-ray/UV single photon detectors with isotropic Seebeck sensors. *Nuclear Instruments and Methods in Physics Research, Section A: Accelerators, Spectrometers, Detectors and Associated Equipment*, 444(1): 232–236.

Gunawardhana, N., Dimov, N., Sasidharan, M., Park, G.J., Nakamura, H. & Yoshio, M. 2011. Suppression of lithium deposition at sub-zero temperatures on graphite by surface modification. *Electrochemistry Communications*, 13(10): 1116–1118. http://dx.doi.org/10.1016/j.elecom.2011.07.014.

Guo, H., Li, H., Lai, A. & Blanchard, J. 2008. Nuclear microbatteries for micro and nano devices. *International Conference on Solid-State and Integrated Circuits Technology Proceedings, ICSICT*: 2365–2370.

Halpert, G., Frank, H. & Surampudi, S. 1999. Batteries and Fuel Cells in Space. *The Electrochemical Society Interface*, 8(3): 25–30.

Hochbaum, A.I., Chen, R., Delgado, R.D., Liang, W., Garnett, E.C., Najarian, M., Majumdar, A. & Yang, P. 2008. Enhanced thermoelectric performance of rough silicon nanowires. *Nature*, 451(7175): 163–167.

Holgate, T.C., Bennett, R., Hammel, T., Caillat, T., Keyser, S. & Sievers, B. 2015. Increasing the Efficiency of the Multi-mission Radioisotope Thermoelectric Generator. *Journal of Electronic Materials*, 44(6): 1814–1821.

Hsu, C.T., Huang, G.Y., Chu, H.S., Yu, B. & Yao, D.J. 2011. Experiments and simulations on low-temperature waste heat harvesting system by thermoelectric power generators. *Applied Energy*, 88(4): 1291–1297. http://dx.doi.org/10.1016/j.apenergy.2010.10.005.

IAEA. 2006. *Environmental Consequences of the Chernobyl Accident and their Remediation: Twenty Years of Exoerience. Report of the Chernobyl Forum Expert Group ‘Environment’*. Vienna.

IAEA. 2008. Estimation of Global Inventories of Radioactive Waste and Other Radioactive Materials. *Nuclear Technology Review*, (June): 128.

IAEA. 2009. *The classification of radioactive wastes*.

Ismail, B.I. & Ahmed, W.H. 2009. Thermoelectric power generation using waste-heat energy as an alternative green technology. *Recent Patents on Electrical Engineering*, 2(1): 27–39.

Jaguemont, J., Boulon, L. & Dubé, Y. 2016. A comprehensive review of lithium-ion batteries used in hybrid and electric vehicles at cold temperatures. *Applied Energy*, 164: 99–114. http://dx.doi.org/10.1016/j.apenergy.2015.11.034.

Jiang, M. 2013. An Overview of Radioisotope Thermoelectric Generators. http://large.stanford.edu/courses/2013/ph241/jiang1/ 9 November 2022.

Kishi, M., Nemoto, H., Hamao, T., Yamamoto, M., Sudou, S., Mandai, M. & Yamamoto, S. 1999. Micro-Thermoelectric modules and their application to wristwatches as an energy source. In *International Conference on Thermoelectrics, ICT, Proceedings*. 301–307.

Kushwah, M. & Patra, A. 2014. PID Controller Tuning using Ziegler-Nichols Method for Speed Control of DC Motor. *International Journal of Scientific Engineering and Technology Research*, 3(13): 2924–2929. www.semargroup.org,.

Lange, R.G. & Carroll, W.P. 2008. Review of recent advances of radioisotope power systems. *Energy Conversion and Management*, 49(3): 393–401.

Larminie, J. & Dicks, A. 2003. *Fuel Cell Systems Explained*. Second. Wiley. https://medium.com/@arifwicaksanaa/pengertian-use-case-a7e576e1b6bf.

Liu, H., Wei, Z., He, W. & Zhao, J. 2017. Thermal issues about Li-ion batteries and recent progress in battery thermal management systems: A review. *Energy Conversion and Management*, 150(August): 304–330. http://dx.doi.org/10.1016/j.enconman.2017.08.016.

Manasse, F.K., Pinajian, J.J. & Tse, A.N. 1976. Schottky barrier betavoltaic battery. *IEEE Transactions on Nuclear Science*, 23(1): 860–870.

Marsh, R.A., Vukson, S., Surampudi, S., Ratnakumar, B. V., Smart, M.C., Manzo, M. & Dalton, P.J. 2001. Li ion batteries for aerospace applications. *Journal of Power Sources*, 97–98: 25–27.

Masih-Tehrani, M. & Yahyaei, R. 2017. Study of lithium battery thermal effect on battery and hybrid battery/ultra-capacitor sizing for an electric vehicle. *Journal of Engineering Technology*, 6: 85–99.

Mathworks. 2008. Battery. https://www.mathworks.com/help/sps/powersys/ref/battery.html 8 November 2022.

McGinnes, D.F. 2007. Waste sources and classification. *Radioactivity in the Environment*, 9(06): 8–40.

Meskani, A. & Haddi, A. 2019. Modeling and Simulation of an Intelligent Hybrid Energy Source based on Solar Energy and Battery. *Energy Procedia*, 162: 97–106. https://doi.org/10.1016/j.egypro.2019.04.011.

Miao, M., Wu, Z., Lou, S. & Wang, Y. 2017. Research on Optimizing Operation of Hybrid PV Power and Pumped Hydro Storage System. *Energy Procedia*, 118: 110–118. http://dx.doi.org/10.1016/j.egypro.2017.07.023.

Moseley, H.G.J. & A, P.R.S.L. 1913. The attainment of high potentials by the use of radium. *Proceedings of the Royal Society of London. Series A, Containing Papers of a Mathematical and Physical Character*, 88(605): 471–476.

Murashko, K., Pyrhonen, J. & Laurila, L. 2013. Three-dimensional thermal model of a lithium ion battery for hybrid mobile working machines: Determination of the model parameters in a pouch cell. *IEEE Transactions on Energy Conversion*, 28(2): 335–343.

NASA. 2006. Radioisotope Thermoelectric Generator. Space Radioisotope Power Systems. https://science.nasa.gov/about-us/smd-programs/radioisotope-power-systems#:~:text=The Radioisotope Power Systems (RPS,enable future space exploration missions. 16 June 2015.

Nelson, R.E. 2003. A brief history of thermophotovoltaic development. *Semiconductor Science and Technology*, 18(5).

Newman, J., Thomas, K.E., Hafezi, H. & Wheeler, D.R. 2003. Modeling of lithium-ion batteries. *Journal of Power Sources*, 119–121: 838–843.

Nuwayhid, R.Y., Rowe, D.M. & Min, G. 2003. Low cost stove-top thermoelectric generator for regions with unreliable electricity supply. *Renewable Energy*, 28(2): 205–222.

Ojovan, M.I. & Lee, W.E. 2014. Naturally Occurring Radionuclides. *An Introduction to Nuclear Waste Immobilisation*: 31–39.

Ojovan, M.I. & Steinmetz, H.J. 2022. Approaches to Disposal of Nuclear Waste. *Energies*, 15(20).

Olsen, L.. 1974. Advanced betavoltaic power sources. In *9th Intersociety Engineering Conference*. 754 – 761.

Olsen, L.C. 1973. Betavoltaic energy conversion. *Energy Conversion*, 13(4): 117–127.

Olsen, L.C., Cabauy, P. & Elkind, B.J. 2012. Betavoltaic power sources. *Physics Today*, 65(12): 35–38.

Ould Amrouche, S., Rekioua, D., Rekioua, T. & Bacha, S. 2016. Overview of energy storage in renewable energy systems. *International Journal of Hydrogen Energy*, 41(45): 20914–20927. http://dx.doi.org/10.1016/j.ijhydene.2016.06.243.

Petzl, M., Kasper, M. & Danzer, M.A. 2015. Lithium plating in a commercial lithium-ion battery - A low-temperature aging study. *Journal of Power Sources*, 275: 799–807. http://dx.doi.org/10.1016/j.jpowsour.2014.11.065.

Pfann, W.G. & Van Roosbroeck, W. 1954. Radioactive and photoelectric p-n junction power sources. *Journal of Applied Physics*, 25(11): 1422–1434.

Prelas, M.A., Weaver, C.L., Watermann, M.L., Lukosi, E.D., Schott, R.J. & Wisniewski, D.A. 2014. A review of nuclear batteries. *Progress in Nuclear Energy*, 75: 117–148. http://dx.doi.org/10.1016/j.pnucene.2014.04.007.

Qiu, K. & Hayden, A.C.S. 2008. Development of a thermoelectric self-powered residential heating system. *Journal of Power Sources*, 180(2): 884–889.

Rahn, C.D. & Wang, C.Y. 2013. *Battery Systems Engineering*.

Rao, K.R. 2001. Radioactive waste: The problem and its management. *Current Science*, 81(12): 1534–1546.

Rappaport, P. 1954. The electron-voltaic effect in p-n junctions induced by beta-particle bombardment. *Physical Review*, 93(1): 246–247.

Ratnakumar, B. V., Smart, M.C., Ewell, R.C., Whitcanack, L.D., Chin, K.B. & Surampudi, S. 2004. Lithium-ion rechargeable batteries on Mars Rovers. *Collection of Technical Papers - 2nd International Energy Conversion Engineering Conference*, 3: 1763–1770.

Rayment, C. & Sherwin, S. 2003. Introduction to Fuel Cell Technology. *Department of Aerospace and Mechanical Engineering, University of Notre Dame*. http://citeseerx.ist.psu.edu/viewdoc/download?doi=10.1.1.129.3231&rep=rep1&type=pdf.

Riffat, S.B. & Ma, X. 2003. Thermoelectrics: A review of present and potential applications.

Applied Thermal Engineering, 23(8): 913–935.

Rinalde, G.F., Juanicó, L.E., Taglialavore, E., Gortari, S. & Molina, M.G. 2010. Development of thermoelectric generators for electrification of isolated rural homes. *International Journal of Hydrogen Energy*, 35(11): 5818–5822. http://dx.doi.org/10.1016/j.ijhydene.2010.02.093.

Rowe, D.M. 2006. Review, Thermoelectric Waste Heat Recovery as a Renewable Energy Source. *International Journal of Innovations in Energy Systems and Power*, 1: 13–23.

Rowe, D.M. 1999. Thermoelectrics, an environmentally-friendly source of electrical power. *Renewable Energy*, 16(1–4): 1251–1256.

Rybicki, G., Branch, P., Vargas-aburto, C. & Uribe, R. 1996. Silicon Carbide Alphavoltaic Battery George Rybicki Photovoltaics Branch. In *25th IEEE Photovoltaic Specialists Conference*. IEEE: 93–96.

Rynkiewicz, R. 1999. Discharge and charge modeling of lead acid batteries. In *IEEE Applied Power Electronics Conference and Exposition - APEC*. IEEE: 707–710.

Sanchez-Torres, A. 2011. Radioisotope Power Systems for Space Applications. In *Applications in Physical Sciences*. Intechopen. https://cdn.intechopen.com/pdfs/21662/InTech-Radioisotope_power_systems_for_space_applications.pdf.

De Sanctis, E., Monti, S. & Ripani, M. 2016. Management of Radioactive Waste. In *International Academy of Ecology and Environmental Sciences*. 229–255.

Schmidt, G.R., Sutliff, T.J. & Dudzinski, L.A. 2011. Radioisotope Power: A Key Technology for Deep Space Exploration. In *Appications in Physical Sciences Sciences*. Intechopen: 225–240. https://www.intechopen.com/books/advanced-biometric-technologies/liveness-detection-in-biometrics.

Scholarly Community Enciclopedia. 2022. Supercapacitor Applications and Developments. https://encyclopedia.pub/entry/history/compare_revision/44508 8 November 2022.

Sethumadhavan, S. & Burger, D. 2006. Powering a Cat Warmer Using Bi2Te3 Thin-Film Thermoelectric Conversion of Microprocessor Waste Heat. In *ASPLOS*.

Shakouri, A. 2011. Recent developments in semiconductor thermoelectric physics and materials. *Annual Review of Materials Research*, 41: 399–431.

Shameer, P.M. & Christopher, D. 2013. Design of Exhaust Heat Recovery Power Generation System Using Thermo-Electric Generator. *International Journal of Science* *and Research (IJSR)*, 4(1): 1522–1526.

Shepherd, C.M. 1965. Design of Primary and Secondary Cells. *Journal of The Electrochemical Society*, 112(7): 657.

Smart, M.C., Ratnakumar, B.., Whitcanack, L.., Puglia, F.., Santee, S. & Gitzendanner, R. 2010. Life verification of large capacity Yardney Li-ion cells and batteries in support of NASA missions. *International Journal of Energy Research*, 34(4): 116–132.

Smart, M.C., Ratnakumar, B. V., Whitcanack, L.D., Puglia, F.J., Santee, S. & Gitzendanner, R. 2009. Performance testing of Yardney Li-ion cells and batteries in support of future NASA missions. In *7th International Energy Conversion Engineering Conference*. Denver. https://trs.jpl.nasa.gov/bitstream/handle/2014/45282/09-2500_A1b.pdf?sequence=1.

Smart, M.C., Ratnakumar, B. V, Ewell, R.C., Whitcanack, L.D., Surampudi, S., Puglia, F. & Gitzendanner, R. 2007. An Update of the Ground Testing of Li-ion Batteries in Support of JPL ' s 2003 Mars Exploration Rover Mission. *American Institute of Aeronautics and Astronautics*: 1–12.

Snyder, G.J. & Toberer, E.S. 2008. Complex thermoelectric materials. *Nature Materials*, 7(2): 105–114.

Snyder, G.J. & Ursell, T.S. 2003. Thermoelectric efficiency and compatibility. *Physical Review Letters*, 91(14): 148301-1-148301–4.

Snyder, J.G. 2008. Small thermoelectric generators. *The Electrochemical Society Interface*, 2002-Janua: 54–56.

Strasser, M., Aigner, R., Lauterbach, C., Sturm, T.F., Franosch, M. & Wachutka, G.K.M. 2004. Micromachined CMOS thermoelectric generators as on-chip power supply. *Sensors and Actuators, A: Physical*, 114(2–3): 362–370.

Surampudi, R., Blosiu, J., Bugga, R., Brandon, E., Smart, M., Elliott, J., Castillo, J., Yi, T., Lee, L., Piszczor, M., Miller, T., Reid, C., Taylor, C., Liu, S., Plichta, E., Iannello, C., Beauchamp, P.M. & Cutts, J.A. 2017. *Energy Storage Technologies for Future Planetary Science Missions*. https://solarsystem.nasa.gov.

Tahir, M.B., Abrar, M., Tehseen, A., Awan, T.I., Bashir, A. & Nabi, G. 2020. *Nanotechnology: the road ahead*. INC. http://dx.doi.org/10.1016/B978-0-12-818908-5.00011-1.

Taniguchi, A., Fujioka, N., Ikoma, M. & Ohta, A. 2001. Development of nickel/metal-hydride batteries for EVs and HEVs. *Journal of Power Sources*, 100(1–2): 117–124.

Tie, S.F. & Tan, C.W. 2013. A review of energy sources and energy management system in electric vehicles. *Renewable and Sustainable Energy Reviews*, 20: 82–102. http://dx.doi.org/10.1016/j.rser.2012.11.077.

Tremblay, O. & Dessaint, L.A. 2009. Experimental validation of a battery dynamic model for EV applications. *24th International Battery, Hybrid and Fuel Cell Electric Vehicle Symposium and Exhibition 2009, EVS 24*, 2: 930–939.

Tritt, T.M. & Subramanian, M.A. 2006. Thermoelectric materials, phenomena, and applications: A bird’s eye view. *MRS Bulletin*, 31(3): 188–194.

Tsai, H.L. & Lin, J.M. 2010. Model building and simulation of thermoelectric module using Matlab/Simulink. *Journal of Electronic Materials*, 39(9): 2105–2111.

Wang, G., Hu, R., Wei, H., Zhang, H., Yang, Y., Xiong, X., Liu, G. & Luo, S. 2010. The effect of temperature changes on electrical performance of the betavoltaic cell. *Applied Radiation and Isotopes*, 68(12): 2214–2217. http://dx.doi.org/10.1016/j.apradiso.2010.06.011.

Weiling, L. & Shantung, T. 2004. Recent developments of thermoelectric power generation. *Chinese Science Bulletin*, 49(12): 1212–1219.

Wilt, D., Chhong, P., Wolford, D., Magari, P. & Crowley, C. 2007. Thermophotovoltaic generation of electricity. In *AIP Proceedings of the 7th World Conference on Thermophotovoltaic generation of Electricity: TP76*.

Xiao, M. & Choe, S.Y. 2013. Theoretical and experimental analysis of heat generations of a pouch type LiMn2O4/carbon high power Li-polymer battery. *Journal of Power Sources*, 241: 46–55. http://dx.doi.org/10.1016/j.jpowsour.2013.04.062.

Ying, T.K., Gao, X.P., Hu, W.K., Wu, F. & Noréus, D. 2006. Studies on rechargeable NiMH batteries. *International Journal of Hydrogen Energy*, 31(4): 525–530.

Yu, C. & Chau, K.T. 2009. Thermoelectric automotive waste heat energy recovery using maximum power point tracking. *Energy Conversion and Management*, 50(6): 1506–1512. http://dx.doi.org/10.1016/j.enconman.2009.02.015.

APPENDIX

Appendix 1: US missions using radioisotope thermoelectric generators

Space Craft	Power Source	#RTG	Mission	Launch Date	Status
Transist 4A	SNAP-3B7	1	Navigational	June 1961	RTG operated for 15 years and shut down
Transist 4A	SNAP-3B8	1	Navigational	Nov 1961	RTG operated for 9 years and shut down
Transist 5BN-1	SNAP-9A	1	Navigational	Sep 1963	RTG operated for 9 months and failed after 9 months
Transist 5BN-2	SNAP-9A	1	Navigational	Dec 1963	RTG operated for over 6 years
Transist 5BN-3	SNAP-9A	1	Navigational	April 1964	Mission aborted
Nimbus B-1	SNAP-19B2	2	Meteorological	May 1968	Mission aborted
Nimbus 111	SNAP-19B3	2	Meteorological	April 1969	RTG operated for 2.5 years
Apollo 12	SNAP-27	1	Science Station	Nov 1969	RTG operated for 8 years and shut down
Apollo 13	SNAP-27	1	Science Station	April 1970	Mission aborted
Apollo 14	SNAP-27	1	Science Station	Jan 1971	RTG operated for 6.5 years and shut down
Apollo 15	SNAP-27	1	Science Station	July 1971	RTG operated for 6 years and shut down
Pioneer 10	SNAP-19	4	Payload & Spacecraft	Mar 1972	Spacecraft now well beyond orbit of Pluto
Apollo 16	SNAP-27	1	Science Station	April 1972	RTG operated for 5.5 years and shut down
Triad-01-1XTransit	Transit	1	Navigational	Sep 1972	Still operating as of mid-1990's
Apollo 17	SNAP-27	1	Science Station	Dec 1972	RTG operated for 5 years and shut down
Pioneer 11	SNAP-19	4	Payload & Spacecraft	April 1973	Spacecraft now well beyond orbit of Pluto
Viking 1	SNAP-19	2	Payload & Spacecraft	Aug 1975	RTG operated for 6 years and shut down
Viking 2	SNAP-19	2	Payload & Spacecraft	Sep 1975	RTG operated for 4years until relay link was lost
LES 8, LES 9	MHW	4	Communication	March 1976	LES 8 shut down in 2004. LES 9 still operating

Voyager 2	MHW	3	Payload & Spacecraft	Aug 1977	Still operating
Voyager 1	MHW	3	Payload & Spacecraft	Sep 1977	Still operating
Galileo	GPHS	2	Payload & Spacecraft	Oct 1989	Still operating
Ulysses	GPHS	1	Payload & Spacecraft	Oct 1990	Operated until 2008 and deactivated
Cassini	GPHS	3	Payload & Spacecraft	Oct 1997	Still operating
New Horizons	GPHS	1	Payload & Spacecraft	Jan 2006	Still operating